

Enhancing Lock Gate Design

Estimation of collision energy through data analysis and non-linear structural models

Sander Koster

Enhancing lock gate design: estimation of collision energy through data analysis and non-linear structural models

MSc thesis

by

Sander Koster

to obtain the degree of Master of Science
at the Delft University of Technology,

Student number:	5159253
Project duration:	September 11, 2023 – May 28, 2024
Thesis committee:	Prof. Dr. Ir. S.N. Jonkman, TU Delft, chairman Dr. Ing. M.Z. Voorendt, TU Delft, 1 st supervisor Dr. F. Kavoura, TU Delft, 2 nd supervisor Ir. B.L. Goeijebier, Witteveen+Bos

An electronic version of this thesis is available at <http://repository.tudelft.nl/>.

Abstract

In the Netherlands, there are hundreds of operational locks for both recreational and inland shipping. Due to the growing economy, inland shipping is expected to increase in the future. The growing economy causes an increased likelihood of ship collisions with infrastructure, currently estimated at approximately 50 cases per year in the Netherlands. It is necessary to determine the collision energy of a vessel to account for collisions, because this clarifies the potential load. In the context of determining the collision energy for ship collision, the guidelines of the Eurocode, PIANC, and AASHTO involve uncertainties and exhibit variability among them. Therefore, this thesis was initiated to provide more accuracy in the estimation of collision energy in the event of ship-lock collisions. The main objective of this thesis was to enhance the structural design process of lock gates regarding ship-lock collisions. This was done by improving the understanding of the effect of potential loads occurring at a ship-lock collision, and using basic mechanics to estimate the energy absorption capacity of the lock gate. Refer to the structural design process in the flowchart of Figure 1. This process was developed and applied based on the Macharen lock, a lock from which data was available at Witteveen+Bos.

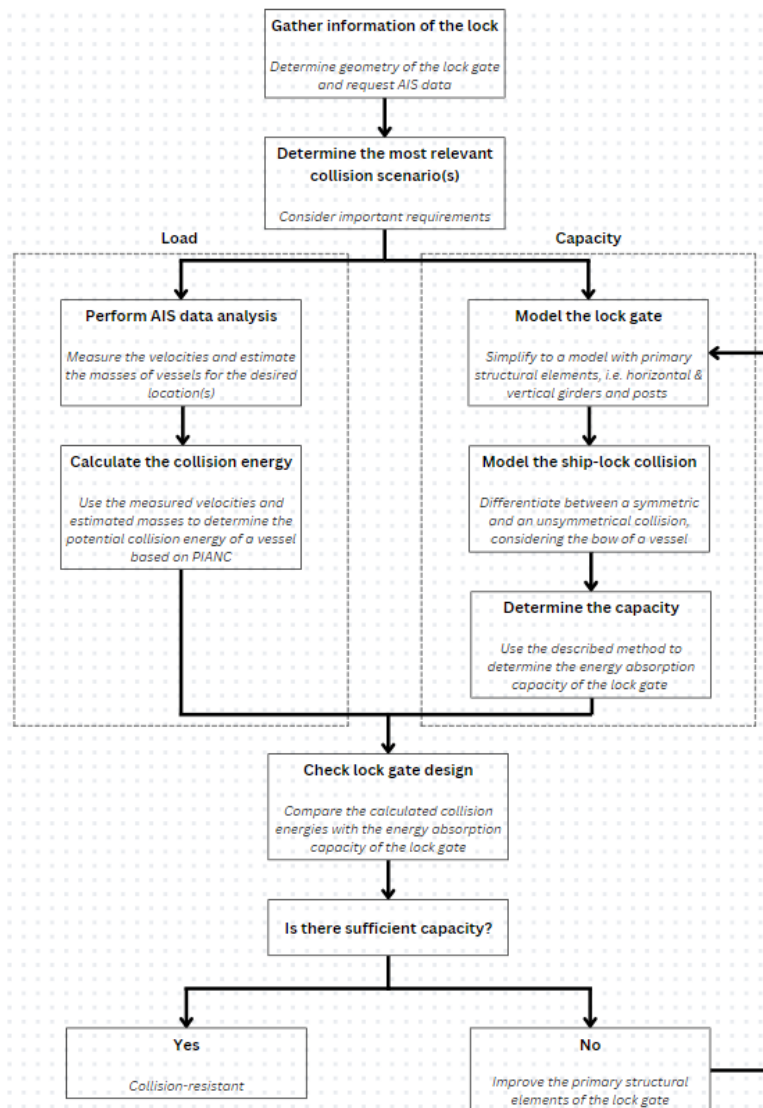


Figure 1: Structural design process of a lock gate for determining the collision resistance

The lock at Macharen is non-operational almost all year round and only becomes operational when the water level on the Meuse River is higher than NAP +5.2 m. For this lock, the potential load, i.e. collision energy, was determined, which depends on two crucial parameters: velocity and mass. AIS data was therefore collected for the Macharen lock case, and vessels were measured around the lock. Following the AIS data analysis, it was concluded that the overall dataset's average velocity and most of the maximum velocities were well below the prescribed velocity of 3 m/s from the Eurocode (2015). The low average velocity resulted in the average calculated collision energy per CEMT class being lower than the prescribed values in the Eurocode. The prescribed range in PIANC was so diverse that both the average and maximum calculated collision energy per CEMT class fell within the extreme values of this norm. The calculated energies from the AIS data were derived for a non-operational lock situation where velocities were generally higher compared to an operational lock situation. For an operational lock only limited data was available, which made it less representative.

After determining the potential load on the lock gate, the Macharen lock gate was modelled using the finite element analysis software RFEM. This software allowed for the incorporation of nonlinear properties in the gate model. The lock gate was modelled with plate elements and included horizontal & vertical girders, stiffeners, a skin plate, struts, and a mitre- & heel post. The influence of the stiffeners, skin plate, and struts on the energy absorption capacity was considered insignificant after conducting a sensitivity analysis. Factors like mesh size and steel quality were found to significantly impact the overall capacity of the lock gate model, with finer mesh sizes and higher steel quality leading to more accurate results and increased capacity, respectively. While hydrostatic water pressure became relevant in later stages of determining energy absorption capacity, the self-weight did not impact the capacity in this context.

The Macharen lock gate model was validated using an analytical model. This was achieved by simplifying the Macharen lock gate model so that it remained representative of the original gate model. Both the critical bending moment and lateral torsional buckling moment were assessed. The differences in outcomes between the analytical and simplified gate model appeared to be at most 10%. The differences were mainly caused by the posts of the lock gate, resulting in the girder behaving more like a clamped girder, and by the fact that the gate model was constructed using plate elements.

After the validation, the validated gate model was used to calculate the energy absorption capacity for the Macharen lock gate. First, the force and deformation of the impacted structural component were determined corresponding to the fracture strain of 5%, i.e. moment of failure, and served as the output of RFEM. The obtained force-deformation diagram from this output was used to construct the force-energy diagram, where the energy was equal to the area beneath the force-deformation diagram. This process was repeated for each impacted girder or set of girders for both an unsymmetrical (eccentric) and a symmetrical (center) collision, respectively. The higher energy absorption capacity was observed in the case of a symmetrical collision, which was because the mitre gates exhibited relatively stiff properties when impacted symmetrically. This property resulted in an higher load capacity but lower deformation compared to that of an unsymmetrical collision. In case of an unsymmetrical collision, a distinction was made in calculation methodology, namely method *a* & *b*. Method *a* assumed an undeformed state as initial state, and the exclusion of a loaded girder from the model after reaching the fracture strain. Method *b* assumed a deformed state as initial state, thereby considering the influence of an already deformed girder on the next girder. It was concluded that the results obtained from calculation method *b* were more reliable because it came closer to what will happen in reality.

The application of the method to determine the energy absorption capacity and the sensitivity analysis revealed that the majority of capacity came from the horizontal girders and the mitre- and heel posts. It was therefore most effective to modify these structural components to improve the lock gate's capacity in terms of energy absorption. Improvements to the original lock gate lay-out were analysed, including an increase in the quantity and cross-sectional dimensions of the horizontal girders, and an improvement involving closing the box profile of the posts. Each improvement individually showed an increase in energy absorption capacity. It was found that adding extra horizontal girders was the most effective individual improvement. The combination of all these improvements in one design resulted in additional energy absorption capacity for the lock gate. This was verified for by comparing the calculated collision energies with the capacity of the lock gate. In this analysis, it was possible to determine which portion of the dataset led to the complete failure of the respective lock gate design.

After completing all the steps of the thesis, these steps, i.e. the used design process, were generalised into an universally applicable methodology for determining the collision resistance of a lock gate (refer to Figure 1). It was concluded that the design process could be applied to other or new locks with varying conditions. The used structural design process of a lock gate concerning ship-lock collisions confirmed therefore its applicability to the Macharen lock and other locks. The structural design process was enhanced based on two steps: accurately determining the load on a lock gate and its energy absorption capacity. This was achieved by using AIS data to determine potential loads during ship-lock collisions and employing basic mechanics to estimate the energy absorption capacity. These enhancements enabled an accurate estimation of the collision resistance of a lock gate.

One of the main recommendations was to consider other collision scenarios. Currently, only a collision with the inner lock gate from the upstream direction was considered in the thesis because it was critical in terms consequence, i.e. flood protection, and probability. Additionally, conducting an additional case study of an operational lock with similar dimensions could provide a more representative comparison with the dataset of the non-operational lock.

Preface

This MSc thesis has been written as the final assignment to obtain my Master of Science degree at the Delft University of Technology, specialising in hydraulic engineering with a focus on hydraulic structures. Throughout the process, I received guidance and support from Ir. Bart Goeijenbier, representing the company Witteveen+Bos. I would like to take this opportunity to thank him for all the assistance over the past few months.

I look back with great pleasure on the past educational period during which I wrote my thesis. I would like to express my gratitude to Witteveen+Bos for providing me with the opportunity to carry out my graduation project at their company. I look forward to working here after my graduation.

I would also like to thank my graduation committee from Delft University of Technology consisting of Prof. Dr. Ir. S.N. Jonkman serving as chairman, Dr. Ing. M.Z. Voorendt as the primary supervisor and Dr. F. Kavoura as second supervisor. Without my committee, this report would not have been as it is now.

Finally, I would like to thank my friends and family for their support during this period, but also throughout the rest of my studies. Without them, none of this would have been possible.

Sander Koster
Rotterdam, 21 May 2024

Contents

Abstract	iii
Preface	vii
1 Introduction	1
1.1 Motivation for this thesis	1
1.2 Relevance of this thesis	2
1.3 Problem analysis	3
1.3.1 Basic collision energy principle	3
1.3.2 Guidelines & standards	3
1.3.3 Present state of research	7
1.3.4 Problem statement	7
1.4 Objective & scope	7
1.4.1 Main objective	7
1.4.2 Research questions	8
1.4.3 Scope	8
1.5 Approach & report structure	8
1.5.1 Main approach	8
1.5.2 Report structure	9
2 Ship-lock physics	11
2.1 Lock characteristics	11
2.1.1 Locking process	11
2.1.2 Gate types	12
2.1.3 Transfer of loads through mitre gate	14
2.1.4 Typical steel properties	16
2.2 Vessel's properties	18
2.2.1 Relevant information coming from AIS data	18
2.2.2 Bow geometry inland vessel	19
2.2.3 Mass approximation inland vessel	20
2.3 Ship-lock interaction	21
2.3.1 Characteristics different types of modelling	21
2.3.2 Collision scenarios	22
2.3.3 Point of contact - mitre gate	23
2.3.4 Determination of the vessel limit speed	23
3 Case description & AIS data analysis - Macharen lock	26
3.1 Lock system overview	26
3.1.1 Case introduction	26
3.1.2 System description	27
3.1.3 Governing vessel dimensions	27
3.1.4 Lock chamber geometry	27
3.2 Inventory of boundary conditions	28
3.2.1 Measurement locations	28
3.2.2 Vessel type movements	29
3.2.3 Average & maximal mass per CEMT class	29
3.2.4 Vessel limit speed	30
3.2.5 Closing data	31

3.3	Velocity analysis	31
3.3.1	Velocities at location E - the inner lock gate	31
3.3.2	Velocities at all locations	33
3.3.3	Velocities at all locations during closing	34
3.4	Collision energy analysis	35
3.4.1	Collision energy non-operational lock	35
3.4.2	Collision energy operational lock	36
3.4.3	Collision energy based on norms	37
3.5	Conclusion on AIS data analysis	38
4	Numerical modelling of ship collision on the Macharen lock gate	40
4.1	Input parameters & boundaries	40
4.1.1	Lock gate structure	40
4.1.2	Modelled steel properties	41
4.1.3	Mesh size	42
4.1.4	Surface contact gates	42
4.1.5	Nodal & line support	42
4.2	Schematisation of a collision between vessel and lock gate	43
4.2.1	Type of collision per CEMT class	43
4.2.2	Determination collision height and depth	44
4.2.3	Applied load (un)symmetrical collision	45
4.3	Sensitivity analysis based on original design Macharen lock	46
4.3.1	Influence of all structural components	46
4.3.2	Mesh size & strength properties	48
4.3.3	Hydrostatic water pressure & self-weight lock gate	49
4.4	Conclusion on numerical modelling gate model	50
5	Validation of the numerical gate model	51
5.1	Development of analytical collision model	51
5.1.1	Description of the static system	51
5.1.2	Determination section values of the horizontal girders	52
5.1.3	Calculation of critical bending moment	54
5.1.4	Calculation of critical lateral torsional buckling moment	54
5.2	Simplified gate model results	56
5.2.1	Geometrically linear analysis	56
5.2.2	Large deformations analysis	57
5.3	Conclusion on validation gate model	58
6	Collision energy absorption capacity of the Macharen lock gate	59
6.1	Description of a method to calculate absorbable collision energy	59
6.1.1	Procedure of the method	59
6.1.2	Description of the collision phases	60
6.2	Application of the collision energy absorption method to Macharen lock	62
6.2.1	Determination of the energy absorption in case of an unsymmetrical collision	62
6.2.2	Determination of the energy absorption in case of a symmetrical collision	68
6.3	Conclusion on energy absorption capacity Macharen lock gate	71
7	Macharen lock gate improvements for better energy absorption capacity	73
7.1	Improvements of the gate layout	73
7.1.1	Change in geometry cross-section horizontal girders	73
7.1.2	Increasing the number of horizontal girders	75
7.1.3	Closing the box profile of the mitre- and heel posts	77
7.1.4	Comparison of improved gate layouts	78
7.2	Quantification of the improvements	79
7.2.1	Principle of quantifying the improvements	79
7.2.2	Energy absorption capacity: Original lock gate design in S235 steel	80
7.2.3	Energy absorption capacity: Original lock gate design in S355 steel	81
7.2.4	Energy absorption capacity: New lock gate design	82

7.3	Conclusion on improving energy absorption capacity	83
8	Generalisation of the used structural design process	84
8.1	Application to other (new) locks	84
8.1.1	Difference in relevant collision scenario(s)	84
8.1.2	Varying measured velocities from AIS data	84
8.1.3	Other types of lock gates	85
8.1.4	Collision of a seagoing vessel with a lock gate	86
8.1.5	Usage of other types of material	87
8.2	Conclusion on generalisation	87
9	Discussion, Conclusions and Recommendations	88
9.1	Discussion	88
9.1.1	AIS data analysis	88
9.1.2	RFEM	88
9.2	Conclusions	89
9.3	Recommendations	90
	References	92
A	CEMT classes	95
B	Vessel bow shape	97
C	Graphs & box plots AIS data	101
C.1	Velocities per location (South-going traffic)	102
C.2	Collision energy per standard	104
D	Results RFEM sensitivity analysis Macharen lock gate	109
D.1	Load & deformation capacity scenario 1 & 2	110
D.2	Load & deformation capacity scenario 3	121
D.3	Load & deformation capacity scenario 4	128
E	Results RFEM gate model validation	135
E.1	Simplified gate model RFEM results	136
F	Buckling capacity horizontal girders	148
F.1	Determination buckling stability	148
G	Results RFEM for determining energy absorption capacity	151
G.1	Unsymmetrical collision phase 1	152
G.2	Unsymmetrical collision phase 2a	158
G.3	Unsymmetrical collision phase 3a	163
G.4	Unsymmetrical collision phase 2b & 3b	168
G.5	Symmetrical collision	175
H	Index vs. Energy plots per CEMT class	192
H.1	Original lock gate design in S235 steel	192
H.2	Original lock gate design in S355 steel	195
H.3	New lock gate design in S355 steel	198

Introduction

1.1. Motivation for this thesis

On August 29 2020, the vessel "Else" collided with the Kiel-Holtenau lock in the Kiel Canal (refer to Figure 1.1). The "Else" proceeded past the pilot's boarding position without taking a sea pilot on board and impacted the closed gate of the new north lock from the outside. The vessel's bow penetrated the metal structure, resulting in it being stuck there for approximately six hours. The collision caused damage to the vessel's forward section, with paint abrasions and minor dents above the waterline. A significant crack was observed in the forepeak below the waterline, causing seawater to flood into the ballast tank up to the waterline (Kaspera, 2022). This damage did not lead to a substantial loss of the vessel's buoyancy or stability.



(a) Multi-purpose vessel "Else" with her bow in the lock gate



(b) Damage to the "Else's" bow above the waterline

Figure 1.1: Multi-purpose vessel "Else" collision with lock gate (Kaspera, 2022)

The lock gate, which was fully closed when the accident occurred, sustained severe deformation due to the impact from the vessel's bow. The bulbous bow of the vessel protruded roughly 2 meters into the tank section of the gate, causing structural damage to the gate and the steel girders in the accident area. Extensive repairs were required, and the gate had to be replaced with a spare one.

Another example of a collision with a lock gate occurred more recently on November 11th 2023, in the South German town of Iffezheim. Due to inattention of the skipper, the vessel collided with the outer gate of the lock while another vessel was in the process of locking through. The collision caused such a powerful impact that nearly the entire gate was removed, creating a large water flow that equalised the water level on both sides of the lock. According to the German water police, it will take months to repair the lock gate. Presumably, it may need to be entirely replaced, incurring an estimated cost of approximately €1.5 million (Bahr, 2023). The vessel itself suffered only minor damage.

1.2. Relevance of this thesis

Locks are used worldwide to connect two waterways with different water levels. In the Netherlands alone, there are hundreds of operational locks for both recreational and inland shipping. Due to the growing economy, maritime traffic is expected to increase in the future. In the year 2021, there was an increase of 5.8% in tonnage of goods observed in the inland shipping industry compared to the year 2020 (CBS, 2022). Not only is the intensity increasing, but the vessels are also becoming larger. This directly affects the potential load on a structure, as an increase in vessel size is accompanied by an increase in load.

Figure 1.2 shows the number of serious collisions on the Dutch waterways from the year 2016 to 2021. An accident is considered serious if:

- a vessel cannot or may not continue to sail as a result of the accident;
- there is serious damage to cargo, infrastructure or the environment and this results in an obstruction of the shipping lane;
- there are fatalities or serious injuries.

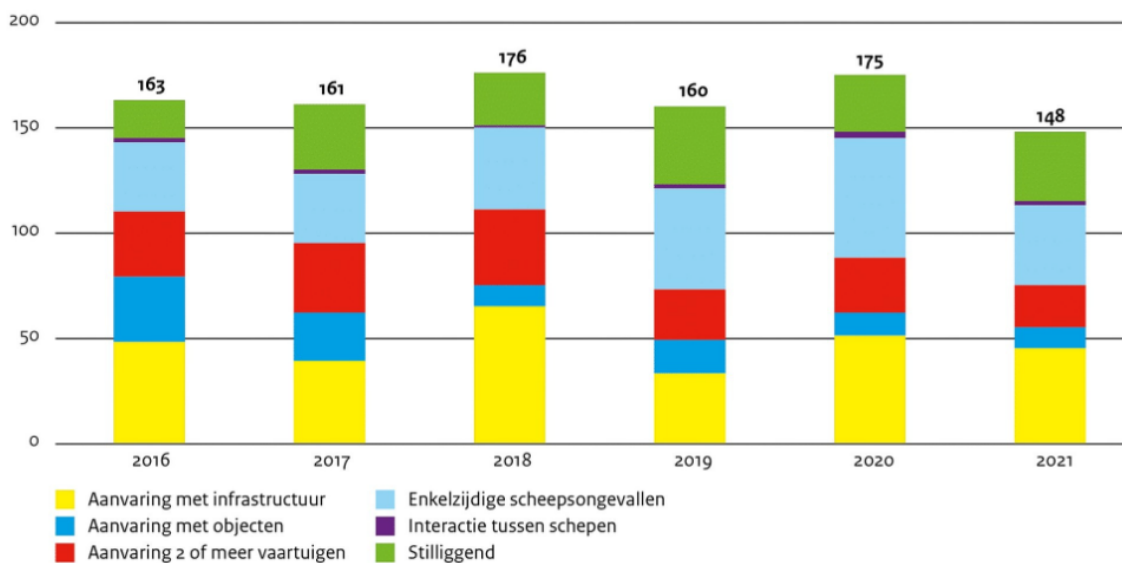


Figure 1.2: Graph with overview of the number of serious shipping accidents between 2016 and 2022. Yellow: collision with infrastructure; dark blue: collision with objects; red: collision involving two or more vessels; light blue: one-sided shipping accidents; purple: interaction between vessels; green: stationary (Buitendijk, 2022)

From Figure 1.2, it can be observed that collisions with infrastructure, including collisions with a lock gate, account for approximately 50 cases each year on Dutch waters. This includes collisions with bridge components (such as bridge piers). In reality, the number of serious collisions with a lock gate is therefore lower than 50 cases per year. However, this still demonstrates that serious damage is frequently caused as a result of a collision, highlighting the relevance of this topic. It should be emphasised that when a collision happens, the damage can be severe. Such damage can result in the temporary or even permanent loss of the primary function of the structure, such as retaining water within a lock or facilitating the passage of vessels. In the worst-case scenario, the lock will lose its water-retaining function, and the safety of the hinterland can no longer be guaranteed. The inability to ensure vessel passages results in vessels arriving late at their final destinations, which is adverse to a country's economy.

In Appendix B of the Eurocode (2015), a table is provided illustrating the relation between consequence and the maximum acceptable risk levels of a collision (see Table 1.1). In this context, consequences are categorised from very low to severe each associated with an acceptable probability of occurrence. Severe denotes the sudden collapse of the structure with a high likelihood of loss of life and injuries. Very low relates to local damage of minor significance. The probabilities increase from 0.00001 to 0.01 for severe to very low consequences respectively. This indicates that the likelihood of a collision is high, but extreme consequences are rare. In the Eurocode it is mentioned that the estimated probabilities are generally at least partially based on an assessment and may for that reason significantly deviate from actual failure frequencies.

Ernstig	X				
Hoog	X				
Gemiddeld		X			
↑ Laag			X		
Zeer laag				X	
gevolg					
kans	0,00001	0,0001	0,001	0,01	> 0,1
X geeft voorbeelden van maximaal aanvaardbare risiconiveaus					

Table 1.1: The table plotting the consequence against the maximum acceptable risk levels. (Eurocode, 2015)

In the coming decades, many of the locks in the Netherlands will either reach or have already reached their design lifespan, which typically ranges from 50 to 100 years. This implies the need for renovation, significant upgrades, or the demolition and replacement of these locks with new navigation structures designed to meet future standards. Failure to perform these activities in a timely manner or neglecting it can result in a weaker overall structure, which may lead to a reduced absorbable energy capacity in the event of a potential collision.

This MSc thesis aims to improve the understanding of potential loads occurring at a ship-lock collision and seeks to enhance the structural design process of lock gates concerning ship-lock collisions.

1.3. Problem analysis

1.3.1. Basic collision energy principle

Various codes and guidelines have been developed to estimate the force exerted by a vessel colliding with an hydraulic structure, often quantified as collision energy. The vessel's velocity is a crucial parameter that significantly influences the collision energy, since this parameter is squared in the calculation of kinetic energy (Equation 1.1).

$$E = \frac{1}{2}mv^2 \quad (1.1)$$

In which:

E = collision energy [Nm]

m = mass of the vessel [kg]

v = approach velocity of the vessel [m/s]

This formula serves as the basis for determining the collision energy, but achieving a more precise value requires further refinement. While standard values for the approaching velocity to a lock are commonly provided, they are not fundamentally fixed. The vessel's mass is often not precisely defined in practice. Various ship classes (CEMT-class) are associated with it, providing a specific range of mass. This range is frequently used as an indication but can be further refined for increased accuracy. The type of cargo and whether the vessel is loaded or not, plays a significant role in this regard. The utilisation of Automatic Identification System (AIS) data can offer valuable insights from practical experiences, enabling more cost-effective future designs and facilitating control checks of existing structures.

1.3.2. Guidelines & standards

The most commonly used standards for determining the collision energy are discussed in this section, along with their respective limitations. One notable difference that is observed upfront is that some methods incorporate more variables into the energy determination than other methods.

Eurocode

In the NEN-EN 1991-1-7 (Eurocode, 2015), a separate chapter is included for extraordinary loads caused by maritime traffic. The Eurocode states that extraordinary loads due to ship collisions should be determined taking into account, among other aspects, the type of waterway, flow conditions, CEMT classification, and

the type of structure and its energy dissipation behaviour. Annex C of the Eurocode provides an indicative classification for such vessels.

In the Eurocode, a distinction is made between elastic deformations (when $E_{def} \leq 0.21$ MNm) and plastic deformations (when $E_{def} > 0.21$ MNm). The deformation energy E_{def} is equal to the available total kinetic energy E_a in the case of a frontal collision. However, in the case of a lateral collision with an angle $\alpha < 45^\circ$, expression 1.2 must be used (Eurocode, 2015).

$$E_{def} = E_a \times (1 - \cos(\alpha)) \quad (1.2)$$

For all possible ship categories, along with their distribution of masses and velocities, the collision energy is calculated using the formula below (Eurocode, 2015).

$$E_a = C_H \times m \times v^2 \quad (1.3)$$

In which:

- C_H = 0.5 plus an extra 10% to take into account the added water mass
- E_a = collision energy [MNm]
- m = mass of the vessel [kg]
- v = approach velocity of the vessel (= 3 [m/s]) (Eurocode, 2015)

Limitations Eurocode:

- When not specified for the project, a recommended design value for the velocity v is 3 m/s added to the water velocity (Eurocode, 2015). In reality, this value could be lower as the vessel will be slowed down by effects within the lock chamber (e.g. cushioning effect and/or return flow effect) and external factors such as braking works / signalling;
- In this model, the dissipation of collision energy takes place entirely in the vessel. This model is correct for structures like massive bridge piers that are the main concern of the Eurocode. For elastically and plastically deformable structures like lock gates this model is, generally, not sufficiently realistic (PIANC, 2014).

An addition to the Eurocode is provided by Richtlijnen Ontwerp Kunstwerken (ROK), where the maximum achievable vessel velocity is specified (Table 1.2). For the velocity of a vessel in the event of a collision, the maximum velocity for a loaded vessel in open water must be observed, increased by the flow velocity of the waterway (Beguin, 2017). The maximum achievable vessel velocity relative to the waterway depends on the ship type, the type of waterway, and the degree of loading. Crucial for determining the collision energy is the velocity of the loaded vessel. A vessel requires a minimum water depth under the keel and a minimum water width alongside the vessel to achieve the maximum velocity indicated in Table 1.2. If the water depth under the vessel becomes too shallow, the vessel's propeller may no longer use its full thrust. If the water width alongside the vessel becomes too narrow, it hinders the return flow and increases the resistance.

Klasse	0	I	II	III	IV	Va	Vb t/m VII
Snelheid [m/sec]	Vaste botskracht	4,1	4,8	5,1	5,3	5,5	4,5

Table 1.2: Prescribed maximum ship velocity per CEMT class based on ROK (Beguin, 2017)

PIANC

The French Institute for Inland and Maritime Waterways (CETMEF) proposes a specific methodology to analyse a collision scenario. CETMEF offers a range of services to government and public entities, including the publication of guidelines for safeguarding lock gates from ship collisions. The main reason for the World Association for Waterborne Transport Infrastructure (PIANC) adopting this approach is that the CETMEF guidelines assume a collision model in which both the vessel and the gate are treated as deformable and capable of dissipating collision energy. Additionally, these guidelines consider the gate to generally dissipate more energy than the vessel (PIANC, 2014). These assumptions typically provide a more accurate representation of the dynamics of a vessel colliding with a lock gate compared to the Eurocode and certain other national

regulations. The impact force of a vessel colliding with a lock gate is directly proportional to the vessel's initial kinetic energy:

$$E = C_m \times C_c \times C_s \times \frac{M_0 \times V_0^2}{2} \quad (1.4)$$

In which:

C_m = the mass coefficient [-]

C_c = the confinement coefficient [-]

C_s = the ship coefficient [-]

M_0 = mass of the striking vessel [kg]

V_0 = velocity of the vessel in collision [m/s]

Mass coefficient

The mass coefficient C_m is used to consider hydrodynamic effects in the analysis. One aspect to consider is the added mass of water, which is typically assumed to be 20% of the vessel's displacement in the longitudinal direction. This value needs to be added to the vessel's mass. Currently, it is common practice to use $C_m = 1.2$ [-] (PIANC, 2014). However, it is important to note that the hydrodynamic aspect is directly influenced by the shape of the striking bow.

Confinement coefficient

When a vessel approaches a closed structure and the gap between its hull and the vertical wall is narrowing, the water between the vessel and the wall will be squeezed away. This phenomenon depends on several factors (PIANC, 2002):

- Keel clearance;
- Velocity and angle of approach;
- Vessel's hull shape.

A laterally mooring vessel can build up a significant "water cushion" when mooring directly, due to its considerable length and relatively small clearance at the bottom. This water cushion helps limit the impact of the vessel on the mooring facilities. If a vessel collides with the gate, it will happen with the bow, which has a limited cross-section and is designed to move through water easily. As a result, it is unlikely that a significant water cushion will build up between the bow of the vessel and the lock gate, which would have a substantial decelerating effect. However, the suggested value in from CETMEF is $C_c = 0.8$ [-] (PIANC, 2014).

Ship coefficient

The softness factor or ship coefficient is determined by the ratio between the elasticity of the fender system (i.e. structure) and that of the vessel's hull. A part of the kinematic energy will be absorbed by elastic deformation of the hull. There is made a distinction between two types of interaction between vessels and structures (PIANC, 2002):

- for soft structures and/or small vessels $C_s = 1.0$ [-];
- for hard structures and/or large vessels $C_s = 0.9 - 1.0$ [-].

So not all of the initial kinetic energy is entirely absorbed by the gate involved in the collision. Consequently, $C_s \leq 1.0$, indicating that the absorbed energy is less than the total initial kinetic energy. The value of C_s depends on the relative stiffness between the striking vessel and the gate. According to the CETMEF, C_s should equal 1.0 for modern vessels, as they are relatively rigid (PIANC, 2014).

Velocity of the vessel

This value is typically ranging from 0.5 m/s to 2 m/s (PIANC, 2002). Based on Equation 1.4, it is evident that the parameter E is primarily influenced by the velocity V_0 , which is raised to the power of 2. Consequently, obtaining an accurate estimation of V_0 is crucial. If statistical data is accessible, it is advisable to determine a representative value of V_0 that corresponds to a probability of occurrence ranging from 10^{-4} to 10^{-3} .

Limitations PIANC:

- The confinement coefficient is recommended to be set at a value of 0.8, indicating that consideration is given to the so-called water cushion effect. However, in practice this value is likely to approach 1.0 because the water cushion effect becomes significant primarily during lateral berthing, rather than during longitudinal displacement. Therefore, an accurate calculation is essential before assuming a specific value for this coefficient;
- When determining the ship coefficient, it is assumed that modern vessels are relatively rigid, meaning that the entire energy is absorbed by the lock gate. However, in practice there will always be some energy absorbed by the vessel, although the exact amount remains uncertain. Additionally, there are still 'older' vessels operational using outdated materials. Therefore, a value of 1.0 [-] can be seen as conservative for the assessment of the respective lock gate.

AASHTO

AASHTO (American Association of State Highway and Transportation Officials) describes the design requirements for protecting bridges against collisions with vessels. The document provides guidelines for determining the kinetic energy of vessels and for designing bridges to withstand this energy. The kinetic energy of a moving vessel to be absorbed during a collision with a bridge pier shall be (AASHTO, 2009):

$$KE = \frac{C_H \times W \times V^2}{29.2} \quad (1.5)$$

In which:

- KE = vessel collision energy [kip-ft = 1.356 kNm]
- C_H = the hydrodynamic mass coefficient [-]
- W = vessel displacement tonnages [t]
- V = vessel impact speed [ft/s = 0.305 m/s]

When translated into metric values, the well-known formula for kinetic energy is obtained.

$$E = \frac{1}{2} \times C_H \times m_s \times v_s^2 \quad (1.6)$$

One difference with the Eurocode is that the hydrodynamic coefficient factor C_H is now presented separately. This coefficient depends on various factors, such as water depth, under-keel clearance, vessel shape, vessel speed, currents, vessel position, direction of the vessel, and the cleanliness of the vessel's hull underwater (AASHTO, 2009). For a vessel moving in a straight line, this factor is determined as follows:

$$\begin{aligned} \text{Under-keel clearances} &\geq 0.5 \times \text{Draft}, C_H = 1.05 \text{ [-]} \\ \text{Under-keel clearances} &\leq 0.1 \times \text{Draft}, C_H = 1.25 \text{ [-]} \end{aligned}$$

AASHTO states that the under-keel clearance is the distance between the bottom of the vessel and the bottom of the waterway. The factor C_H between the large and small limit discussed above may be estimated by interpolating.

Limitations AASHTO:

- AASHTO presents guidelines in the context of the United States, a continent where the characteristics of rivers are not comparable to those of Europe. This may result in an overestimation of the hydrodynamic mass coefficient. Additionally, barges are commonly used in the United States (with assistance of tugboats), so the energy dissipation in the event of a collision may differ from that of a typical inland vessel;
- The guideline does not prescribe a specific velocity for the vessel collision design, rather it recommends that the velocity should be determined based on acquired data. Furthermore, in the event of a collision with a bridge pier no consideration is given to any beneficial effects of the return flow or cushioning effect, which can potentially attenuate the velocity of the vessel.

Conclusions

In the context of determining collision velocities for ship collisions, the guidelines of the Eurocode, PIANC, and AASHTO involve uncertainties and exhibit variability among them. The Eurocode recommends a design velocity of 3 m/s but underscores its limitations, particularly for elastically and plastically deformable structures such as locks. PIANC suggests velocities ranging from 0.5 m/s to 2 m/s, emphasising the utilisation of statistical data for accuracy. AASHTO, on the other hand, highlights regional differences and refrains from specifying a particular design velocity, instead recommending its determination based on data analysis.

The Eurocode and the AASHTO method do not provide specific numerical values for ship collision loads on gates. Instead, they offer indicative values for such loads on structures like dam piers, bridge pillars, quay walls and other hydraulic structures. These values are primarily estimated for "hard collisions", where the energy is absorbed through elastic and plastic deformation of the vessel. This stands in contrast to the common engineering approach for hydraulic gates, where energy dissipation is typically assumed to occur within the gate itself.

None of the standards provide a method for determining the load transfer caused by a ship collision. Some standards only prescribe a certain area over which the collision is active or a specific collision load based on ship class and velocity. They all provide an equation to determine the collision energy per vessel, but not how this translates into the force exerted on the gate, and therefore impacts the capacity of the lock gate.

1.3.3. Present state of research

Certainly, this is not the first thesis where ship collisions with a lock gate (or other structure) are investigated. In order to make the problem analysis as specific as possible, it is very useful to examine the recommendations made in previous research on this topic. This is done in several master's theses from Delft University of Technology. These theses were conducted to address the identified limitations in the standards and guidelines.

Edmondson (2017) investigated the applicability of Fiber Reinforced Polymers (FRP) in lock gates. One of the objectives in this thesis was to determine whether the FRP lock gate constructed in Tilburg was able to withstand the governing collision scenario and if the coinciding damage was repairable without replacing the entire gate (Edmondson, 2017). A relevant recommendation of this thesis concerns the effects of minor collisions to the structure. The collision simulated in Edmondson (2017) represents an high-velocity impact designed to simulate the worst-case scenario. The majority of collisions that occur are of a much lesser magnitude. Therefore, documenting the structural response to these less severe collisions holds practical significance.

Research on a deformable, energy-absorbing structure was conducted by van Oorschot (2017). This thesis focused on the protection of static objects against potential ship collisions. Static objects in this context refer to fender systems, dolphin structures, pile-supported systems, etc. The differences between various guidelines (Eurocode, PIANC & AASHTO) become problematic when considering collision speed. This is because the Eurocode prescribes a fixed value, irrespective of the ship class, while the other guidelines calculate velocity based on the maximum velocity of the individual ship classes (van Oorschot, 2017). A relevant recommendation for this thesis is to gain more insight in the collision velocity and thus the energy associated with ship collisions, such that uniformity between the different guidelines is established.

1.3.4. Problem statement

Modelling collisions is a challenging task due to their complex and dynamic nature. These scenarios involve numerous variables. Therefore, they are often simplified in a conservative manner to ensure safety. However, this approach can result in overdimensioned structures, which is undesirable because it can lead to high costs. The problem statement can be formulated as follows:

The determination of the collision energy for ship collisions in the context of structural design is hindered by varying and conservative guidelines from Eurocode, PIANC and AASHTO, leading to uncertainty and potential overdesign. A structural design approach for assessing the impact of this energy could bring improvement, but it is still insufficiently developed for this application.

1.4. Objective & scope

1.4.1. Main objective

The main objective of this thesis is to enhance the structural design process of lock gates regarding ship-lock collisions by improving the understanding of the effect of potential loads occurring at a ship-lock collision.

1.4.2. Research questions

In order to reach the objective formulated in Section 1.4.1, the following main question needs to be answered:

"How can the structural design process of lock gates be enhanced by including ship-lock collision impacts?"

The following knowledge¹ and research^{2,3,4,5,6,7} questions will contribute to answering the main question:

1. What are the collision scenarios that need to be considered in analysing the impact on a lock gate?
2. How can practical information from AIS data improve the accuracy of input parameters for collision energy estimation?
3. How can the collision impact on the lock gate be schematised, and which factors are relevant in this context?
4. Which method can accurately determine the energy absorption capacity of a lock gate?
5. What is the capacity of a lock gate in terms of energy absorption?
6. How can the design of the lock gate be improved to enhance its energy absorption capacity?
7. How can the used structural design process be applied to other locks?

1.4.3. Scope

The scope of this thesis is summarised in Table 1.3.

Scope limitation	Explanation
Collision energy	Only two improvements are investigated in the field of collision energy for this thesis. Firstly, a more accurate estimation of the velocity v is determined, which is a crucial parameter in the formula for calculating collision energy. Additionally, the force transfer is more precisely estimated to closely align with the reality.
CEMT class	This thesis focuses exclusively on vessels categorised under CEMT classes, excluding small recreational boats. Additionally, within the CEMT classes, both vessels and barges are categorised, but this thesis exclusively examines individual, uncoupled vessels. This decision is made because barges and coupled vessels exhibit distinct collision behaviours that require a separate estimation approach, which falls outside the scope of this thesis.
Bow stiffness	Hydraulic structures can be categorised as either stiff or flexible, and this classification influences the calculation methods employed for their analysis. In this thesis, the vessel is considered infinitely rigid, requiring all energy to be absorbed by the lock gates. The energy absorption by the bow has not been included in the thesis. This can be regarded as a conservative approximation.
Gate's material	Large locks typically have gates constructed from steel, hence calculations concerning this type of material are conducted during the course of this thesis.

Table 1.3: Scope limitations plus explanations

1.5. Approach & report structure

1.5.1. Main approach

The thesis is divided into nine steps, which are discussed in this section.

Step 1 - Literature study

A literature study of the physics to understand the way in which collision impact is resisted by lock gates, is discussed in the first step of the thesis. The information from this is necessary for the data analysis of step 3 and building the gate model in step 4. Investigating aspects such as force distribution, material properties and ship-lock interaction. Sub-question 1 is answered in this step of the thesis.

Step 2 - Case description

Following that, an existing lock is analysed to serve as input of the gate model. In this context, the parameters of a lock available at Witteveen+Bos are used as the basis. These parameters include dimensions of the lock chamber, types of lock gates, material usage and other environmental characteristics.

Step 3 - Vessel data analysis

Furthermore, AIS data is analysed to determine the vessel speed and mass of vessels for the case in step 2. This data is obtained from Rijkswaterstaat for the Macharen Lock. This step is executed simultaneously with step 2 and sub-question 2 is answered here.

Step 4 - Model the Macharen lock gate

In this step, the Macharen lock gate is modelled using the finite element analysis software RFEM. Multiple gate layouts are modelled to examine the influence of different structural components of the lock gate on its capacity. In step 4, these layouts are modelled. Research question 3 is answered in this step of the thesis.

Step 5 - Generate and analyse results for Macharen lock gate model

After building and verifying the Macharen lock gate model, initial results are obtained. As explained in step 4, several gate layouts are modelled, each varying in the type of load and the completeness of the structure. The results of these gate layouts are discussed in step 5.

Step 6 - Validate Macharen lock gate model

The Macharen lock gate model is validated by creating a simplified gate model that remains representative of the original gate model. The simplification involves excluding certain components of the lock gate, such as the skin plate, vertical girders, stiffeners, and struts. A suitable approach for accomplishing the validation is by comparing the simplified model with an analytical model, because there is no information available about a real-life case involving a collision. The analytical model here serves to gain a basic understanding of the situation and as comparison for the results of the simplified gate analysis. In this step of the thesis, the analytical model is developed and used for the validation of the simplified gate model in RFEM.

Step 7 - Determine the energy absorption capacity of Macharen lock

After validation, a method is described to determine the energy absorption capacity, and applied to the Macharen lock gate. This is done for both a symmetrical and an unsymmetrical collision. At the end of this step sub-questions 4 & 5 are answered.

Step 8 - Improve the Macharen lock gate model

After applying the described method to the current design of the lock gate, improvements are made to the gate layout to enhance its energy absorption capacity. The results of the improved gate layouts are generated in this step. In addition, the results are compared with the analysed (AIS) data from step 3 to quantify the improvements and determine what percentage of the vessels from the dataset can be stopped by the respective lock gate. At the end of this step sub-question 6 is answered.

Step 9 - Generalisation of the used structural design process

Finally, an examination is conducted in the last step of this thesis to determine whether the used structural design process is applicable to other or new locks. All the above steps are generalised into a universally applicable methodology, followed by a discussion of the differences compared to the Macharen lock. At the end of this step sub-question 7 is answered.

1.5.2. Report structure

By dividing the thesis into these nine steps and applying distinct methodologies to each, the aim is to gain insights into both collision energy quantification and the design of a collision-resistant lock gate. To maintain clarity regarding the steps taken during the thesis, they are summarised in Figure 1.3.

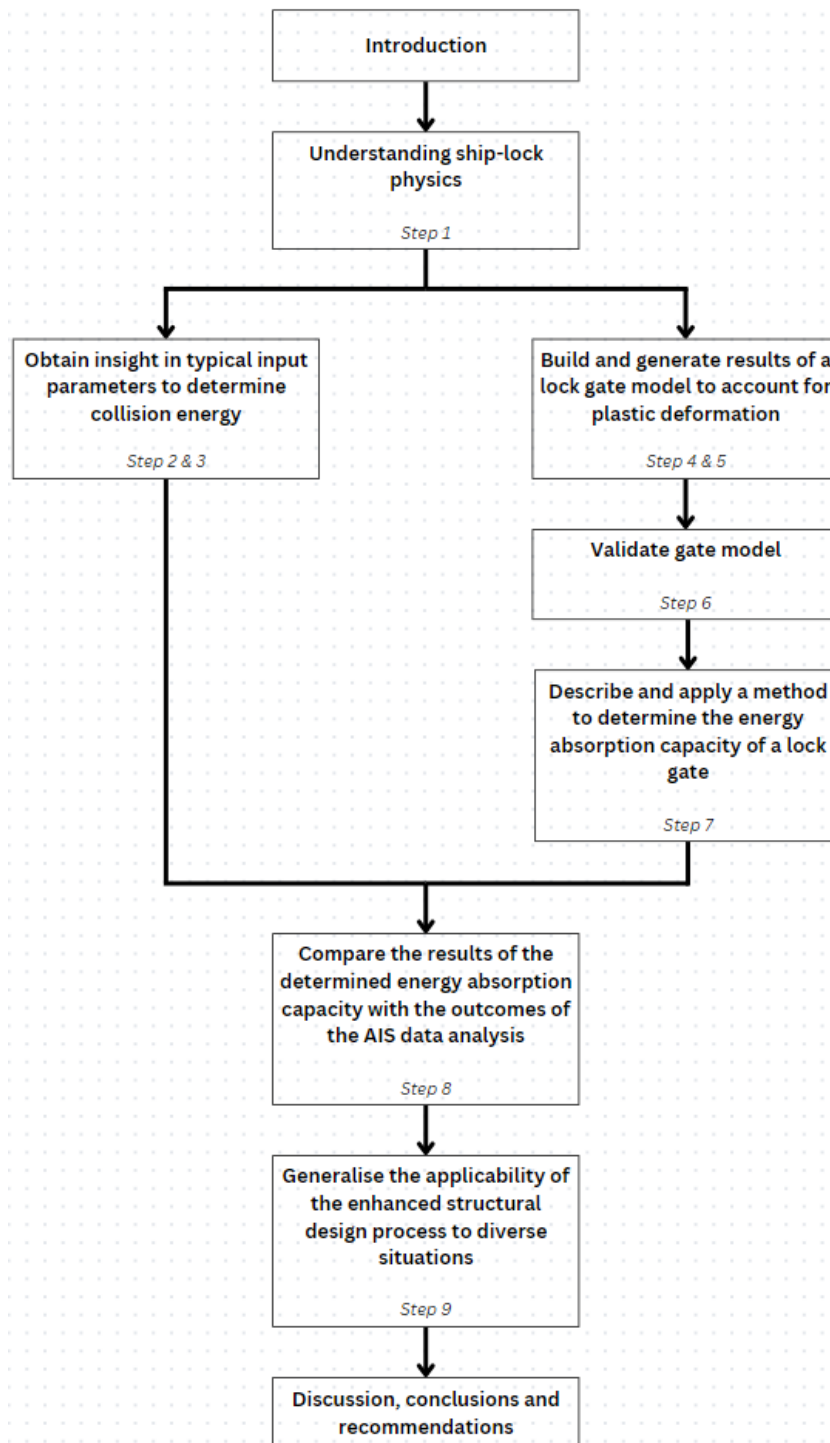


Figure 1.3: Flowchart of the report structure including all steps

2

Ship-lock physics

The objective of this chapter is to gather information from available literature, which serves as the basis for the thesis. Matters discussed in this chapter serve as input for the developed gate model in RFEM and provide justification for specific choices made. First, topics related to a lock in general are discussed. This includes the passage process, types of lock gates, force distribution and used steel properties. Subsequently, vessel characteristics that influence the damage caused by a collision are discussed. Important properties in this context include the bow shape and CEMT-class. The final part of the literature study concerns the interaction between the lock gate and the vessel. In this last part the answer to knowledge question 1: "What are the collision scenarios that need to be considered in analysing the impact on a lock gate?" can be found.

2.1. Lock characteristics

2.1.1. Locking process

The lock process involves several important steps, which are explained in this section and also shown in Figure 2.1. The following actions are consistently maintained for every passage (Rijkswaterstaat, 2017):

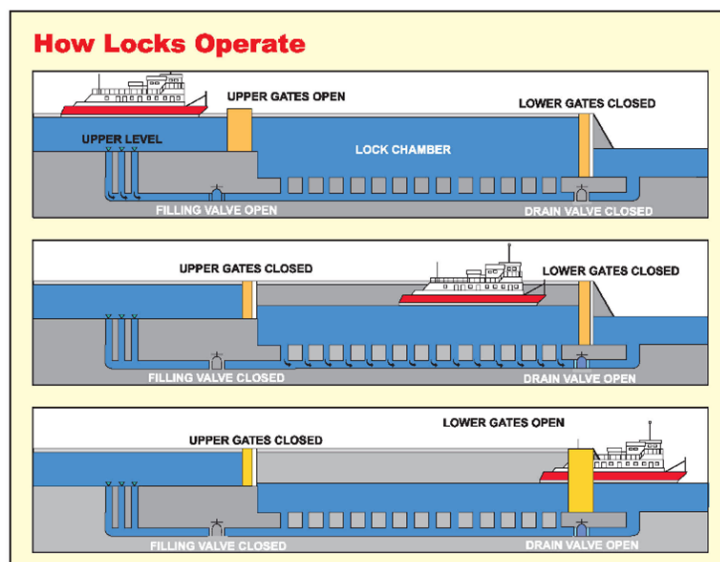


Figure 2.1: Schematic view of how locks operate (District, 2023)

- The initial state assumes that the signal light is red;
- When approaching a lock, the skipper initiates contact with the operator via the VHF radio. The skipper provides their identification, approach direction, and expresses the intention to pass through the lock.

The operator, if applicable, assigns the skipper to a specific chamber, provides the designated passage time, and determines the sequencing or positioning in relation to other vessels;

- Depending on the timing, the skipper either continues sailing or brings the vessel to a halt;
- The operator opens the first lock gate(s) (as seen from the vessel);
- The operator switches the lights in the chamber to green;
- The skipper enters the chamber;
- After the vessels have entered, the operator switches the lock lights to red, closes the rear gates, and then opens the water valves for water leveling. Once the water level is equalised, the operator opens the front gates. After fully opening the gates, they switch the light to green;
- The skipper exits the chamber.

2.1.2. Gate types

In this section, several relevant types of lock gates are discussed including their respective advantages and disadvantages. Gathering information on various types of lock gates is essential, especially considering the presence of multiple types just within the Dutch waterways. This section exclusively focuses on the most prevalent types of gates in Dutch inland navigation. The information obtained from this is used for the generalisation in Chapter 8, where multiple gate types are evaluated.

Mitre gate

A mitre gate comprises two gate panels attached vertically to the lock's top corners within a gate recess. When in the closed position, both panels converge at an angled orientation towards the cross-sectional plane of the chamber, bearing a striking resemblance to the pointed headwear known as a "miter" worn by Catholic bishops. It is from this likeness that the mitre gate derives its name (Daniel and Paulus, 2019). Mitre gates represent one of the earliest and most commonly employed gate types in maritime locks, dock entrances, and port-impounding basins. For small recreational locks these gates are crafted from timber, but larger and more advanced versions are constructed using steel.



Figure 2.2: Mitre gate at Gatun Locks (Safa et al., 2019)

The two common properties of the mitre gate are as follows (Daniel and Paulus, 2019):

- miter-like shape of the two gate leaves in top view, and
- hydraulic load transfer by both bending and compression in the gate leaves.

These two characteristics result in a highly efficient load transfer mechanism. Some engineers argue that the water pressure itself effectively manages the control of mitre gates (Daniel and Paulus, 2019). It places the gate leaves under compression, which stabilises their position and helps seal any potential leakage gaps. In this fixed position, the bending moment is concentrated over a span that is nearly half as long as that in a single-leaf gate. Furthermore, it is possible to position the normal force on girders with some eccentricity toward the downstream side, which generates a reverse bending moment.

The most relevant advantages and disadvantages of mitre gates for collision research are listed below (Daniel and Paulus, 2019).

Advantages mitre gate:

- Water head itself fixes and seals the gate;
- No limit to overhead space for navigation.

Disadvantages mitre gate:

- Closing under flow very difficult;
- Single-sided operation, although low reverse loads can be carried under some provisions.

Vertical lift gate

Vertical lift gates are raised vertically from their static positions using winches and wire ropes or hydraulic cylinders. Typically, the gate is balanced using counterweights. There are different versions, including the double lift gate, which consists of two gate sections placed either adjacent to each other or stacked vertically. These gates feature intricate gate guiding systems, operational mechanisms, and a costly support structure, all of which necessitate routine inspection and maintenance (Charles, 2017).

The majority of existing vertical lift gates primarily transmit hydraulic loads to the piers. This can be referred to as the "traditional" approach for this gate type. It is uncommon for arrangements to transfer hydraulic loads to gate sills, and in exceptional cases, to additional structures along the top edges of closed gates (Daniel and Paulus, 2019). However, such arrangements are feasible and may be preferred under specific conditions. There is also an intermediate approach where most of the loads are directed towards the piers, but the load from the lowest part of the gate's surface is distributed partially to the sill to aid in sealing potential leakage gaps. These arrangements, known as the "elastic plate" concepts, are more commonly associated with rolling and sliding gates.

The most relevant advantages and disadvantages of vertical lift gates for collision research are listed below (Daniel and Paulus, 2019).

Advantages vertical lift gate:

- Closing usually driven by gravity force;
- Closing under flow is possible;
- Double-sided operation easy to realise;
- Many different structural systems possible;
- In locks, hydraulic load transferred in plane of chamber walls.

Disadvantages vertical lift gate:

- Limited navigation due to height restriction;
- Obstacle to sight and radar communication;
- Complex seals and expanding devices when guide wheels are used rather than slide pads;
- Operation in winter can present a problem.

Sector gate

Radial gates with a vertical axis of rotation are commonly known as sector gates. The use of sector gates in navigation locks can be observed in many countries, but the largest and most frequently operated structures of this kind are in the United States (Daniel and Paulus, 2019). The gate's skin plate has a curved shape resembling part of a cylindrical circle and must be reinforced to withstand hydrostatic water pressures, see Figure 2.4. The lower and upper gate arms, which are triangular-shaped trusses in the horizontal plane, provide horizontal and vertical support to the reinforced skin plate. Diagonal braces or struts, are positioned between the upper and lower arms to ensure the necessary vertical stability.

At the rear ends of the gate arms the loads are transmitted to pivot points, which are cast into the lock head wall (Molenaar, 2011). Due to the shape of the skin plate, the resulting force from hydrostatic pressure acts along the pivot's working line.

In contrast to sector gates that hinge horizontally, their vertically hinged counterparts are still commonly used in construction. They are also consistently taken into account in new projects involving navigation lock



Figure 2.3: Vertical lift gate at Gatun Locks (Havang, 2010)

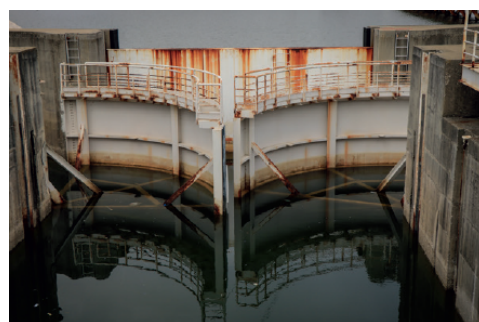


Figure 2.4: Sector gate on the Keitele-Päijänne Canal, Finland (Charles, 2017)

gates and gates for flood and tide barriers. Nevertheless, sector gates also come with their own set of pros and cons, which can be articulated as follows (Daniel and Paulus, 2019):

Advantages sector gate:

- Performs well in control of small as well as large water heads;
- Can carry normal and reverse water heads;
- High availability, gate can be operated both in standing water and under flow;
- Low vulnerability to ship collision on concave side;
- Low hydraulic resistance during motion, fast opening and closing.

Disadvantages sector gate:

- Number of system components relatively high, increased risk of failure;
- High loads during motion;
- Needs a heavily founded, high-precision sill for sealing and roller track;
- The most sensitive components (bottom pin-tles) practically inaccessible for maintenance.

Dalton (2014) conducted research on the nature of global deformation, both elastic and plastic, resulting from ship collisions for three of the most commonly used types of lock gates on American waterways: the mitre gate, the vertical lift gate, and the vertically hinged sector gate. The findings revealed that the sector gate experiences significantly greater deformation before collapsing compared to the other two gate types. Assuming that the kinetic energy of the colliding vessel is the same for all three gates, it follows that the maximum collision force is lower for the sector gate than for the other gate types. To simplify the analysis, Dalton (2014) assumed that the entire kinetic energy is absorbed by the gates, and the deformation response to the load is linear. This implies that the loads resulting from ship collisions are influenced not only by the vessel's geometry and kinetic energy but also by the specific type of gate in use.

2.1.3. Transfer of loads through mitre gate

Lock gates are subjected to loads from various forces in the environment, examples of which include water pressure, self-weight, wind and wave loads. The load transfer of some of these forces is discussed in this section. Which forces are critical for the gate depends on the position in which the gate is located, the position includes being closed, open, or in the process of moving between these positions. However, this thesis focuses exclusively on the closed position of the gate.

When the lock gates are closed, it is possible to equalise the water level inside the lock with the water level outside. This process ensures that the inner gate of the lock does not experience force due to a difference in water level. However, the outer gate will be subjected to a force as a result of this difference. This also applies the other way around. In reality, the forces acting on the lock gates are not only determined by the water level difference; they also include forces generated by wind and waves. However, these loads are negligible in comparison to the collision in inland shipping and are therefore not considered in the thesis.

Water force

The mitre angle α , which is the angle between the plane of the chamber cross-section and the plane of the closed gate leaf, has historically been tightly defined in engineering practice. In both European and American design practices, the recommended value of α should closely align with the angle determined by (Daniel and Paulus, 2019):

$$\tan(\alpha) = \frac{1}{3} \quad (2.1)$$

Figure 2.5 illustrates the geometrical relations and load transfer of a mitre gate (top view). In this simplification, the water force is represented as a point load (W), which can also be applied across the entire cross-section ($W = q \times l$). This resultant hydrostatic load is counteracted by two forces: the force between the two gates of the mitre gate (H) and the force acting on the lock head and vice versa (S). Due to symmetry considerations, the forces H between the two gates at the contact points of the mitre posts are in a state of equilibrium. They possess equal magnitudes but opposite directions. Both H and S can be decomposed into components: one parallel (N) and one perpendicular (F) to the gate. The normal forces are illustrated with an eccentricity (Daniel and Paulus, 2019). N is equal to $1.5 W$ and F is equal to $0.5 W$ if Equation 2.1 holds.

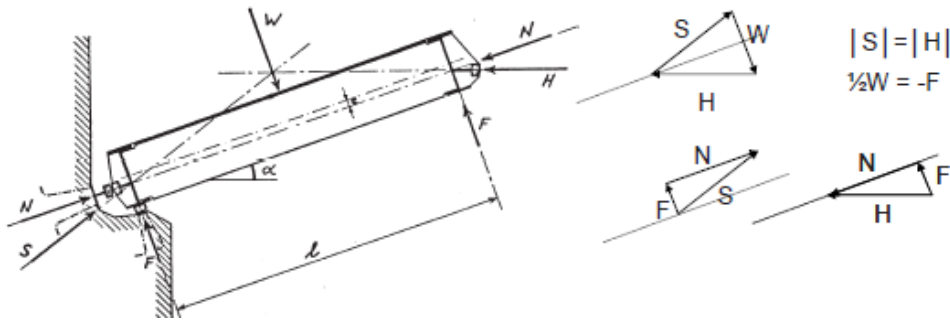


Figure 2.5: Mitre gate geometrical proportions and load transfer (Molenaar, 2011)

The uniformly distributed load is determined based on the difference in water levels. The maximum force is exerted from the height of the downstream water level down to the bottom. The equation describing the distribution of this load is expressed as (Molenaar and Voorendt, 2023):

$$q = \rho_w \times g \times \Delta h \times h_q \quad (2.2)$$

In which:

ρ_w = water pressure [Pa]

g = acceleration due to gravity [m/s^2]

Δh = water level difference [m]

h_q = height over which max. force is exerted (= height of the gate for simplicity) [m]

A cross-section of the structure where the highest distributed force is applied should be considered to determine the stresses. Typically, the cross-section that requires examination is the second or third horizontal girder from the bottom (Schönfeld, 2013). The first girder at the bottom cannot be used because it will deform under the load against the bottom edge, and the girder above the lowest water level will experience a less evenly distributed force. The bending moment for such a cross-section can be expressed as follows (Daniel and Paulus, 2019):

$$M_{max} = \frac{W \times l}{8} - N \times e \quad (2.3)$$

In which:

W = shear force due to water pressure [kN]

l = width of one gate [m]

N = normal force in the cross-section [kN]

e = eccentricity [m]

In a more general scenario, where Equation 2.1 is not necessarily equal to 1/3, the total compression force (N) in the gate and the force between the two doors (H) can be expressed as follows (Molenaar, 2011):

$$N = \frac{W}{2 \times \tan(\alpha)} \quad S = H = \frac{W}{2 \times \sin(\alpha)} \quad (2.4)$$

In which:

$W = \rho_w \times g \times \Delta h \times h_q \times l$

$W = \rho_w \times g \times \Delta h \times A$

To calculate the stresses at the outermost fiber, the bending moment is divided by the section modulus and the normal force by the cross-sectional area. The equation can be expressed as follows (Molenaar, 2011):

$$\sigma = \frac{M}{W} + \frac{N}{A} \quad (2.5)$$

In which:

W = section modulus [m^3]

A = area of the cross-section [m^2]

The distribution of water force on the lock gate depends on the structural design. As can be seen in Figure 2.6a, the gate rests on the lock head wall along the entire height of the heel post. This is possible when there are a relatively large number of horizontal girders in the lock gate, spaced approximately at the same center-to-center distance. The primary load transfer of horizontal water pressure occurs through horizontal internal forces. In agreement with the equal distribution the pivots should have quite some clearance to allow contact, either direct or via sealing (Molenaar, 2011). Consequently, the transfer of loads along the post of the lock head involves distributed line loads N and F from Figure 2.5.

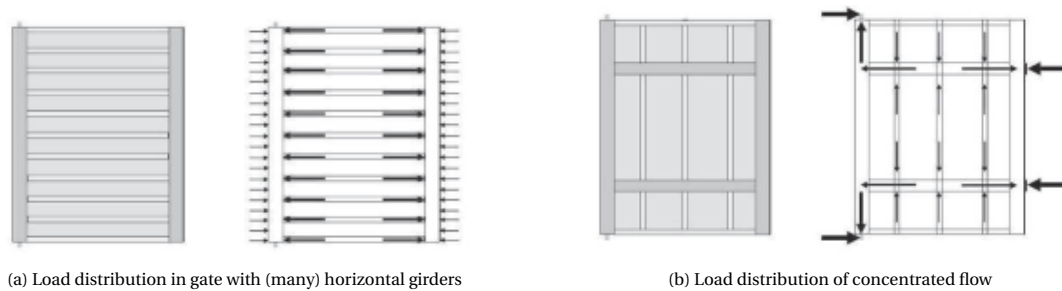


Figure 2.6: Load distribution of different gate design (Molenaar, 2011)

When the design incorporates fewer horizontal girders, the load distribution takes on a different pattern, as illustrated in Figure 2.6b. Instead of a predominant horizontal force flow, a larger proportion of the load is transferred to the supports through vertical routes. The water pressure is transferred from vertical girders to horizontal girders and from there to the heel post, eventually being absorbed by the supports. Both the heel and mitre posts are configured as simply supported. The heel post relies on the upper and bottom pivot, while the mitre post is equipped with two contact points or surfaces that can vary in visibility. Minimal or no clearance will be permitted in the pivots at the heel post (Molenaar, 2011).

Dead weight

Another force that may be significant during the collision process is the self-weight of the lock gate. The downward dead weight (W) is countered by an upward reaction force at the lower pivot point (F_V) (see Figure 2.7). The self-weight applies eccentrically, resulting in a moment that is balanced by an upward tension force at the top F_{Htop} and a compression force at the bottom F_{Hbot} support, both of equal magnitude.

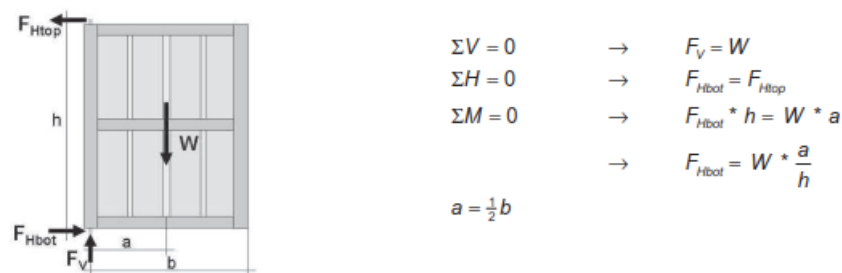


Figure 2.7: Balance of forces self-weight of lock gate (Molenaar, 2011)

2.1.4. Typical steel properties

In this section, the fundamental properties of steel are explained. Structural steel is by far the most frequently used material for the construction of hydraulic gates in inland shipping. This results from high strength and stiffness requirements that are generally comparable to those for bridges (Daniel and Paulus, 2019). The most common types of construction steel are S235 and S355. For most important properties, see Table 2.1. In this context, the yield stress marks the boundary between elastic and plastic deformation of the material. What this means is explained further in this section.

material property ↓ / steel quality →	S235	S275	S355
yield stress f_y at 20 °C [N/mm ²]	235	275	355
tensile strength f_u [N/mm ²]	360	430	510
Young's modulus	$E = 210\,000 \text{ N/mm}^2$		
Shear modulus (<i>glijdingsmodulus</i>)	$G = \frac{E}{2(1+\nu)} \approx 81\,000 \text{ N/mm}^2$		
Poisson's ratio in elastic stage	$\nu = 0,3$		
Coefficient of linear thermal expansion	$\alpha = 12 \cdot 10^{-6} \text{ per } ^\circ\text{C}$ (for $T \leq 100 \text{ } ^\circ\text{C}$)		

Table 2.1: Steel characteristics (Molenaar and Voorendt, 2023)

Stress-strain relation steel

When the external stress remains below the material's yield stress, the material experiences elastic deformation. This means that when the applied stress is removed, the material tends to return to its original size and shape. In the elastic range, stress and strain increase in direct proportion, following Hooke's Law precisely (Williams, 2015). Hooke's law states that, for relatively small deformations of an object, the displacement or size of the deformation X is directly proportional to the deforming force or load F (Equation 2.6). The negative value indicates the displacement of the spring once it is stretched; k is the spring constant and determines just how stiff it is.

$$F = -kX \quad (2.6)$$

The young's modulus E is the slope of this linear elastic part of the stress-strain curve for the material under tension or compression, it characterises the stiffness (k) during the elastic phase. Point P in Figure 2.8 represents the proportionality limit, where the linear nature of the graph disappears, and point E represents the yield strength (elastic limit) of the material. Here, the maximal elastic stress σ_E is associated with the maximal elastic strain ϵ_E .

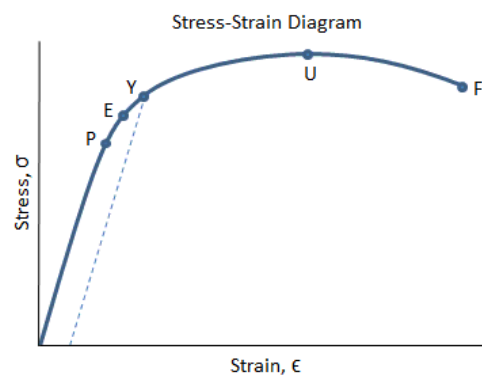


Figure 2.8: Steel characteristics (MechaniCalc, 2024)

As the applied stress surpasses the yield point (point Y), it triggers the onset of plastic deformation. During this stage, the material deforms much more rapidly and irreversibly. Within the plastic region, both elastic and plastic deformation coexist (Buldgen et al., 2012). During plastic deformation, cracks may form and propagate until the material eventually fractures. This type of deformation does not disappear when the initiating stress is removed. The fracture point or the break point, which is the point at which the material fails and separates into two pieces, is defined as point F.

Strain energy

Similar to a spring, steel can deform and store potential energy when subjected to a load. The strain energy (i.e., the amount of potential energy stored due to the deformation) is equal to the work done in the deformed material. This work depends on the applied load and corresponding deformation of the material. The total strain energy corresponds to the area under the force-deformation curve; refer to Figure 2.9. Elastic strain

energy can be recovered, so if the deformation remains within the elastic limit, then all of the strain energy can be recovered.

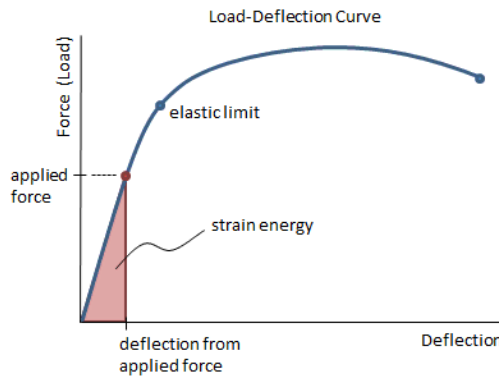


Figure 2.9: Load-deformation curve steel (MechaniCalc, 2024)

The amount of potential energy E_{strain} stored due to the deformation (u) is determined using Equation 2.7. This is straightforward for the elastic zone, as deformation and force are proportional to each other. It becomes more challenging when the plastic zone is reached; however, the same principle can be applied.

$$E_{strain} = \int_0^{u_i} F_i du_i \quad (2.7)$$

When the structure is elastic and linear, that is $F_i(u_i) = k_i u_i$, the work, i.e. energy, of a force increasing from 0 to F_i , moving through corresponding deformations from 0 to u_i is (Gavin, 2012):

$$\begin{aligned} E_{strain} &= \int_0^{u_i} k_i u_i du_i \\ &= \frac{1}{2} k_i u_i^2 \\ &= \frac{1}{2} F_i u_i \end{aligned}$$

2.2. Vessel's properties

In this section, several aspects are discussed that are important for determining the location and magnitude of a collision on a lock gate. Section 2.2.1 elaborates on the purpose of AIS data, which is used for analysis in Chapter 3. Within AIS data, the geometric parameters and velocity are crucial for determining the collision energy. After that, various types of bow shapes are discussed in Section 2.2.2. This is relevant for determining the potential point of impact on the gate by the vessel. Finally, an approach is discussed for determining the mass of a vessel in Section 2.2.3. The AIS data provides input parameters for the length, width and draft. Determining the mass of a vessel is important for assessing the magnitude of collision energy.

2.2.1. Relevant information coming from AIS data

AIS (Automatic Identification System) is the mariner's most significant development in navigation safety since the introduction of radar. This is a digital positional awareness system operating in the Very High Frequency (VHF) maritime band. Its purpose is to help identify vessels, assist in target tracking, assist in search and rescue operation, simplify information exchange and provide additional information to assist situational awareness (NATO, 2021). Initially developed for collision avoidance, AIS enables commercial vessels to achieve clearer visibility in all conditions and provides skippers with improved environmental information.

The system achieves this by continuously transmitting a vessel's identity, position, speed, course, and other relevant details to all nearby AIS-equipped vessels. When integrated with shore stations, AIS enables port authorities and maritime safety bodies to manage maritime traffic effectively and mitigate navigation hazards. There are three categories of AIS (Watcheye, 2023):

- Class A: Type of AIS that is designed for professional shipping, with cargo vessels (both maritime and inland navigation) using this type of AIS transponder;

- Class B: Type of AIS that is intended for yachts. While it shares similar functionalities with Class A, Class B is adapted for recreational boating. For example, this system transmits signals less frequently than a Class A system;
- AIS Receivers: Type of AIS that only receive information from surrounding vessels (both Class A and Class B). These receivers are ideal if the skipper prefers not to disclose its own location, course, or speed.

In addition, a distinction exists in the transmission of static and dynamic AIS data. Static information, including MMSI number, IMO number, name and call sign, length and width, type of vessel and the location of the position-fixing antenna is sent every 6 minutes or upon request. The IMO number consists of the three letters "IMO" followed by a seven-digit number and is never reassigned to another vessel. The MMSI number (Maritime Mobile Service Identity) is a unique nine-digit number for identifying a vessel. AIS also contains the vessel's draft which requires manual input by the captain, introducing some level of inaccuracy.

newtimestamp	timestamp	oldindex	sog	callsign	imo	vesseltype	width	length	toport	to stern	to starboard	draughtInland	cog
2022-04-12 10:37:48	2022-04-12 10:37:48+00:00	115554	4.3	PH10200	1020000	99	5.0	20.0	1.0	11.0	4.0	2.2	211.699997
2022-04-12 10:37:56	2022-04-12 10:37:56+00:00	115670	3.9	PH10200	1020000	99	5.0	20.0	1.0	11.0	4.0	2.2	196.899994
2022-04-12 10:37:58	2022-04-12 10:37:58+00:00	115685	4.2	PH10200	1020000	99	5.0	20.0	1.0	11.0	4.0	2.2	191.000000
2022-04-12 10:38:02	2022-04-12 10:38:02+00:00	115745	4.1	PH10200	1020000	99	5.0	20.0	1.0	11.0	4.0	2.2	185.800003
2022-04-12 10:38:06	2022-04-12 10:38:06+00:00	115800	4.4	PH10200	1020000	99	5.0	20.0	1.0	11.0	4.0	2.2	178.300003

Figure 2.10: Measured data testship from dataset 2022 Macharen

On the other hand, the transmission frequency of dynamic information depends on the vessel's speed, generally increasing with higher velocities. Dynamic data includes the vessel's position with accuracy indication, position timestamp (in UTC) and Course Over Ground (COG). COG indicates the vessel's direction in degrees. The parameters belonging to static and dynamic data are presented in table form in Figure 2.10, using one of the vessels from the analysed dataset in Chapter 3 as an example. to_{port} , to_{stern} and $to_{starboard}$ indicate the distance from the position-fixing antenna to the corresponding part of the vessel. In this case, they represent the port side (left side), the stern (rear) and the starboard side (right side) of the vessel, respectively. Speed Over Ground (SOG) is the vessel's speed in one hour concerning the land or any other fixed object such as buoys. This parameter is measured in knots and can be easily converted to meters per second.

The use of AIS is mandatory on waters governed by the Inland Navigation Regulations since 2016. This requirement applies to all professional vessels of CEMT class I and higher, as well as recreational vessels longer than 20 meters.

2.2.2. Bow geometry inland vessel

When it comes to designing the bow of a vessel, designers have various bow shape options to choose from. Throughout the years, different bow forms have been applied for inland vessels. The pontoon-shaped bow, which was mostly used before 1970 due to its straightforward structure and cost-effectiveness, is now less common due to its increased resistance in shallow water (Zöllner, 1991). In deep water, the selection of bow shape is generally less critical because the differences in resistance are typically minimal. According to Heuser (1987), the U-shaped bow form is recommended, provided that the required bow block coefficient is not large. In most scenarios, the V-shaped bow is considered the optimal choice for inland vessels (Rotteveel et al., 2014).

In the case of the V-shaped bow, incorporating a bulbous bow (see Figure 2.11b) can result in a reduction in propulsion power by up to 20 percent at a speed of 12 km/h for a Class Va vessel (Landgraf, 1990). However, it's worth noting that the advantage of the bulbous bow diminishes when the vessel operates at a different draught from its design draught. Additionally, factors like the vessel's draught and water depth (especially keel clearance) play a significant role in determining the effectiveness of the bulb. Given that inland vessels often operate at varying draughts and encounter diverse water depths, the bulbous bow may be less advantageous in such cases (Rotteveel et al., 2014). For this reason, the bow illustrated in Figure 2.11a will be further considered throughout the thesis.

The bow structure of an inland vessel is typically constructed using steel components. Usually, the section in front of the collision bulkhead is designated as the fore-end or bow structure. In many traditional vessels,

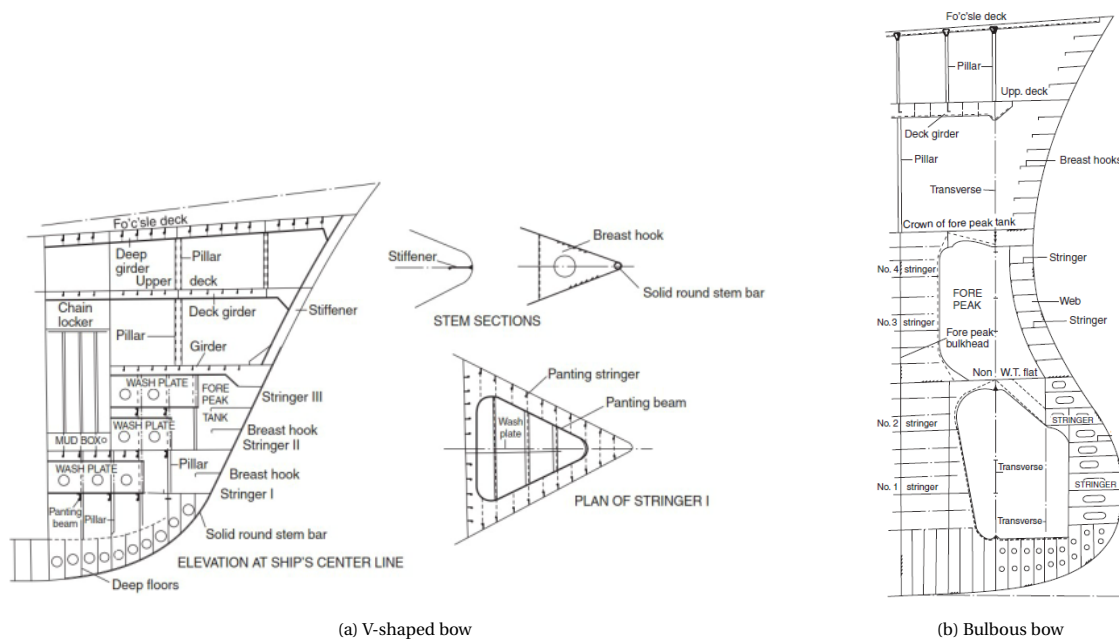


Figure 2.11: Bow variations for traditional inland waterway vessels (Eyres and Bruce, 2012)

a solid round bar known as a "stem bar" extends from the keel to the waterline region, and a curved plate is positioned above the waterline to create the upper portion of the stem. This configuration results in what is commonly referred to as a "soft nose" stem. In the event of a collision, this soft nose stem is designed to deform under the applied load, thereby minimising the extent of impact damage. In contrast, older vessels featured solid bar stems that were square in cross-section and were fastened with rivets (Eyres and Bruce, 2012). These stems lacked the characteristic slope found in modern designs, and their rigidity meant that they could cause considerable damage on impact.

Appendix B includes a side and top view to provide a more clearly representation of the bow shape and dimensions of an inland navigation vessel. Note: this concerns a vessel of CEMT class III.

2.2.3. Mass approximation inland vessel

The mass of a vessel needs to be estimated based on its geometric parameters such as length, width and draft. The following formula can be applied to approximate the mass of a vessel (Papanikolaou, 2014):

$$\Delta = w_s \times \Delta' \quad (2.8)$$

Where:

w_s = specific weight of water: = 1.0 [t/m³]

Δ' = corrected moulded hull volume = $C_B \times L_{pp} \times B \times T \times K$

Where:

C_B = block coefficient for design draft: 0.8 - 0.93 [-] (Liu et al., 2014a)

L_{pp} = length between perpendiculars: 0.96 - 0.98 $\times L_{WL}$ [m] (MAN, 2018)

L_{WL} = length on waterline [m]

B = width [m]

T = design draft [m]

K = moulded hull correction coefficient: 1.005 [-]

Blockiness of the submerged vessel

When floating in water, a vessel displaces a certain volume of water which creates an upward force known as buoyancy that keeps the vessel afloat. This buoyant force is equal to the weight of the water displaced by the vessel's hull. The weight of this displaced water is known as the vessel's displacement, which is a characteristic

of the hull's shape and depends on its physical dimensions. The hull form of a vessel is unique to its design and can be assessed by comparing it to a simple cubic block at the same level of submersion. This comparison involves considering the vessel's length, width and draft, where the draft represents how much of the hull is submerged. The length used in this calculation is typically the Length Between Perpendiculars (LBP) (Ghosh, 2023).

The block coefficient (C_B) is a mathematical ratio that represents the actual volume displacement of a vessel compared to the volume displacement of an equivalent cuboid with the same dimensions at a specific draft. Mathematically, it is the vessel's volume displacement divided by the volume of the rectangular cuboid with the same length, draft, and breadth (see Figure 2.12).

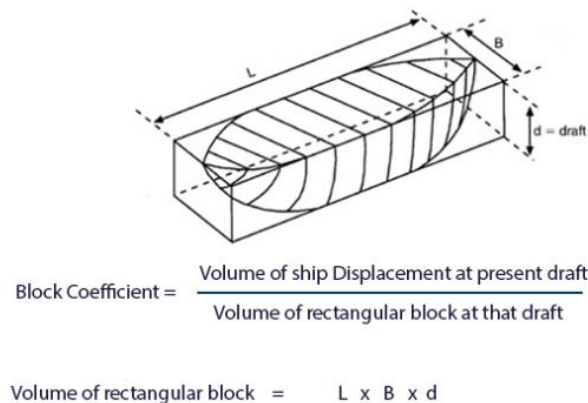


Figure 2.12: Block coefficient visualisation vessel (Jassal, 2016)

The block coefficient value always falls in the range from 0 to 1, and it characterises the hull form's fullness or fineness. Higher C_B values indicate a fuller hull form, while lower values suggest a finer hull shape. This parameter provides insights into a vessel's design and how it interacts with the surrounding water. Inland vessels are commonly designed with a large block coefficient and high width/draft ratio in order to carry more cargo. As the vessel width and draft are constrained by the waterways, the range of block coefficient among inland vessels is limited between 0.8 and 0.93, while those for sea-going vessels between 0.4 and 0.85 (Liu et al., 2014a).

2.3. Ship-lock interaction

In this section, all relevant aspects regarding the interaction between the vessel and lock in general are discussed. Section 2.3.1 begins by explaining various methods for modelling a collision. This is crucial for making a choice among the available methods. After that, Section 2.3.2 outlines the different collision scenarios that may occur when a vessel approaches a lock. Section 2.3.3 transitions into discussing the point of contact of a potential collision, focusing on an upstream collision and distinguishing between types of collisions. This section is relevant for modelling the point of application of the load. Finally, the vessel limit speed for vessels within a lock chamber is discussed in Section 2.3.4. The information in this section is essential for the data analysis in Chapter 3, where vessel speeds are analysed. Occasionally, unrealistic values may be obtained during data analysis, but by setting a vessel limit speed most of these values can be filtered out.

2.3.1. Characteristics different types of modelling

The collision of a vessel with a lock gate can be approached through an analytical or numerical method, as mentioned in Section 1.5. Modelling the collision of a vessel with a lock gate is a challenging event due to its dependency on different parameters. The analytical method allows for a simplified version of the event. Therefore, this method may be considered inaccurate, but it represents a good approximation of reality and can be compared with the outcomes of a numerical method. Numerical models are based on a numerical procedure such as the finite difference or finite element method. These models enable a more realistic simulation by considering various factors such as non-linear material properties and boundary conditions.

Edmondson (2017) made a distinction between an analytical and numerical approach in his thesis. Several shortcomings of using an analytical method over a finite element model are mentioned here:

- The load is considered as a point load, which is a decent assumption for the first point of impact, but will become less accurate as the displacements increase;
- The situation has been considered as two dimensional which enforces both equal deformations over the entire height of the gate and the entire gate cross section being activated by a local force;
- The final deformation is given as a single value for the maximum deformation, the general shape of the deformation is not determined.

For initial insights or validating results from a numerical model, an analytical model is suitable. However, for accurately determining specific physics behind events such as a ship collision, it is necessary to approach this using a numerical model.

2.3.2. Collision scenarios

There are four possible gate collision scenarios, where both sets of gates are approached from both sides (Rijkswaterstaat, 2017), refer to Figure 2.13 for visualisations. In scenarios 1 and 3, the consequences are relatively minor due to the fact that either the inner gate or the outer gate is closed. In the event of a collision, if one lock gate were to be pushed outward, the other gate would remain closed at all times. From a flood protection perspective, this is highly advantageous. Furthermore, the likelihood of collisions in both scenarios is low. This is because the first set of gates to enter the lock are closed, and the traffic light is red. The skipper must wait at the designated mooring facilities before entering the lock.

Scenario	Visualisatie	Kans	Gevolg
1		klein	klein
2		mogelijk	beperkt
3		klein	klein
4		mogelijk	groot

Figure 2.13: Visualisation of collision scenarios (Goeijenbier et al., 2022)

The probability of scenarios 2 or 4 occurring is higher than the other two scenarios. This is attributed to the fact that the first lock gate (as seen from the vessel) is open. This can result in some negligence on the part of the skipper or, due to inexperience, the skipper may make an error in judging the stopping distance. The only difference between scenario 2 and 4 is that scenario 2 benefits from favourable water pressure acting in the opposite direction of the potential collision force. Consequently, the consequences are also less severe because it is unlikely that the entire gate will be pushed out. Based on probability and consequences, only scenario 4 (collision of the inner gates when the outer gates are open) is considered relevant within the context of flood protection. Therefore, this scenario is analysed in this thesis. In this situation, the water pressure difference across the lock gate imposes an unfavourable load.

The likelihood of the outer gate being closed after a collision with the inner gate depends on the extent of damage to the inner gate and the associated flow velocities in the lock chamber. Pointing out that mitre gates generally cannot be closed when the head is greater than 5-10 cm, corresponding to flow velocities in the order

of 1 m/s (Rijkswaterstaat, 2021). The amount of damage is influenced by factors such as the vessel's speed and weight (including cargo), water level, location of impact on the gate and the gate's redistribution capacity.

2.3.3. Point of contact - mitre gate

The collision scenarios on the inner gate from the chamber consist of various points of contact between the vessel and the gate, refer to Figure 2.14. There is a distinction made here between two types of collisions (Daniel and Paulus, 2019):

- Unsymmetrical collision: a collision involving a single barge occurring at a distance of one barge width or more from the lock wall;
- Symmetrical collision: a collision involving a wider barge at the point of the mitre post.

The force distribution and the anticipated failure mechanism of the gate differ in case of both types of collision. In the case of a symmetrical collision, only normal force is exerted on the horizontal girders, which could potentially cause them to buckle. This scenario makes the system stiff, resulting in minimal deformation. In the case of an unsymmetrical collision, primarily bending forces act on the girders and with this type of load significant local deformations occur.

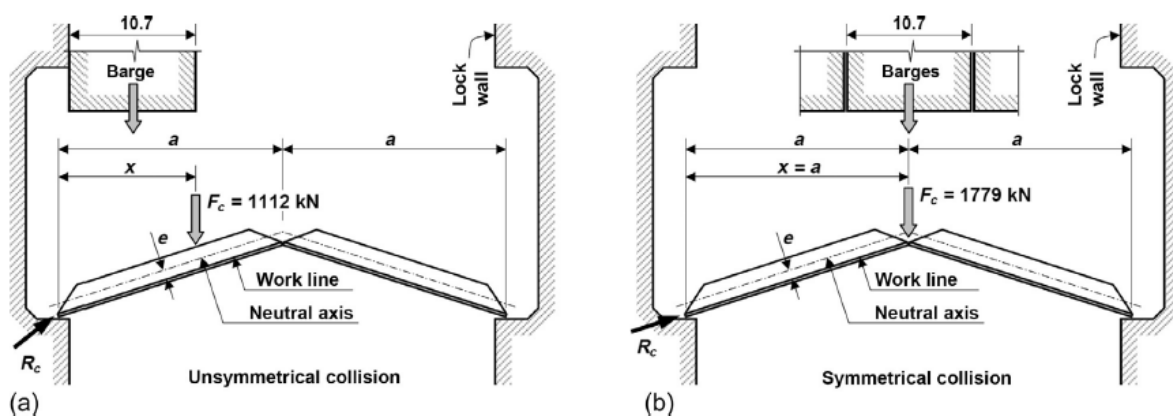


Figure 2.14: Ship collision load schemes for waterways in the United States (Dalton, 2014)

The width and bow shape of a vessel are critical factors in determining whether a vessel may collide (a)symmetrically with the mitre gate. With a blunt bow shape, it is still possible to engage with the mitre posts after the initial contact, even if the vessel is outside the centerline of the lock chamber. Additionally, when determining the point of contact for collisions next to the mitre post a minimum edge distance is taken into account, which is the distance between the vessel's side and the chamber wall. Vessels that make contact with the chamber wall lose energy due to friction between the vessel and the wall.

2.3.4. Determination of the vessel limit speed

The primary ship wave is the phenomenon of a decreasing water level around a moving vessel, resulting from the displacement of water in front of the vessel towards the rear. The accompanying water flow along and beneath the vessel, naturally in the opposite direction of travel, is referred to as the return flow. As the additional return flow induces an increase in velocity along the vessel, the local speed height increases. Due to this the water level must decrease. For a situation in which a vessel is navigating in a prismatic channel without natural currents, this phenomenon was first theoretically demonstrated by Schijf (1949). Initially, a coordinate system is assumed to move with the vessel, making all velocities relative to the vessel's velocity. As a result, the vessel's velocity becomes zero and the relative water flow velocity is then in absolute value equal to the vessel's velocity relative to the water (van Koningsveld et al., 2023).

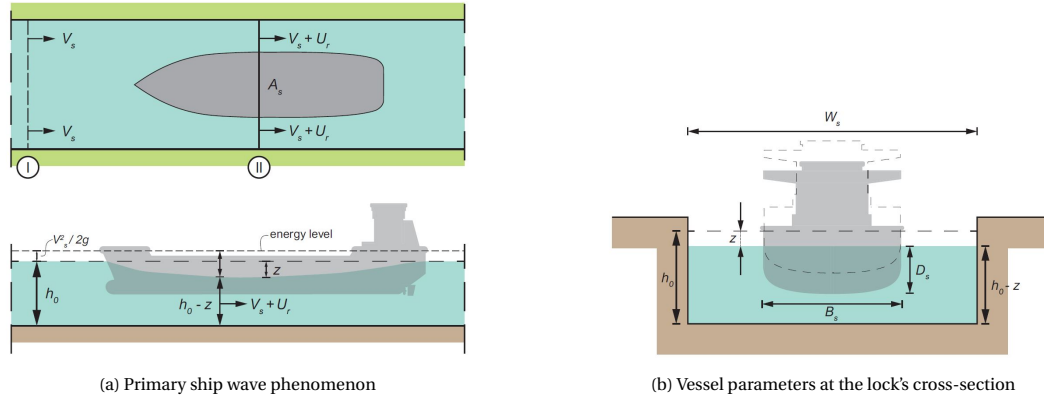


Figure 2.15: Visualisation of the water level decrease in a prismatic channel (van Koningsveld et al., 2023)

By using the continuity equation for mass conservation, the following relation can subsequently be established:

$$Q_1 = V_s \times A_c = Q_2 = (V_s + u_r)(A_c - A_s - W_s \times z) \quad (2.9)$$

Where:

- V_s = vessel's velocity [m/s]
- $A_c = W_s \times h_0$ = wet cross-sectional area of undisturbed channel [m²]
- u_r = return current velocity [m/s]
- $A_s = B_s \times D_s$ = vessel's underwater cross-section [m²]
- W_s = width of the water surface of undisturbed channel [m]
- z = maximum water level depression [m]

To approximate the increase in velocity head, Bernoulli's law is used. It is assumed that the energy head in front of the vessel H_1 is equal to the energy head at the rear end of the vessel H_2 .

$$H_1 = h_0 + \frac{V_s^2}{2g} = H_2 = (h_0 - z) + \frac{(V_s + u_r)^2}{2g} \quad (2.10)$$

Where:

- h_0 = water depth far before or after the vessel [m]

Rewriting to z results in:

$$z = \frac{(V_s + u_r)^2}{2g} - \frac{V_s^2}{2g} = \frac{V_s \times u_r}{g} + \frac{u_r^2}{2g} \quad (2.11)$$

The velocity of a vessel is influenced by the depth and width limitations of the waterway it navigates. Schijf developed a method based on energy conservation to calculate the maximum achievable sailing speed V_{lim} for a particular vessel in a restricted waterway with specific dimensions, which is particularly relevant in shallow water conditions. According to Schijf, a vessel reaches its vessel limit when the return current reaches a critical state, characterised by a Froude number equal to 1. If the vessel were to further increase its velocity, the water movement alongside the vessel would become supercritical, causing a significant drop in water depth (van Koningsveld et al., 2023). In such a situation, the continuity condition is no longer met, despite the higher current velocity. As a result, water accumulates in front of the vessel's bow, making it impossible for a self-propelled vessel to overcome. In the further derivation of the limit speed V_{lim} , $(V_s + U_r)$ are replaced in Equation 2.9 with the use of Equation 2.11. In this context, A_c/W_s has been rewritten as the average depth of the channel, denoted as \bar{h} , and the Froude number is equal to $Fr^2 = V_s^2/(g \times \bar{h})$.

$$\left(\frac{z}{\bar{h}}\right)^3 + \left(\frac{z}{\bar{h}}\right)^2 \left[\frac{Fr^2}{2} - 2\left(1 - \frac{A_s}{A_c}\right) \right] + \frac{z}{\bar{h}} \left[\left(1 - \frac{A_s}{A_c}\right)^2 - Fr^2 \left(1 - \frac{A_s}{A_c}\right) \right] - Fr^2 \frac{A_s}{A_c} \left(1 - \frac{A_s}{2A_c}\right) = 0 \quad (2.12)$$

If the vessel sails at its limit speed, $V_s = V_{lim}$, then Equation 2.9 & 2.10 yield:

$$V_{lim} + u_r = \sqrt{V_{lim}^2 + 2gz} \quad (2.13)$$

$$Q = V_{lim} \times A_c = \sqrt{V_{lim}^2 + 2gz} \times (A_c - A_s - W_s z) \quad (2.14)$$

This expresses the discharge Q for cross-section 2 as a function of z , so the value z_{lim} at which the maximum discharge occurs is found by setting dQ/dz equal to zero. When this is done, the following equation remains:

$$\frac{z_{lim}}{\bar{h}} = \frac{1}{3} \left(1 - \frac{A_s}{A_c} - \frac{V_{lim}^2}{g\bar{h}} \right) \quad (2.15)$$

The maximum discharge Q_{max} are now obtained by substituting Equation 2.15 into Equation 2.14.

$$Q_{max} = \sqrt{V_{lim}^2 + \frac{2}{3}g\bar{h} \left(1 - \frac{A_s}{A_c} - \frac{V_{lim}^2}{g\bar{h}} \right)} A_c \left[1 - \frac{A_s}{A_c} - \frac{1}{3} \left(1 - \frac{A_s}{A_c} - \frac{V_{lim}^2}{g\bar{h}} \right) \right] \quad (2.16)$$

$$\frac{Q_{max}}{A_c \sqrt{g\bar{h}}} = \left[\frac{2}{3} \left(1 - \frac{A_s}{A_c} + \frac{V_{lim}^2}{2g\bar{h}} \right) \right]^{\frac{2}{3}} \quad (2.17)$$

Since $Q_{max} = V_{lim} A_c$ this means that:

$$\frac{V_{lim}}{\sqrt{g\bar{h}}} = \left[\frac{2}{3} \left(1 - \frac{A_s}{A_c} + \frac{V_{lim}^2}{2g\bar{h}} \right) \right]^{\frac{2}{3}} \quad (2.18)$$

In the scenario where the ratio of the vessel's cross-sectional area A_s to the channel's cross-sectional area A_c is equal to 1, resulting in the vessel occupying the entire channel space, the solution yields the expected outcome: V_{lim} is 0. In the extreme situation where A_s/A_c equals 0, signifying that the vessel has no impact on the channel's cross-section, the solution yields $V_{lim} = \sqrt{g\bar{h}}$. This means that in extremely wide and shallow water, a vessel's maximum speed matches the celerity of a shallow water wave. In the majority of inland waterways, the value of A_s/A_c typically falls within the range of 0.1 to 0.3 (van Koningsveld et al., 2023). However, due to the smaller dimensions of lock structures compared to most inland waterways, a separate investigation is required to address this specific case.

3

Case description & AIS data analysis - Macharen lock

In this chapter, a case is described which serves as the basis for the development of the gate model in the next chapter. The lock at Macharen is selected, a lock from which parameters are known at Witteveen+Bos. The lock is selected because there is a substantial amount of available data and because a distinction can be made between a non-operational (open) and operational (closed) lock. This is further explained in this chapter. Furthermore, the chapter focuses on the analysis of AIS data at the Macharen lock location. An answer to the third sub-question: "How can practical information from AIS data improve the accuracy of input parameters for collision energy estimation?" is given at the end of this chapter.

3.1. Lock system overview

3.1.1. Case introduction

The "Meanderende Maas" project aims to improve flood protection on the Brabant side of the Meuse River, while also seizing opportunities for the integrated development of the river's winter bed. It has been demonstrated that these objectives are achievable through an approach involving dike reinforcement, river expansion, and floodplain design, known as the preferred alternative "Meandering Meuse". An essential component of the Meandering Meuse project is ensuring that the dike section complies with the requirements of the Water Act. Macharen lock is part of this dike section, and its location is shown in Figure 3.1. The lock, dating back to the 1960s, is owned by the municipality of Oss.

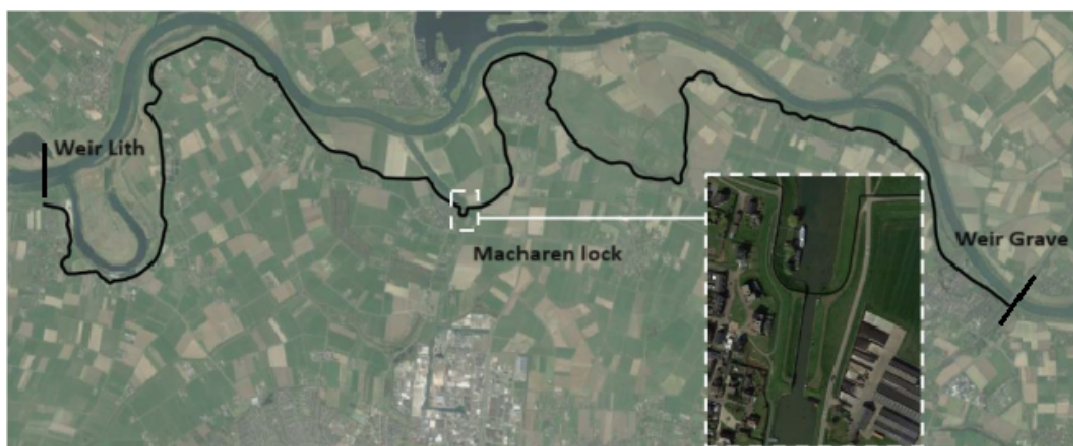


Figure 3.1: Project surroundings of Macharen lock, North-Brabant province (Google, nd)

For compliance with the Water Act requirements, the collision resistance might be relevant if it significantly contributes to the risk of flooding. In this chapter, all assumptions of project Macharen lock are utilised to assess the potential impact resistance at this location. This analysis is performed using AIS data.

3.1.2. System description

Macharen lock connects the Meuse River to the inland harbour of Oss (along the Burgemeester Delen canal). The lock is part of a primary water defense system, located between the Meuse weirs at Grave and Lith, as indicated in Figure 3.1. Because the lock is a primary water defense system, it must comply with the Water Act. By categorising the lock structure in consequence class CC3, based on Eurocode 0 (Eurocode, 2019), a safety level has been applied that is at least equivalent to the requirements set by the Water Act.

The water level in the Meuse is equivalent to the weir level for a significant part of the year, approximately at NAP +4.9 m (Amsterdam Ordnance Datum). The lock remains open for most of the time, which means that the water level in the Burgemeester Delen canal is equal to the Meuse water level. When water levels rise, starting from around NAP +5.2 m in the current situation, the lock will be closed. From this water level, the lock is operational because water inundation and damage will occur at water levels of around NAP +5.5 m in the harbour. Chamber locking operations are conducted as long as there is river traffic on the Meuse. In the event of extreme discharge rates, shipping may be halted and locking operations will cease. The maximum chamber water level is given at NAP +7.0 m and no further locking operations occur when the water level exceeds this threshold.

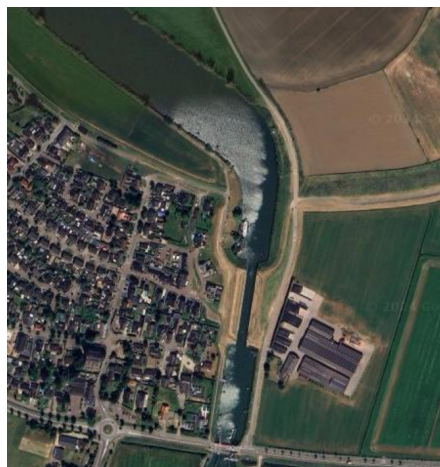


Figure 3.2: Macharen lock zoomed in (Google, nd)

When a vessel approaches the lock from the north, it is required to make a turn towards the lock when nearing it (see Figure 3.2). This already leads to a significant reduction in velocity compared to a situation with a straight channel. Besides that, traffic lights are set to red as standard for vessels coming from the Meuse. This reduces the velocity vessels have as well. Mooring facilities are located on the west side of the Meuse river, just before and immediately after the turn. These mooring facilities serve as waiting areas when the lock is operational. When a vessel is traveling from the harbour to the Meuse, these facilities are located on the east side of the Burgemeester Delen canal.

3.1.3. Governing vessel dimensions

An important first step in determining collision energy begins with identifying the ship classes. According to the municipality of Oss, CEMT Class Va inland vessels can enter the port of Oss. However, the typical dimensions of these vessels exceed the length of Macharen lock. These vessels can only pass through the lock when it is non-operational, i.e. when the water level is lower than NAP +5.2 m. On the website of the municipality of Oss, the following is indicated: "The vessel may not exceed a length longer than 135 meters and a width wider than 12 meters. The draft may not exceed 3.50 meters" (n.d., 2023).

The largest vessels that can pass during an operational lock have a length of 85 meters; anything larger does not fit in the lock chamber, as stated by the municipality of Oss. According to Appendix A, this corresponds to a maximum of CEMT IVa vessels. The associated characteristics include a length of 85 m, a width of 9.5 m and a draft of 2.5 m.

3.1.4. Lock chamber geometry

The lock chamber has the following geometry (see Figure 3.3):

Distance from gate casing to gate casing	96 m;
Width of the lock chamber	14 m;
Lock floor level	NAP +0.50 m;
Top of lock wall	NAP +7.20 m.

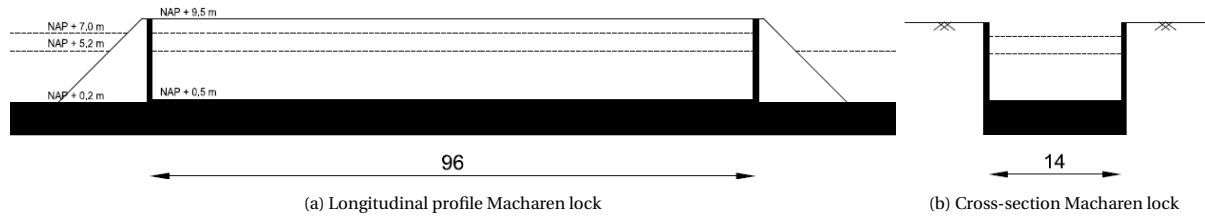


Figure 3.3: Longitudinal and cross-section of the lock at Macharen, including the minimum lock level NAP +5.2 m and the maximum lock level NAP +7.0 m

3.2. Inventory of boundary conditions

Python is used to analyse the AIS dataset obtained for the year 2022. This dataset is provided in tabular form with relevant information including timestamps, latitude and longitude coordinates, Course Over Ground (COG), geometric parameters, and velocities per coordinate, as explained in Section 2.2.1. Before calculating the potential collision energies, it is essential to consider any boundary conditions. This involves categorising the dataset into CEMT classes and measurement points, determining the masses of the vessels, and implementing the vessel limit speed. These aspects are further discussed in this section.

3.2.1. Measurement locations

The trajectory is divided into various measurement points (A - F). The desired analyses are carried out for these locations and compared with each other. The locations are linked to coordinates in latitude and longitude. These coordinates need to be manually adjusted in the Python file in order to conduct analyses for the desired location. Figure 3.4 displays the locations on a map of the respective area.

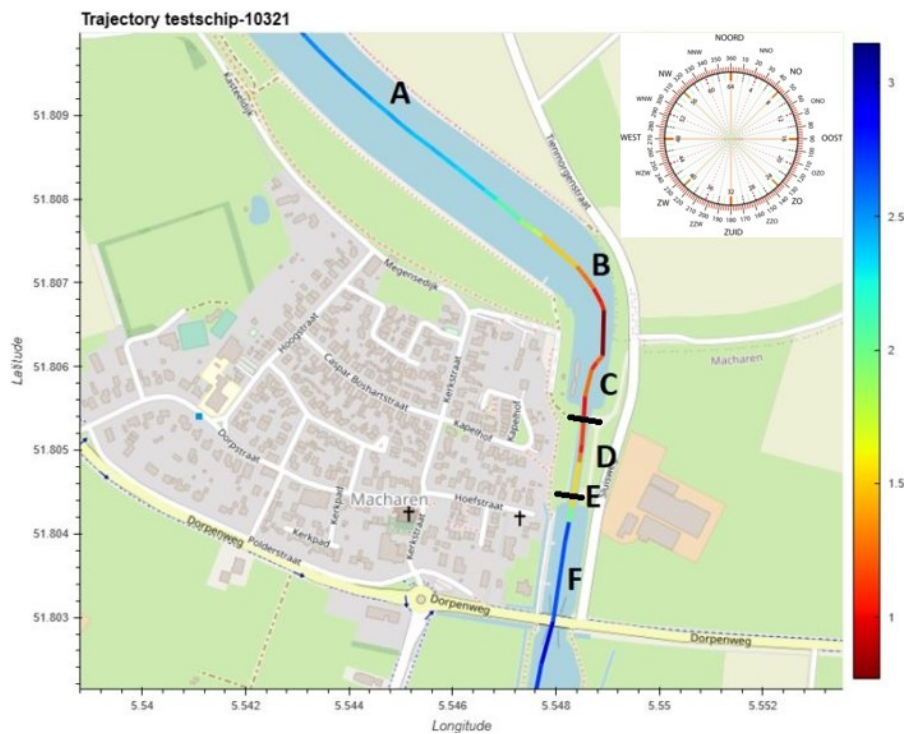


Figure 3.4: Trajectory of an arbitrary test ship, including specifications of all measurement points and displaying the vessel on the right-hand side in m/s

Where:

- $A = 500$ [m] upstream (north) of the lock chamber
- $B =$ at the curve
- $C = 10$ [m] upstream (north) of the lock chamber
- $D =$ in the middle of the lock chamber
- $E =$ at the inner lock gate
- $F = 100$ [m] downstream (south) of the lock chamber

The dataset is divided into different trajectories, with each trajectory corresponding to a single vessel. Many of these trajectories have multiple data points throughout the year since a particular vessel may visit the port of Oss several times a year. Thus, a distinction can be made between a vessel approaching the port and the same vessel departing from the port. The data includes the direction of a vessel through the Course Over Ground (COG). The unit for this parameter is given in degrees from 0° to 360° . For ship traffic heading towards the port (south), the COG value falls between 130° and 230° . Defining this for traffic departing from the port (north) is somewhat more challenging to define. For locations A and B the COG value for vessels heading north ranges between 250° and 360° , while for the other locations it falls between 0° and 100° . Later in this chapter the differences and similarities between north- and south-going ship traffic, along with their respective causes, are discussed.

3.2.2. Vessel type movements

The vessels are initially categorised into CEMT classes based on their length and width. This is done by first examining the appropriate combination of length and width, as described in Appendix A and Richtlijnen Vaarwegen (Koedijk, 2020). When this combination does not match the measured data, consideration is given to either the length or the width individually. There are a few vessels that can not be classified due to missing parameters, this amounted to approximately 50 vessels for the 2022 dataset. These vessels are excluded from further analysis. In the bar chart of Figure 3.5, the number of vessels passing through the Macharen lock is shown for the year 2022.

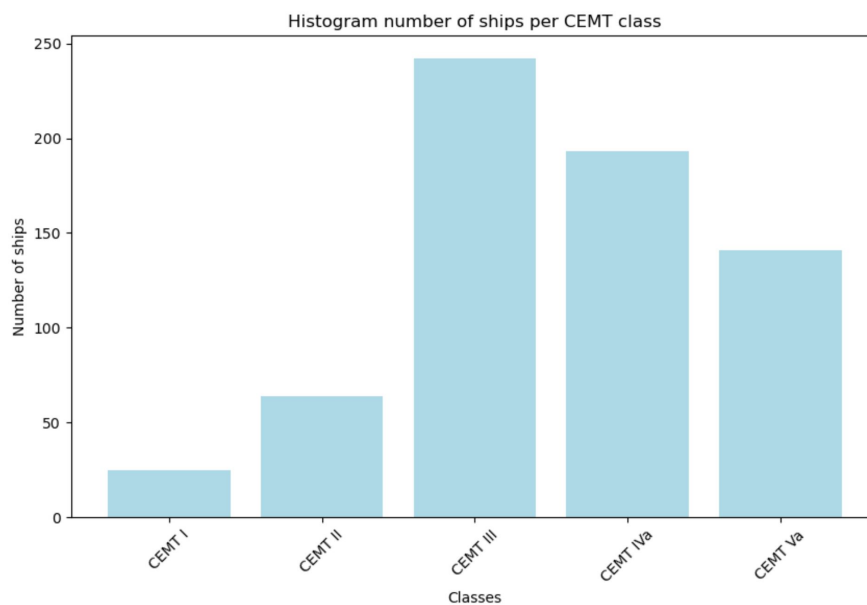


Figure 3.5: Histogram of all passing ship classes in the year 2022 at Macharen lock

From the histogram, it can be concluded that CEMT classes III, IVa, and Va clearly dominate over the smaller classes I and II.

3.2.3. Average & maximal mass per CEMT class

The determination of the mass per vessel is based on Equation 2.8. This equation assumes that the mass of the total displaced volume of water is equal to the total weight of the vessel. The block coefficient is crucial

here and varies for each vessel. It is conservative to assume that for each vessel this value is 0.93 [-], as this upper limit of the respective coefficient generates the highest values for mass. In reality, the block coefficient fluctuates between values of 0.8 and 0.93 [-] (Liu et al., 2014a). Therefore, a slightly lower value than the median is chosen for the analysis, namely 0.85 [-].

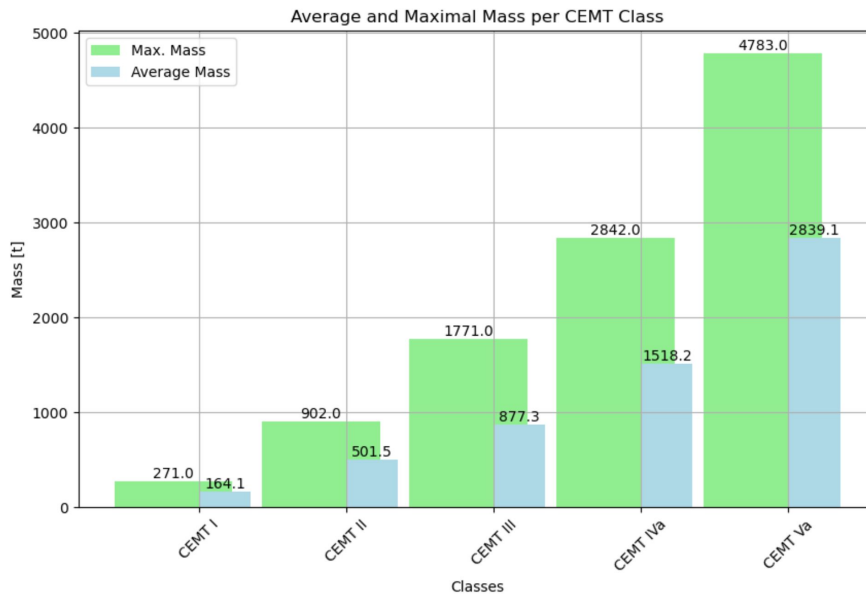


Figure 3.6: Bar chart with the average mass and maximal mass per CEMT class

The bar chart in Figure 3.6 illustrates the distribution of masses per CEMT class, with the average mass measured in the blue bar chart and the maximum mass per class in the green bar chart. It is anticipated that the class with the lowest mass is Class I, while the class with the highest mass is Class Va. During the programming of the desired analyses in Python, limits are set on the lower and upper limits of the mass. This is done to prevent irrelevant data and unrealistic outliers. The lower limit is set at 100 tons to filter out irrelevant data. Besides that, the mass of a vessel should never exceed 3.5 times its width times its length. This limit is based on the potential maximum value that can arise from Equation 2.8.

3.2.4. Vessel limit speed

When a large inland vessel passes through a narrowed waterway, it can cause a braking effect. To avoid unrealistic values for a vessel's velocity in relation to the vessel and lock cross-sectional ratio A_s/A_c , the Schijf method for return flow is taken into account. Information regarding this method is provided in section 2.3.4. Formula 2.18 is implemented in the data analysis, in which some parameters (A_c & \bar{h}) are already known in advance. The unknown parameter(s) (A_s) are obtained from the dataset of the year 2022.

Where:

$$W_s = 14 \text{ [m]}$$

$$h_0 = 4.7 \text{ [m]}$$

The value for the width of the free surface level W_s and undisturbed water depth h_0 within the lock are based on information from Section 3.1.4. The bottom of the lock chamber is situated at NAP +0.50 m and the lowest water level at which the lock becomes operational is NAP +5.2 m. This reaches the upper limit of 4.7 meters. The data is predominantly measured during lower water levels.

Furthermore, it should be noted that this method is only applied at locations D and E, as these are the locations where the cross-sectional area of the canal suddenly narrows. The measured velocity of the vessels at these locations are compared to the calculated limit speed, and subsequently overwritten with the limit speed if the measured velocity exceeded the limit speed. Within the lock chamber, the velocity is overwritten for 9 vessels in total, with 4 of the vessels belonging to CEMT class Va. For the other locations, this phenomenon is not taken into account because the A_s/A_c ratio is much lower and thus not or barely affects the vessel's velocity.

3.2.5. Closing data

Lock Macharen remains open for almost the entire year, as explained in Section 3.1.2. This effectively simulates the scenario in which a fictitious vessel collides with the lock gate at a certain velocity due to various reasons. The critical scenario arises from a situation where the skipper expects the gate to be open, but in practice, it is actually closed. To gain an understanding of a situation with the lock closed (operational) and open (non-operational), both scenarios are compared in this chapter. However, in the year 2022 the lock was never closed. After consulting the harbour master of the port in Oss, it is known that the lock was closed twice in 2021. Therefore, the data for the specific closure dates in that year are compared with the data from 2022.

The lock at Macharen was operational in the year 2021 during the weeks of January 31 to February 7 and July 16 to July 22. During these periods, a total of 11 vessels passed through the lock. This is considerably less compared to the amount of vessels in the dataset of 2022, which consequently provides less reliability for the analyses. Nevertheless, an examination is conducted on the velocities and collision energies of the vessels within the lock chamber to analyse similarities and differences compared to a non-operational lock.

3.3. Velocity analysis

In this section, the velocities of vessels around the Macharen lock are analysed and compared with each other. Relations are established between different CEMT classes, i.e., the masses that vessels have, and the impact this has on velocity. Particularly, velocity is an important parameter for determining the collision energy, which is based on the formula for kinetic energy:

$$E = \frac{1}{2} \times m \times v^2$$

Initially, the velocities are analysed at the inner gate of the lock chamber. The velocities of vessels at this point represent the moment of impact. This analysis is conducted for both south- and north-going traffic (Section 3.3.1). Subsequently, velocities at the remaining measuring points are analysed and compared to each other. This approach highlights vessel behaviour and identifies potential influencing factors (Section 3.3.2). Finally, velocities are analysed for an operational lock. It is observed that these velocities are lower than during a non-operational lock, as vessels may need to wait before entering the lock (Section 3.3.3).

3.3.1. Velocities at location E - the inner lock gate

South-going traffic

The most relevant location for this thesis is location E, which characterises the measuring point at the inner gate of the lock. The reason for this is explained in Section 2.3.2. The velocities of the various vessels at this location are considered as potential collision velocities. In Figure 3.7, all the data collected from the entire dataset is presented.

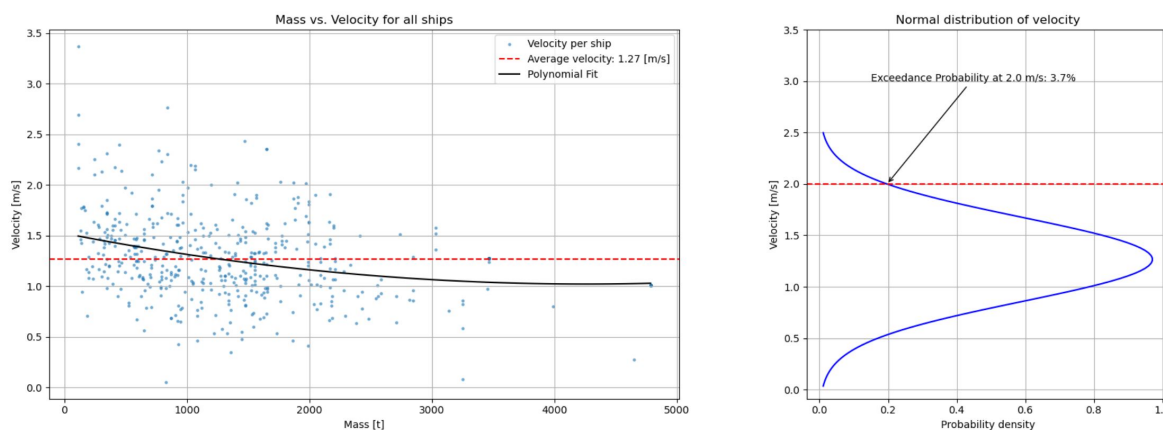


Figure 3.7: Mass vs. velocity for all vessels at the inner lock gate of the lock chamber including polynomial moving in south direction (left) and probability density function velocity (right)

The vessel's mass on the x-axis, determined using the method discussed in Section 2.2.3, is plotted against the velocity on the y-axis. From the graph it can be concluded that, especially for lower tonnages, there are significant differences in velocity compared to the average velocity of 1.27 m/s. As the tonnages increase, it is

observed that this is associated with a reduction in velocity. This is logical since the maneuverability of a vessel decreases with an increase in mass.

In order to represent the behaviour of the various data points as accurately as possible with a curve, a polynomial function is added to the graph. This function takes three parameters: a, b and c, which are the coefficients of a polynomial in the form:

$$ax^2 + bx + c$$

The function takes a single value x as input and returns the result of the polynomial for that value x. Essentially, the function calculates the predicted outcome of the velocity based on the input x. The polynomial function is used to find the best fit for the data. The objective is to determine the coefficients a, b and c that best match the actual velocity data in the dataset. In Figure 3.7, it is seen that this polynomial function is incorporated and a trend is presented that closely resembles a first-order polynomial. Starting with smaller values for mass, it is observed that the polynomial is almost linearly decreasing as the mass increases. From approximately 3,500 t the velocity remains constant towards the end of the polynomial. The graphs for the other locations are presented in Appendix C.

Finally, a normal distribution is added to the graph for the vessel's velocity. This is useful for visualising how the velocities compare to a normally distributed curve. However, the addition of this distribution does not imply that the actual data itself is normally distributed. The distribution shows that most points are clustered around the mean of 1.27 m/s and, for example, the exceedance probability for a velocity of 2 m/s is a only 3.7%. This simply confirms that these measured velocities are lower than the suggested values from the Eurocode (3 m/s).

North-going traffic

For shipping traffic heading north, it is concluded that the velocities are much higher than for traffic heading towards the port, i.e. the south (see Figure 3.8). The average velocity in this situation is 2.35 m/s, which makes a difference of 1.08 m/s compared to the average velocity for all vessels towards the port at this location.

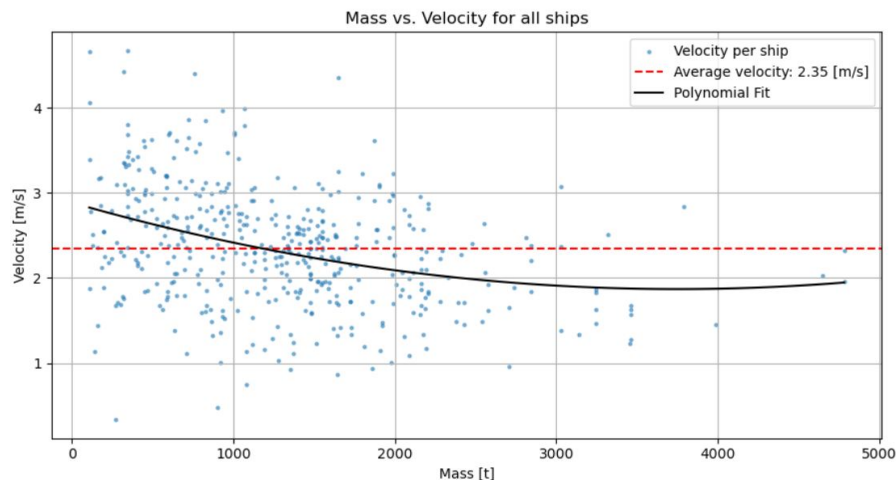


Figure 3.8: Mass vs. velocity for all vessels at the inner lock gate of the lock chamber moving in north direction

The difference is explained by the fact that the traffic light of the lock is initially green when a vessel leaves the port of Oss to return to the Meuse. This creates a situation where the skipper assumes that he or she has priority and therefore maintains a higher velocity. In addition, vessels coming from the Meuse must make a turn before approaching the lock. Making this turn already results in a significant reduction in velocity, which will make it lower compared to a situation where vessels approach the lock from a straight canal. Finally, the difference is explained by simply following the purposes of the port of Oss: the unloading of cargo. From Figure 3.8 it can be concluded that high velocities occur especially for lower masses. However, it is not possible to draw a clear line here, as the vessels can of course also load goods in the port. Furthermore, the data on mass for both north- and south-going traffic shows no extreme differences. This may be due to the fact that skippers have to manually enter their draft after loading and unloading their cargo. The polynomial of Figure 3.7 shows the same trend as that of Figure 3.8.

3.3.2. Velocities at all locations

South-going traffic

When all the polynomials from each location are presented in one graph, Figure 3.9 is obtained as the result. In this graph, each polynomial per location is presented with mass on the x-axis and velocity on the y-axis. It is evident that for every location the velocity decreases as mass increases.

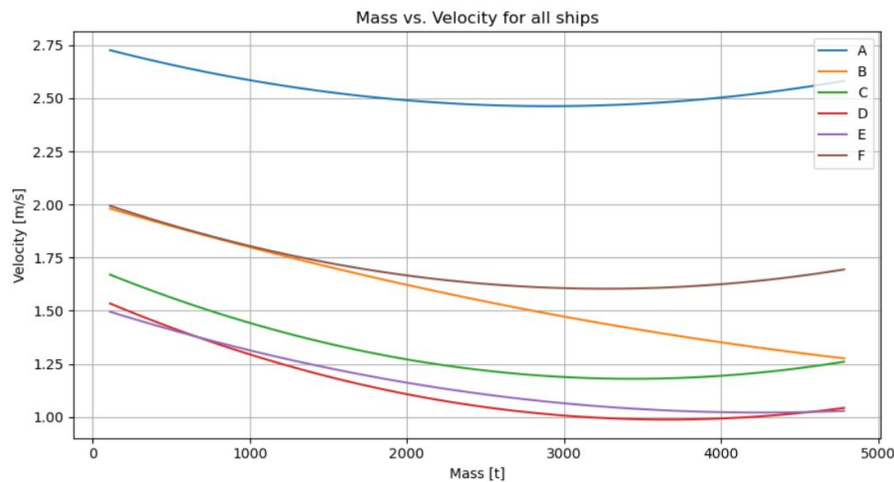


Figure 3.9: Mass vs. velocity polynomials for all vessels at all locations moving in south direction. A = 500 [m] upstream (north) of the lock chamber, B = at the curve, C = 10 [m] upstream (north) of the lock chamber, D = in the middle of the lock chamber, E = at the inner lock gate and F = 100 [m] downstream (south) of the lock chamber

Furthermore, the arrangement of the locations also appears logical. Location A, 500 m upstream of the lock chamber, measures the highest velocities. This point is the furthest from the lock, and it is the location where the vessels begin to decelerate. The polynomial for location B, where velocity is measured in the bend, starts relatively high for lower mass classes. However, the velocity decreases rapidly, which can be explained by the fact that vessels with greater masses have lower maneuverability compared to vessels with lower masses. Until approximately 1,400 t, the polynomials of locations B and F closely follow each other. After that point, the polynomial for location B shows a further linear decline, while the polynomial for location F exhibits a more gradual decrease. The reason why the velocity at location F decreases more gradually than at location B is likely due to the fact that the longitudinal profile of the river at location F is primarily straight. The fact that almost all polynomials bend upwards is also due to the lack of data points for the higher masses.

Finally, it can be concluded from the graph that the lines C, D and E all follow the same pattern. The velocities corresponding to location C, 10 m upstream of the lock chamber, are slightly higher compared to the other two locations. This effectively illustrates the transition from the channel to the lock chamber. As explained in Section 3.2.4 earlier, this is attributed to the braking effect of return flow in the lock chamber. The polynomials for the location in the middle of the lock chamber (D) and at the inner gate of the lock (E) appear to be almost identical.

North-going traffic

The polynomials based on all data from vessels heading north are shown in Figure 3.10. Once again it can be concluded that an higher mass is associated with a lower velocity and that the lines therefore correspond in trend to Figure 3.9. The only major difference is observed in the lines from locations D & E, where the velocity in Figure 3.9 decreases gradually and ultimately gives approximately 0.50 m/s difference between the lowest and highest mass. There in Figure 3.10 a rapid constant decrease (linear) in velocity is seen accompanied by an increasing mass, resulting in a final difference of approximately 1.90 m/s between the lowest and highest mass. However, the polynomials end up at a velocity which corresponds to Figure 3.9.

The order from high to low velocities for all locations also seem almost identical compared to Figure 3.9, one difference is that the velocities at location F are lower than the velocities at B. This can be explained by the fact that skippers may be more cautious when approaching the lock, knowing that their vessel has an high mass.

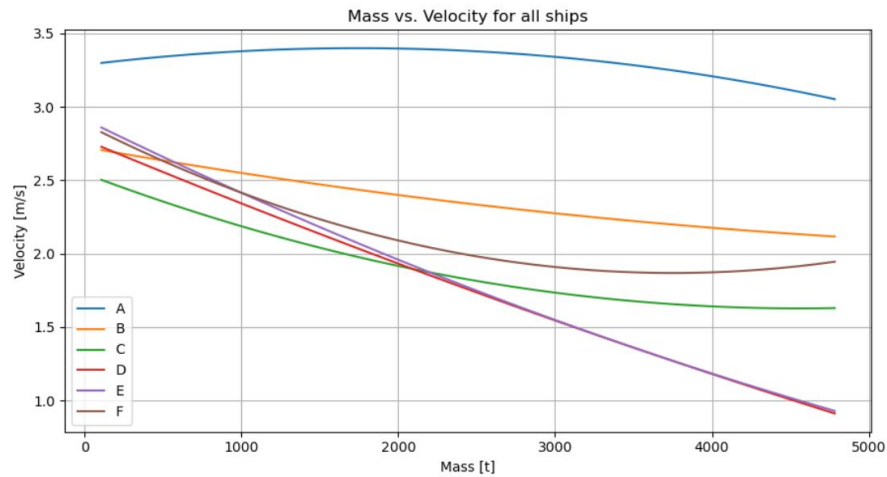


Figure 3.10: Mass vs. velocity polynomials for all vessels at all locations moving in north direction. A = 500 [m] upstream (north) of the lock chamber, B = at the curve, C = 10 [m] upstream (north) of the lock chamber, D = in the middle of the lock chamber, E = at the inner lock gate and F = 100 [m] downstream (south) of the lock chamber

3.3.3. Velocities at all locations during closing

Figure 3.11 displays all polynomials per location for south heading maritime traffic during the selected data period when the lock was operational. When comparing this graph with the one from Figure 3.9, several observations are made.

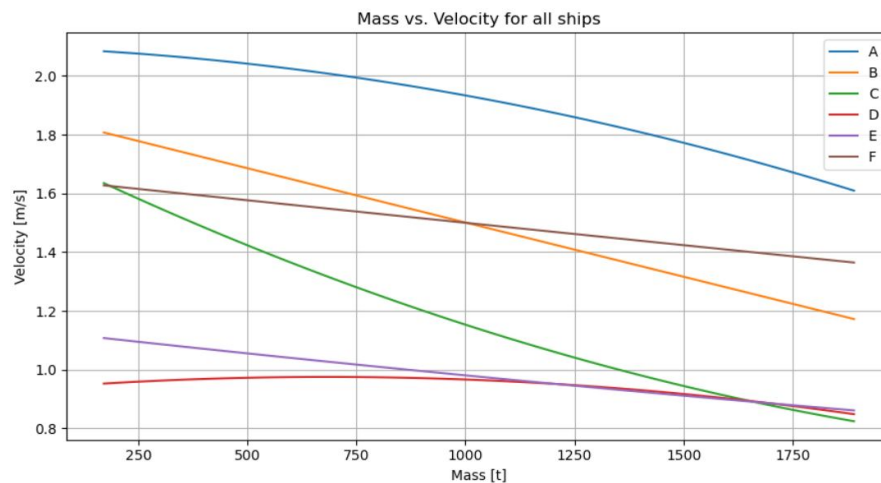


Figure 3.11: Mass vs. velocity polynomials for all vessels at all locations moving in south direction during operational lock. A = 500 [m] upstream (north) of the lock chamber, B = at the curve, C = 10 [m] upstream (north) of the lock chamber, D = in the middle of the lock chamber, E = at the inner lock gate and F = 100 [m] downstream (south) of the lock chamber

Firstly, it is notable that the masses on the x-axis in Figure 3.11 are approximately a factor of 2 smaller than those in the graph from Figure 3.9. This is because the lock is only operational for vessels with dimensions up to CEMT class IVa (see Appendix A), excluding CEMT class Va from this analysis. This results in lower masses, given the smaller dimensions vessels has.

Another clear difference arises from the parameter on the y-axis, the velocity. The initial values of the polynomials in Figure 3.11 experience a decrease ranging from approximately 10% to 20% compared to those in Figure 3.9. The same decrease applies to the end values of the polynomials, except for the polynomial at location A, where a decrease of 35% is observed for the same mass. This confirms that vessel velocities are lower in the case of an operational lock, which is favourable in terms of potential collision energy.

3.4. Collision energy analysis

In this section, the potential collision energy is determined per vessel at the inner gate of the lock. For this analysis, only shipping traffic towards the port (south-going) is considered, as this situation is deemed critical (refer to Section 2.3.2). The average and maximum collision energies per CEMT class are analysed in this chapter for an open (Section 3.4.1) and a closed (Section 3.4.2) lock. Finally, the analysed energy is compared with the prescribed energy from existing standards (Section 3.4.3). The expectation is that the prescribed energy from the Eurocode is higher than most of the analysed energy, since the measured velocities are lower than the prescribed 3 m/s.

3.4.1. Collision energy non-operational lock

A bar chart + box plot of the expected collision energy are generated for each standard, and these are presented in Appendix C. The results for the collision energy per CEMT class are summarised in Table 3.1 & 3.2.

	Mass [t]	Velocity [m/s]	Collision energy [kNm]		
			Eurocode	PIANC	AASHTO
CEMT I	164	1.94	344	301	329
CEMT II	502	1.51	743	648	709
CEMT III	877	1.35	908	793	867
CEMT IVa	1,518	1.24	1,434	1,252	1,373
CEMT Va	2,839	1.03	1,792	1,564	1,802

Table 3.1: Average collision energies per CEMT class for location E

	Mass [t]	Velocity [m/s]	Collision energy [kNm]		
			Eurocode	PIANC	AASHTO
CEMT I	271	3.37	692	604	661
CEMT II	902	2.77	3,525	3,077	3,365
CEMT III	1,771	2.40	3,122	2,724	2,980
CEMT IVa	2,842	2.43	5,023	4,384	4,795
CEMT Va	4,783	1.91	4,323	3,773	4,127

Table 3.2: Maximal collision energies per CEMT class for location E

Note: The average and maximum collision energy values do not correspond with the values defined for the measured average/maximum velocity and mass. The collision energy is individually determined for each vessel and from there an average and maximum value for the collision energy is derived per CEMT class. The maximum collision energy for example, will in practice be a combination of an high velocity versus a somewhat lower mass or a low velocity versus a somewhat higher mass. The occurrence of both high velocity and high mass is not practical, as observed in the data analysis.

First of all, the difference between norms is noticeable. With the Eurocode generating the highest value for collision energy, closely followed by the method described by AASHTO. Looking back at the literature, these methods closely align each other in approach and are both essentially intended for a collision with a so-called hard structure. The lowest collision energy is generated by the method of PIANC, which is specifically designed for collisions with a lock gate.

Furthermore, it can be concluded that for the lower classes the mass is not extremely high and, compared to the higher classes, the velocities are higher. Velocities vary by class, and only Class I exceeds a maximum velocity of 3 m/s. This, again, proves that the value from the Eurocode is a conservative estimate. Vessels in higher CEMT classes show maximum velocities around 2 m/s.

Besides that, it can be concluded from the diagrams in Appendix C and Table 3.1 that there is a gradual increase in average collision energy as the CEMT class increases. This is explained by the results presented earlier in this chapter, where an increase in mass leads to a reduction in velocity. On average, this results in a smooth and gradual rise in collision energy, but when examining the maximum values occasional outliers are observed. It is noticeable that the maximum collision energy of classes II and IVa are higher than the

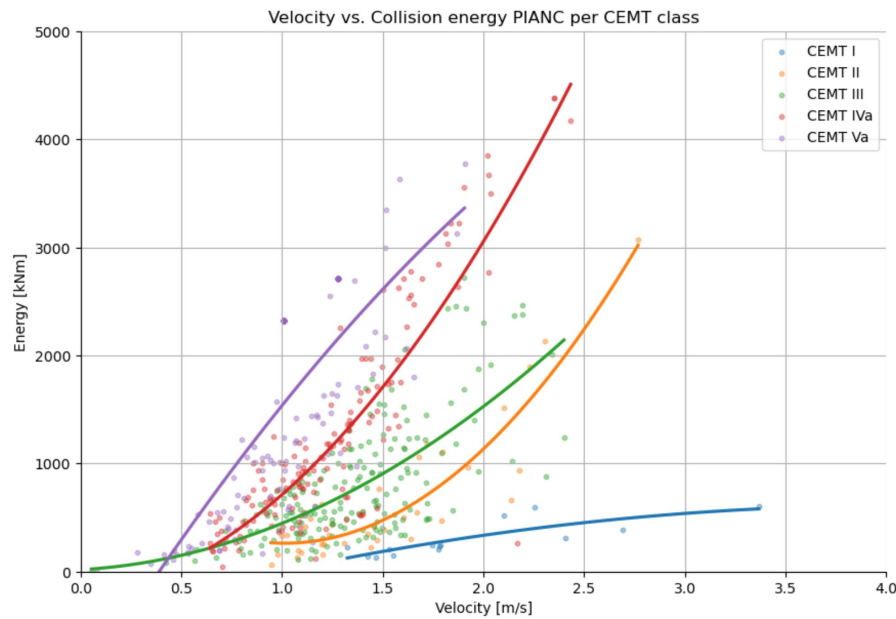


Figure 3.12: Velocity vs. collision energy based on PIANC data points + polynomials per CEMT class at location E

geometrically larger classes III & Va respectively. The reason for this is due to the higher velocity vessels have. In Figure 3.12, this is clearly observable by following the orange (Class II) and red line (Class IVa). Both of these lines exhibit a steep increase in velocity. This, combined with a large mass, results in higher values for collision energy. With an emphasis on the combination of a relatively high mass and velocity, as the polynomial for CEMT class I demonstrates that despite an high velocity, the collision energy is low due to a low mass.

The analysis in this section demonstrates that it is not always accurate to consider the largest possible navigation class as dominant. In this case for instance, CEMT class IVa yields the highest collision energy overall due to the combination of an high velocity with a relatively large mass. This may be the result of the fact that vessels larger than 135 m are not allowed in the port of Oss, resulting in an 'incomplete' dataset for class Va. But it could also be due to the fact that vessels in this class generally have an higher velocity, as discussed in the previous paragraph. It is of course advisable to conduct such analyses for any other location, as there are numerous factors that can vary.

3.4.2. Collision energy operational lock

The analysis for the collision energy during an operational lock is less representative than when the lock is not operational for this location. Simply because there is less data available. The box plots are therefore not included in Appendix C for this analysis. The bar charts are included in the appendix and the results are presented in Table 3.3 and 3.4.

	Mass [t]	Velocity [m/s]	Collision energy [kNm]		
			Eurocode	PIANC	AASHTO
CEMT I	256	1.01	142	124	136
CEMT II	171	1.21	137	119	131
CEMT III	1,103	1.04	714	623	682
CEMT IVa	615	1.15	444	387	424

Table 3.3: Average collision energies per CEMT class for location E during closing

From the results of classes I, II and IVa it can again be concluded that it is a small dataset, as the average collision energy is identical to the maximum collision energy. CEMT class III contains the most vessels, namely 8 vessels of the 11 vessels in total.

The first noticeable aspect is the significantly lower values for collision energy. The results of the average and maximum values do not even come close to the results from Tables 3.1 and 3.2. This is caused by the lower velocity and mass vessels has. It is straightforward that a vessel approaches the lock with a lower velocity,

	Mass [t]	Velocity [m/s]	Collision energy [kNm]		
			Eurocode	PIANC	AASHTO
CEMT I	256	1.01	142	124	136
CEMT II	171	1.21	137	119	131
CEMT III	1,891	1.53	1,640	1,565	1,627
CEMT IVa	615	1.15	444	387	424

Table 3.4: Maximal collision energies per CEMT class for location E during closing

given that it is operational. Often, the vessels need to wait before they can enter the lock. Only class III yields relatively high numbers for maximum collision energy, making it dominant in this situation. The average and maximum mass of this class are even larger than the values in Table 3.1. However, the measured collision energies are considerably lower due to the lower velocities vessels have.

Although the analysis from this section involves a small dataset, it does provide a certain perspective from which conclusions can be drawn. The relatively lower velocities and masses of the vessels result in a much lower potential collision energy. Besides that, it excludes an entire CEMT class because it is practically not possible for vessels with a length longer than 85 m to reach the port of Oss. To make this analysis more representative, more data would need to be available to perform the desired analyses.

3.4.3. Collision energy based on norms

The calculated collision energy based on the measured AIS data is compared with the values prescribed by the available norms, per CEMT class, in this section. Table 3.5 presents the results based the Eurocode and PIANC.

	Mass ¹ [t]		Velocity [m/s]		Collision energy [kNm]	
	Eurocode	PIANC	Eurocode	PIANC	Eurocode	PIANC
CEMT I	200 - 400	0 - 200	3	0.5 - 2	990 - 1,980	0 - 384
CEMT II	400 - 650	200 - 500	3	0.5 - 2	1,980 - 3,218	24 - 960
CEMT III	650 - 1,000	500 - 1,500	3	0.5 - 2	3,218 - 4,950	60 - 2,880
CEMT IVa	1,000 - 1,500	1,500 - 3,000	3	0.5 - 2	4,950 - 7,425	180 - 5,760
CEMT Va	1,500 - 3,000	3,000 - 5,700	3	0.5 - 2	7,425 - 14,850	360 - 10,944

Table 3.5: Collision energies per CEMT class based on the Eurocode and PIANC

¹: based on Table C.3 from (Eurocode, 2015) and Figure 4.2 from (PIANC, 2022)

The method described by AASHTO is excluded from analysis due to a lack of prescribed data. The Eurocode effectively represent the AASHTO method, since they closely align with each other. Originally, PIANC does not take into account CEMT classes so these are translated based on the length of the respective vessels. The collision energies from Table 3.1 & 3.2 are added once again in a table, alongside those based on the Eurocode and PIANC. This is done for the reader's convenience; refer to Table 3.6.

	Collision energy [kNm]					
	Eurocode			PIANC		
	Norm	Data mean	Data max.	Norm	Data mean	Data max.
CEMT I	990 - 1,980	344	692	0 - 384	301	604
CEMT II	1,980 - 3,218	743	3,525	24 - 960	648	3,077
CEMT III	3,218 - 4,950	908	3,122	60 - 2,880	793	2,724
CEMT IVa	4,950 - 7,425	1,434	5,023	180 - 5,760	1,252	4,384
CEMT Va	7,425 - 14,850	1,792	4,323	360 - 10,944	1,564	3,773

Table 3.6: Collision energies per CEMT class based on the Eurocode and PIANC. The column 'Norm' represents the calculated energies based on the prescribed masses and velocities from the norms. The columns 'Data mean' and 'Data max.' represent the calculated energies based on the measured masses and velocities from the AIS dataset.

Firstly, the differences and similarities in collision energy for the Eurocode are examined. The average collision energy based on AIS data (Data mean) is significantly lower than the calculated values based on the norm. The masses appear to fall within the prescribed range, but the velocities are much lower than prescribed.

The maximum collision energy based on AIS data (Data max.) seems to be moving closer to the prescribed values. This is because higher masses are measured compared to the prescribed masses from the Eurocode. Although the velocity for the measured data is lower than the prescribed 3 m/s, the higher mass results in significant maximum collision energies. For some CEMT classes, a collision energy is calculated that falls outside the prescribed range. In most cases, this is due to a significant deviation in mass or velocity compared to the prescribed standard. For example, for vessels belonging to CEMT class Va this is caused by the restriction that vessels longer than 135 meters are not allowed to pass through the lock.

The masses prescribed by PIANC lie closer to the measured masses from the AIS dataset (Data mean). This is concluded for both the average and maximum measured masses. They all fall (almost) within the prescribed range, as well as the collision energies. However, since the range in collision energy is quite large this is not surprising. The wide range is caused by the velocity PIANC prescribes, namely between 0.5 and 2.0 m/s. As the mass increases, the gap between the lowest and highest prescribed collision energy increases as well due to the fact that the velocity is squared. This highlights the importance to specify the velocity of a vessel as accurately as possible. To further support the significance of this, Figure 3.13 is included. In the left graph of this figure, all measured velocities are plotted against the calculated energy per passing vessel in the lock chamber. The adjacent histogram on the right side illustrates the cumulative distribution of the calculated collision energies. This immediately clarifies the percentage of the dataset exceeding a certain energy threshold. In the histogram, the calculated energy corresponding to four velocities, namely 0.5, 1.0, 1.5, and 2.0 m/s, is plotted based on PIANC. Based on these four lines, the influence of the varying velocity on the potential collision energy is examined for a fictitious vessel belonging to CEMT class Va with a mass of 3,000 tons. This is the low mass limit according to PIANC for this CEMT class.

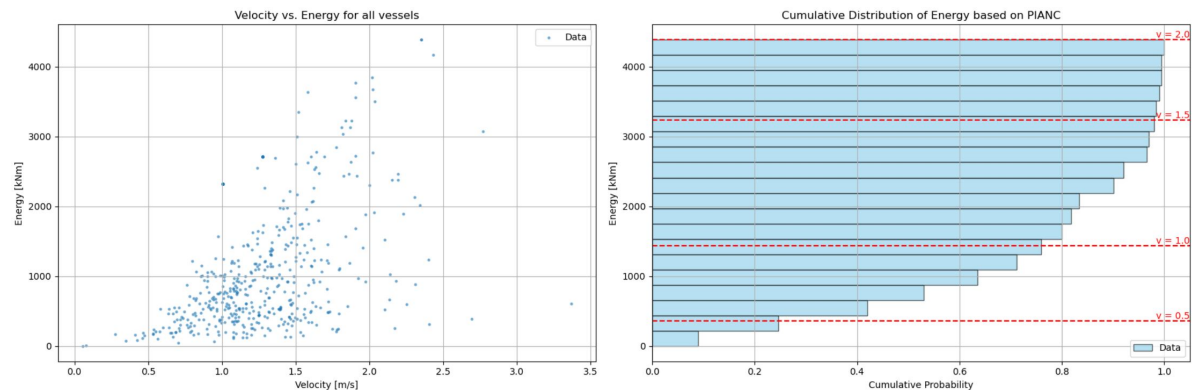


Figure 3.13: Measured velocities vs. calculated collision energies based on PIANC (left) and cumulative distribution collision energy including prescribed energy from PIANC based on a vessel with a mass of 3,000 t, with a velocity ranging from 0.5 to 2.0 m/s (right)

The histogram shows that the collision energy caused by the fictitious vessel at a velocity of 0.5 m/s has a cumulative probability of approximately 0.25. In other words, about 25% of the calculated collision energies from the dataset are equal to or lower than this value. When the velocity is equal to 1.0 m/s, this percentage changes to about 75%. This increase indicates that the potential collision energy of the majority of all vessels, i.e. 50%, lies between the range corresponding to a velocity of 0.5 m/s and 1.0 m/s based on PIANC and the fictitious vessel. As the velocity is further increased to 1.5 m/s, it becomes evident that the calculated collision energy corresponding to this velocity is exceeded by only a few vessels. The energy associated with a velocity of 2.0 m/s is so high that no vessel manages to reach it. This point is not visualised in the histogram but is considered equal to the maximum measured energy. This demonstrates that the difference in collision energy can be significant between a velocity of 0.5 m/s and 2.0 m/s, highlighting the importance of AIS data analysis.

3.5. Conclusion on AIS data analysis

At the beginning of the chapter, the research question is stated: "How can practical information from AIS data improve the accuracy of input parameters for collision energy estimation?" This data is collected for an existing lock in Macharen in order to determine the potential collision load on the lock gate. Where available standards prescribe conservative or varying values, the AIS data analysis provides more accuracy in determining the input parameters: velocity and mass. Through the AIS data analysis, a better understanding is gained of the actual velocities that vessels have at a desired measurement point. One of the key findings of the data analysis

of Macharen lock is that the average measured velocity and most maximum measured velocities fall below the prescribed 3.0 m/s from the Eurocode. This varies for each project and therefore also offers many possibilities. The analysis reveals differences between CEMT classes, and thus does not result in a constant velocity that should be used for every vessel as prescribed in the Eurocode.

The comparison of the calculated collision energies based on the AIS dataset with the prescribed energies from the Eurocode shows that the average values are below the prescribed values as well. The maximum calculated collision energies seem to be more in line. Vessels belonging to CEMT class II and IVa even show results towards the prescribed upper limit from the standards. This confirms the usefulness of the data analysis and concludes that it is not always correct to assume that the highest CEMT class generates the highest collision energy. PIANC prescribes a fairly wide range for collision energy, which only increases the need for accurate data analysis. The prescribed velocities in this standard range from 0.5 m/s to 2.0 m/s. The analysis from Section 3.4.3 demonstrates that this can lead to significant differences in terms of collision energy and underscores the necessity of a thorough analysis for a collision-resistant design of a lock gate.

4

Numerical modelling of ship collision on the Macharen lock gate

In this chapter, all aspects regarding the development of the gate model in RFEM are discussed. The aim is to determine the performance of the overall structure. Therefore, multiple layouts of the lock gate are modelled for comparison and the influence of various structural components, choice of mesh size and steel strength are analysed. After that, the differences between these layouts are addressed. The lock gate at Macharen is chosen as a reference from practical experience. Internal integrity is considered as the verification of the numerical gate model. This is achieved by filtering out errors and making adjustments during the development of the model. Research question 3: *"How can the impact on the lock gate be schematised, and which factors are relevant in this context?"* is answered in this chapter.

4.1. Input parameters & boundaries

In this section, the manual implementation of input parameters and boundary conditions required in the gate model are discussed. Firstly, the overall structure of the lock gate is examined, drawing insights from the design of the Macharen lock as a basis (Section 4.1.1). Additionally, consideration is given to the properties of the steel used and how it is modelled (Section 4.1.2). Subsequently, various aspects necessitating adjustment within RFEM are addressed, including mesh size and the contact between the lock gates (Sections 4.1.3 and 4.1.4, respectively). Finally, the types of nodal and line supports used in the gate model are defined (Section 4.1.5).

4.1.1. Lock gate structure

Macharen lock is equipped with two sets of mitre gates, both of which have the same dimensions and properties. The gates are modelled with plate elements, with five horizontal girders, vertical girders, the heel post and mitre post of both gates. The gate characteristics are summarised in Table 4.1. Modelling with plate elements allows for a more accurate consideration of connections between elements and stiffeners. For instance, the skin plate of the lock gate can be attached only to the upper flange, as it is in reality. With beam elements it is as if one line is modelled and in this case the skin plate becomes fixed to the entire beam. The same applies to the connection of the stiffeners to the horizontal girders and the girders to the heel- and mitre posts.

	Up- and downstream gate
Gate width, [m]	7.38
Gate width including heel post, [m]	8.20
Gate height, [m]	8.52
Gate height including balustrade, [m]	10.30
Closed state ratio, [-]	1:3
Canal bottom, [m]	NAP +0.20
Sill level, [m]	NAP +0.50

Table 4.1: Gate characteristics Macharen lock (Goeijenbier et al., 2022)

The structural components of the lock gate are provided in Table 4.2, where all components are named along with their respective dimensions. The bottom horizontal girder is located at NAP +0.50 m, and the center-to-center distance between the second girder is 2.13 m. The top horizontal girder is positioned at NAP +9.02 m, which corresponds to approximately 4.1 m above the lowest water level (NAP +4.9 m) when the lock is operational. Given the shape of common vessel bows in inland navigation (refer to Section 2.2.2), it is assumed that the second highest girder at NAP +6.89 m bears the entire initial load. Since this critical girder is above the waterline most of the time, differential loading due to water level changes is considered irrelevant. It is possible that this girder may fail due to a high collision force. The vessel will then penetrate further through the lock gate, loading the next horizontal girder. This process repeats until the vessel comes to a stop, i.e., all energy is absorbed. This process is discussed in Chapter 6.

	Height	Flange width	Flange thickness	Web thickness
Skin plate	8,520	-	-	10
Horizontal girders DIN550	550	300	30	16
Vertical girders half INP200	100	90	11.3	7.5
Stiffeners HP160x7	160	29	-	7
Diagonal struts L120x120x12	120	120	12	12

Table 4.2: Structural components steel mitre gate, all dimensions are in mm (Van Rinsum, 2021)

In reality, the mitre post at the contact point of the gates consists of a wooden bar clamped between steel plates (refer to Figure 4.1a). This wooden bar is excluded in the model. It is assumed that, despite its massive cross-section, it has a limited contribution to the bending stiffness of the mitre post. In reality, the wooden bar ensures load transfer. It will deform along with the steel to which it is attached. However, the stiffness is so low that the contribution is negligible. A simplified model in which the wooden bars are replaced by triangular box profiles seems to have the same effect on the stability of the mitre posts. This is verified through a calculation where all other parameters are kept the same. The steel stiffening bulkheads around the mitre post in the model extend over the height of the gate. Only at the locations of the horizontal girders, locally triangular boxes are formed to facilitate the load transfer from the contact point between the two mitre posts (see Figure 4.1b).

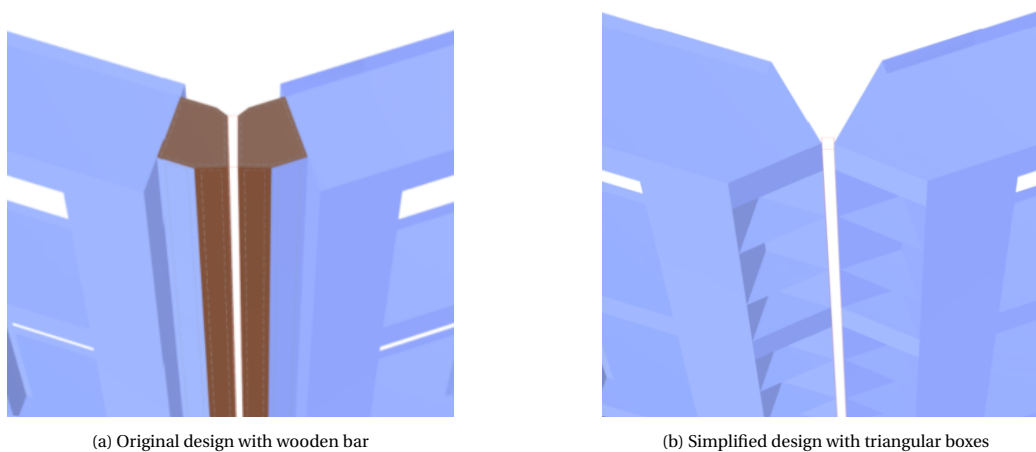


Figure 4.1: Modelling of the mitre posts

4.1.2. Modelled steel properties

The steel of the gate is modelled as elasto-plastic behaviour. In this case, graph c from Figure C.2 of NEN-EN 1993-1-5 (Eurocode, 2012) is used, as illustrated in Figure 4.2a. The approach in this graph maintains stiffness after the yielding of the steel. The redistribution of forces occurs more gradually, aiding the model in remaining stable. The intention of using this approach is to incorporate the strain hardening behaviour of steel in a simplified manner when compared to Figure 2.1 in Section 2.1.4.

The steel used for the lock gate is specified as S235 with a yield strength of 235 N/mm². Beyond the yield strength the Young's modulus is reduced to 1/100 of the original Young's modulus, which is 2,100 N/mm². Additionally, Eurocode (2012) prescribes a maximum value for the principal strain of $\epsilon_{max} = 5\%$. From this

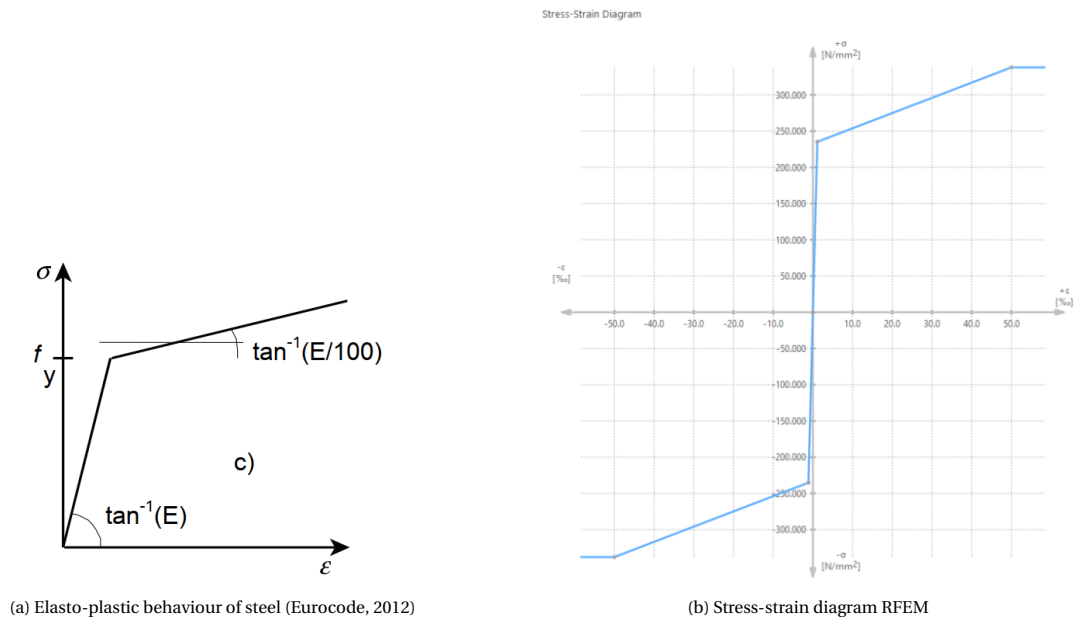


Figure 4.2: Modelled stress-strain behaviour of steel S235

point onward, the steel will yield without being able to withstand further increasing loads, i.e. an infinite strain occurs at an equal force. This takes into account the calculated failure behaviour of the steel into the analysis. However, in the case of local failure behaviour the analysis can continue until global failure occurs, leading to instability in the model. In Figure 4.2b, it is observed how this behaviour is implemented in the model. The stress corresponding to a strain of 5% is approximately 338 N/mm^2 .

4.1.3. Mesh size

The initial mesh size is set at 0.5 m in RFEM. For finer results a smaller mesh size can be chosen, but this may increase computation time. Nevertheless, several models with a mesh size of 0.25 m are computed to observe the differences and, expectedly, increased accuracy. For the models in Chapter 6, a mesh size of 0.25 m is used for calculations.

4.1.4. Surface contact gates

The connection between the gates is modelled as a 'surface contact' in the gate model (see Figure 4.3). At the mitre posts two parallel plates are modelled, which are considered in contact by RFEM. The condition applied here is that under tension the contact disappears in all directions, allowing the gate to deform freely. Forces are transferred if there is pressure in the surface contact. This approach allows for an investigation into whether the gates move apart upon collision. It ensures that the gates cannot detach from each other on a global scale.

4.1.5. Nodal & line support

The geometry of the lock gate features five horizontal girders with a constant center-to-center distance. The lock gate rests on the lock head wall along the entire height of the heel post. Therefore, a line support has been applied at the heel posts over the full height with the condition that no tensile forces can be absorbed. If this occurs, for example during significant deformation of an horizontal girder, the heel post will detach from its support resulting in leakage. This non-linear characteristic is considered in the model.

For conceptual purposes, nodal supports are added at the top and bottom of the heel posts. The supports on both sides can absorb horizontal forces, but if the gate is closed the load is primarily transferred through the posts. The load seeks the quickest path to a support. Therefore, a girder in the middle of the gate will not horizontally transfer loads to the nodal supports (refer to Figure 2.6a). The support at the bottom may be relevant when considering the self-weight of the gate. This vertical load generates a support reaction at the bottom of the heel post. Additionally, as indicated in Section 2.1.3, this creates a moment that results in a tension force at the top and a compression force at the bottom of the heel post.

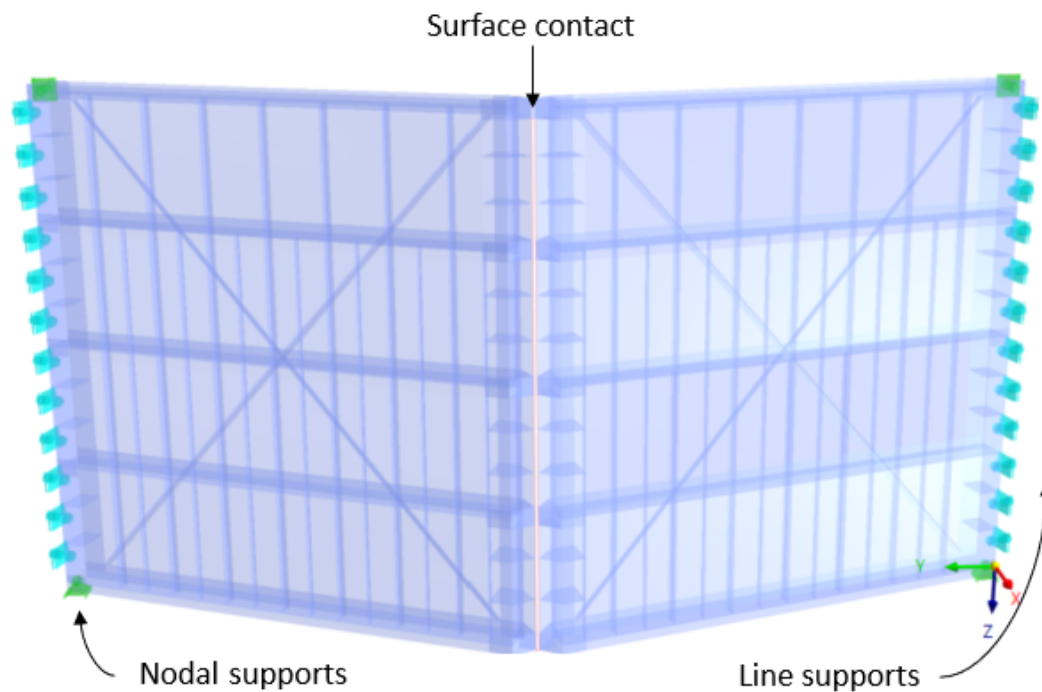


Figure 4.3: Modelled gate structure in RFEM with skin plate, horizontal and vertical girders, stiffeners, struts, surface contact, line supports (blue) and nodal supports (green)

4.2. Schematisation of a collision between vessel and lock gate

Several gate layouts are modelled in this section, varying in structural properties, loads and/or structure. To accurately compare the influence of the desired analysed aspects, the gate layouts are kept consistent with each other. For example, the collision characteristics vary for vessels of different dimensions, i.e., CEMT class, and are only compared with classes exhibiting similar characteristics. In this, a distinction is made between a symmetrical and an unsymmetrical collision (Section 4.2.1). Additionally, the contact points of the vessel with the gate is important, which are determined based on the collision height and depth (Section 4.2.2). After that, an approximation is made for the load to be applied to the lock gate. A symmetrical collision differs from an unsymmetrical collision in this regard. Section 4.2.3 provides an estimate for the width of the applied load, which is derived from a sketch from the thesis "Ship Impact Energy on Rigid Structures" (1993).

4.2.1. Type of collision per CEMT class

The collision scenarios on the inner gate of the lock consist of various points of contact between the vessel and the lock gate. Distinctions are made based on CEMT class, considering the varying widths vessels has. The required energy is determined in the case of collision at the mitre post (symmetrical) and collision alongside the mitre post (unsymmetrical), as explained in Section 2.3.3. The force application and the anticipated failure mechanism of the gate differ for these collision types. In the case of a symmetrical collision, normal force is applied to the horizontal girders potentially causing them to buckle. In the case of an unsymmetrical collision, bending is particularly prominent in the girders.

All vessels are narrow enough to potentially impact the gate asymmetrically, except for those of class IVa and Va. The order of magnitude in this depends on the vessel's width and bow shape. With a blunt bow shape engaging at the mitre post is still possible after the initial contact, even if the vessel is outside the centerline of the lock chamber. Additionally, when determining the contact point for an unsymmetrical collision, a minimum edge distance is considered — the distance between the side of the vessel and the lock chamber wall. Vessels that sail with their side against the lock chamber wall lose energy due to friction between the vessel and the wall. This scenario is therefore not considered critical and not taken into account.

The point of impact farthest away from the lock chamber wall occurs at $0.5 \times$ vessel width in case of an unsymmetrical collision (refer to Figure 4.4). The characteristic width per CEMT class is provided in Appendix A. With a lock width of 14 m, this results in the following collision scenarios. Vessels belonging to:

- (a) CEMT class I can collide asymmetrically: max. $x = 4.47$ m from the chamber center;

- (b) CEMT class II can collide asymmetrically: max. $x = 3.70$ m from the chamber center;
- (c) CEMT class III can collide asymmetrically: max. $x = 2.90$ m from the chamber center;
- (d) CEMT class IVa collides symmetrically;
- (e) CEMT class Va collides symmetrically.

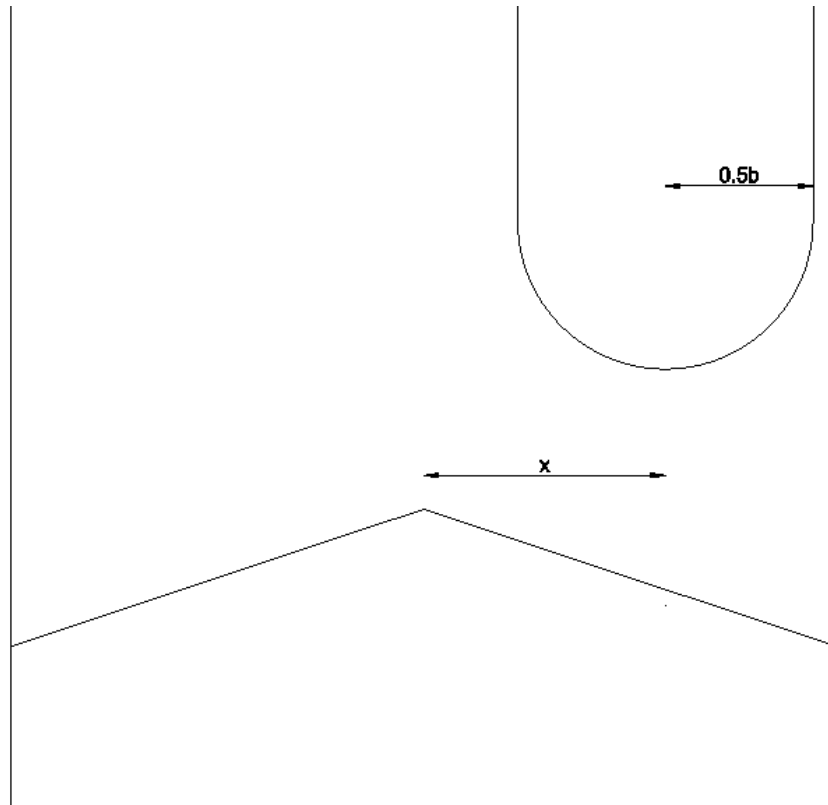


Figure 4.4: Top view unsymmetrical collision with varying x , maximum distance between lock chamber center and vessel center, per CEMT class

Note: in case of an unsymmetrical collision these are theoretical values. In practice, in the event of a serious collision the vessel will most likely navigate in the center of the lock chamber and not along the chamber wall.

The potential rotation of the vessel is neglected in this case, as it is constrained by the lock chamber's geometry. Rotation occurs in the case of a collision at an angle, leading to the back of the vessel making contact with the chamber wall. Both the rotation and the impact with the chamber wall result in energy dissipation, which is favourable for lowering the potential collision energy. For these considerations, this situation is not considered critical. Therefore, it is not elaborated further.

4.2.2. Determination collision height and depth

Collision of the gate is considered for water levels on the River Meuse between NAP +5.9 m and NAP +7.0 m, as explained in Section 3.1.2. The prescribed point of application height for the load in the absence of detailed information according to NEN-EN 1991-1-7 (Eurocode, 2015) is 1.5 m above the water level. Based on this, the collision height is determined where the load can be applied to the gate. This is graphically represented in Figure 4.5. The collision force applies between NAP +7.4 m and NAP +8.5 m. This plane is situated between the two upper horizontal girders of the lock gate.

The draft of the vessel is of great importance for determining the collision depth. It determines which horizontal girders can be loaded. This approach assumes a water level of NAP +5.20 m and that the draft per vessel is defined as described in the Richtlijnen Vaarwegen (2020). Based on this, it is concluded that only CEMT class I does not have sufficient draft to reach the second lowest girder at NAP +2.63 m. All the other classes could potentially load this girder if the energy of the respective vessel is not absorbed by the two horizontal girders above it.

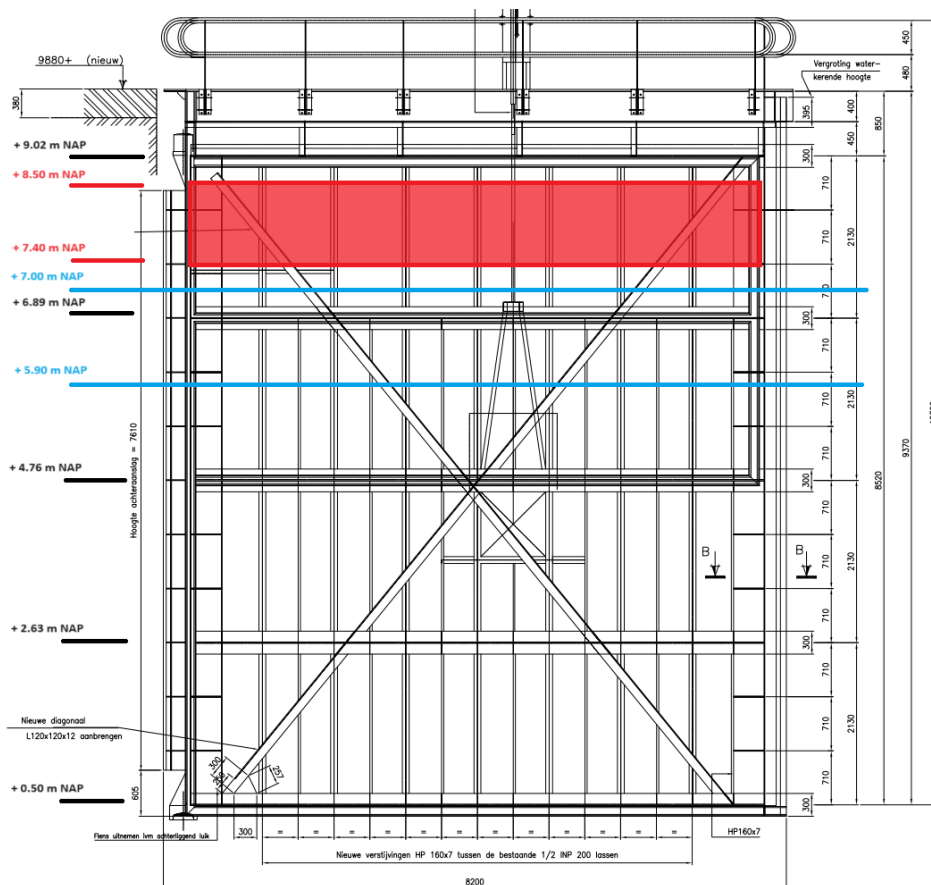


Figure 4.5: Potential collision height Macharen lock

4.2.3. Applied load (un)symmetrical collision

Modelling a collision between a vessel and a lock gate as a point load is a conservative approach. In reality, this load is more distributed across the width and height. Especially with the characteristic blunt bow shape of a typical inland waterway vessel this is the case. The Eurocode (2015) provides an approximation for both the width and height of an approaching object. Specifically, $h = 0.5$ m and $b =$ width of the obstacle in the waterway. However, this guideline concerns a collision with a bridge pier and the width of the obstacle (i.e., the vessel) varies in the case of a collision with a lock gate. The sketch in Appendix B is used to estimate the collision width of a typical inland vessel, by using the scale and known dimensions in the sketch. After the initial contact surface between the bow and the lock gate, a linear increase proportional to the deformation/penetration of the vessel is assumed (see Figure 4.6). However, in RFEM it is not possible to implement a function of the width dependent on the deformation. For this reason, the width belonging to the initial contact ($B = 300$ mm) is maintained as a conservative estimate for all applied loads.

Furthermore, modelling of a surface load acting on the lock gate is considered. However, yielding occurred more rapidly in the upper flange of the horizontal girder compared to modelling with a line or point load for an unsymmetrical collision. This is caused by the load now being eccentrically positioned on the upper flange, inducing a bending effect. It is assumed that the height of the applied load is equal to the width of the upper flange (300 mm). In reality, the flange will never bend due to the shape of the bow. Additionally, all stress is transferred to the web of the horizontal girder, which provides the greatest stiffness. For this reason, a line load is chosen for the schematisation of a unsymmetrical collision. On the other hand, schematising with a surface load is a good approximation in case of a symmetrical collision as the mitre posts generate stiffness across the entire height of the lock gate. The triangular box profiles at the level of the horizontal girders are used to apply this surface load. These surfaces each have a height of 300 mm and a width of 814 mm.

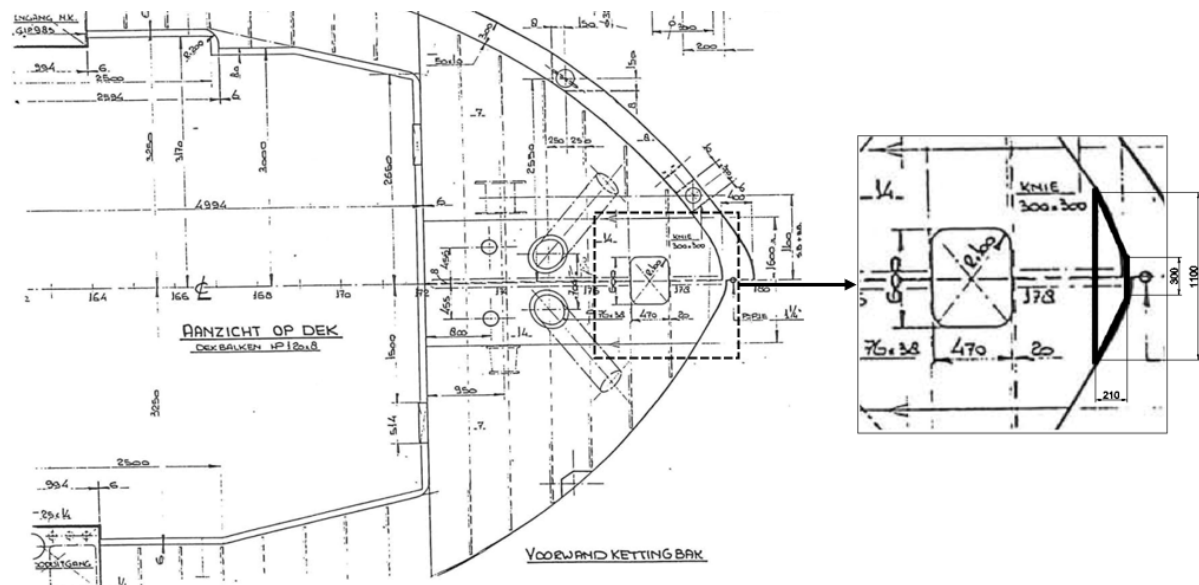


Figure 4.6: Linear approximation for estimating the width (mm) belonging to the initial contact of a typical inland waterway vessel based on the top view of the sketch in Appendix B (Joustra and Pater, 1993)

4.3. Sensitivity analysis based on original design Macharen lock

In this section, a sensitivity analysis is conducted to exclude certain aspects that simplify and/or make the modelling of the gate model more accurate. First, the influence of all the different components of the lock gate on the load capacity is considered. This is done for four scenarios, the results of which are discussed in Section 4.3.1. After that, variations are made between steel quality and mesh size. The aim is to demonstrate that a higher steel quality yields different results that favour the capacity of the lock gate and that a finer mesh size provides different, generally more accurate, results than a larger mesh size (Section 4.3.2). Finally, an examination of a collision in combination with hydrostatic water pressure and/or self-weight of the lock gate is done (Section 4.3.3).

4.3.1. Influence of all structural components

The influence of the different structural components used in the lock gate is discussed in this section. A lock gate with all components consist of a skin plate, horizontal and vertical girders, stiffeners and struts. Distinction is made between four scenarios, namely a lock gate with:

- all components, load on skin plate (Scenario 1);
- all components, load on girder (Scenario 2);
- all components except the skin plate, load on girder (Scenario 3);
- all components except the skin plate, stiffeners and struts, load on girder (Scenario 4).

For all four scenarios, the point of fracture strain $\epsilon_{max} = 5\%$ and associated deformation is determined. To effectively analyse the influence of all components it is assumed that an unsymmetrical collision occurs. At the end of this section, the results are discussed and the analysis is expected to allow for a simplified model without the skin plate, struts and bulb stiffeners. This is because it is expected that the skin plate fails on local buckling, and yields before the horizontal girder. It is therefore not considered to significantly contribute to the overall structure. The same applies to the bulb stiffeners and diagonal struts.

For each scenario, a line load of 300 mm width is applied with a varying initial force. For scenario 1, this load is placed on the skin plate, at the point where the vessel will approximately first impact the lock gate. This is somewhere between the top horizontal girder at NAP +9.02 m and second highest girder at NAP +6.89 m, refer to Section 4.2.2. For scenarios 2, 3 & 4, this load is placed in the middle of the second highest horizontal girder. The incremental method is used in RFEM, where the load is increased by 50 kN at each calculation step. If the model becomes unstable, the last step is divided in steps ten times smaller than the initial step size until the model fails or if it reaches the defined criterion. For this analysis, the steel is specified as S235 and a mesh size of 0.25 m is used. The results are documented in Table 4.3 and in Appendix D for the output of RFEM.

	F_{yield} [kN]	u_{yield} [mm]	F_{max} [kN]	$ u_{max} $ [mm]	$\sigma_{Mises,Max}$ [N/mm ²]	ϵ_{max} [%]
Scenario 1	90	12.2	900	129.6	337.8	50.2
Scenario 2	990	14.0	990	14.4	235.2	1.2
Scenario 3	810	22.3	1,683	275.6	337.8	50.2
Scenario 4	810	22.6	1,584	304.4	336.8	49.8

Table 4.3: Force and deformation capacity for all formulated scenarios at the point of yielding and failure with a line load of 300 mm and mesh 0.25 m

The first noticeable aspect from the Table 4.3 is that scenario 1 yields the lowest forces and deformations for the same stresses and strains compared to the other three scenarios. This is because the load is applied at the skin plate and not at the rigid horizontal girder. Due to the early failure of the skin plate, the vessel thus transfers almost all of its initial force to the second girder at NAP +6.89 m, which is well represented by scenarios 2, 3 & 4. The results on stress distribution in Appendix D.1 indicate that this girder is influenced by the load on the skin plate of scenario 1. The yield stress seems to be exceeded in a part of the girder, as a result of this load. However, this is not significant enough to cause the girder to fail. Later, in Chapter 6, it is explained whether this initial contact on the skin plate is important for determining the energy absorption capacity.

The results of scenario 2 show that the model fails when reaching the yield stress, indicating that modelling with a skin plate results in an unstable model. As a result, the skin plate fails on local buckling before the capacity of the girder is reached. Looking at the results of the deformation in Appendix D.1 and Figure 4.7, the results corresponding to the final computation step are illustrated. From the figure, it becomes clear that the skin plate locally bulges due to pressure stresses. The problem appears to be resolved when the skin plate is removed. This represents the situation accurately where the skin plate has failed and thus no longer affects the capacity of the gate.

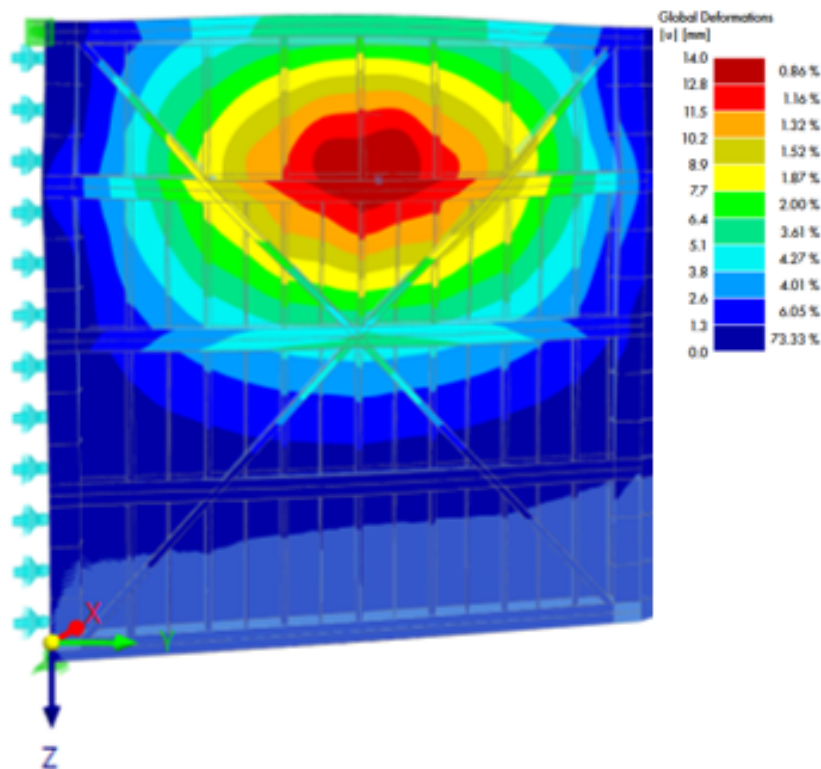


Figure 4.7: Rear view of the lock gate during maximum deformation leading to failure with a distributed load on horizontal girder at NAP +6.89 m

The models of scenarios 3 and 4 are constructed without a skin plate. There are no differences in the force and deformation corresponding to reaching the yield stress for these scenarios, but there are differences corresponding to reaching the fracture strain. Scenario 3 yields a slightly higher maximum load capacity

and lower deformation compared to scenario 4. This difference is explained by the fact that the model in scenario 3 receives slightly more stiffness from the bulb stiffeners. This higher stiffness results in an higher load capacity coupled with a slightly lower deformation of the girder. In terms of energy absorption, both scenarios are approximately equal to each other because the higher force of scenario 3 is compensated by the higher deformation of scenario 4. For this reason, the simplified model of scenario 4 is used for further analysis. The results of both scenario 3 & 4 can be found in Appendix D.2.

4.3.2. Mesh size & strength properties

In this section, the results of four variations in modelling used on the layout corresponding to scenario 4 are discussed. The variations involve changes in mesh size and steel quality to demonstrate the difference and influence on the capacity of a single horizontal girder. For this analysis, an unsymmetrical collision is assumed, and the results are presented in Table 4.4.

Scenario 4	F_{yield} [kN]	u_{yield} [mm]	F_{max} [kN]	$ u_{max} $ [mm]	σ_{max} [N/mm ²]	ϵ_{max} [‰]
S235, mesh = 0.25 m	810	22.6	1,584	304.4	336.8	49.8
S235, mesh = 0.50 m	734	19.1	1,917	428.5	337.8	50
S355, mesh = 0.25 m	1,193	33.3	2,138	273.3	456.5	49.9
S355, mesh = 0.50 m	1,101	28.8	2,619	414.8	456.5	49.6

Table 4.4: Results of variations in mesh size and steel strength properties for the model without skin plate, stiffeners and struts

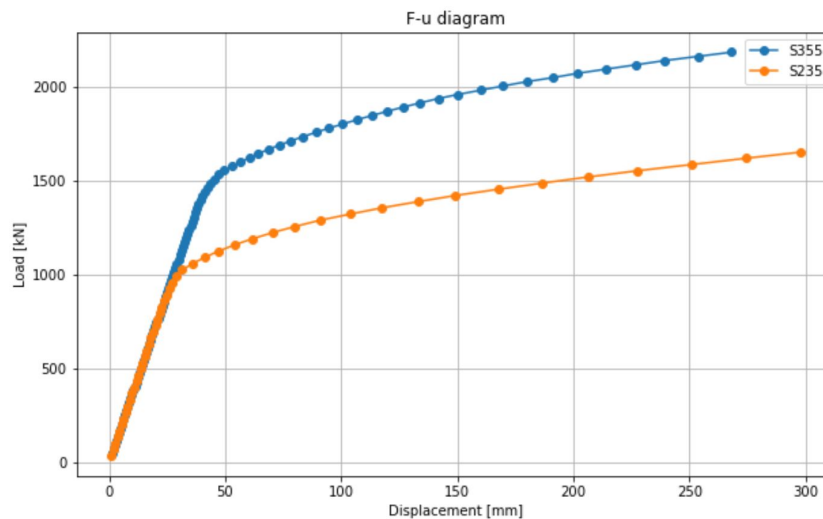


Figure 4.8: Force (F) - Displacement (u) diagram for an unsymmetrical collision regarding a girder made of S235 & S355 steel with mesh size = 0.25 m

Starting with the variation in steel quality between S235 and S355. It is concluded that S355 generates an higher force at the onset of yielding, because this threshold for elastic to plastic deformation simply lies higher for S355 compared to S235 (also refer to Figure 4.8). Additionally, an higher force is measured at which the fracture strain is reached, which is accompanied by a lower deformation compared to the S235 steel. Although S355 steel is stronger than S235 steel, resulting in a higher capacity to withstand force, S235 steel generally has greater ductility than S355 steel. This means that S235 steel can undergo more deformation before failing compared to S355 steel.

Elements in the gate model become larger when using a coarser mesh (0.50 m), which can lead to discretisation errors. This means that the model may not accurately represent the actual behaviour of the structure. It is possible that the coarser mesh does not capture the local effects of the load well, resulting in calculated forces being lower or higher than for a finer mesh. From Table 4.4, it can be concluded that a coarser mesh generates an higher force and consequently higher deformation compared to a finer mesh. Ideally a mesh-independent model should be used, which is obtained by performing iterative analyses to verify that the results do not significantly change with variations in mesh size. However, due to time constraints a mesh size of 0.25 m is chosen and considered accurate.

4.3.3. Hydrostatic water pressure & self-weight lock gate

In reality, there are constant loads acting on the lock gate, such as hydrostatic water pressure and the self-weight of the gate itself. The force and energy released during a collision are much more abrupt and intense compared to these constant forces. However, a difference in water level can cause the lock gate to be subjected to high loads, thereby using a portion of its energy absorption capacity. This section examines the influence of both constants on the gate's capacity.

Hydrostatic water pressure

The majority of the lock gate is located below the waterline, which results in hydrostatic pressure against the gates. The maximum head that can occur is 1.8 m, resulting in a pressure of 18 kN/m^2 on the gate. The second horizontal girder from the top, at level NAP +6.89 m, is loaded lightly since the maximum water level can rise to NAP +7.00 m. The two girders below it experience more load and therefore a situation with water pressure against the lock gate is considered.

The water pressure is applied as a distributed load on all loaded horizontal girders, this simplification is possible because the force is transmitted through these girders to the heel posts (refer to Figure 2.6b). Figure 4.9 shows that the second girder from the bottom is the most heavily loaded due to the water pressure. The water pressure results in a stress of up to 65 N/mm^2 in the upper flange of this girder, in the web of the same profile a stress of approximately 20 N/mm^2 is measured. When this water pressure occurs in combination with a collision, it could potentially result in a reduced capacity. Unfortunately, it is not possible to keep a constant (water) force active in RFEM during the calculation process of a collision.

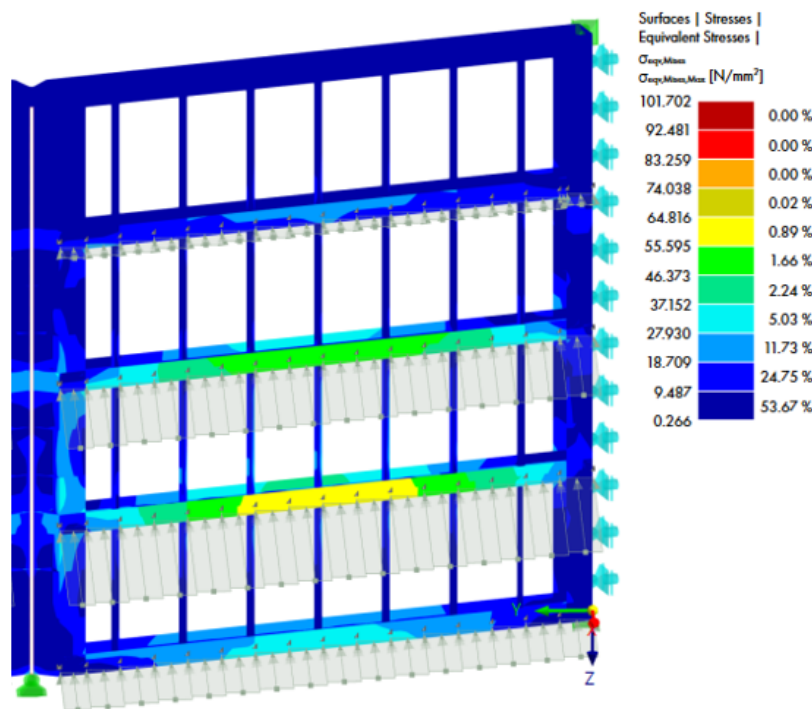


Figure 4.9: Stresses in the loaded horizontal girders due to hydrostatic water pressure

Given the inability to maintain a constant water force in RFEM during collision calculations, an approximation is made using the stress-strain diagram of steel and the definition of energy to determine the influence of water pressure on the lock gate's capacity. Energy is determined by two parameters, namely force and deformation (refer to Section 2.1.4). Both parameters are known and serve as output from RFEM. When examining the modelled behaviour of steel in Figure 4.2, it is concluded that the stresses in the upper flange and the web of the profile fall within the elastic zone. Characteristic of this zone is that the strain in the steel is very low, resulting in low deformation. The output from RFEM confirms this with a maximum deformation of 7.4 mm in the middle of the girder, caused by the water pressure. Now that the deformation is known, only the force needs to be determined. By multiplying the distributed load by the length of the girder, a value of 315 kN is obtained.

Only the elastic zone of the loaded girder is affected by the water pressure, so the force $F_w = 315$ kN and deformation $u_w = 7.4$ mm are proportional to each other. Due to the load caused by hydrostatic water pressure, the collision force at which plastic behaviour will be reached is lower. As a result, the total contribution to the force-displacement diagram due to collision is also lower. The area beneath the force-displacement diagram, i.e. the energy that needs to be absorbed due to the water pressure, is now equivalent to a strip with x-values ranging from 0 to u_{max} and y-values from 0 to 315 kN. Here, u_{max} is equal to the maximum deformation at which fracture strain occurs in the impacted horizontal girder. With this characteristic, Equation 2.7 from Section 2.1.4 is used to estimate the energy absorbed by the girder due to hydrostatic water pressure.

$$E = \frac{1}{2} \times F_w \times u_w + F_w \times (u_{max} - u_w)$$

This approach for determining the energy absorption due to the water pressure is further elaborated in Chapter 6 for the most critical girder at level NAP +2.63 m. This demonstrates whether the influence of this load is significant for determining the energy absorption capacity of the lock gate.

Self-weight lock gate

The self-weight of a lock gate generally has a limited impact on the gate's capacity during a collision. Since the self-weight does not directly contribute to the horizontal load, it has less influence on the gate's capacity compared to the forces generated by a collision. Additionally, in the gate model the self-weight of the gate is considered, but it does not yield varying results compared to a model where the self-weight is not included. Therefore, the influence of the self-weight has been neglected.

4.4. Conclusion on numerical modelling gate model

At the beginning of this chapter, research question 3 is formulated as follows: "How can the impact on the lock gate be schematised, and which factors are relevant in this context?". The decision is made to model the lock gate using finite element analysis software, namely RFEM. The advantage of this over an analytical method is that it allows for the inclusion of nonlinear properties of different components.

The chapter clarifies that modelling a lock gate depends on various factors, starting with the overall structure of the gate. The structure is modelled using plate elements rather than beam elements, as it allows for a more accurate consideration of connections between structural elements. Additionally, the load caused by a ship collision with a lock gate is schematised in two different ways, namely symmetrically and asymmetrically. The degree of asymmetry depends on the ship class. In the case of a symmetrical collision, a surface load is transferred from the vessel to the triangular box profile of the mitre posts. In the case of an unsymmetrical collision, a distributed line load is applied with a width derived from a sketch of a typical inland waterway vessel. The collision height and depth depend on the water level and ship class.

From the sensitivity analysis, it proves beneficial to exclude certain structural components from the schematisation of the lock gate in RFEM. These components cause the calculation process to halt due to the failure of the respective component. Additionally, factors such as mesh size and steel quality play a significant role in determining the overall capacity of the lock gate model. A finer mesh size generally leads to more accurate results, and a higher steel quality results in increased capacity of the lock gate. While the influence of hydrostatic water pressure may be relevant in the later stages of determining the energy absorption capacity of the lock gate, the self-weight does not have an impact here.

5

Validation of the numerical gate model

The Macharen lock gate model is validated by creating a simplified gate model that remains representative of the original gate model. The simplifications are introduced due to the significant complexity of the collision with a lock gate. This includes the simplification of the load as a point load and excluding the skin plate, vertical girders, stiffeners and struts from the model. A suitable approach for accomplishing the validation is by comparing the simplified model with an analytical model. The ideal option would be to validate using information from a real collision between a lock gate and a vessel. However, such information is not available and validation through an analytical model serves as a reasonable alternative. The analytical model here serves to gain a basic understanding of the situation and as comparison for the results of the simplified gate analysis. Both the simplified lock gate model and the analytical model are compared through two analyses, namely geometrically linear analysis and large deformations analysis. The geometrically linear analysis checks the structure for pure bending and does not include deformations of the structure in the calculation. On the other hand, the large deformations analysis does consider these deformations. Different results are expected for both analyses.

5.1. Development of analytical collision model

The analytical model is checked for two failure mechanisms, namely pure bending and lateral torsional buckling. Both failure mechanisms generate different results, but it is expected that pure bending generates the lowest force. Equations 5.1 indicate the limits of the critical bending moment $M_{y,pl}$ and critical lateral torsional buckling moment M_{cr} , respectively.

$$M_{max} \leq M_{y,pl} \qquad M_{max} \leq M_{cr} \qquad (5.1)$$

These are determined in this section, but first the used static system is explained. Following this, the section moduli and moments of inertia are calculated for the used steel profile of the horizontal girders.

5.1.1. Description of the static system

It is essential to establish a static system that allows for the determination of values such as geometry and stiffness, to assess the gate's behaviour post-collision. The simplest static system for mitre gates involves treating each gate independently as a girder supported by two hinges (refer to Figure 5.1a). In this model, the contact point between the two gates is considered stationary and all load at the center support is transferred to the other gate. In reality, the center point and the cross connections via the posts to other girders may not behave as a true hinge due to frictional forces.

An improvement to this model for enhanced accuracy involves representing both gates connected by a hinge (see Figure 5.1b). In this system, the center point is free to deform as long as the gate tips remain in contact with each other. The mitre posts of both gates can become detached at the top and bottom due to tensile forces. This phenomenon is considered in the RFEM model (see Section 4.1.4). Since the deformations of the unaffected gate are relatively small due to the gate's higher axial stiffness compared to bending stiffness, the difference between the two discussed systems is minimal. The small increase in accuracy does not justify

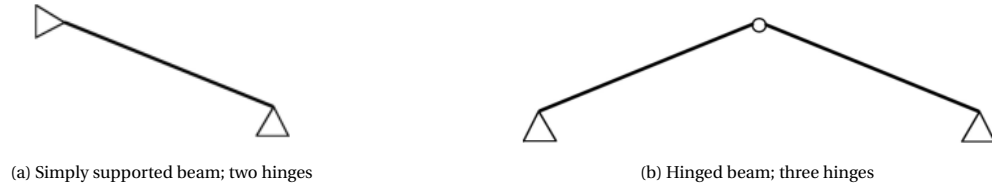


Figure 5.1: Static system mitre gate (Edmondson, 2017)

the added complexity of the model. Therefore, the beam on two hinged supports is further elaborated for the analytical calculations.

5.1.2. Determination section values of the horizontal girders

In this section, both the moment of inertia (I) and section modulus (W) are determined for the profile of the horizontal girders. After all, these are the components that will bear the most force. The horizontal girders are designed as DIN550 profiles and have a length of 8.2 meters, as shown in Figure 5.2 for the cross-sectional profile.

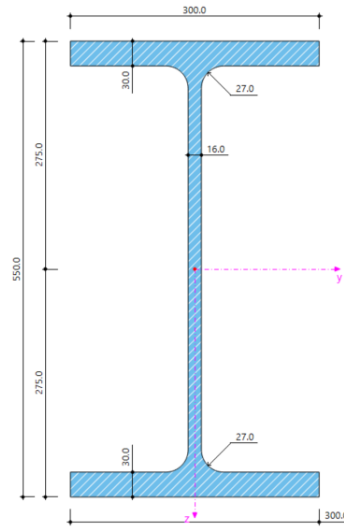


Figure 5.2: Cross-sectional profile DIN550

Moment of inertia

The parallel axis theorem is used to determine the total moment of inertia around the y- and z-axes of the I-beam. For this calculation the profile is divided into rectangular sections and the moment of inertia is determined for each individual rectangle. The sum of these three moments of inertia in total represents the inertia moment of the defined cross-sectional profile. The radius between the flanges and the web is not considered in the analytical calculation.

$$I_y = \sum (\bar{I}_{yi} + A_i z_i^2) \quad I_z = \sum (\bar{I}_{zi} + A_i y_i^2) \quad (5.2)$$

Where:

A_i = area of an individual rectangle [mm^2]

z_i = vertical distance from the centroid of an individual rectangle to the centroid of the beam [mm]

y_i = horizontal distance from the centroid of an individual rectangle to the centroid of the beam: 0 for I-beam

\bar{I}_{yi} = moment of inertia rectangular cross-section about y-axis: $\frac{b_i h_i^3}{12}$ [mm^4]

\bar{I}_{zi} = moment of inertia rectangular cross-section about z-axis: $\frac{h_i b_i^3}{12}$ [mm^4]

The elaboration yields the following values:

$$I_y = \frac{300 \times 30^3}{12} + 300 \times 30 \times \left(\frac{550}{2} - 15\right)^2 + \frac{16 \times 490^3}{12} + \frac{300 \times 30^3}{12} + 300 \times 30 \times \left(\frac{550}{2} - 15\right)^2 = 1.38 \times 10^9 \text{ mm}^4$$

$$I_z = \frac{30 \times 300^3}{12} + \frac{490 \times 16^3}{12} + \frac{30 \times 300^3}{12} = 1.35 \times 10^8 \text{ mm}^4$$

Section modulus

The elastic section moduli for both y- and z-axis are determined by using Equation 5.3. In this context, the section modulus about the y-axis depends on the so-called y_{max} , which for an I-profile is equal to $1/2h$ (refer to Figure 5.3a). The section modulus about the z-axis depends on z_{max} , which for an I-profile is equal to $1/2b$. With this information all parameters are known and the section moduli is calculated.

$$W_y = \frac{I_y}{y_{max}} = 5.00 \times 10^6 \text{ mm}^3 \qquad W_z = \frac{I_z}{z_{max}} = 9.01 \times 10^5 \text{ mm}^3 \qquad (5.3)$$

Additionally, it is essential to determine the plastic section modulus to account for plastic behaviour in this analytical approach. However, only the plastic section modulus about the y-axis is relevant in this case. In the cross-section of the I-beam in Figure 5.2, only a bending moment occurs about the y-axis given that the load is applied to the upper flange of the profile in z-direction. This moment causes compressive stresses above the neutral axis, which coincides with the y-axis of the cross-section. Tensile stresses occur below the neutral axis, refer to Figure 5.3b. All stresses (σ) are equal in value to the plastic section capacity $f_{y,pl}$.

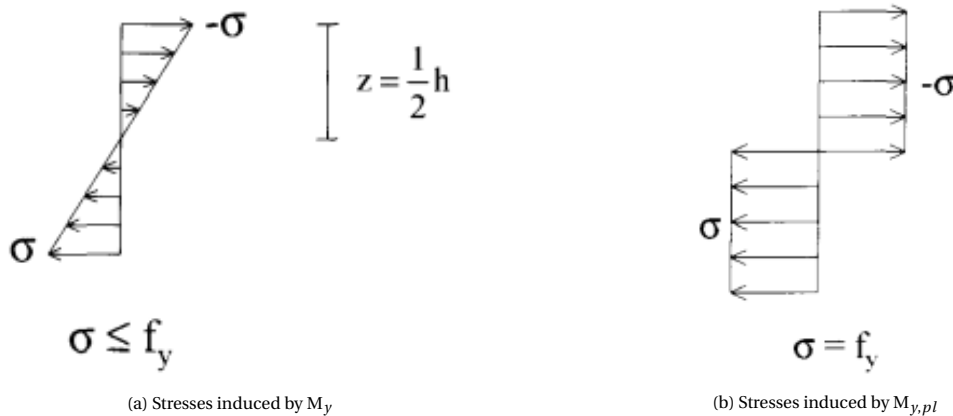


Figure 5.3: Stress diagrams due to elastic (a) and plastic (b) deformation (Roes, 2001)

To determine the plastic section modulus, first the plastic neutral axis must be located. This is accomplished by assuming that the area in tension is equal to the area in compression. However, using this method for an I-profile results in locating the neutral axis again at $1/2h$.

$$W_{y,pl} = \sum A_i z_{i,pl} \qquad (5.4)$$

Where:

$z_{i,pl}$ = vertical distance from the centroid of an individual rectangle to plastic neutral axis [mm]

The I-profile is now divided into 4 rectangular sections. This gives:

$$\begin{aligned}
 W_{y,pl} &= 300 \times 30 \times \left(\frac{550}{2} - \frac{30}{2} \right) \\
 &+ 16 \times \left(\frac{550}{2} - 30 \right) \times \left(\frac{\frac{550}{2} - 30}{2} \right) \\
 &+ 300 \times 30 \times \left(\frac{550}{2} - \frac{30}{2} \right) \\
 &+ 16 \times \left(\frac{550}{2} - 30 \right) \times \left(\frac{\frac{550}{2} - 30}{2} \right) = 5.64 \times 10^6 \text{ mm}^3
 \end{aligned}$$

5.1.3. Calculation of critical bending moment

The critical bending moment of the horizontal girder is initially determined assuming pure bending. For this calculation a simple beam model is considered with two hinged supports, as explained earlier in this chapter, with a point load at the center of the girder. In reality, the gate is positioned at an angle of 1:3, but for validation purposes a model with a single lock gate without an angle is used. When the gate is placed under an angle, there will be a normal force in the horizontal girder that is not considered significant because the angle at which the gate is positioned is relatively gentle.

Because analytical calculations involving the plastic behaviour of steel are highly complex, the stress-strain relation explained in Section 4.1.2 is used. In this approach, it is assumed that stress increases linearly with strain for both the elastic and plastic zones. The critical elastic and plastic bending moments are calculated using Equation 5.5. Here, stress diagrams for the cross-section in Figure 5.3 are used. The elastic section capacity is reached when this stress equals the yield strength f_y maximally, and the plastic section capacity when this stress equals the ultimate stress that can be sustained $f_{y,pl}$. Since the cross-section of the girder is classified as Class 1, the following formula may be used for the calculation of the design resistance for bending about the y-axis:

$$M_y = \frac{W_y f_y}{\gamma_{M0}} \qquad M_{y,pl} = \frac{W_{y,pl} f_{y,pl}}{\gamma_{M0}} \qquad (5.5)$$

Where:

$$\begin{aligned}
 f_y &= \text{elastic section capacity: } 235 \text{ [N/mm}^2\text{]} \\
 f_{y,pl} &= \text{plastic section capacity: } 338 \text{ [N/mm}^2\text{]} \\
 \gamma_{M0} &= 1.0 \text{ [-]}
 \end{aligned}$$

The force corresponding to this moment can easily be determined, as the maximum moment for this static system is equal to $1/4Fl$. After some rewriting, Equation 5.6 is obtained for the force corresponding to the critical elastic and plastic bending moment. In this equation, the angle α is equal to 0° .

$$F_y = \frac{4W_y f_y}{l \cos(\alpha)} \qquad F_{y,pl} = \frac{4W_{y,pl} f_{y,pl}}{l \cos(\alpha)} \qquad (5.6)$$

$$F_y = \frac{4 \times 5.00 \times 10^6 \times 235}{8,200 \times \cos(0)} = 5.73 \times 10^5 \text{ N} = 573 \text{ kN}$$

$$F_{y,pl} = \frac{4 \times 5.64 \times 10^6 \times 338}{8,200 \times \cos(0)} = 9.27 \times 10^5 \text{ N} = 927 \text{ kN}$$

5.1.4. Calculation of critical lateral torsional buckling moment

Because I-beams loaded in bending are susceptible to lateral torsional buckling, they must be checked for stability in addition to strength. This phenomenon is analytically determined in this section and later in the chapter it is compared with the results from the gate model in RFEM.

The analytical approach for determining lateral torsional buckling is based on formulas from the national annex of NEN-EN 1993-1-1 (Eurocode, 2016b). It states that the critical elastic lateral torsional buckling moment must be calculated as follows:

$$M_{cr} = k_{red} \frac{C}{L_g} \sqrt{EI_z G I_t} \quad (5.7)$$

Where:

- E = elastic modulus: 210,000 [N/mm²]
- G = shear modulus: 81,000 [N/mm²]
- I_z = moment of inertia about the z-axis: 1.35×10^8 [mm⁴]
- L_g = length of the beam: 8,200 [mm]
- I_t = torsional moment of inertia [mm⁴]
- k_{red} = reduction factor [-]
- C = coefficient [-]

Torsional moment of inertia I_t

The torsional moment of inertia depends on the chosen profile, DIN550 in this case, and is determined using Equation 5.8. In this equation, t_i represents the thickness of the flanges and the web, and b_i represents the width and height respectively.

$$I_t = \frac{1}{3} \sum b_i t_i^3 \quad (5.8)$$

$$I_t = \frac{1}{3} (2 \times 300 \times 30^3 + 490 \times 16^3) = 6.07 \times 10^6 \text{ mm}^4$$

Reduction factor k_{red}

The reduction factor k_{red} depends on the deformability of the web of the girder in relation to the girder length. If h/t_w is less than or equal to 75, this factor is equal to 1. For the DIN550 profile this ratio is 34, so $k_{red} = 1$ [-].

Coefficient C

Depending on the nature, the point of application of the load and the dimensions of the girder's cross-section, the coefficient C is determined using the following formula:

$$C = \frac{\pi C_1 L_g}{L_{kip}} \left(\sqrt{1 + \left(\frac{\pi^2 S^2}{L_{kip}^2} (C_2^2 + 1) \right)} + \frac{\pi C_2 S}{L_{kip}} \right) \quad (5.9)$$

The coefficients C_1 and C_2 are coefficients to take into account the loading & boundary conditions, and position of the load with respect to the shear centre respectively. In Eurocode (2016b), there are charts to determine the values of these coefficients, but for the defined static system these are fixed at 1.35 for C_1 and 0.55 for C_2 . C_2 is entered into Equation 5.9 with a negative sign because the load acts at the centroid of the upper flange.

There are still two unknown parameters remaining from the above equation and those are L_{kip} and S . L_{kip} is the length of the equivalent laterally unrestrained girder (= 8,200 mm). For I-profiles, an approximation can be used for S :

$$S = \frac{h}{2} \sqrt{\frac{EI_z}{GI_t}} \quad (5.10)$$

$$S = \frac{550}{2} \times \sqrt{\frac{210,000 \times 1.35 \times 10^8}{81,000 \times 6.07 \times 10^6}} = 2,090 \text{ mm}$$

Now that all parameters are known, the coefficient C can be determined by substituting into Equation 5.9.

$$C = \frac{\pi \times 1.35 \times 8,200}{8,200} \left(\sqrt{1 + \left(\frac{\pi^2 \times 2,090^2}{8,200^2} (-0.55^2 + 1) \right)} + \frac{\pi \times -0.55 \times 2,090}{8,200} \right) = 3.88$$

Critical force lateral torsional buckling

Equation 5.7 is now filled in with all the known parameters from which the critical elastic buckling moment is determined.

$$M_{cr} = 1.0 \times \frac{3.88}{8,200} \sqrt{210,000 \times 1.35 \times 10^8 \times 81,000 \times 6.07 \times 10^6} = 1.77 \times 10^9 \text{ Nmm} = 1,770 \text{ kNm}$$

The corresponding critical lateral torsional buckling force is:

$$F_{cr} = \frac{4 \times 1.77 \times 10^9}{8,200 \times \cos(0)} = 8.63 \times 10^5 \text{ N} = 863 \text{ kN}$$

5.2. Simplified gate model results

In this section, the results of the analytical model from Section 5.1 are compared with the results of the simplified lock gate model in RFEM. This comparison validates that the constructed gate model is a good representation of reality. A single lock gate is built in RFEM without skin plate, vertical girders, bulb stiffeners, and struts, as shown in Figure 5.4. Additionally, the model is not placed at an angle as explained earlier in Section 5.1.3.

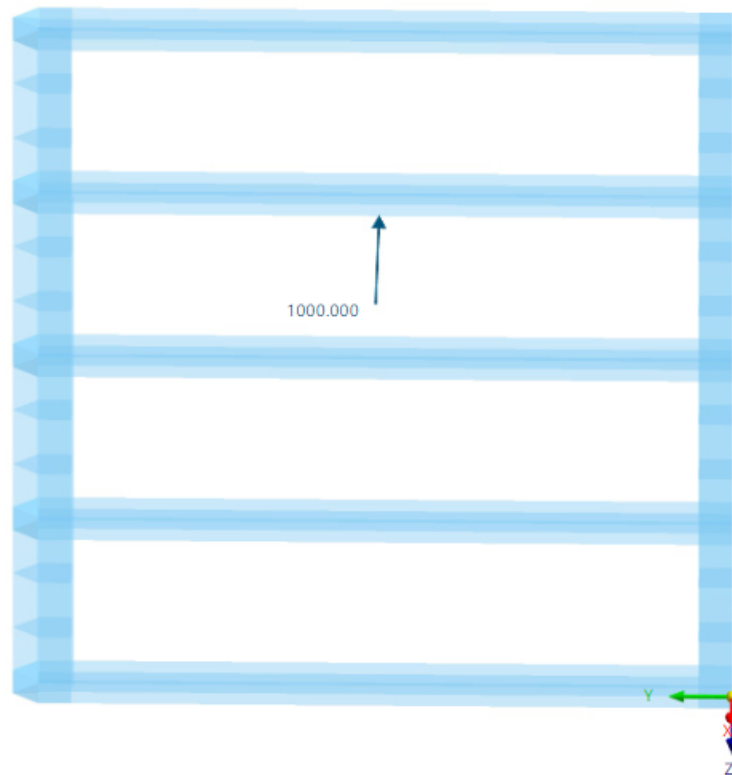


Figure 5.4: Simplified model lock gate RFEM

5.2.1. Geometrically linear analysis

During the geometrically linear analysis (first-order), equilibrium is examined based on an undeformed structural system. The analysis is linear, as it does not incorporate deformations of the components in the calculation. During this analysis, the girder is primarily calculated for strength. The results from this RFEM analysis are documented in Appendix E.

By means of load increments, a load of 1,000 kN is reached and the force at which the yield stress of 235 N/mm² occurs is determined. This is the stress at which the stress-strain diagram in the gate model transitions to plastic behaviour. The yield strength is first reached in the upper flange of the horizontal girder, at a force of 420 kN. A reasoning for the initial occurrence of yielding in the upper flange is that the model is constructed

from plate elements rather than beam elements. This can result in a less 'perfect' stress diagram, as shown in Figure 5.3a. At a force of 580 kN, the yield strength in the lower flange is reached as well. This force is approximately the same as the calculated F_y from Section 5.1.3, indicating minimal difference between the analytical model and the simplified gate model regarding the critical elastic bending moment.

As the load is further increased, the stresses begin to rise in the web of the profile. This continues until a force of 1,034 kN is reached, at which point the plastic section capacity appears to be reached. In Figure 5.5, the stress distribution corresponding to this force is shown. The compressive stress in the upper half of the cross-section (blue contour) has already exceeded the ultimate stress of 337 N/mm^2 . In reality, the stress cannot increase further after reaching this ultimate value. Just one load increment prior to this ($F = 1,012 \text{ kN}$), the stress was equal to 332.8 N/mm^2 , which is why the results of Figure 5.5 are chosen to show. Again, it can be concluded that the compressive stress in the upper half of the profile (blue contour) is higher than the tensile stress in the lower half of the profile (red contour). This is once again attributed to the fact that the model is constructed using plate elements.

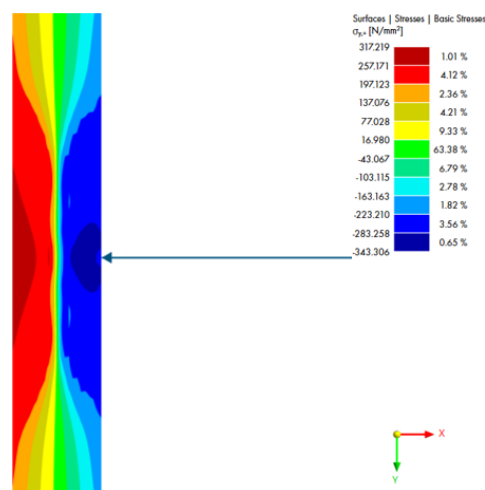


Figure 5.5: Top view of loaded girder; blue contours indicate the compressive region, while red contours indicate the tensile region. The load is applied to the top flange

The force of 1,034 kN is higher than the calculated value of 927 kN. An explanation for this could be that the modelling of the mitre- and heel post in RFEM generates a clamped effect on the girder, resulting in slightly higher stiffness compared to the analytical model. Increased stiffness in this case allows the girder to withstand more force.

5.2.2. Large deformations analysis

The large deformations analysis takes into account the rotation of the structure. It is a nonlinear calculation, which corresponds to a third-order analysis. Deformation of the structure is thus considered in the determination of force distribution. After each iteration step, the stiffness matrix of the deformed system is generated, and the calculation continues until equilibrium is reached. The results from this RFEM analysis are documented in Appendix E.

The incremental stability analysis gradually applies the load in steps of approximately 50 kN until the structure collapses. The final increase in force is divided into 10 smaller load increments to ensure a refined result. The results in RFEM show that the last load increment has a factor of 0.755, equivalent to 755 kN. From Figure 5.6 & 5.7, it is observed that for this force the top flange attempts to deform away from the original position of the girder due to a kink in z-direction. This is the direction corresponding to the weak axis of the profile. In both figures, the global deformations are shown. In Figure 5.6, the force acts perpendicular to the girder from the reader's perspective. The fracture strain is not reached yet, but a significant jump in deformation is observed in RFEM. This indicates that the structure has collapsed. To achieve exact values, a more refined load increment is required. However, this often comes at the expense of computational time.

The determined force is lower compared to the value calculated in Section 5.1.4. The reason the force from the gate model in RFEM is lower than the analytical model is likely due to the fact that the model is composed of plate elements in combination with a point load and therefore the upper flange experiences an higher stress earlier in the process.

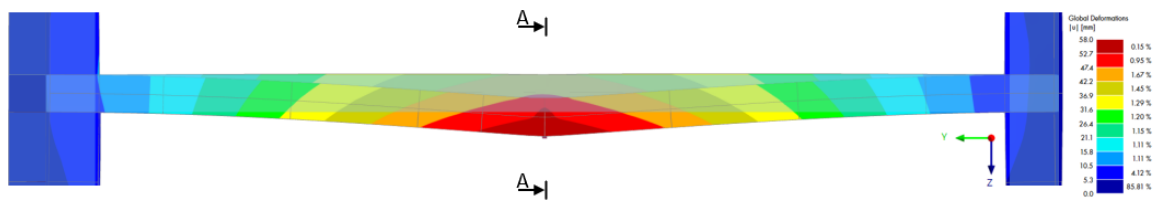


Figure 5.6: Front view of loaded girder; global deformations in z-direction. Load is applied to the top flange from reader's perspective

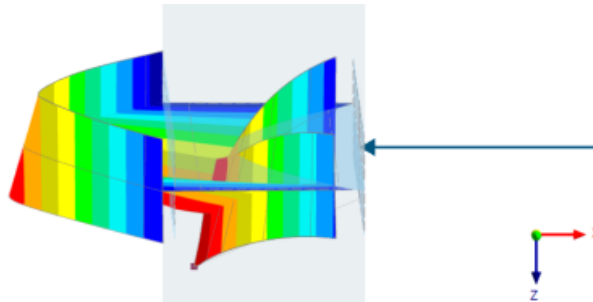


Figure 5.7: Side view A-A of loaded girder; global deformations in z-direction

5.3. Conclusion on validation gate model

Small differences were found in the results between the analytical and simplified gate (RFEM) model. For the geometric linear analysis, forces of 573 and 580 kN were respectively found corresponding to the critical elastic bending moment M_y . Forces of 927 and 1,034 kN were respectively found corresponding to the critical plastic bending moment $M_{y,pl}$. The reason why the RFEM model generates higher values here is most likely due to the slightly higher stiffness caused by the mitre- and heel post to the horizontal girder.

For the large deformations analysis, forces of 863 and 755 kN were found corresponding to the critical buckling moment M_{cr} for the analytical and simplified gate model respectively. This difference can be explained by the fact that the simplified gate model is composed of plate elements. The output from RFEM shows that the yield stress is locally reached faster in the top flange, resulting in earlier failure. In case of an analytical approach, a 'perfect' stress distribution is assumed throughout the entire cross-section, resulting in a slightly higher force being found. This outcome is favourable for the developed gate model and is considered conservative. With this, sufficient validation seems to be achieved and the gate model in RFEM appears to be suitable for further analyses.

6

Collision energy absorption capacity of the Macharen lock gate

In this chapter, the aim is to determine the capacity of the Macharen lock gate in terms of energy absorption using the validated gate model. This is done for the original design of the lock gate, constructed with S355 steel. A method for determining energy absorption is described in case of both a symmetrical and an unsymmetrical collision (Section 6.1). This method is applied to the current design of the Macharen lock gate, to determine the energy absorption capacity of the gate (Section 6.2). With this, by the end of this chapter an answer is provided to research question 4: "*Which method can accurately determine the energy absorption capacity of a lock gate?*" and 5: "*What is the capacity of a lock gate in terms of energy absorption?*".

6.1. Description of a method to calculate absorbable collision energy

In this section, a method is described to translate the results from RFEM into an absorbable collision energy. The method is applied in Section 6.2 to the Macharen lock gate model without a skin plate, stiffeners and struts.

6.1.1. Procedure of the method

The method for determining the energy absorption capacity of the Macharen lock gate consists of several steps, namely:

1. Loading the first impacted girder / part of mitre post;
2. Determining the maximum force F_{max} and maximum deformation u_{max} corresponding to the fracture strain ϵ_{max} (= 5%);
3. Exporting the results of the force and deformation per calculation step in tabular format (Excel) ;
4. Importing the results in Python and visualise the force-deformation diagram;
5. Constructing a force-energy diagram by integrating the force-deformation diagram;
6. Repeating all the above steps for each impacted girder / part of mitre post;
7. Determining the energy absorption capacity by summing up the calculated energies per girder / part of mitre post.

These steps are carried out per horizontal girder or mitre post at the level of a set of horizontal girders for an unsymmetrical collision and symmetrical collision, respectively. Figure 6.1 shows a schematic representation of the moment just before a collision of an inland vessel with the lock gate. Due to the characteristic sloping bow shape of an inland vessel, the first point of contact with the girder(s)¹ is at NAP +6.89 m. If not all the

¹In the case of an unsymmetrical collision one horizontal girder is impacted, while in the case of a symmetrical collision the mitre post is impacted at the level of two horizontal girders.

energy of the vessel can be absorbed by these girder(s), the vessel will penetrate further into the lock gate until the girder(s) at NAP +4.76 m are loaded. This process repeats until all the energy is absorbed or the entire lock gate has failed. A more detailed description of the different collision phases is provided in Section 6.1.2.

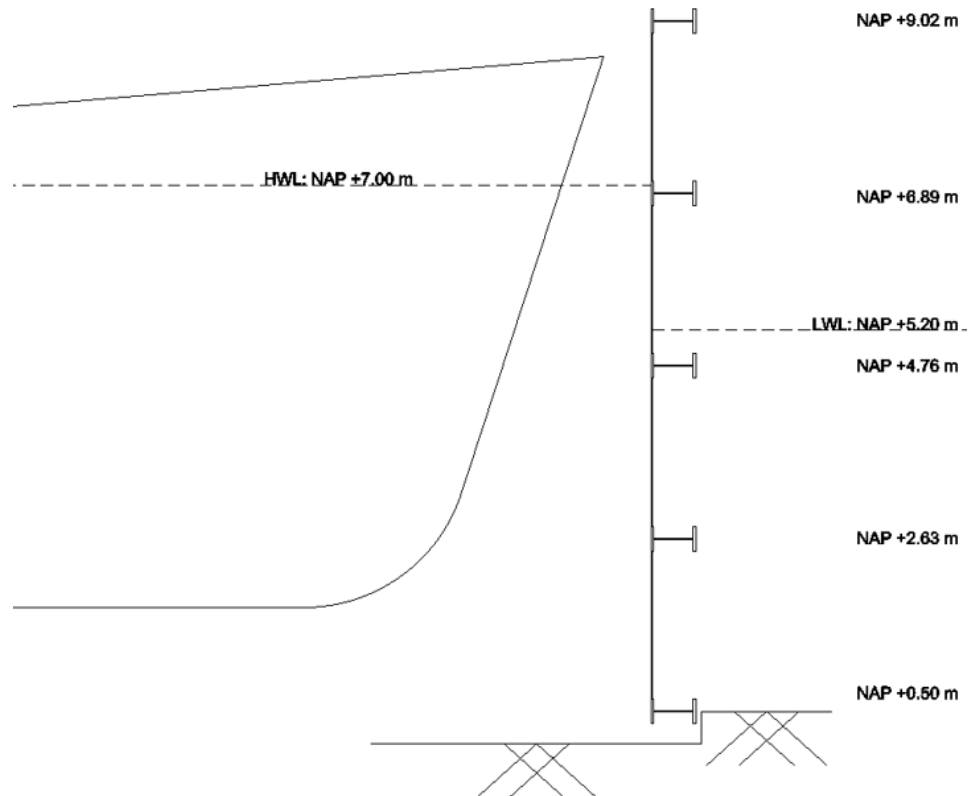


Figure 6.1: Side view schematic representation of the bow of a vessel just before collision with the Macharen lock gate

6.1.2. Description of the collision phases

An important step in the procedure just discussed is that the process is repeated for each impacted girder / part of mitre post. This step is related to the collision process, which consists of several collision phases. These phases are discussed in this section for both an unsymmetrical and a symmetrical collision. The flowchart, illustrated in Figure 6.2, is provided for clarification.

Phase 1

The first contact of both types of collision is defined as phase 1 of the method. Since the skin plate is excluded from the Macharen lock gate model, the first contact occurs with the girder at level NAP +6.89 m in case of an unsymmetrical collision. This girder is loaded with a line load of 300 mm in the center. Vessels belonging to CEMT class III can not reach the center of the girder because these vessels are generally wider. The vessels belonging to this class can impact the girder at a maximum of $0.35l$, where l is the length of the girder and the distance is measured from the centerline of the lock chamber (see Section 4.2.1). Nevertheless, the method for an unsymmetrical collision is applied using a force at the center of the girder.

In the case of a symmetrical collision, the first contact between the vessel and the lock gate is somewhere between the top and second set of girders (see Section 4.2.2). This part of the mitre post is able to absorb some of the energy, but relatively quickly fails because there are no stiff horizontal girders present here. After the failure of this part of the mitre post, the vessel moves further until it loads the first set of girders.

Reaching the fracture strain ϵ_{max} is set as the moment of failure. When this threshold is reached and not all energy has been absorbed, the vessel continues to move through the gate until the next girder or set of girders is loaded (phase 2). Because the bow of a typical inland vessel slopes, this phase can only occur if the first set of impacted girders has failed (see Figure 6.1).

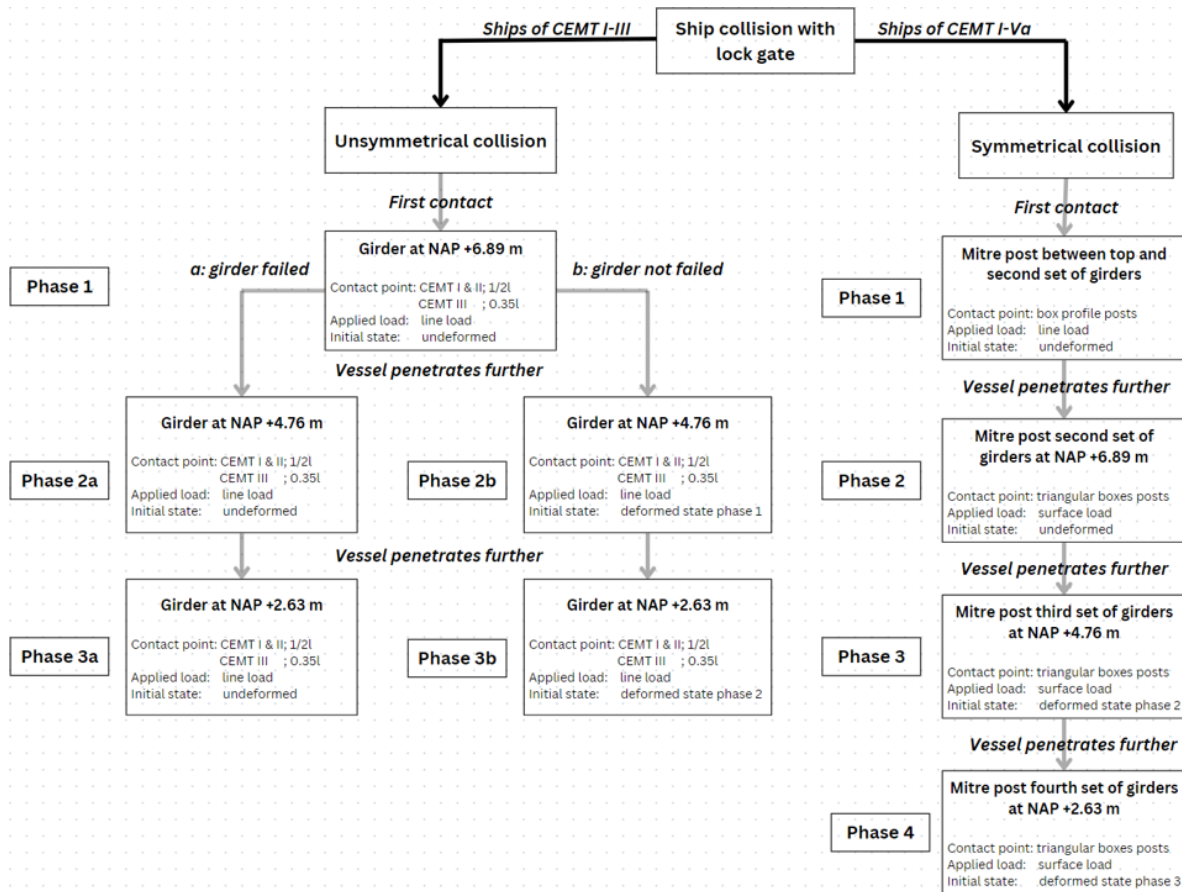


Figure 6.2: Flowchart for process symmetrical and unsymmetrical collision based on the design of Macharen lock. The 'l' in contact point stands for the length of the girder (=8.2 meters) and the given value is measured from the centerline of the lock chamber (refer to Section 4.2.1).

Phase 2

The first set of horizontal girders is subjected to loading during phase 2 in case of a symmetrical collision. The load is applied as a local surface load on the triangular boxes (300 x 407 mm each) at the level of the horizontal girders (NAP +6.89 m) and contact point of the gates. This way, the force transfer occurs directly to the girders, causing them to be subjected to compression. The aim is to determine the force at which the fracture strain is reached in the mitre post. Once this strain is reached, the vessel fully rests on the girders after which the resulting normal force in the girders is determined. This force must not exceed the buckling capacity.

There is a notable difference between the two types of collisions for this collision phase. Phase 2 for an unsymmetrical collision is subdivided into calculation methods *a* and *b*. The difference between these phases lies in the initial state from which further calculations are carried out. For phase 2a, it is assumed that the impacted girder from phase 1 has mathematically failed and can no longer absorb any loads. Therefore, this girder and its vertical connections (INP-profiles) to the other girders are excluded from the model. The girder from phase 2a is thus loaded from an undeformed state. For phase 2b, the deformed state from phase 1 is used as the initial state. This means that the loaded girder from phase 2b already experiences stresses and deformations due to the loading from phase 1. Both calculation methods are compared to determine which method provides more reliability. The calculation method *b* must be used for a symmetrical collision, as calculation method *a* is not applicable for this type of collision.

Phase 3 & 4

When not all energy is absorbed from the colliding vessel, it continues to seek further penetration through the lock gate after phase 2. This behaviour further develops in phases 3a & 3b and 3 & 4 for an unsymmetrical and a symmetrical collision respectively, until all energy is absorbed or no further energy can be absorbed. The load is applied in the same manner as described in phase 2. The girders at level NAP +2.63 m are the

lowest point where energy can be absorbed in the lock gate for vessels belonging to CEMT classes II-Va. Vessels belonging to CEMT class I have insufficient draft to reach these girders. If not all energy is absorbed after this point, the lock gate(s) have completely failed.

6.2. Application of the collision energy absorption method to Macharen lock

In this section, the method described in Section 6.1 is applied to the Macharen lock. The method is applied based on the defined collision phases.

6.2.1. Determination of the energy absorption in case of an unsymmetrical collision

Phase 1 - Collision with first girder at NAP +6.89 m

The first contact between the vessel and the lock gate for an unsymmetrical collision, occurs at the level of the girder at NAP +6.89 m. The vessel continues to move forward until all the energy is absorbed, i.e. until the vessel comes to a complete stop. The output of RFEM can be found in Appendix G.1, where the applied load and the maximum deformation corresponding to a strain of 5% are shown. The maximum load F_{max} at which this strain is reached, is determined by incrementally increasing it up to 2,250 kN (7,500 kN/m) in steps of 22.5 kN. At a force of 2,138 kN the strain limit is reached in the upper flange of the profile, resulting in a maximum deformation of 269.7 mm at the location of the load. Additionally, at a force of $F_{yield,flange} = 1,193$ kN, the top and bottom flanges begin to yield. From this moment on the deformation does not significantly increase, since the web of the horizontal girder has not yet reached the yield stress. At a force of $F_{yield,web} = 1,485$ kN, the web of the horizontal girder begins to yield as well and the deformation increases rapidly. This is illustrated in the F-u diagram obtained as output from Python, see Figure 6.3. In the diagram, the moment of reaching $F_{yield,web}$ is well represented by the 'kink' in the graph, followed by the plastic zone where the girder deforms rapidly. The area beneath the F-u diagram is equal to the energy absorption (refer to Section 2.1.4), which is obtained by integrating for each load increment (see Figure 6.4).

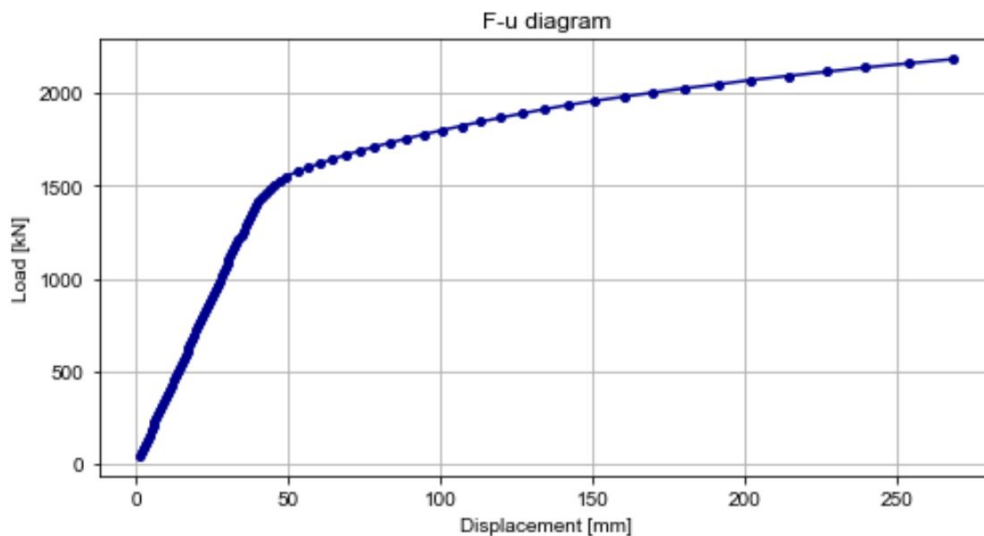


Figure 6.3: Load (F) - Displacement (u) diagram gate model without skin plate, stiffeners and struts step 1 unsymmetrical collision

The absorbed collision energy by the first girder amounts to 468 kNm. The load primarily causes deformation of the girder. The significant deformation results in the detachment of the mitre and heel posts. This is caused by the defined non-linear behaviour in the contact surface between both gates and line supports. In Figure 6.5 the detachment becomes evident from the deformation and the absence of a support reaction. In the mitre post between the two gates, a difference in deformation is observed of -14.0 mm with respect to the global y-axis (left is positive direction). In contrast, the deformation in the heel post is approximately the same with a value of 14.1 mm. As a consequence of this detachment, stresses exceeding the yield strength occur in the mitre- and heel post (refer to Appendix G.1).

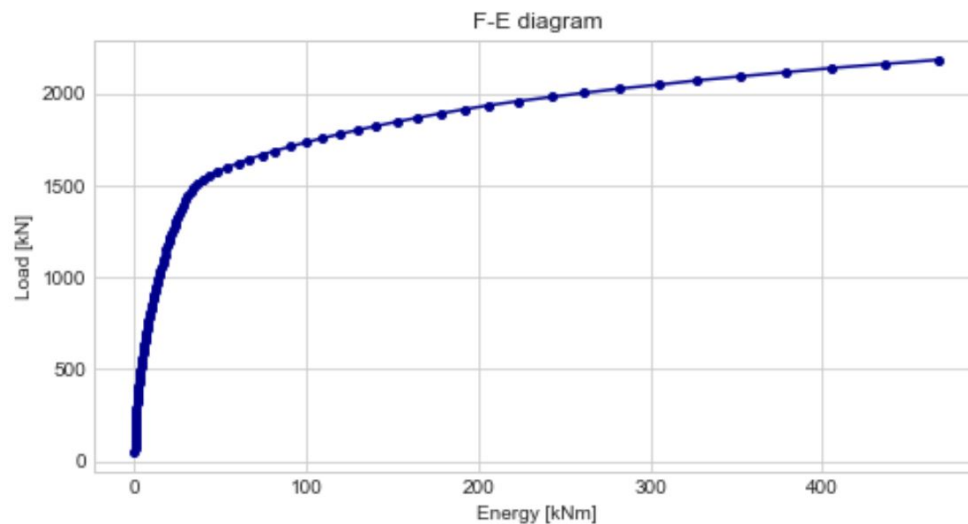


Figure 6.4: Load (F) - Energy (E) diagram gate model without skin plate, stiffeners and struts phase 1 unsymmetrical collision

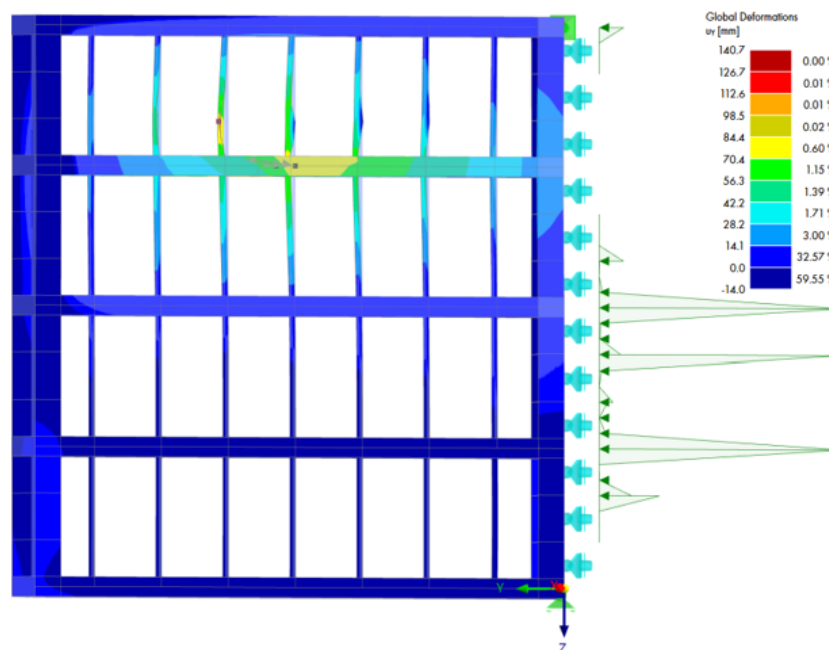


Figure 6.5: Deformations of the mitre- and heel post for an unsymmetrical collision

Phase 2a - Collision with second girder at NAP +4.76 m from undeformed state

If insufficient energy is absorbed, meaning the vessel has not come to a stop due to the first impacted girder, the vessel then loads the next girder at NAP +4.76 m. This girder is loaded in exactly the same manner. However, the first impacted girder and its connection to the second girder via the vertical INP profiles are left out. This is because it is assumed that these components mathematically failed and no longer affect the capacity of the lock gate (refer to Figure 6.6). The load is incremented to a force of 1,800 kN (6,000 kN/m) in steps of approximately 15 kN (48 kN/m), where the maximum strain and stress were reached at 1,757 kN accompanied by a deformation of 262 mm. This is approximately 500 kN less than the absorbed force from phase 1. With the absence of the already failed girder, the mitre- and heel post can more easily twist because the distance to the next girder has increased. Consequently, this girder fails at a lower force compared to the girder in phase 1. The output of RFEM can be found in Appendix G.2.

Reaching the fracture strain of the second impacted girder occurs at an almost equal deformation but at a lower force compared to the previous phase. The girder behaves the same way, but it can transfer less force to

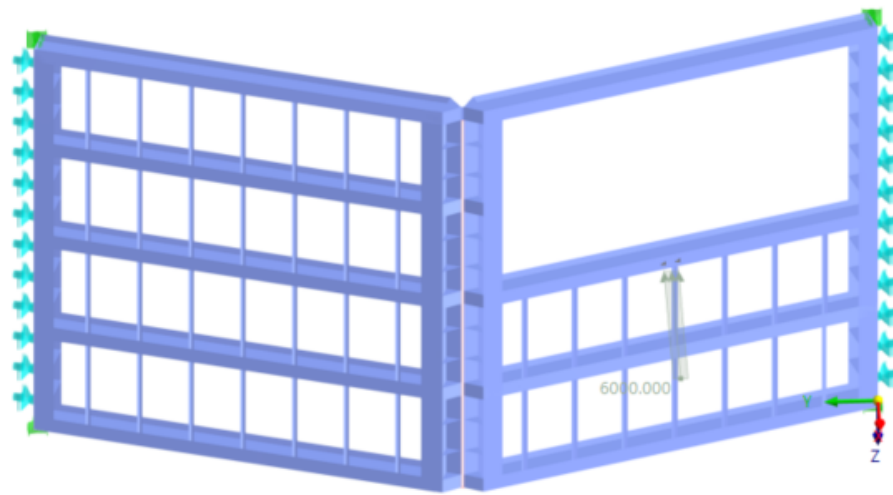


Figure 6.6: Load scheme phase 2 for an unsymmetrical collision using calculation method α ; excluding damaged girders and vertical connections

the connecting structure due to excluding the girder above it. Strain is a direct consequence of the girder itself, so this occurs with the same total displacement. Consequently, the energy absorption is lower with a value of 404 kNm. The force-energy diagram appears to have a similar shape to that from the previous phase (refer to 6.7). An important difference is observed in the lower force at which the yield strength is reached for phase 2a.

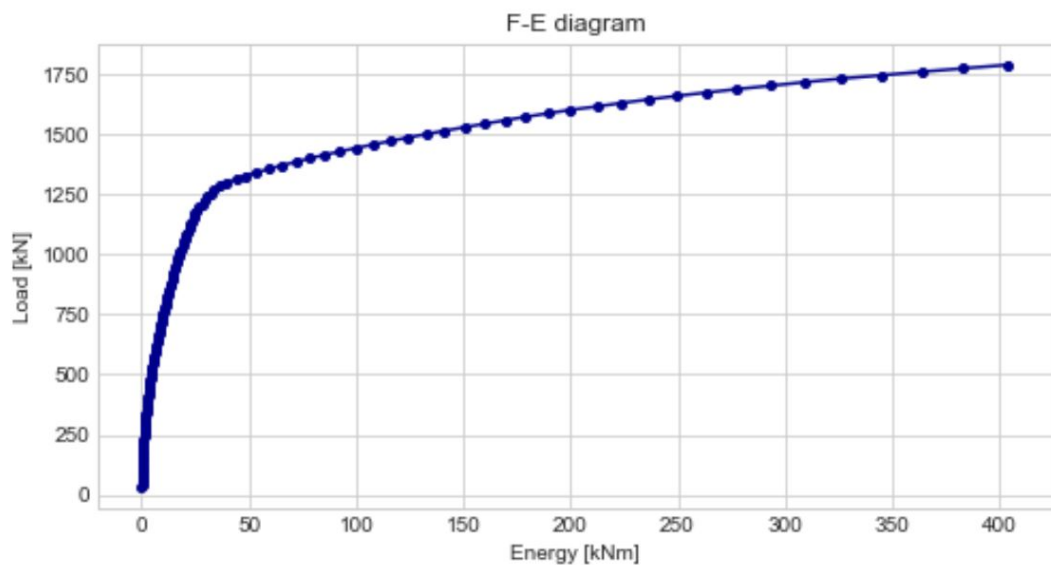


Figure 6.7: Load (F) - Energy (E) diagram gate model without skin plate, stiffeners and struts phase 2a unsymmetrical collision

In this phase, the deformations in the mitre and heel posts are higher compared to the first girder because they can twist more easily. When examining the displacements in the y-direction for the global coordinate system, displacements of -15.5 mm and 22.3 mm are found for the mitre and heel posts, respectively. These results look similar to what is shown in Figure 6.5.

Phase 2b - Collision with second girder at NAP +4.76 m from deformed state

In this phase, the girder at NAP +4.76m is once again impacted, but with a different computational method. It is now assumed that the girder from phase 1 has not completely failed and can still transfer some stiffness to the girder in this phase. For this calculation step, the initial state function in RFEM is used. With this function, the deformed structure of one load case (phase 1) is used as the starting point for another load case (phase 2b). However, a limitation of this calculation method is that the girder from phase 1 will no longer be loaded

during the calculation of the girder in this phase. As a result, the unloaded girder partially tends to elastically deform back. In reality, this can never happen because the vessel continues to penetrate through the gate. The plastic modulus for the impacted girder remains equal to $2,100 \text{ N/mm}^2$, so it is assumed that this limitation not contributes much additional stiffness.

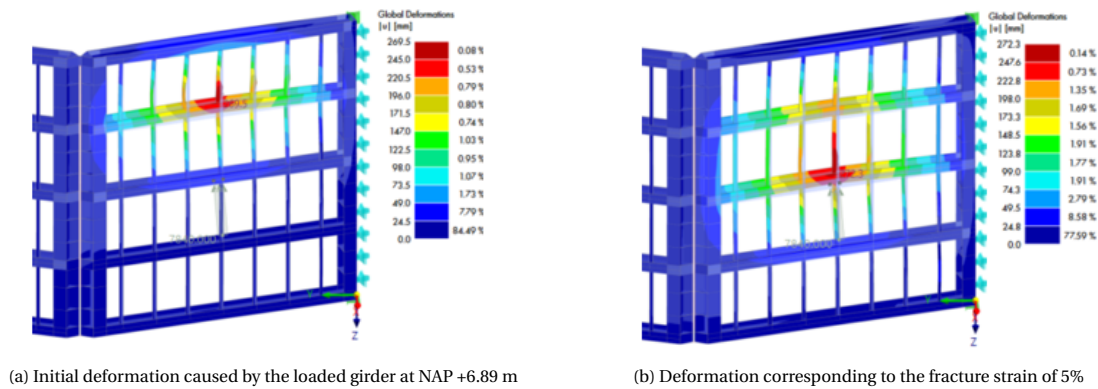


Figure 6.8: Deformation of the impacted girder at NAP +4.76 m for calculation method *b*; using the deformed state of phase 1 as initial state for phase 2

The load is incrementally increased as in any other phase, until the force at which the fracture strain occurs in the impacted girder is found. For this method, a force of 2,352 kN is determined. Remarkably, this force is not only higher than the force found in phase 2a but also higher than the force found in phase 1. This is explained by the fact that this phase involves the middle horizontal girder of the lock gate. The girder is expected to transfer more force to the girders above and below it. This behaviour is checked by individually loading all girders (including the two outer ones) without considering the deformed state of the other girders. As a result, it is found that the middle girder at NAP +4.76 m indeed generates the highest load capacity. The girders at NAP +2.63 m and NAP +6.89 m exhibited similar behaviour, with both girders having an equal capacity. The capacity of the two outer girders is the lowest and also identical to each other. The reason these girders have the lowest capacity is because they are not enclosed by the structure.

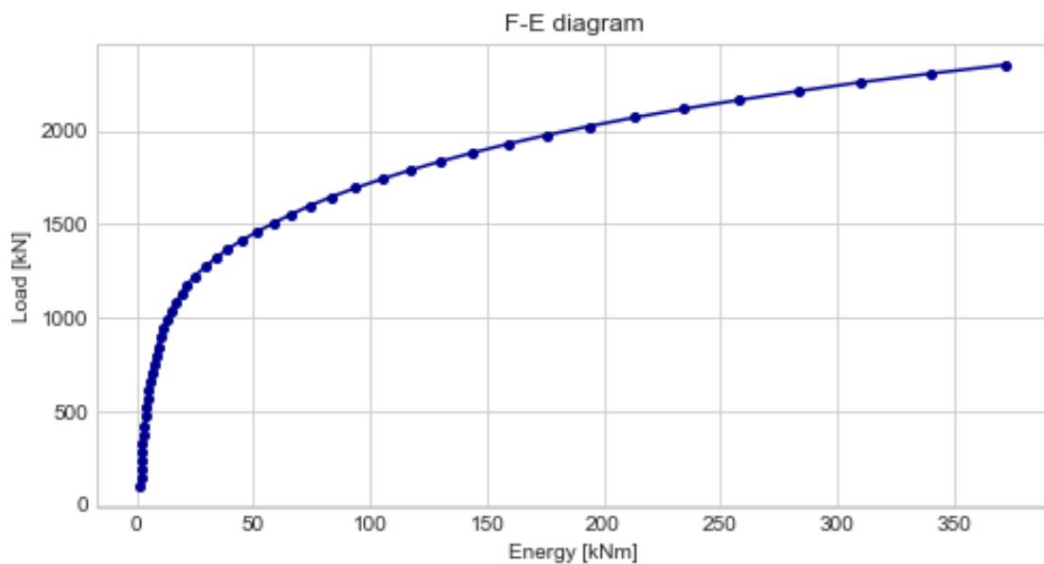


Figure 6.9: Load (F) - Energy (E) diagram gate model without skin plate, stiffeners and struts phase 2b unsymmetrical collision

Although the horizontal girder at NAP +4.76 m may have an higher load capacity, it does not necessarily imply an higher energy absorption capacity. Another notable finding namely lies in the deformation of the impacted girder. Due to the loading from phase 1, the girder experiences a slight deformation of approximately 33 mm (refer to Figure 6.8a). Thus, when the respective girder is first loaded it already experiences

an initial deformation of 33 mm. This effect influences the energy absorption of the impacted girder. The total deformation of this girder is approximately 242 mm (see Figure 6.8b), so the relative deformation is $242 - 33 = 209$ mm. The results from Figure 6.9 show that the energy absorption is 373 kNm. The transition in the force-energy diagram from elastic to plastic behaviour of the girder is slightly more gradually for this method. This is because there is already some stress in the girder due to the loaded girder above it. The fact that the calculated energy absorption of this phase is lower than from phase 2a does not necessarily mean that the calculation method from phase 2a is not conservative, as the difference lies between 5 - 10%. The load scheme and the deformations of the lock gate are documented in Appendix G.4.

Phase 3a - Collision with third girder at NAP +2.63 m from undeformed state

Once the second girder at NAP +4.76 m has failed and not all energy is absorbed, the vessel continues to move further through the gate until it reaches the last girder at NAP +2.76 m. As previously explained, only vessels belonging to CEMT class II and III can collide with this girder. Assuming a water level of NAP +5.2 m, vessels require a minimum draught of 2.57 m to reach the respective girder. The collision of the this girder is conducted exactly following the same method as in phase 2a. The second impacted girder failed, so it is excluded from the model. The load is increased to 1,650 kN (5,500 kN/m) in increments of 15 kN and the fracture strain is reached at a force of 1,624 kN. The results from Appendix G.3 show that the deformation remains the same but occurs at a slightly lower force. Additionally, the force-energy diagram corresponds to that from phase 2a. This results in a slightly smaller absorbed energy of 389 kNm. The differences in displacement for the mitre and heel posts are negligible as well, with values of -17.7 mm and 19.9 mm respectively.

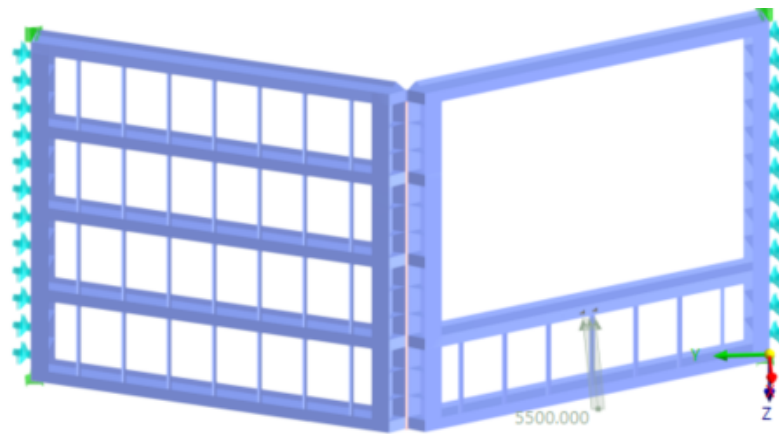


Figure 6.10: Load scheme phase 3 for an unsymmetrical collision using calculation method α ; excluding damaged girders and vertical connections

Phase 3b - Collision with third girder at +2.63 m NAP from deformed state

Again, it is assumed that the girder from phase 2b has not completely failed and can still transfer some stiffness to the girder in this phase. The method explained in phase 2b is applied in the same manner here, see Appendix G.4 for results in RFEM. At a force of 2,280 kN, the fracture strain is reached and the deformation corresponding to this force is equal to 278 mm. The initial deformation that the respective girder has due to the load from the girder above is 37 mm. The force-energy diagram follows a similar pattern to that of phase 2b, but it is noteworthy that a higher energy of approximately 406 kNm is now measured. This is because the relative deformation is higher for this phase, while the force remains approximately the same.

In Section 4.3.3, the influence of hydrostatic water pressure on the capacity of the lock gate was discussed, with the conclusion that this influence may be significant. Additionally, it was concluded that the girder at NAP +2.63 m NAP is most heavily loaded by the water pressure. Therefore, the theory from Section 4.3.3 is now applied to the force-deformation diagram of this girder. Figure 6.11 indicates which part of the force-deformation diagram is affected by the water pressure. The energy resulting from this is equal to the area of this part, with x-values ranging from 0 to u_{max} and y-values from 0 to 314 kN. This force is equal to the force caused by the hydrostatic water pressure.

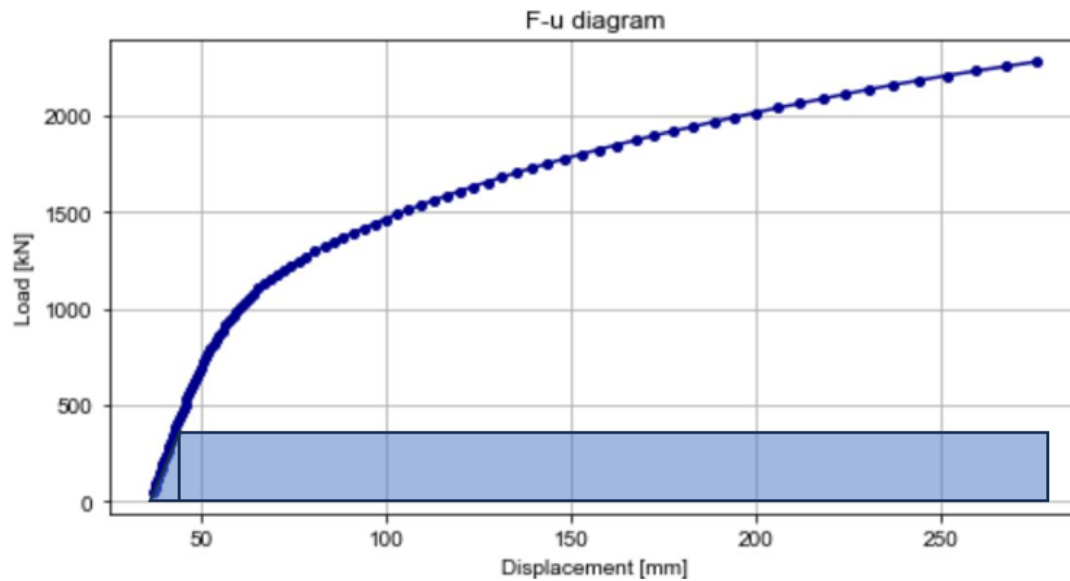


Figure 6.11: Load (F) - Deformation (u) diagram gate model without skin plate, stiffeners and struts phase 3b unsymmetrical collision including the influence of hydrostatic water pressure

Thus, the energy capacity addressed by the hydrostatic water pressure is equal to:

$$\begin{aligned}
 E &= \frac{1}{2} \times F_w \times u_w + F_w \times (u_{max} - u_w) \\
 &= \frac{1}{2} \times 314 \times \frac{7.4}{1000} + 314 \times \frac{278 - 37 - 7.4}{1000} = 75 \text{ kNm}
 \end{aligned}$$

This is approximately 18% of the total energy absorption capacity of the respective girder. This percentage indicates that it is relevant to consider the influence of water pressure when determining the energy absorption capacity. A water level of NAP +7.0 m is taken into account for this analysis, which is an extreme water level for the Macharen lock. In reality, a more accurate assessment of the critical water level and the corresponding head difference needs to be considered. For further analyses in this thesis, the influence of water pressure is considered irrelevant and will not be further addressed.

Conclusion unsymmetrical collision

When comparing both calculation methods of in Table 6.1, several observations are made. Method *a* yields lower forces at which the fracture strain is reached, due to the fact that the respective girder experiences less stiffness from the already removed girder above. However, this results in a higher deformation. The deformation is an important factor for determining energy absorption capacity and higher values for this generally result in a high capacity in terms of energy absorption. For phase 2, this method yields a slightly higher energy absorption capacity of approximately 8% compared to calculation method *b*.

Unsymmetrical	$F_{yield,web}$ [kN]	F_{max} [kN]	u_i [mm]	u_{max} [mm]	$E_{absorbable}$ [kNm]
Phase 1	1,485	2,138	-	273	468
Phase 2a	1,325	1,757	-	262	404
Phase 2b	1,176	2,352	33	242	373
Phase 3a	1,214	1,624	-	263	389
Phase 3b	1,176	2,280	37	278	406
Total calculation method <i>a</i>					1,261
Total calculation method <i>b</i>					1,247

Table 6.1: Results of all collision phases for an unsymmetrical collision

Method *b* yields higher forces at which the fracture strain is reached because the respective girder experiences more stiffness from the girder above, which is not excluded for this method. However, by using the

deformed state of the girder above as the initial state, the respective girder experiences an initial deformation u_j . The relative deformation ($u_{max} - u_j$) is therefore lower, which impacts the energy absorption capacity negatively.

Method *a* generates slightly more capacity for the second phase, but it scores lower in the third phase. The difference in energy absorption capacity between both calculation methods is considered negligible for this gate design. Whereas method *a* performs better in terms of local deformations, method *b* excels in higher load capacity. The results underscore the differences between them. Given that method *b* better aligns with real-world scenarios, it is advisable to use this computational approach in future calculations. While method *a* may suffice for the current lock gate design, its suitability for other designs is not guaranteed. For instance, in Chapter 7, adjustments are made to the center-to-center distance between the horizontal girders, adjusting their influence on each other. The improved gate layouts are analysed using both methods, and the most suitable one is subsequently documented.

6.2.2. Determination of the energy absorption in case of a symmetrical collision

In contrast to an unsymmetrical collision, a symmetrical collision can happen with any vessel type. However, there is a theoretical likelihood that a vessel belonging to CEMT class IV or Va will hit the mitre post of the lock gate, given the large width of these vessels. These are the vessels expected to generate the most energy. It is advantageous that these vessels can only collide symmetrically with the gate, because it is expected that the gate can absorb more energy in the event of this type of collision.

Phase 1 - Collision mitre post in between top and second set of girders

The initial contact point for a symmetrical collision between the vessel and the lock gate occurs somewhere between the top girders and the girders below it. The bow of the vessel first impacts both mitre posts. The load is placed on the edges of the open box profile in the mitre posts to prevent local peak deformations in unsupported areas. This load is applied as a line load between the top and second set of girders over an height of 500 mm, a value recommended in Eurocode (2015). The yield strength of 355 N/mm^2 is reached at a force of 900 kN. Initially, this is a local effect around the point of application of the load. However, with increasing load this area rapidly increases in size as is illustrated in Figure 6.12.

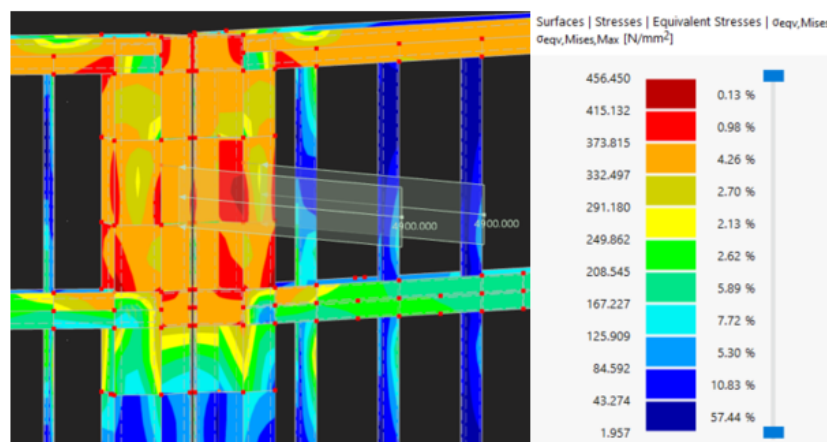


Figure 6.12: Stresses in the structure due to the line load applied on the mitre posts between the top and second from the top girders

At a force of 2,450 kN, the fracture strain is reached at the location of the applied load. Figure 6.12 clearly shows that for this force, the stresses around the first set of girders increase. Due to the relatively rapid deformation of the flexible posts between the top and second set of girders, it is assumed that these components do not absorb any energy. Consequently, the vessel immediately transfers its force to the mitre posts at the location of the girders. On one hand, this is a conservative assumption as less energy is absorbed, but on the other hand the first set of girders retain their full capacity. This capacity is determined in phase 2 of this method.

Phase 2 - Collision mitre post first girders at NAP +6.89 m

In the previous phase, it is assumed that the mitre posts between the top and second set of girders cannot absorb energy. Therefore, the set of girders at NAP +6.89 m are loaded from an undeformed state. The approaching vessel exerts all its force on the two triangular box profiles of the mitre post. A load of 2,500

kN/m² is applied initially and it is increased in increments of 250 kN/m². Using the incremental method in RFEM, the results are obtained corresponding to the fracture strain in the mitre post and it is reached at a force of 8,974 kN. Fracture strain only occurs in the mitre posts due to the bending of the triangular plates on which the load is placed. For RFEM output, refer to Appendix G.5. These plates serve as the only contact points in the posts, thus bearing all forces. This force generates a compressive force in the profile of the horizontal girder, which is transmitted from the mitre post to the heel post. As a result, an high strain occurs at the heel post with the connection to the line support (see Figure 6.13a). However, this strain is lower than the strain in the mitre post and does not reach the fracture strain.

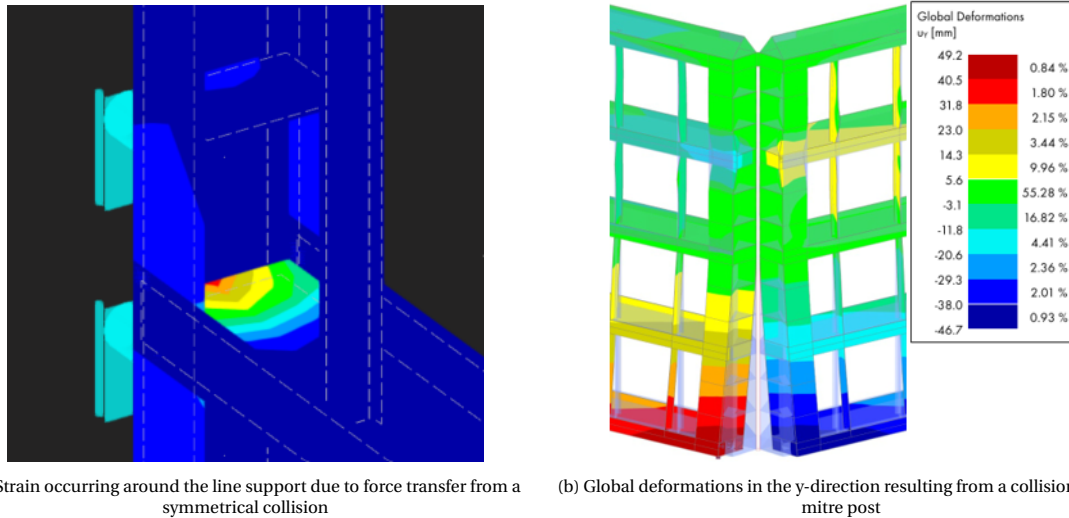


Figure 6.13: Strain and deformation resulting from a collision at the mitre post at NAP +6.89 m

The deformation corresponding to the force of 8,974 kN is approximately 115 mm at the location of the applied load. Consequently, the absorbed energy by the first girders at NAP +6.89 m is 747 kNm, as illustrated in Figure 6.14.

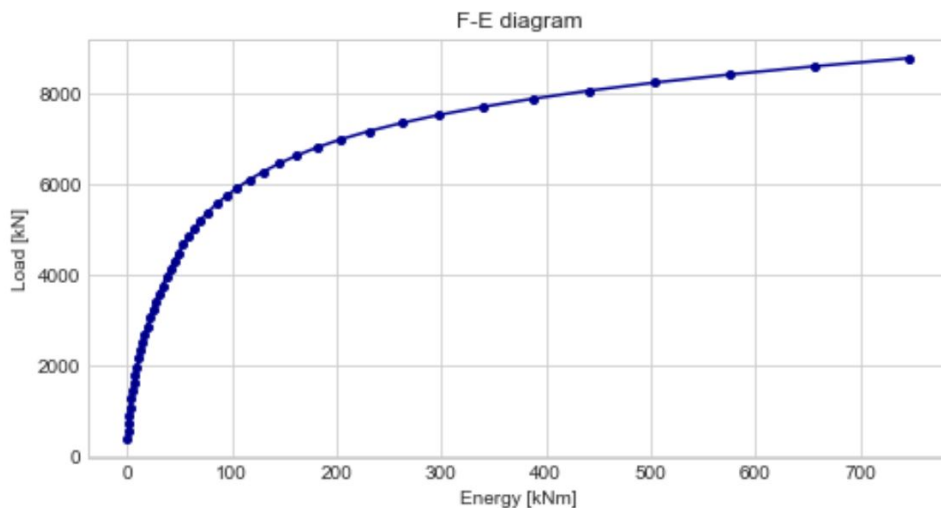


Figure 6.14: Load (F) - Energy (E) diagram gate model without skin plate, stiffeners and struts phase 2 symmetrical collision

When observing the global displacements in RFEM, a displacement is noticeable at the bottom of the mitre posts. It is evident that a rocking effect occurs, with the bottom two girders bending in the opposite direction from the bottom post. This is documented in Appendix G.5 by the positive values of displacement in the x-direction, with a maximum value of 154.7 mm. Due to this rocking effect, a tensile force wants to develop in the girders. However, the defined contact surface 'failure under tension' (see Section 4.1.4) prevents this. Consequently, the gates spread apart, as indicated by the displacement results in the y-direction in Appendix

G.5 and Figure 6.13b. The impacted girders move towards each other while the bottom two girders diverge, creating a gap. The gap between the bottom girders has a maximum opening of approximately $49.2 + 46.7 = 95.9$ mm. The occurrence of such global deformations in reality is debatable, as it is countered by the water pressure. The water pressure tends to keep the gates in their original position by providing counterpressure.

Phase 3 - Normal force in the impacted girder

Because both girders are subjected to compression, they are checked for buckling. The resulting normal force in the girder is determined using RFEM and amounts to 4,492 kN, as shown in Appendix G.5. Along the strong z-axis, the buckling length is equal to the girder length. Along the weak y-axis the girder is supported by the vertical INP profiles, which means buckling is not expected to be critical for this direction. From the calculations performed in a spreadsheet and included in Appendix F, buckling unity checks of 0.54 and 0.49 about the z- and y-axis respectively are obtained. This indicates that buckling indeed not occurs for the loaded horizontal girders.

Phase 4 - Collision mitre post second and third set girders

After the set of girders at NAP +6.89 m has mathematically failed and not all energy is absorbed, the vessel continues to move forward, thereby loading the set of girders at NAP +4.76 m. The influence of the first set of girders on the second set of girders for a symmetrical collision is difficult to assess. Again, the initial state function of RFEM is used to consider an initial state from a certain load case. This is done for the collision on the mitre posts at the level of the second set of girders at NAP +4.76 m, where the collision at the first girders is considered as initial state. In this way, it is determined whether the capacity of the second set of girders is the same as the first set, and how the lock gates behave relative to each other.

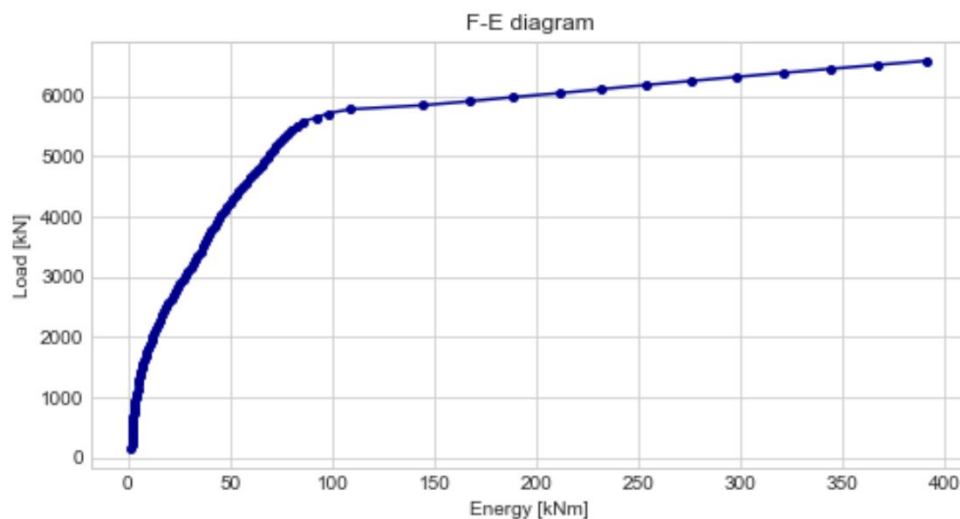


Figure 6.15: Load (F) - Energy (E) diagram gate model without skin plate, stiffeners and struts phase 4 symmetrical collision

When the load is increased in increments of 65 kN (275 kN/m^2), it is concluded that the fracture strain in the mitre posts at the level of the second set of girders is reached at a lower force, namely 6,245 kN. This demonstrates that the collision of the first girders does influence the capacity of the second set of girders. The absorbed energy by the second set of girders is determined from the F-E diagram in Figure 6.15 and amounts to 392 kNm. This is considerably less than the absorbed energy from phase 2 (747 kNm) for this type of collision. The energy translates into a local displacement where the load is applied of approximately 91.8 mm, as seen in Appendix G.5. In this appendix, it is also evident that the global displacement of the load case of this phase (LC9) differs compared to that of the other phase (LC6). The rocking effect is now less pronounced and the effect of spreading out at the bottom of the posts seems to have disappeared. This behaviour can be explained by the fact that the contact between the posts in the first load case failed in tension, resulting in the posts coming loose. Subsequently, a second load at the level of the second set of girders pushes these posts back. Because the posts failed in tension during the first load case, they can move freely during the second load case. In Figure 6.16, it is clear to see that the posts have shifted above and below each other. Whether this actually occurs in reality is debatable, as in reality the gates will come back together. Additionally, there will likely be

a sill where the gates make contact when globally deforming towards it. Due to the fact that the gates can move freely from each other in RFEM, it results in the unrealistic behaviour that they move through each other. Failing on buckling is not considered significant because the normal force in the loaded horizontal girders is lower than the impacted girders from phase 2.

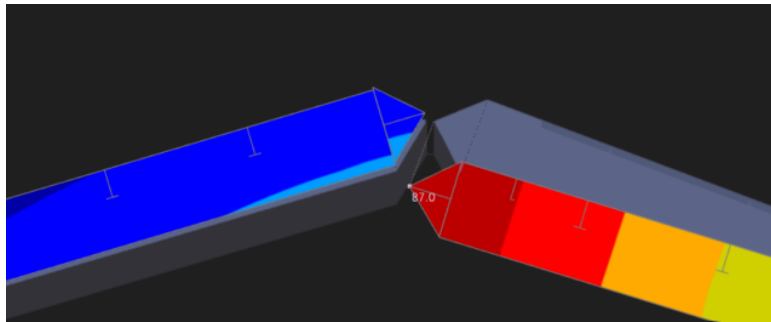


Figure 6.16: Displacement of the lower mitre posts due to surface loading on the set girders at NAP +4.76 m

The capacity is assumed to be the same for the third set of girders at NAP +2.63 m, as these are loaded in a similar manner with a comparable situation. With this assumption, the absorbed energy of the third set of girders is equal to 392 kNm as well. Consequently, the total energy absorption capacity of the lock gate is equal to 1,531 kNm for a symmetrical collision. This is nearly 300 kNm more than in case of an unsymmetrical collision.

Conclusion symmetrical collision

A symmetrical collision results in a much stiffer response of the lock gate compared to an unsymmetrical collision. This leads to forces up to 4 times higher, as seen in Table 6.2. Initially, the mitre posts are loaded, after which the force is transferred through the horizontal girders via the heel posts to the lock heads. The horizontal girders are thus subjected to compression and must have sufficient buckling capacity. For the current design of the lock gate, this is not a problem since the capacity is not reached.

Symmetrical	$F_{yield,post}$ [kN]	F_{max} [kN]	u_i [mm]	u_{max} [mm]	$E_{absorbable}$ [kNm]
Phase 2	3,114	8,974	-	115	747
Phase 3	-	6,245	32.0	91.8	392
Phase 4	-	6,245	32.0	91.9	392
Total					1,531

Table 6.2: Results of all collision phases for a symmetrical collision

Despite the higher load capacity, the stiffer response of the lock gate results in a reduction in deformation. This is significantly lower than in case of an unsymmetrical collision. The set of girders at NAP +2.63 m and NAP +4.76 m already experience an initial deformation u_i of approximately 32 mm due to the first loaded set of girders at NAP +6.89 m. This results in a reduced relative deformation ($u_{max} - u_i$), adversely affecting the energy absorption capacity. However, the reduction in deformation is compensated for by a higher load capacity. The energy absorption capacity in the case of a symmetrical collision is higher compared to the capacity in the case of an unsymmetrical collision for the analysed design of the Macharen lock gate. However, this does not necessarily apply to other lock gate designs.

6.3. Conclusion on energy absorption capacity Macharen lock gate

At the beginning of this chapter, two research questions are formulated which can be answered through this chapter, namely: "Which method can accurately determine the energy absorption capacity of a lock gate?" and "What is the capacity of a lock gate in terms of energy absorption?". By using basic mechanics, a method is described for determining the energy absorption capacity in case of an unsymmetrical and a symmetrical collision. For both types of collisions, the force in RFEM is increased until the fracture strain is reached in the respective impacted component. Important results include the load and deformation at which this strain is reached. These results are exported for each collision phase, allowing the determination of the capacity of the

lock gate in terms of energy absorption. In the case of an unsymmetrical collision, a distinction has been made in calculation methodology, namely methods *a* & *b*. An important conclusion drawn from this is that method *b* comes closer to reality, and it is therefore recommended to further use this method in subsequent analyses.

The original design of the Macharen lock gate, constructed in S355 steel, exhibits an higher energy absorption capacity in case of a symmetrical collision. This is caused by its higher load capacity, resulting from a rigid reaction of the gate when impacted at the mitre posts. Conversely, an unsymmetrical collision leads to higher deformations in the lock gate, which is beneficial for its energy absorption capacity. However, the load capacity for this type of collision is lower, resulting in a lower overall capacity compared to a symmetrical collision. Since both the load capacity and the total local deformation play crucial roles in determining this energy absorption capacity, it does not necessarily mean that more capacity is generated in the case of a symmetrical collision for all lock gates.

The calculated values for the energy absorption capacity are approximately 1,247 & 1,531 kNm in case of an unsymmetrical and symmetrical collision, respectively. When comparing these values with Table 3.6 from Chapter 3 (added below for better readability), it is observed that the energy absorption capacity is not out of proportion with the calculated average values for collision energy based on the AIS data (Data mean). This indicates that a significant percentage of the potential collision energy generated by vessels can be absorbed. In addition, this means that the described method for determining the energy absorption capacity can be validated in this manner. The order of magnitude in energy for both the calculated energy absorption capacity in this chapter and the calculated collision energy from Chapter 3 is similar.

	Collision energy [kNm]					
	Eurocode			PIANC		
	Norm	Data mean	Data max.	Norm	Data mean	Data max.
CEMT I	990 - 1,980	344	692	0 - 384	301	604
CEMT II	1,980 - 3,218	743	3,525	24 - 960	648	3,077
CEMT III	3,218 - 4,950	908	3,122	60 - 2,880	793	2,724
CEMT IVa	4,950 - 7,425	1,434	5,023	180 - 5,760	1,252	4,384
CEMT Va	7,425 - 14,850	1,792	4,323	360 - 10,944	1,564	3,773

However, the calculated maximum values (Data max.) far exceed the calculated capacities. Vessels with such high energy levels would cause the lock gate to completely fail. As mentioned in Section 3.5, it is debatable whether these values are representative, given that the data is obtained from a non-operational lock. Regardless of whether these values are representative or not, in the event of insufficient capacity of the lock gate, concessions need to be made to improve the energy absorption capacity. Applying the method for determining the energy absorption capacity in this chapter has shown that the lock gate attributed most of its capacity to the horizontal girders and mitre- and heel posts. In the next chapter, improvements to the gate layout are made which increases the energy absorption capacity.

7

Macharen lock gate improvements for better energy absorption capacity

In this chapter, the aim is to estimate the portion of measured vessels for which the potential collision energy can be absorbed based on the capacity of the various designs of lock gates. After applying the described method to the current design of the lock gate in Chapter 6, adjustments are made to the gate layout to enhance its energy absorption capacity (Section 7.1). The improvements are combined into one lock gate design and compared with the analysed (AIS) data from Chapter 3, as well as the design of the original lock gate. In this way, insight is gained into what percentage of the vessels from the dataset can be absorbed by the respective lock gate (Section 7.2). This analysis allows to answer research question 6: *"How can the design of the lock gate be improved to enhance its energy absorption capacity?"*.

7.1. Improvements of the gate layout

In addition to the adjustment in steel quality from S235 to S355, the original design of the Macharen lock gate is modified to improve energy absorption. These modifications to the lock gate are discussed and analysed in this section. Two of these modifications involve a change of the horizontal girders. It is expected that increasing the quantity and the dimensions of the steel profile have a favourable impact on the force capacity and thus the energy absorption capacity. At the end of Section 7.1.1, it is clear how the cross-section of the horizontal girders is improved in terms of energy absorption. Section 7.1.2 demonstrates whether a shorter center-to-center distance makes a significant difference in terms of energy absorption.

Finally, an investigation is conducted to determine whether a modification to the posts of the lock gate affects energy absorption. In the original design, the posts have an open box profile, whereas in the modified design they are closed with an additional plate. It is expected that this modification provides more stiffness to the horizontal girders and improve force distribution. The findings of this investigation are discussed in Section 7.1.3.

7.1.1. Change in geometry cross-section horizontal girders

In this section, the analysis focuses on the influence of a different cross-sectional profile for the horizontal girders on the energy absorption capacity. This examination is limited to an unsymmetrical collision since the improvement has an insignificant impact on energy absorption during a symmetrical collision. This is because the fracture strain predominantly occurs in the mitre posts, where the cross-section of the horizontal girders exerts minimal influence. However, a profile with larger dimensions proves advantageous for buckling capacity, as it resists buckling with greater ease. As demonstrated in Section 6.2.2, fracture occurs in the mitre posts long before reaching the buckling capacity, making it irrelevant for this analysis.

The analysis is exclusively conducted for the first impacted girder at NAP +6.89 m, as this provides a good representation of the ratio in energy absorption between the analysed improvements of this section. This ratio is expected to be approximately the same for the remaining girders. At the end of this section, it is clear how the cross-section of the horizontal girders is improved in terms of energy absorption. The following improvements are made to the original layout in order to compare and discuss them:

- Improvement 1: $t_{flange,upper}$: 30 mm → 50 mm;

- Improvement 2: $t_{flange,upper}$: 30 mm \rightarrow 50 mm, $t_{flange,lower}$: 30 mm \rightarrow 50 mm;
- Improvement 3: $t_{flange,upper}$: 30 mm \rightarrow 50 mm, $t_{flange,lower}$: 30 mm \rightarrow 50 mm, t_{web} : 16 mm \rightarrow 27 mm.

The results of the improvements in terms of energy absorption are illustrated in Figure 7.1. It includes the results of the original design for comparison purposes. The length and height of the girder is kept the same as the original design for simplicity.

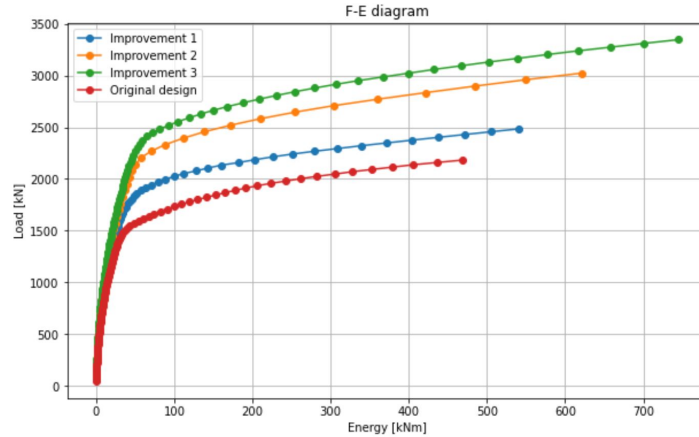


Figure 7.1: Energy absorption of enhanced cross-section for the first impacted horizontal girder at NAP +6.89 m during an unsymmetrical collision

The graphs in Figure 7.1 clearly indicate that the original design yields the lowest energy absorption. A stepwise approach is undertaken to identify which part of the cross-section contributes to an higher energy absorption capacity. Initially, focus is placed on thickening only the upper flange of the profile, as this is where the load applies and where fracture strain is often first reached. However, this results in an unsymmetrical profile, with the neutral axis laying higher than for a symmetrical profile. The additional material in the upper flange increases the moment of inertia and consequently the section modulus around the neutral axis. The moment of inertia and section modulus for the section above the neutral axis are relatively higher than below it. This results in reaching fracture strain faster in the bottom flange, as shown in Figure 7.2. However, the increase in section modulus leads to better resistance against bending for the profile with a thicker upper flange. The results in Figure 7.1 demonstrate an increase in energy absorption compared to the original design, but the cross-section of 'Improvement 2' is capable of absorbing more energy. This is because both flanges are thickened for this design, resulting in a significant increase in the section modulus for the entire cross-section.

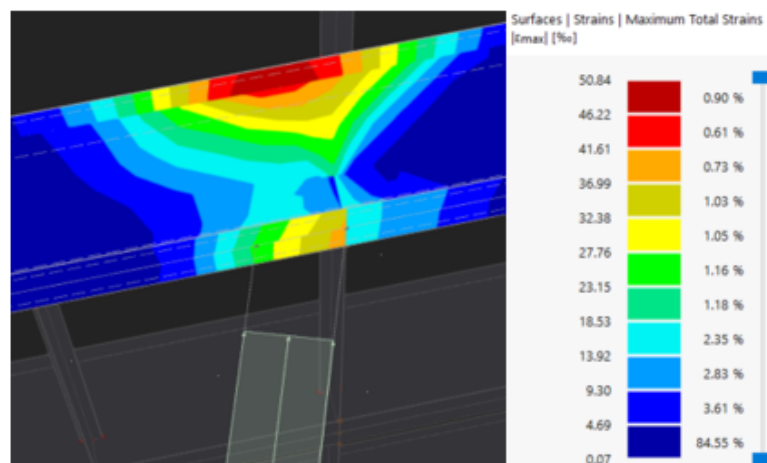


Figure 7.2: Strain for cross-section with a thicker upper flange ($t_f = 50$ mm) due to an unsymmetrical collision

Finally, consideration was given to thickening both flanges and the web of the profile, defined as 'Improvement 3'. Once again, an increase in energy absorption is observed, with an increment of approximately 60%

compared to the original design. This suggests that choosing for a larger profile overall is advantageous for energy absorption. The increase in thicknesses was arbitrarily assumed for this analysis to visualise its impact. However, the thickness of the web is kept in the same proportion with the flange thickness as in the original design. In reality, consideration should be given to common types and sizes of cross-section profiles.

7.1.2. Increasing the number of horizontal girders

The application of a smaller center-to-center distance between the horizontal girders is examined in this section. Since these are the components that contribute the most to energy absorption, simply having more of these girders could result in an higher energy absorption capacity. For this analysis, a center-to-center distance of 50% smaller than the original design is considered. Resulting in a center-to-center distance of approximately 1.07 meters (see Figure 7.3). The highest and lowest possible horizontal girders that can be impacted are indicated by arrows, based on the approach outlined in Section 4.2.2. The energy absorption is recalculated for both symmetrical and unsymmetrical collisions and compared to that of the original design from Section 6.1.

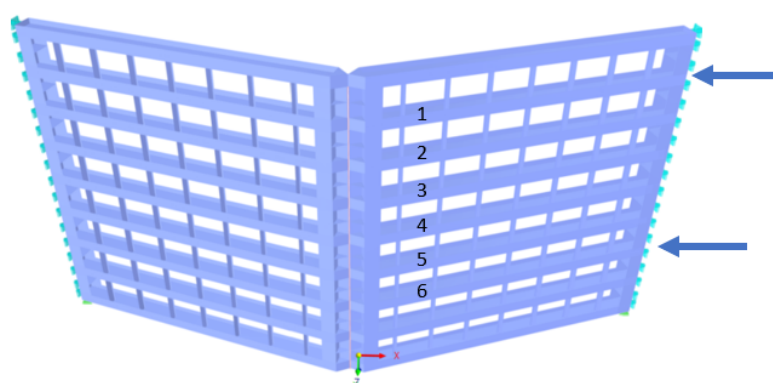


Figure 7.3: New lock gate design with adjusted center-to-center distance of 1/2 the original distance. The numbered girders are related to the different phases and the arrows indicate the highest and lowest possible impacted girder.

Unsymmetrical collision

As previously explained in the analysis of the unsymmetrical collision for the original design in Section 6.2.1, both calculation methods (*a* & *b*) are applied to the modified design. The smaller center-to-center distance results in the girders exerting a different influence on each other. Calculation method *b* offers more certainty in this regard, as it incorporates the deformed state of one girder into the next girder to be loaded. During the analysis for the energy absorption of the modified design, it is revealed that calculation method *a* now yields an higher capacity compared to calculation method *b*. The difference in energy absorption of phase 2 is 479 kNm for method *a* versus 385 kNm for method *b*. For phase 3, this difference is reduced to 457 kNm versus 428 kNm respectively. Since the process maintained in calculation method *b* aligns closer to reality, these results are considered accurate. The results are presented in Table 7.1, alongside the results of the original design for comparison.

Unsymmetrical	$F_{yield,flange}$ [kN]	F_{max} [kN]	u_i [mm]	u_{max} [mm]	E_{new} [kNm]	E_{old} [kNm]
Phase 1	798	2,346	-	101.3	150	468
Phase 2b	-	2,955	38.5	225.2	385	373
Phase 3b	-	2,880	65.6	266.5	428	406
Phase 4b-6b	-	-	-	-	3 × 400	-
Total					2,163	1,247

Table 7.1: Results of the lock gate model with adjusted center-to-center distance for an unsymmetrical collision

The yield stress $F_{yield,flange}$ is already reached for phases 2-6 due to the force from their respective previous phase. Additionally, it can be concluded from Table 7.1 that the relative deformation ($u_{max} - u_i$) has a significant influence on energy absorption. Phase 3b generates a slightly lower force F_{max} at which fracture

strain is reached, but on the other hand it generates a slightly higher relative deformation. As a result, the energy absorption E_{new} is approximately 50 kNm higher than that from phase 2b. The energy absorption for the remaining impacted girders (phases 4b to 6b) is estimated to be around 400 kNm, as they will exhibit the same behaviour as the girders from the analysed phases. This results in a total energy absorption capacity of approximately 2,163 kNm, which is nearly 75% higher than the capacity of the old lock gate design.

Symmetrical collision

Determining the energy absorption for a symmetrical collision for the improved lock gate design is carried out in exactly the same manner as described in Section 6.2.2. The deformation of the first set of impacted girders is used as the initial state for the second set of impacted girders. However, defining the 'failure under tension' criteria between the contact of both gates does not yield results for the second set of girders. The model indicates instability and stops calculating long before reaching fracture strain. For this reason, it is chosen to define the contact between the gates as 'full force transmission'. This criteria ensures that all (compression and tension) forces are transferred at the contact between the gates. This does not significantly affect the capacity of the girders, as now the focus is more on the local failure of the mitre posts. Only the global deformations are slightly different, but that is not the aim of this analysis.

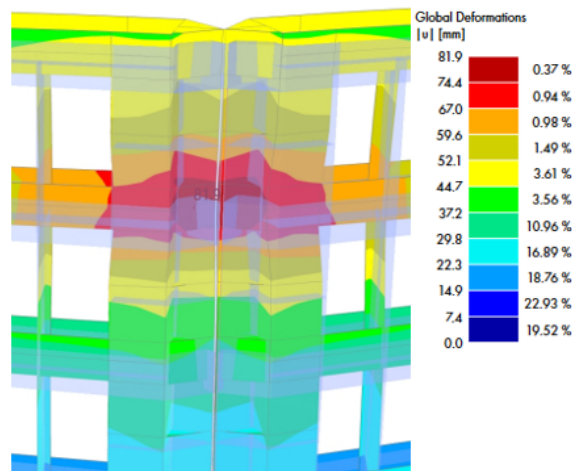


Figure 7.4: Initial deformation of the second set of girders (turquoise) due to the first loaded set (red) above for the lock gate design with adjusted center-to-center distance

During the determination of the energy absorption per set of girders, it becomes clear that each set has the same capacity in terms of force. However, the energy absorption of the first set of impacted girders varies from the other sets of girders. This is because only the first girder is loaded from an undeformed state and thus uses its full capacity from the initial loading. All other girders experience an initial deformation due to the previously loaded girder above them, as illustrated in Figure 7.4. In this figure, the load is applied at the level of the first set of girders, where the deformation is greatest (indicated by the red contour). Consequently, the set of girders beneath this loaded set experiences a deformation of approximately 37 mm (indicated by the turquoise contour). It is assumed that all sets of girders, except the first one, have the same energy absorption.

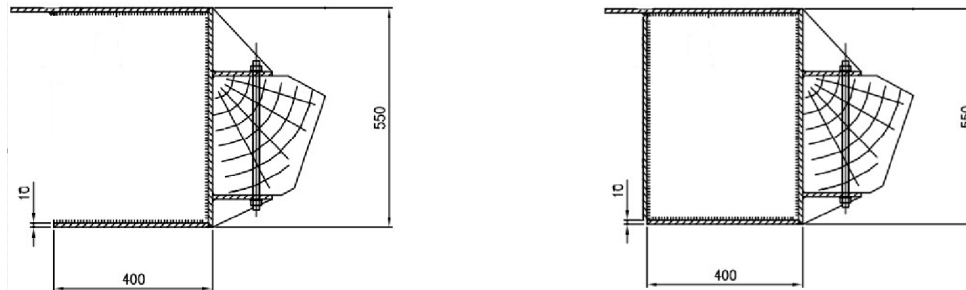
The results from Table 7.2 indicate that the energy absorption per set of girders for the new design is lower than that of the current design. The deformation u_{max} is lower because the center-to-center distance between the girders is smaller, resulting in greater resistance from the adjacent girders. However, due to the fact that the improved design has more sets of girders, the total energy absorption is higher. While the improved design has 6 sets of girders to be loaded, the original design only has 3. This ultimately results in an increase in energy absorption of approximately 40% for the improved design.

Symmetrical	$F_{yield,post}$ [kN]	F_{max} [kN]	u_i [mm]	u_{max} [mm]	E_{new} [kNm]	E_{old} [kNm]
Phase 1	4,225	10,562	-	81.9	561	747
Phase 2-6	-	10,562	37	79.4	5×309	2×392
Total					2,106	1,531

Table 7.2: Results of the lock gate model with adjusted center-to-center distance for a symmetrical collision

7.1.3. Closing the box profile of the mitre- and heel posts

The current design of the lock gate features an open box profile for the mitre and heel posts, as shown in Figure 7.5a. Closing this profile increases the rotational stiffness of the posts, which is advantageous for force transmission during a collision. This section analyses whether closing the box profile, as illustrated in Figure 7.5b, has a significant impact on the energy absorption of the entire lock gate. The plates used to close the posts are attached to the flanges of the respective upper and lower laying girder.



(a) Open structure of the mitre and heel posts original design lock gate (b) Closed structure of the mitre and heel posts improved design lock gate

Figure 7.5: Cross-section as seen from above of the open and closed structure of the mitre post

Both the mitre and heel posts are closed for the improved design. Only the first impacted girder at NAP +6.89 m is analysed because its behaviour and relation to the other girders are assumed to be the same as that of the original design. Figure 7.6 shows the results regarding the force F versus displacement u . Both symmetrical and unsymmetrical collisions are examined. They both exhibit similar behaviour, with slightly more nuanced differences in one compared to the other.

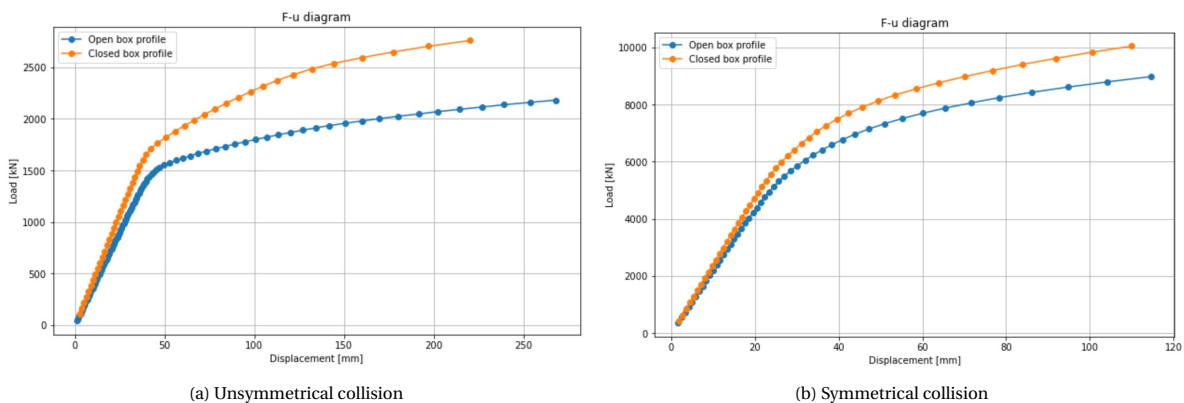


Figure 7.6: Load (F) - displacement (u) diagrams at the first set of girders at NAP +6.89 m for the lock gate with an open box profile (original design) vs. a closed box profile mitre- and heel posts

The F-u diagram from Figure 7.6a reveals that the loaded girder from the improved design with a closed box profile has a higher capacity in terms of force compared to the original design where the box profile is open. In other words, the force at which the girder reaches its yield strength and fracture strain is higher. This property is explained by the fact that the girder now experiences more stiffness from the posts. By closing almost the entire post the torsional stiffness increases, causing the girder to behave more like a clamped girder. The increased stiffness affects the deformation of the girder, which is lower compared to the design with an open box profile. Due to an increase in load capacity and a decrease in total deformation for the impacted horizontal girder, the energy absorption is more or less the same as that of the original design. This is evidenced by an energy absorption of 464 kNm for the improved design compared to the calculated 468 kNm from Section 6.2.1, respectively. This example proves that a higher load capacity does not always mean that more energy can be absorbed.

During a symmetrical collision, the mitre posts also exhibit stiffer behaviour. From Figure 7.6b, it is evident that a slightly higher force is absorbed before reaching fracture strain for the design with a closed box profile. The deformation of both designs is approximately equal, resulting in slightly higher energy absorption of

approximately 8% for the improved design.

7.1.4. Comparison of improved gate layouts

Through the use of an Excel spreadsheet, an estimation of the material usage per gate layout is made. This allows for a visualisation of the relation between the additional material usage per improved layout, and the increase in energy absorption capacity. The current design of 1 set of mitre gates consists of approximately 4.0 m³, i.e. 31 tons of steel, including the steel used for the skin plate, horizontal girders, vertical INP-profiles, and mitre- and heel posts. In Table 7.3, the results are presented in terms of material, energy absorption capacity, and the ratio of additional energy absorption capacity to additional material usage. Where the extra energy and steel are relative to the original layout of the lock gate.

	Material [t]		Energy [kNm]		Δ Energy / Δ Material [kNm/t]	
	m_{steel}	Δm_{steel}	Unsymmetrical	Symmetrical	Unsymmetrical	Symmetrical
Original layout	31.0	-	1,250	1,530	-	-
Layout 1	41.5	10.5	2,000	1,530	71.4	-
Layout 2	44.3	13.3	2,165	2,105	68.8	43.2
Layout 3	32.3	1.3	-	1,650	-	92.3

Table 7.3: Results of all improved gate layouts including the relation between increased energy absorption capacity and additional material usage

Layout 1: Increase in cross-sectional profile of the horizontal girder

A larger cross-section of the profile of the horizontal girder logically results in an increase in steel usage. With the addition of 10.5 extra steel to the cross-section of the profile, the energy absorption capacity increases by 60% (750 kNm) in the case of an unsymmetrical collision. The ratio between the material usage and the energy absorption capacity for an unsymmetrical collision is then an increase of $\frac{750}{10.5} = 71.4$ kNm/t. Since the mitre posts fail before the buckling capacity in the horizontal girders is reached, the energy absorption capacity is not affected by this improvement in case of a symmetrical collision. If the mitre posts had not failed yet, this improvement could lead to an increase in capacity. Generally, an increase in the cross-sectional area of a girder results in a higher buckling capacity when the length of the girder remains the same.

Layout 2: Increase in number of horizontal girders

A reduction in the center-to-center distance between the horizontal girders results in an increase in the number of horizontal girders. Since the distance between the girders is now halved, the total number of girders is 18 instead of 10 for one set of mitre gates. This brings about an increase of 13.3 tons more material. In addition to an increase of almost 75% (900 kNm) in energy absorption capacity for an unsymmetrical collision, this gate layout result in an increase in capacity of approximately 40% (600 kNm) for a symmetrical collision. The advantage of this improvement is that it has an effect on both types of collision.

Layout 3: Closing the mitre- and heel posts

The closing of the mitre- and heel posts involves adding an extra plate of 10 mm thickness to each post. This modification results in a steel usage increase of only 1.3 tons. The results from this analysis show that the energy absorption capacity in the case of an unsymmetrical collision is not affected by closing the posts. Despite the increased load capacity, the new design results in a reduction in local deformation for this type of collision. However, the capacity in the case of a symmetrical collision experiences a small increase of 8% (120 kNm) compared to the old layout of the lock gate. The ratio between the material usage and the energy absorption capacity for a symmetrical collision is then an increase of $\frac{120}{1.3} = 92.3$ kNm/t. Despite being a small increase in energy absorption capacity, this is achieved by adding a small amount of steel. However, there is a limit to this modification as further optimisation is constrained.

Conclusion on comparison of the improved gate layouts

From this analyses, it is concluded that adding additional horizontal girders, formulated as layout 2, is the most effective for increasing energy absorption capacity. Both the capacities in case of an unsymmetrical and symmetrical collision are improved as a result. The combination of various improvements could potentially yield even greater benefits. Further research should be conducted on this matter. Section 7.2 compares three designs, including one design incorporating all discussed improvements in this section.

7.2. Quantification of the improvements

In this section, the total energy absorption capacity of three designs is compared using the analysed potential collision energy from Chapter 3. In this way, the improvements made to the gate layout are quantified based on a percentage of vessels. The following designs are discussed in this section:

1. Original design of the Macharen lock gate constructed with S235 steel;
2. Original design of the Macharen lock gate constructed with S355 steel;
3. New design of the Macharen lock gate constructed with S355 steel.

The new design of the lock gate incorporates all discussed improvements from the previous Section 7.1. The capacity in terms of energy absorption for the original design of the Macharen lock gate constructed with S355 steel is elaborated in Chapter 6, for both a symmetrical and an unsymmetrical collision. The capacity for the remaining two designs is determined in a similar manner and are not further elaborated upon.

7.2.1. Principle of quantifying the improvements

The improvements made to the gate layout are determined by looking at the percentage of vessels whose potential collision energy is below the energy absorption capacity of the respective lock gate. As previously explained, the energy absorption capacity is determined using the same method outlined in Chapter 6. This method results in four different values for the energy absorption capacity per lock gate design, namely the capacity in case of:

- an unsymmetrical collision for vessels belonging to CEMT class I (US-I);
- an unsymmetrical collision for vessels belonging to CEMT classes II-III (US-II/III);
- a symmetrical collision for vessels belonging to CEMT class I (S-I);
- a symmetrical collision for vessels belonging to CEMT classes II-Va (S-II/Va).

Per type of collision, there is a difference in CEMT class, as vessels belonging to CEMT class I have insufficient draft to collide with the girder at NAP +2.63 m. And, vessels belonging to class IV and Va are too wide to collide with the gate asymmetrically. These four generated capacities are used to compare it with the calculated collision energies from Chapter 3, once again showed in Figure 7.7.

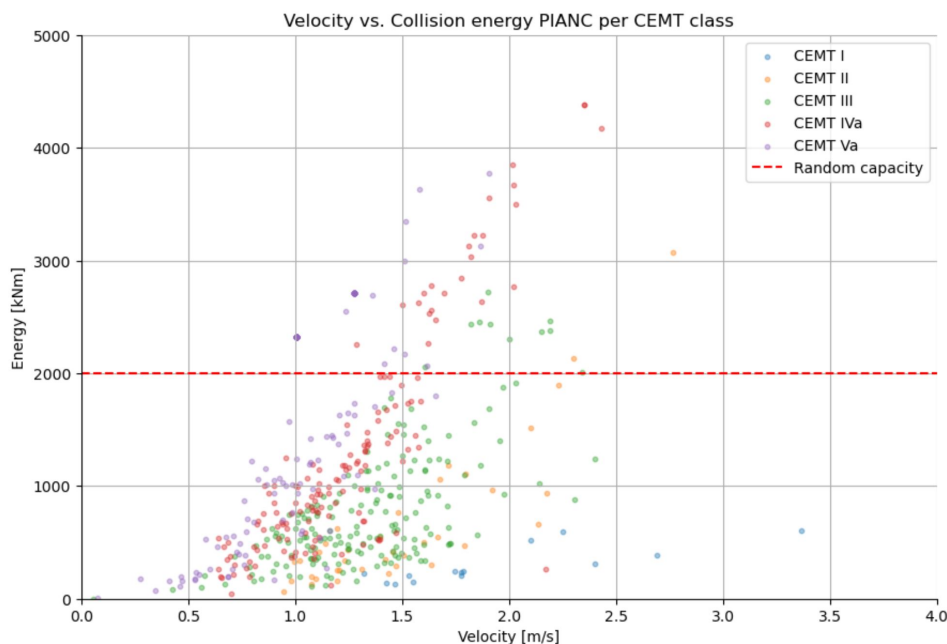


Figure 7.7: Velocity vs. collision energy based on PIANC data points per CEMT class at location E + random energy absorption capacity of 2,000 kNm

In this figure, a distinction is made between the energies of vessels belonging to different CEMT classes, indicated by varying colors. The graph includes a constant line with a value of Energy = 2,000 kNm representing a random value for the energy absorption capacity. In this way, the design of the lock gate is verified by determining the number of vessels above and below the specified energy absorption capacity. The data points represent all vessels with their potential collision energy (load), and the red line represents the capacity of the lock gate in terms of energy absorption. The red line, with a value of 2,000 kNm, illustrates that the majority of the calculated collision energies are below this value. In other words, when the capacity of a lock gate in terms of energy absorption is approximately 2,000 kNm, the majority of vessels will not cause the lock gate to fail. The vessels that do exceed this capacity belong to the higher CEMT classes, namely CEMT classes III, IVa & Va.

In the next sections, a more precise comparison is made for each design of the Macharen lock gate. Here, all calculated collision energies per vessel are sorted from low to high on the x-axis. No distinction is made in CEMT class; all data points have an uniform color. This is done because the difference per CEMT class cannot be visualised due to the overlap of some data points with each other. In Appendix H, the dataset is split per CEMT class, making it easier to identify which vessels exceed the capacity.

7.2.2. Energy absorption capacity: Original lock gate design in S235 steel

Firstly, the original design of the Macharen lock gate constructed with S235 steel is compared to the calculated collision energies from the AIS dataset. Figure 7.8 displays these calculated collision energies per vessel from low to high, alongside the four computed capacities for the lock gate design. From Appendix H.1, it becomes evident that no vessel belonging to CEMT class I exceeds the calculated capacity for both a symmetrical and an unsymmetrical collision.

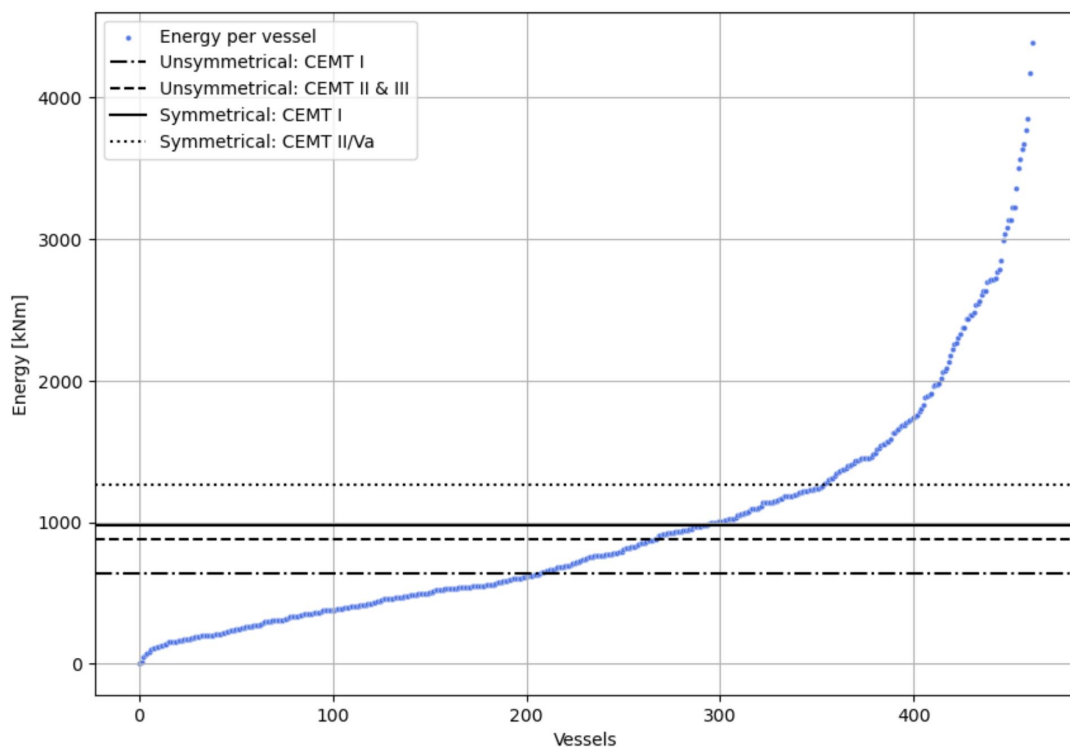


Figure 7.8: Calculated collision energies from the AIS dataset vs. determined energy absorption capacity for the original lock gate design in S235 steel, with 4 constant lines plotted for energy absorption capacity in case of a symmetrical (S) and an unsymmetrical (US) collision

It becomes clear from Figure 7.8 that an unsymmetrical collision involving a vessel belonging to CEMT class I (US-I) generates the lowest capacity in terms of energy absorption. On the contrary, when considering the calculated capacity of a symmetrical collision for vessels belonging to CEMT class II to Va (S-II/Va), it is noticeable that this generates the highest energy absorption. The likelihood of this type of collision is greater compared to an unsymmetrical collision because in the event that a skipper expects the lock to be open but in reality it is closed, the vessel will most likely be positioned in the middle of the waterway. Through the programmed data in Python, it is calculated that 77% of the calculated collision energies are absorbed for this

type of collision with the current lock gate design constructed in S235 steel. It is also possible to graphically read this from Figure 7.8, by examining the intersection point of the S-II/Va threshold and the measured energy per vessel. This occurs approximately at $x = 355$ [-], while the total number of indices is around 465 [-]. This results in $\frac{360}{465} \times 100\% = 77\%$.

7.2.3. Energy absorption capacity: Original lock gate design in S355 steel

In this section, the design of the lock gate is kept the same as the original design, with the only modification being the increase in steel quality to S355. This design is used to describe the method for determining the energy absorption capacity, and the results of this are therefore documented in Section 6.1. In Figure 7.9, the calculated capacities in terms of energy absorption are again used to compare them with the calculated potential impact energies from Chapter 3. In Appendix H.2, these capacities are plotted per CEMT class.

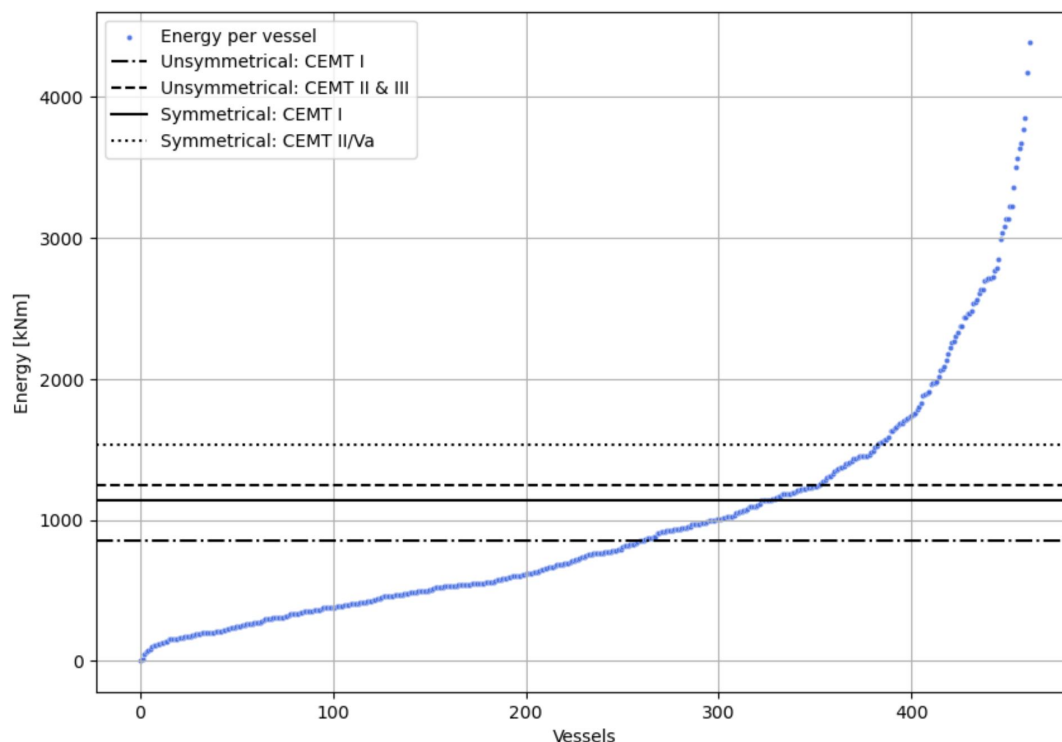


Figure 7.9: Calculated collision energies from the AIS dataset vs. determined energy absorption capacity for the original lock gate design in S355 steel, with 4 constant lines plotted for energy absorption capacity in case of a symmetrical (S) and an unsymmetrical (US) collision

From Figure 7.9, it becomes evident that the capacity for this design of the lock gate, constructed with S355 steel, generates slightly higher capacities compared to the design executed in S235 steel. The capacity in the case of an unsymmetrical collision seems to increase slightly more compared to a symmetrical collision. This is explained by the fact that load capacity increases relatively more with approximately equal deformations, two important parameters for determining energy absorption.

The capacity in the case of a (un)-symmetrical collision for vessels belonging to CEMT class I (US-I & S-I) is once again not reached, simply because the capacity of the lock gate for this design is higher and the capacity of the design in Section 7.2.2 was also not reached. The higher energies are measured for vessels belonging to CEMT class IVa and Va, due to their characteristic larger dimensions, i.e., higher masses. Despite this often being accompanied by a reduction in velocity, it results in an higher potential collision energy. In the case of a symmetrical collision for vessels belonging to CEMT class IVa & Va (S-II/Va), the same percentage of vessels is stopped, refer to Appendix H.2. The fact that the energy of the same percentage of vessels is absorbed for both classes, further proves that an higher CEMT class does not necessarily mean that the vessels generate an higher collision energy. In total, 83% of all vessels in this dataset are stopped by the original design of the lock gate in S355 in the event of a symmetrical collision. This is 6% more compared to the original design in S235 steel.

7.2.4. Energy absorption capacity: New lock gate design

The new design of the lock gate incorporates all the discussed improvements from Section 7.1. This includes increasing the cross-sectional area of the horizontal girders, reducing the center-to-center distance to 1/2 times the original center-to-center distance, and closing the posts with a 10 mm thick steel plate. Section 7.1 demonstrates that each of these improvements individually has a beneficial effect on the energy absorption capacity. This section discusses the capacity of the design with all three of these improvements implemented together in one design. However, this does require a significant amount of additional material. The material usage for the old design of the lock gate is estimated to be approximately 4.0 m³ for 1 set of mitre gates. The material usage for the new design, including all improvements, is estimated to be 8.2 m³. This means that approximately 4.2 m³ (equivalent to 33.5 tons) of extra steel is required for the new design.

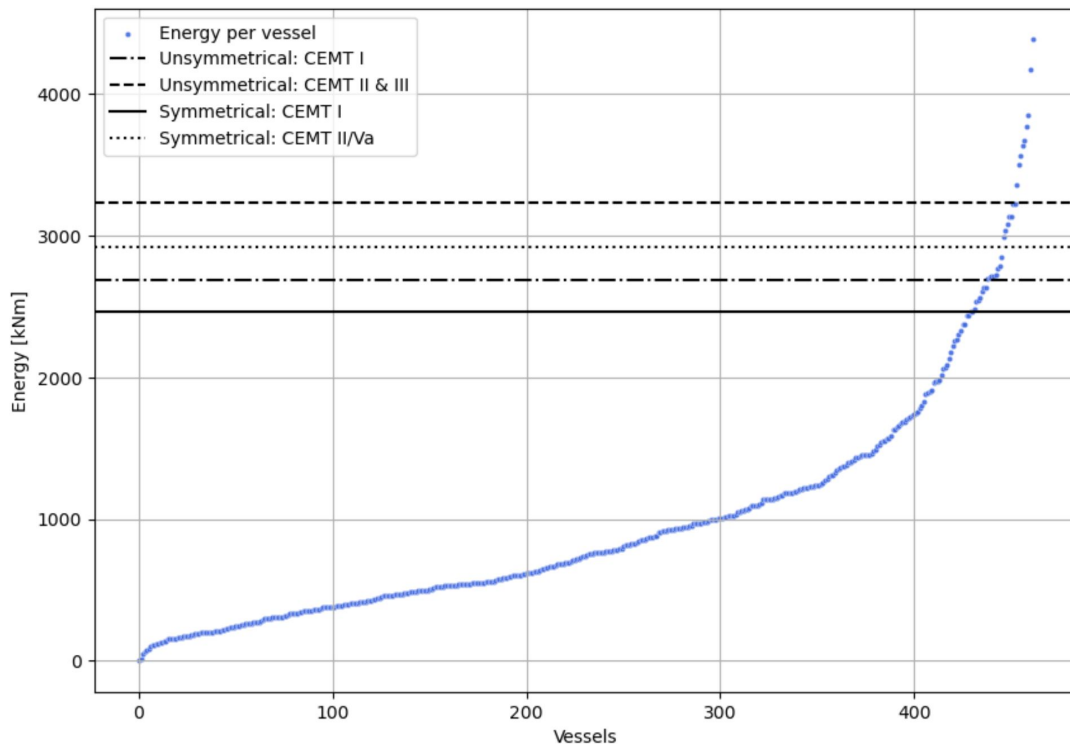


Figure 7.10: Calculated collision energies from the AIS dataset vs. determined energy absorption capacity for the new lock gate design in S355 steel, with 4 constant lines plotted for energy absorption capacity in case of a symmetrical (S) and an unsymmetrical (US) collision

It quickly becomes evident from Figure 7.10 that the capacity of this lock gate design is significantly higher than the two designs discussed earlier. For example, there is already a factor of 2 to 3 difference between the energy absorption capacity of this design and the original design executed in S355 steel. Additionally, it is noticeable that in the case of an unsymmetrical collision for vessels belonging to CEMT class II & III (US-II/III), the capacity is now higher than in the case of a symmetrical collision for vessels belonging to CEMT class II to Va (S-II/Va). The same is true for vessels belonging to CEMT class I. This is explained by the fact that the lock gate has received so much extra capacity from the new design that in the case of an unsymmetrical collision, it can handle more force along with significant deformations. In the case of a symmetrical collision, a relatively lower increase in load capacity is found, and aside from that, the deformations are considerably smaller because the structure responds more rigidly. This process is explained in Chapter 6.

In Appendix H.3, the plots are once again presented per CEMT class for determining the percentage of vessels whose energy are absorbed. From these plots, it becomes clear that for this design, almost all vessels do not exceed the calculated limits for energy absorption capacity. The energy of one vessel belonging to CEMT class II is not fully absorbed in the event of a symmetrical collision. For vessels belonging to CEMT class IVa and Va, the energy of slightly more vessels is not absorbed. In total, the potential collision energy of 97% of all vessels from the dataset can be absorbed in the event of a symmetrical collision with the lock gate. This is 20% more than for the original design of the lock gate, made of S235 steel. In the case of an unsymmetrical collision, the potential collision energy of all vessels are absorbed. These include all vessels belonging to CEMT classes I through III. Note: this does not mean that no damage is caused to the lock gate, but rather that the lock gate

will not completely fail by the collision.

Besides the fact that the energy of over 20% extra vessels can be absorbed with the new design, it brings some disadvantages. For example, more and higher quality material is required to manufacture the lock gate, which directly translates to higher costs. An increase of approximately 96% (33.5 tons) in material leads to an increase in energy absorption capacity of $\frac{3,235-882}{882} \times 100\% = 267\%$ (2,353 kNm) and $\frac{2,916-1,267}{1,267} \times 100\% = 130\%$ (1,649 kNm) in case of an unsymmetrical and symmetrical collision, respectively. The ratio between the extra material usage and the increase in energy absorption capacity for both an unsymmetrical and a symmetrical collision for this new design of the lock gate is then $\frac{2,353}{33.5} = 70.2$ kNm/t and $\frac{1,649}{33.5} = 49.2$ kNm/t respectively. These ratios demonstrate that the efficiency of this new design is in line with the individual improvements discussed in Section 7.1.4. Approximately the same ratios are achieved, with a few exceptional cases. This is because some improvements have no effect on the capacity of a certain type of collision, or they do have an effect with a very small addition of steel.

7.3. Conclusion on improving energy absorption capacity

At the beginning of this chapter, research question 6 is formulated: *"How can the design of the lock gate be improved to enhance its energy absorption capacity?"* In order to answer this question, attention is focused on the structural components that provide the most capacity in terms of energy absorption, namely the horizontal girders and the mitre- and heel posts. When the following improvements are made to the gate layout, an increase in energy absorption capacity is observed:

- Applying an higher steel quality;
- Increasing the cross-sectional profile of the horizontal girders;
- Increasing the number of horizontal girders;
- Closing of the box profile of the posts.

After the sensitivity analysis in Chapter 4, it was already concluded that an higher steel quality has a positive impact on the capacity of the lock gate. Considering the other individual improvements, it is concluded that adding extra horizontal girders is the most effective improvement. Additionally, combining different improvements in one design provides additional capacity to the lock gate. This is verified by comparing the energy absorption capacity of the lock gate with the calculated collision energies from the AIS dataset. This comparison between the load on the lock gate and the capacity of the lock gate provides a quantification of the improvements made to the gate layout based on a percentage of vessels. The design for the original lock gate made of S235 steel generates the lowest capacities as expected, and the potential collision energy of 23% of the vessels is not absorbed. In contrast to this design, the design for the new lock gate generates the highest capacities, and the potential collision energy of only 3% of the vessels is not absorbed. However, this increase in energy absorption capacity comes at the expense of a significant amount of steel of 96%, and therefore brings additional costs.

The analyses for these designs were conducted exclusively to demonstrate that changes in geometry, quantity, and quality of the steel have significant effects on the energy absorption capacity of the lock gate. A more thorough examination is needed to determine the appropriate balance between energy absorption capacity and material usage. With this analyses, it is also demonstrated how the method described in Chapter 6 can be compared with the AIS dataset to check the design and determine what percentage of vessels can be stopped.

8

Generalisation of the used structural design process

Now that all the steps of the thesis have been completed, it is time to consider whether followed the steps, i.e., the used structural design process, can be generalised to other or new locks. This marks the final research question of this thesis: "How can the used structural design process be applied to other locks?". In Section 8.1, the design process applied to the Macharen lock is generalised into a universally applicable methodology. Here, the key steps are presented in a flowchart along with relevant findings from this thesis. Furthermore, this section discusses relevant factors that may vary compared to the Macharen lock and whether this influences the overall design process.

8.1. Application to other (new) locks

The steps outlined in Chapter 1, and followed throughout the thesis are applied to the Macharen lock but are generalised into a universally applicable methodology. The universally applicable methodology in this case refers to the structural design process of a lock gate, taking into account ship-lock collisions. With this design process, the collision resistance of a lock gate is estimated. The flowchart in Figure 8.1 can be used for this. Within the process, two different components play an important role in determining collision resistance: the load on the lock gate and the capacity of the lock gate. Various factors influence one or both of these components, potentially impacting the applicability of the design process in different situations. The influence of these factors on the applicability of the design process is discussed in this section.

8.1.1. Difference in relevant collision scenario(s)

The most relevant collision scenario(s) must be determined, which may vary from lock to lock. For example, because water safety plays a crucial role at the Macharen lock, a collision from upstream direction with the inner gate was considered most critical. A collision scenario does not directly affect the capacity of a lock gate, but it may result in an increased or a decreased load on the gate due to varying ship velocities and/or masses. The load necessitates adjustments to the capacity of the lock gate and can thus yield various outcomes. This does not affect the steps to be followed in the overall design process.

8.1.2. Varying measured velocities from AIS data

The measured velocities from the AIS dataset based on Macharen lock mostly relate to a non-operational lock situation, which makes Macharen lock unique. This uniqueness reduces the representativeness of the measured velocities for other locks. It is expected that the velocities for an operational lock will be lower, thereby reducing the potential collision load on the gate. The vessel velocities vary for each lock, and the extent of this variation depends on various factors. The existence of general rules for approaching a lock should foster some uniformity in vessel velocities. Therefore, the velocities concerning locks of the same dimensions and control system are expected to cluster around a line. However, conducting an AIS data analysis is an essential part of the structural design process concerning ship-lock collisions and will always provide more accuracy.

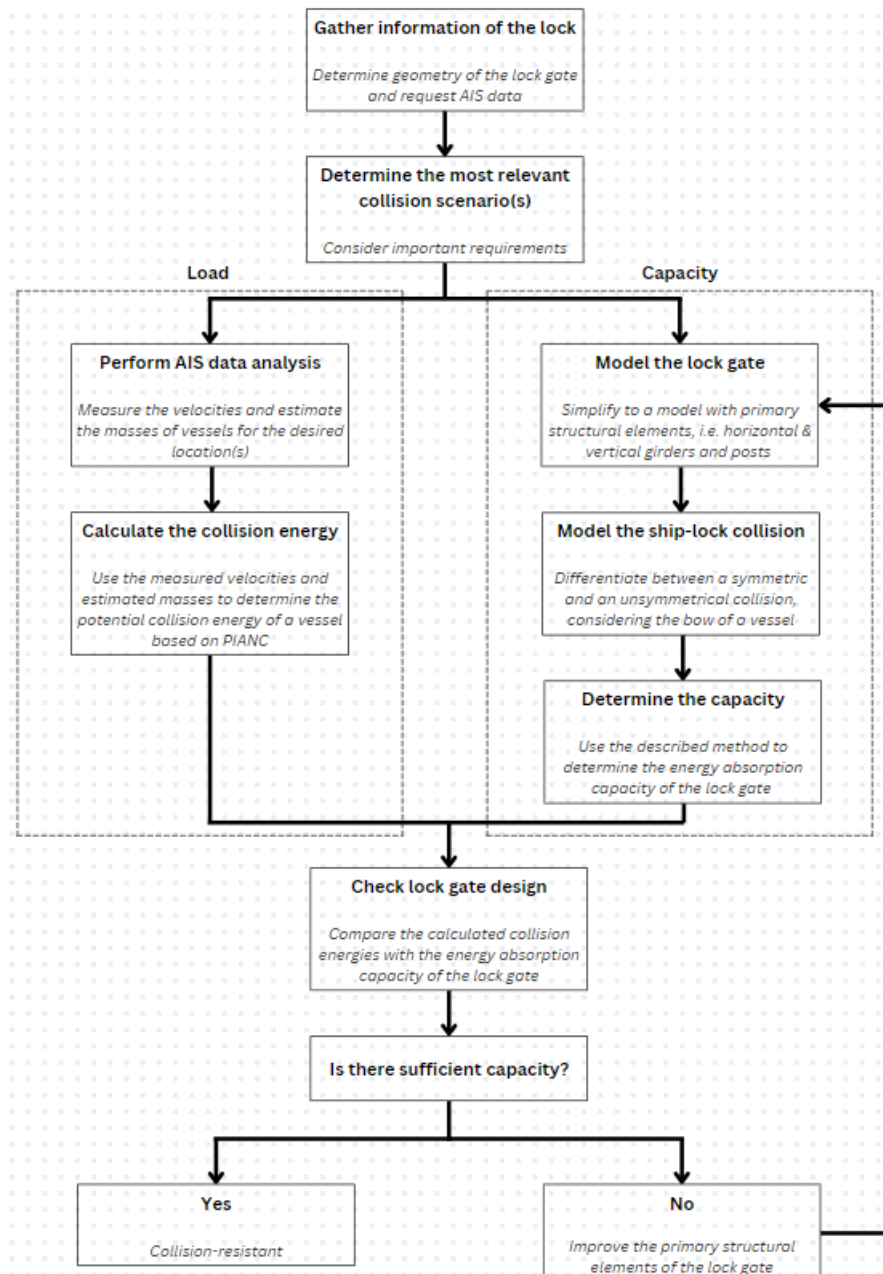


Figure 8.1: Flowchart of the universally applicable structural design process for determining the collision resistance of a lock gate

8.1.3. Other types of lock gates

A difference in lock gate type relates to the steps in the flowchart of Figure 8.1 concerning the capacity of the lock gate. The capacity will be influenced when the overall structure of the gate changes. This section discusses whether the design process can be applied to three different types of gates compared to the mitre gate: the vertical lift gate, the roller gate and the sector gate.

Vertical lift gate & Roller gate

The vertical lift gate's structure resembles that of a rolling lock gate. The difference between the two types relates to their suitability in the environment. Rolling lock gates are often used in sea locks, where there is sufficient space available. The method for determining the energy absorption capacity can be applied to a vertical lift gate or rolling lock gate, since the framework of these type of gates are similar to that of a mitre gate. The collision of a vertical lift or roller gate is similar to what occurs during an unsymmetrical collision of a mitre gate. The only difference now is that the lock gate consists of a single gate instead of two separate

gates and it is not placed at an angle. This affects the force distribution towards the lock head. There is no normal force acting on the horizontal girders and as a result it responds less rigidly, especially in the case of a symmetrical collision. However, this does not necessarily mean it is disadvantageous for its energy absorption capacity, provided that the gate is adequately reinforced.

Sector gate

The sector gate is less frequently used in the Netherlands but is very popular in the United States. Figure 8.2 illustrates the framework of a typical sector gate, including all the important components identified. From the figure, it can be concluded that this type of gate consists of more connections compared to a mitre gate. The force is transmitted from the horizontal girders through the truss to the hinges. Assuming that a vessel cannot collide with the top of the sector gate, the first point of contact with the gate is somewhere between the top and the middle. This means that the horizontal girder in the middle of the sector gate bears all the force initially (see Figure 8.2b). Subsequently, the vessel penetrates further if not all energy is absorbed. The described method for determining the energy absorption capacity could also be applied here. Assuming the sector gate is made of steel, the force and deformation at a strain of 5% can be determined once again. However, the collision process will differ compared to a mitre gate, due to the overall structural differences between them. It is expected that a collision with a sector gate allows for higher forces compared to a vertical lift gate, given the rounded shape of the sector gate. This rounded shape facilitates better distribution of forces.

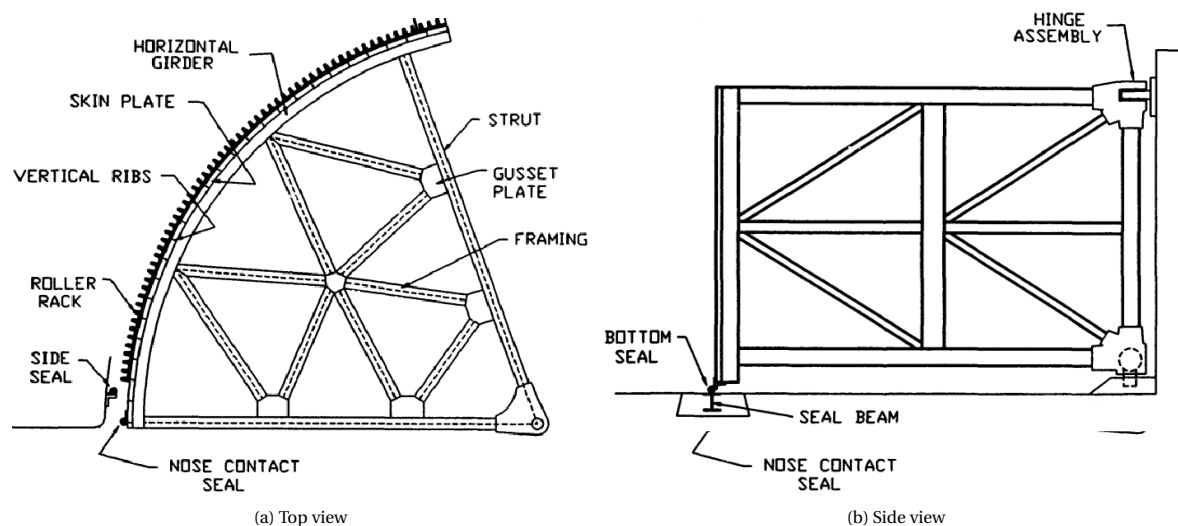


Figure 8.2: Framework of a sector gate with vertical axis rotation (Greimann et al., 1993)

8.1.4. Collision of a seagoing vessel with a lock gate

This thesis focuses on the collision of an inland vessel with a lock, but it is also possible for seagoing vessels to encounter similar situations. The difference in vessel type mainly impacts the "Model the ship-lock collision" step from the flowchart, which relates to a difference in bow shape of the vessel. Additionally, roller gates are almost always used in sea locks, but Section 8.1.3 concludes that the structural design process remains applicable.

Difference in bow shape

In Section 2.2.2 of the literature study, two types of bows are mentioned: the V-shaped bow and the bulbous bow. The V-shaped bow is commonly used for inland vessels, while the bulbous bow is used for seagoing vessels. In contrast to the V-shaped bow, the bulbous bow has a protrusion at the bottom (also called the bulb). This bulb helps reduce a vessel's resistance and thus save fuel consumption by up to 20%. However, it is also considered a threat in collision accidents because it can penetrate the side shell of the vessel, potentially causing the leakage of hazardous goods (Liu et al., 2014b). This risk applies to collisions between seagoing vessels and lock gates as well, and differs from collisions involving inland vessels. In the case of a collision, there are two points of contact with the lock gate: one at the level of the bulb and one at the level of the part of the bow above water. Whether the contact of both points with the lock gate occurs simultaneously will need to be further investigated, but this should not pose a problem for the structural design process. Although the

force dynamics from vessel to gate are different, the design process remains applicable.

8.1.5. Usage of other types of material

The material used for the Macharen lock gate is steel. While this type of material is widely used for such applications, there are instances where other (innovative) materials are used. The influence of other materials primarily affects the capacity of the lock gate due to variations in their failure behaviour compared to steel. By modelling the lock gate in finite element analysis software RFEM, any type of material can be used provided that the material properties are known. This flexibility makes the method for determining the energy absorption capacity highly applicable for different types of materials. Essentially, only one model needs to be developed, from which the material can be adjusted. Therefore, the structural design process is also applicable when using other materials.

8.2. Conclusion on generalisation

At the beginning of this chapter, the final research question of this thesis is formulated, namely: *"How can the used structural design process be applied to other locks?"*. The structural design process is coupled to the steps followed in the thesis and generalised into a universally applicable method. Several aspects are important in this regard and vary per lock, including environmental conditions, type of lock gate, material and type of vessel. The generalisation in this chapter demonstrates that none of these aspects affect the steps to be followed in the design process. Thus, it is concluded that the design process can be applied to other or new locks by following the steps outlined in the flowchart in Figure 8.1.

9

Discussion, Conclusions and Recommendations

9.1. Discussion

In the process of enhancing the structural design process of lock gates concerning ship-lock collisions, a couple of assumptions were incorporated to simplify the problem. This comes with some limitations of the outcome, which are explained in this section. Distinction is made between limitations arising from the AIS data analysis and the use of the finite element analysis software RFEM.

9.1.1. AIS data analysis

Inaccurate draft. The measured draft in AIS data can be considered inaccurate since skippers manually input this value. In the used dataset, there were instances where the draft value for a vessel was missing, resulting in the exclusion of these vessels from the dataset. In contrast, the presence of a draft value did not guarantee accuracy, particularly after loading and unloading at the Port of Oss. As a result, the estimated mass of a vessel can be either too high or too low, resulting in a variable value for the potential collision energy. This is not a limitation of the methodology, but rather of the quality of the results.

Limited data available operational lock. The data available for an operational lock is very limited with only 14 days out of an entire year. During high water levels, the dataset included 11 vessels. This limitation renders the results non-representative. Some CEMT classes had only 1 vessel, making it problematic to compare with the data for a non-operational lock.

Measured velocities not representative for other locks. The measured velocities mostly relate to a non-operational lock situation, which makes Macharen lock unique. This lowers the representativeness for other locks, as explained in the generalisation of Chapter 8. A limitation here is that the measured velocities in this thesis are not considered representative for other locks with the same dimensions.

9.1.2. RFEM

No combination of a collision with hydrostatic water pressure. RFEM lacks the capability to calculate with a constant force (hydrostatic water pressure) while another force (collision) is gradually applied. This limitation can yield incomplete results for the desired analyses, as it hinders a thorough analysis of the water pressure's contribution to reaching the lock gate's capacity. It may suggest that the calculated energy absorption capacity for this particular girder is overestimated due to the exclusion of water pressure, as confirmed by the approach based on the F-u diagram in Section 6.2.1. Furthermore, the limitation of not being able to compute with a constant water pressure leads to the occurrence of a rocking effect at the bottom of the lock gates in the event of a symmetrical collision. If the water pressure could be taken into account it would counteract this effect, thereby mitigating its occurrence or reducing its magnitude.

Mesh size. In this thesis, a mesh size of 0.25 m was chosen, but a finer mesh size could potentially provide greater accuracy. However, this does come at the expense of computational time.

No relation between deformation and width of the load. The width of a load cannot be directly linked to the deformation of a structural component, such as a horizontal girder in this case. In the thesis, a line load of 300 mm has been chosen, but it is expected that this width could increase as the deformation of the girder increases. From a sketch of a typical inland vessel from (Joustra and Pater, 1993), a relation between width and deformation has been derived, indicating that after a deformation of 210 mm the width increases to 1100 mm. However, this is only the case if the deformation of the girder precisely follows the shape of the vessel's bow. If RFEM were capable of applying such function, greater gains could be achieved in terms of energy absorption capacity.

Initial state function. A convenient addition in RFEM is the use of the initial state function, where the deformed state of one loading case serves as the initial state for another loading case. However, this function comes with a limitation. It is not possible to maintain the load from the first loading case active during the calculation process of the second loading case, in which the deformed state of the first loading case is used. This results in the loaded girder or mitre post from the first loading case being unloaded or relaxed during the analysis, attempting to elastically return to its original shape. In reality, the oncoming vessel would not allow this because it continues to penetrate further through the lock gate. However, it is assumed in the thesis that this limitation does not yield unrealistic results, given that the modulus of elasticity of the girder remains constant at $2,100 \text{ N/mm}^2$.

9.2. Conclusions

The main objective of this thesis was to enhance the structural design process of lock gates regarding ship-lock collisions by improving the understanding of potential loads resulting from a ship-lock collision. This was achieved by using the lock at Macharen as a case, where inland vessels up to and including CEMT class Va ($L_{max} = 135 \text{ m}$) are allowed to pass.

By utilising an obtained (AIS) dataset from Rijkswaterstaat at the location of the Macharen lock, greater insight was gained into the potential loads in terms of velocity and mass, two important parameters for determining the collision energy. Through the AIS data analysis, it was possible to answer the research question: *"How can practical information from AIS data improve the accuracy of input parameters for collision energy estimation?"*. The measured velocities at the inner gate of the lock were considered most relevant for the thesis, and the average velocity at this location during a non-operational lock was 1.27 m/s . This was lower than the prescribed value of 3 m/s from the Eurocode (2015). During operational lock periods, only vessels up to CEMT class IVa ($L_{max} = 85 \text{ m}$) are allowed to pass, and even a lower average velocity was measured of 1.06 m/s . The analysis revealed differences between CEMT classes, and thus did not result in a constant velocity that should be used for every vessel as prescribed in the Eurocode. In conclusion, when the lock was non-operational the potential collision energy tended to be higher compared to an operational lock, influenced by higher velocities and larger masses vessels had. The operational status of the lock significantly influenced the collision energy, with lower velocities and masses resulting in a reduced potential collision energy. However, the reliability of these specific conditions when the lock gates were closed may be compromised due to limited data availability.

The collision between the vessel and the lock gate was schematised using the finite element analysis software RFEM. In doing so, the first part of the research question, *"How can the impact on the lock gate be schematised, and which factors are relevant in this context?"* was partially answered. The gate model was built in RFEM by considering factors such as overall gate structure, collision types and load distributions. The model was built using plate elements rather than beam elements, which allowed for a more accurate consideration of connections between structural elements. The sensitivity analysis revealed the importance of excluding certain structural components, optimising mesh size, and considering steel quality to accurately determine the lock gate's capacity. Furthermore, while the hydrostatic water pressure turned out to be relevant in later stages, self-weight did not significantly impact the energy absorption capacity of the lock gate.

By using basic mechanics, a method was described for determining the energy absorption capacity in the case of both unsymmetrical and symmetrical collisions. This addressed research question 4: *"Which method can accurately determine the energy absorption capacity of a lock gate?"* The relevant impacted horizontal girders were individually loaded in RFEM until a 5% strain was reached. The force and deformation corresponding

to this strain were then used to determine the energy absorption capacity. The application of this method to the Macharen lock gate answered research question 5: *"What is the capacity of a lock gate in terms of energy absorption?"* and revealed that in the case of a symmetrical collision more energy was absorbed compared to an unsymmetrical collision. The miter shape of the gate contributed to its rigid response during symmetrical collisions, leading to an higher load capacity. As a consequence, compressive forces significantly increased in the loaded horizontal girders, without reaching their buckling capacity. Despite the high load capacity, the gate's rigid response resulted in low local deformations. The results from RFEM indicated that the lock gate exhibited less rigidity during an unsymmetrical collision, resulting in a lower load capacity but higher deformation. For this type of collision, a distinction was made in calculation methodology, namely methods *a* & *b*. An important conclusion drawn from this was that method *b* came closer to reality. Finally, it was concluded that it may be relevant to consider the influence of hydrostatic water pressure on the energy absorption capacity in case of an unsymmetrical collision. For the Macharen lock, the water pressure accounted for approximately 20% of the overall capacity.

The analyses from the Chapter 4 & 6 of the thesis indicated that almost all capacity in terms of energy absorption came from the horizontal girders and the mitre- & heel posts. Therefore, the answer to research question 6: *"How can the design of the lock gate be improved to enhance its energy absorption capacity?"* concerns these structural components. By changing the geometry and center-to-center distance of the horizontal girders, and closing the box profile of the mitre- and heel posts, significant enhancements in energy absorption were achieved for each individual improvement. Particularly in the case of an unsymmetrical collision, these improvements demonstrated the potential to increase energy absorption capacity of the lock gate. From the individual improvements it was concluded that reducing the center-to-center distance between the horizontal girders was the most effective improvement. Additional capacity in terms of energy absorption was achieved in both symmetrical and unsymmetrical collisions for this improvement. Later in the Chapter 7, three gate designs were evaluated for capacity, including one design with all discussed improvements. This design showed an increase in energy absorption capacity of 267% and 130% for unsymmetrical and symmetrical collisions, respectively. Remarkably, the capacity in the case of an unsymmetrical collision exceeded that of a symmetrical collision. From this, it was concluded that an higher load capacity does not always imply an higher energy absorption capacity.

The generalisation of the used structural design process to an universally applicable structural design process answers the final research question: *"How can the used structural design process be applied to other locks?"*. It was concluded that the design process could be applied to other or new locks, and none of the varying aspects affect the steps to be followed in this process. In conclusion, by following the steps outlined in the universally structural design process, the collision resistance of a lock gate could be determined for any lock.

The main question this thesis addressed is: *"How can the structural design process of lock gates be enhanced by including ship-lock collision impacts?"*. The structural design process was improved based on two components: more accurately determining both the load on a lock gate and the gate's capacity in terms of energy absorption. The load on the lock gate was more accurately determined by better understanding the effect of potential loads occurring at ship-lock collisions using AIS data. Basic mechanics were used to estimate the energy absorption capacity of the lock gate, a method never before applied to lock gates regarding ship-lock collisions. Additionally, design enhancements aimed at increasing energy absorption capacity were identified by refining collision schematisation and using the finite element analysis software RFEM. Conducting the AIS data analyses and applying the method for determining energy absorption capacity in this thesis allowed for an enhanced structural design process of the lock gate concerning ship-lock collisions, thereby answering the main research question and achieving the thesis objective.

9.3. Recommendations

During this thesis, several aspects came to light for which direct information was not available. Additionally, there were instances where assumptions had to be made for certain matters. These limitations have already been discussed in the discussion, from which several recommendations are derived.

Taking into account all collision scenarios. Based on probability and consequences, only a collision of the inner gates when the outer gates are open was considered relevant within the context of flood protection. This

scenario was therefore further elaborated upon in the thesis. However, when designing a lock gate for collision resistance, consideration should also be given to the collision of the outer gates. Additionally, the analysed scenario involves an upstream collision, while it could as well be a downstream collision. So, if flood protection is less relevant, it is recommended to also consider the other collision scenarios.

Coupling AIS data with IVS data. The measured draft of vessels in AIS data can be inaccurate because it needs to be manually entered by the skipper. For the Inland Vessel Tracking and Information System (IVS) data, the draft value is considered more accurate, as it is automatically recorded. Since IVS data does not include information about the velocities vessels have, it is recommended to integrate this type of data with AIS data. This way, the potential collision energy of the vessel can be better approximated.

Implementing failure probability (AIS) data analysis. The results of the AIS data analysis in this thesis are based on the average and maximum occurring velocity and mass. By considering the probability of a collision with a certain velocity and mass, i.e., the statistics of collision energy, the design of the lock gate could be further optimised.

Adding an additional case study. The lock at Macharen is open for most of the year, making it non-operational. This effectively simulates the velocities at which vessels travel during a collision when the skipper expects the lock to be open but it is actually closed. The lock at Macharen closes when the water level exceeds NAP +5.2 m. However, this occurrence is rare, resulting in limited data availability during operational periods. Therefore, it is recommended to seek a similar lock in the Netherlands with approximately the same dimensions. Subsequently, conducting the same (AIS) data analysis will allow for comparison with the analyses conducted in this thesis. The comparison between a non-operational and operational lock in this thesis demonstrates that the differences are not negligible.

Refining mesh size. For the analyses in this thesis, a mesh size of 0.25 m was used. However, even more accurate results can be achieved by using a finer mesh size. The mesh size at which no changes are observed in the results can be determined iteratively. However, this process requires a significant amount of computational time, as do calculations with a smaller mesh size.

Validation of the described method. The described method in Chapter 6 could benefit from further validation. This could be possible if information is available from a real collision between a vessel and a lock gate. It is recommended to conduct this validation if feasible. This would add significant value to the described method and provide stronger support for its validity.

Apply more realistic (ship) load. Since RFEM cannot account for the relation between a vessel's bow and the deformation of an impacted component, there is potential for improvement in this aspect. It is expected that the load will spread more as the vessel penetrates the lock gate. In this case, a better distributed load would result in an higher load capacity.

References

- AASHTO (2009). Vessel collision design of highway bridges. Technical report, American Association of State Highway and Transportation Officials.
- Bahr, R. (2023). Nederlandse binnenvaartschipper vaart duitse sluisdeur aan gort. *Zeilen*.
- Beguïn, J. (2017). Richtlijnen ontwerp kunstwerken rok 1.4. Technical report, Rijkswaterstaat.
- Binnenvaart, B. V. (n.d.). Klassenindeling vaarwegen. <https://bureauvoorlichtingbinnenvaart.nl/de-binnenvaart/basiskennis/vaarwegen/#:~:text=De%20binnenvaart%20is%20in%20Europa,a%20fmetingen%20van%20het%20schip%20vastgelegd>. Accessed: 16-10-2023.
- Buitendijk, M. (2022). Number of shipping accidents on dutch waters in 2021 drops. *SWZ Maritime*.
- Buldgen, L., Le Sourne, H., and Philippe, R. (2012). Simplified analytical method for estimating the resistance of lock gates to ship impacts. *Journal of Applied Mathematics*.
- CBS (2022). Binnenvaart vervoerde nooit zoveel als in 2021. <https://www.cbs.nl/nl-nl/nieuws/2022/10/binnenvaart-vervoerde-nooit-zoveel-als-in-2021>.
- Charles, K. (2017). Lock & dock gates. Technical report, Allianz.
- Dalton, J. (2014). Design of hydraulic steel structures. Technical report, US Army Corps of Engineers.
- Daniel, R. and Paulus, T. (2019). *Lock gates and other closures in hydraulic projects*. Matthew Deans.
- District, L. (2023). Louisville district locks and dams. <https://www.lrl.usace.army.mil/Missions/Civil-Works/Navigation/Locks-and-Dams/>.
- Edmondson, B. (2017). Collision resistance of fibre reinforced polymer lock gates. Master's thesis, Delft University of Technology.
- Eurocode (2012). *NEN-EN 1993-1-5+C1 Eurocode 3: Design of steel structures - Part 1-5: Plated structural elements*. Nederlands Normalisatie-instituut.
- Eurocode (2015). *NEN-EN 1991-1-7+C1+A1 Eurocode 1: Actions on Structures - Part 1-7: General Actions - Accidental Actions*. Nederlands Normalisatie-instituut.
- Eurocode (2016a). *NEN-EN 1993-1-1+C2+A1 Eurocode 3: Design of steel structures - Part 1-1: General rules and rules for buildings*. Nederlands Normalisatie-instituut.
- Eurocode (2016b). *NEN-EN 1993-1-1+C2+A1/NB Eurocode 3: Design of steel structures - Part 1-1: General rules and rules for buildings*. Nederlands Normalisatie-instituut.
- Eurocode (2019). *NEN-EN 1990+A1+A1/C2 Eurocode: Basis of structural design*. Nederlands Normalisatie-instituut.
- Eyres, D. and Bruce, G. (2012). Ship construction (seventh edition). Technical report, Butterworth-Heinemann.
- Gavin, H. (2012). Strain energy in linear elastic solids. Technical report, Duke University Department of Civil and Environmental Engineering.
- Ghosh, S. (2023). Understanding block coefficient of a ship. *Naval Architecture*.
- Goeijenbier, B., van Rinsum, G., and Verheijen, A. (2022). Sluis macharen - aanvaaranalyse. Technical report, Witteveen+Bos.

- Google (n.d.). Google maps location macharen lock. <https://maps.app.goo.gl/L2eY7s2G7FoZdSmX8>. Accessed: 16-10-2023.
- Greimann, L., Stecker, J., and Rens, K. (1993). Condition rating procedures for sector gates. Technical report, Engineering Research Institute Iowa State University.
- Havang (2010). Nijmegen, sluiscomplex weurt, nieuwe sluis, noordzijde gesloten. *Wikipedia*.
- Jassal, R. (2016). Five questions that can help in understanding of squat effect on ships. *MySeaTime*.
- Joustra, N. and Pater, R. (1993). Aanvaarbelasting door schepen op starre constructies. Master's thesis, Delft University of Technology.
- Kaspera, U. (2022). Allision with a lock gate at kiel-haltenau on the kiel canal (nok) by the multi-purpose vessel else on 29 august 2020. Technical report, Federal Bureau of Maritime Casualty Investigation.
- Koedijk, O. (2020). Richtlijnen vaarwegen 2020. Technical report, Rijkswaterstaat Water, Verkeer en Leefomgeving (WVL) Afdeling BNSV.
- Landgraf, J. (1990). Modellmäßige Untersuchung der Widerstandsminderung von Flachwasserschiffen durch Anbringung eines Bugwulstes. Technical report, Zeitschrift für Binnenschifffahrt und Wasserstrassen.
- Liu, J., Hekkenberg, R., and Rotteveel, E. (2014a). A proposal for standard manoeuvres and parameters for the evaluation of inland ship manoeuvrability. Technical report, Delft University of Technology, Department of Ship Design.
- Liu, Y., Zhang, L., Sun, L., and Li, B. (2014b). Numerical study on effects of buffer bulbous bow structure in collisions. Technical report, APCFS/SIF.
- MAN (2018). Basic principles of ship propulsion. Technical report, MAN Energy Solutions.
- MechaniCalc (2024). Mechanical properties of materials. <https://mechanicalc.com/reference/mechanical-properties-of-materials#stress-strain-approx>. Accessed: 17-04-2024.
- Molenaar, W. (2011). *Hydraulic Structures - Locks*. Delft University of Technology.
- Molenaar, W. and Voorendt, M. (2023). *Hydraulic Structures - Locks*. Delft University of Technology.
- NATO (2021). Ais (automatic identification system) overview. [https://shipping.nato.int/nsc/operations/news/2021/ais-automatic-identification-system-overview#:~:text=The%20Automatic%20Identification%20System%20\(AIS,both%20vessels%20and%20shore%20stations](https://shipping.nato.int/nsc/operations/news/2021/ais-automatic-identification-system-overview#:~:text=The%20Automatic%20Identification%20System%20(AIS,both%20vessels%20and%20shore%20stations). Accessed: 12-12-2023.
- n.d. (2023). Haven oss melden en informatie. <https://loket.oss.nl/Loket/product/21dce1a419caca757b58f511e92b06d5>. Accessed: 07-11-2023.
- Papanikolaou, A. (2014). Ship design - methodologies of preliminary design. Technical report, School of Naval Architecture & Marine.
- PIANC (2002). Guidelines for the design of fenders systems. Technical report, International Navigation Association.
- PIANC (2014). Design of lock gates for ship collision. Technical report, The World Association for Waterborne Transport Infrastructure.
- PIANC (2022). Ship dimensions and data for design of marine infrastructure. Technical report, PIANC - The World Association for Waterborne Transport Infrastructure.
- Rijkswaterstaat (2017). Handreiking kwantificering aanvaarrisico. Technical report, Rijkswaterstaat.
- Rijkswaterstaat (2021). Schematiseringshandleiding sterkte en stabiliteit kunstwerk. Technical report, Rijkswaterstaat.

- Roes, M. (2001). *Plastische doorsnedecapaciteit van stalen profielen*. Master's thesis, Eindhoven University of Technology.
- Rotteveel, E., Hekkenberg, R., and Liu, J. (2014). *Design guidelines and empirical evaluation tools for inland ships*. Technical report, European Inland Waterway Navigation Conference.
- Safa, P., Weeks, K., Safa, M., and Zelbst, P. (2019). How digitalization and iot can improve the operations of panama canal. *Journal of Business and Management Sciences*, pages 140–146.
- Schönfeld, D. (2013). *Fatigue of steel lock gates*. Master's thesis, Delft University of Technology.
- van Koningsveld, M., Verheij, H., Taneja, P., and de Vriend, H. (2023). *Ports and Waterways - Navigating the changing world*. Delft University of Technology.
- van Oorschoot, N. (2017). *Deformable and energy absorbing protection against ship collision*. Master's thesis, Delft University of Technology.
- Van Rinsum, G. (2021). *Project meanderende maas, planuitwerking*. Technical report, Witteveen+Bos.
- Watcheye (2023). *Ais systemen*. <https://watcheye.nl/ais-systemen>. Accessed: 12-12-2023.
- Williams, M. (2015). *What is hooke's law?* *Universe Today*.
- Zöllner, J. (1991). *Einfluß der Bug- und Heckform in Koppelverbänden aus schiebendem Gütermotorschiff und Leichter auf den Antriebsleistungsbedarf*. Technical report, Kurzfassung. *Zeitschrift für Binnenschifffahrt* 23.

A

CEMT classes

In Europe, inland shipping is categorised into what are known as CEMT classes to standardise vessel dimensions for waterways in Western Europe. Maximum vessel dimensions are specified for each class. Having knowledge of these classes on board is practical because it allows a skipper to determine which canals are passable for their vessel. In this appendix, the various classes with their corresponding dimensions are provided (Binnenvaart, nd). This information is used to categorise the obtained AIS dataset from Chapter 3 into CEMT classes.

Scheepstypen

Bureau Voorlichting Binnenvaart

Klasse			
I		Spits Lengte 38,5 meter - breedte 5,05 meter - diepgang 2,20 meter - laadvermogen 350 ton	 14 x
II		Kempenaar Lengte 55 meter - breedte 6,60 meter - diepgang 2,59 meter - laadvermogen 655 ton	 26 x
III		Dortmund-Eemkanaalschip (Dortmunder) Lengte 67 meter - breedte 8,20 meter - diepgang 2,50 meter - laadvermogen 1.000 ton	 40 x
IVa		Rijn-Hernekanaalschip (Europaschip) Lengte 85 meter - breedte 9,50 meter - diepgang 2,50 meter - laadvermogen 1.350 ton	 54 x
IVa		Verlengd Rijn-Hernekanaalschip Lengte 105 meter - breedte 9,50 meter - diepgang 3 meter - laadvermogen 1.750 ton	 70 x
Va		Groot Rijnschip Lengte 110 meter - breedte 11,40 meter - diepgang 3,00 meter - laadvermogen 2.750 ton	 110 x
Va		Verlengd Groot Rijnschip Lengte 135 meter - breedte 11,40 meter - diepgang 3,5 meter - laadvermogen 4.000 ton	 160 x
Vb		Tweebaksduwstel Lengte 170 / 190 meter - breedte 11,40 meter - diepgang 4 meter - laadvermogen 3.351 / 7.250 ton	 220 x
Vlb Vlc		Vier- of zesbaksduwstel Lengte 193 meter - breedte 22,80 / 34,20 meter - diepgang 4 meter - laadvermogen 11.000 / 16.500 ton	 440 x /660 x

B

Vessel bow shape

In this appendix, a detailed front-, side- and top view is provided for the structure of an inland navigation vessel with CEMT class III. The side view corresponds to the shape discussed in Section 2.2.2 of the literature study, including dimensions. The top view is relevant for the gate model, where the relation between the deformation of an horizontal girder and the bow shape is considered. These drawings are sourced from the research on collision loads by vessels on rigid structures (Joustra and Pater, 1993).

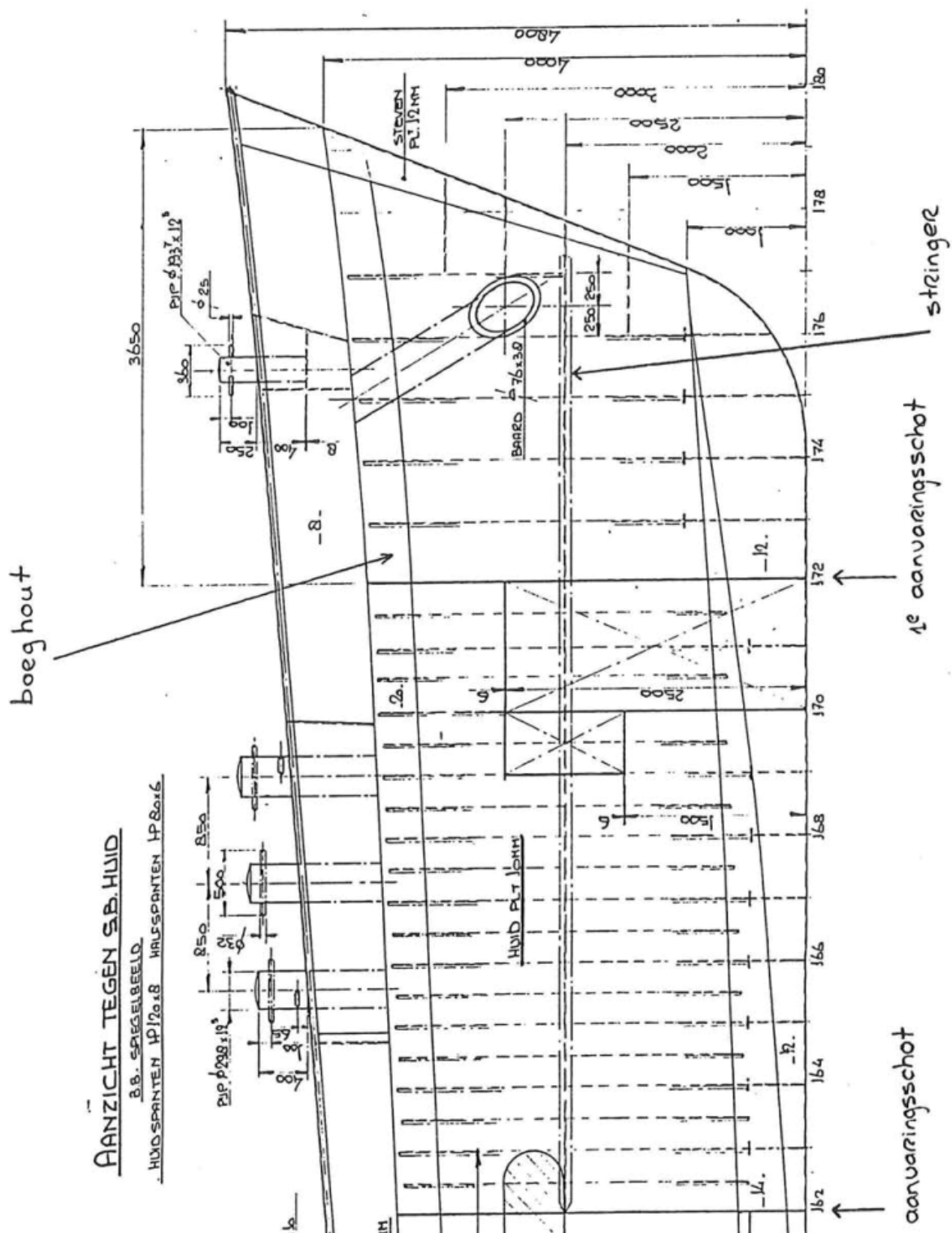


Figure B.2: Side view inland navigation vessel CEMT III (Joustra and Pater, 1993)

C

Graphs & box plots AIS data

In this Appendix, all the additional data analyses that are not included in the report are documented. These primarily include analyses of locations outside the lock chamber and other bar charts + box plots. The data was obtained from Rijkswaterstaat and subsequently analysed using Python. The graphs from Section C.1 are used to compare with the relevant velocities at the inner gate of the lock. The box plots from Section C.2 are used as input for the tables in Chapter 3.

C.1. Velocities per location (South-going traffic)

In this section, all the graphs display mass on the x-axis and velocity on the y-axis. Each graph represents a specific location.

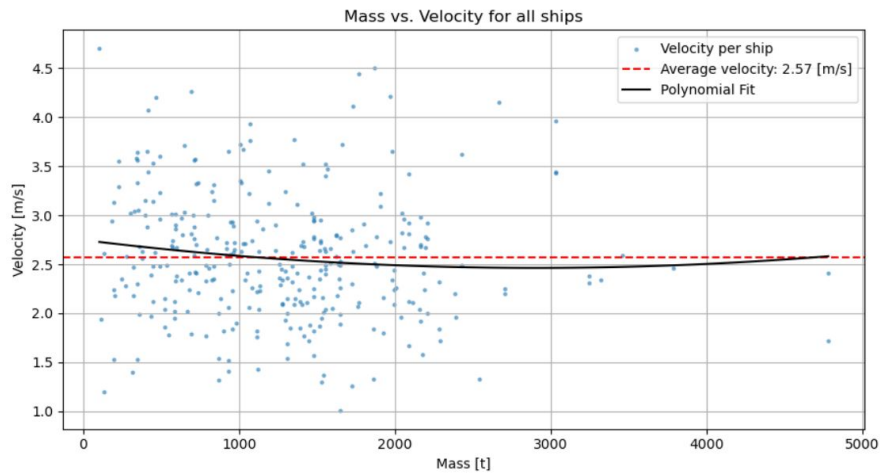


Figure C.1: Mass vs. velocity for all classes including polynomial at location A - 500 [m] upstream of the lock

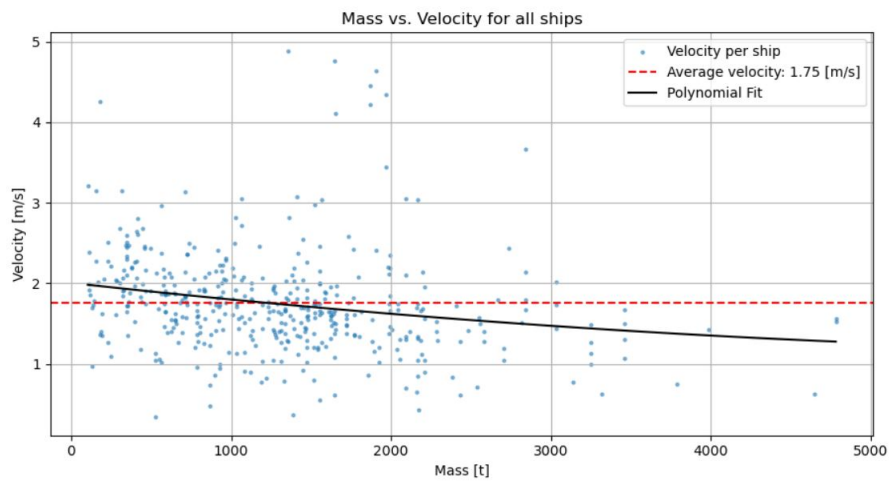


Figure C.2: Mass vs. velocity for all classes including polynomial at location B - at the curve

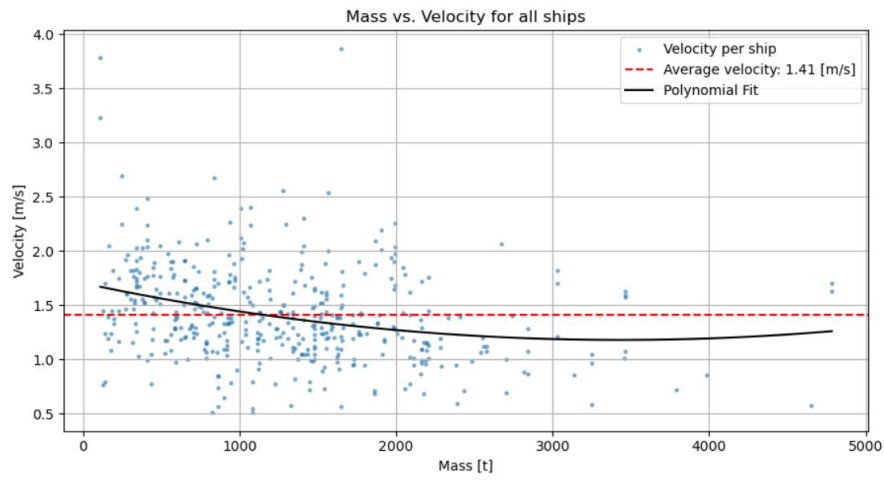


Figure C.3: Mass vs. velocity for all classes including polynomial at location C - 10 [m] upstream of the lock

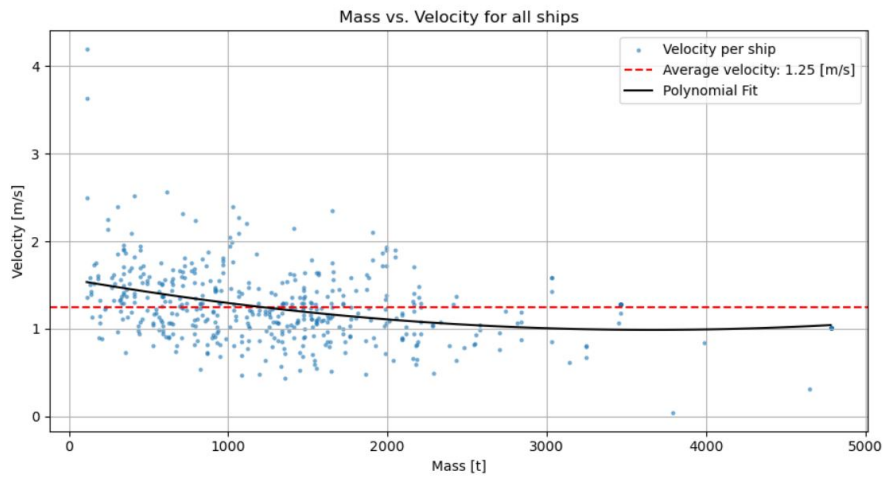


Figure C.4: Mass vs. velocity for all classes including polynomial at location D - in the middle of the lock chamber

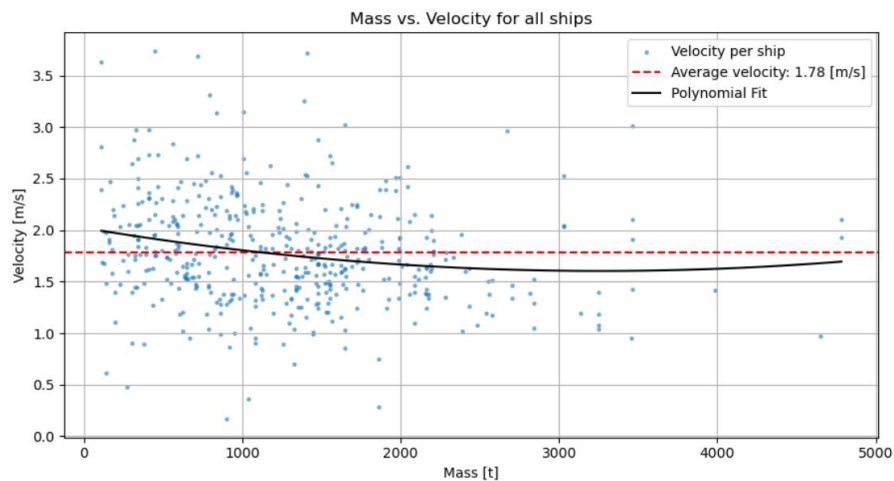


Figure C.5: Mass vs. velocity for all classes including polynomial at location F - 100 [m] downstream of the lock

C.2. Collision energy per standard

In this section all bar charts, including boxplots, of the collision energy per standard are presented. The boxplots provide a better visualisation of the distribution per CEMT class. Outliers are also more clearly visible.

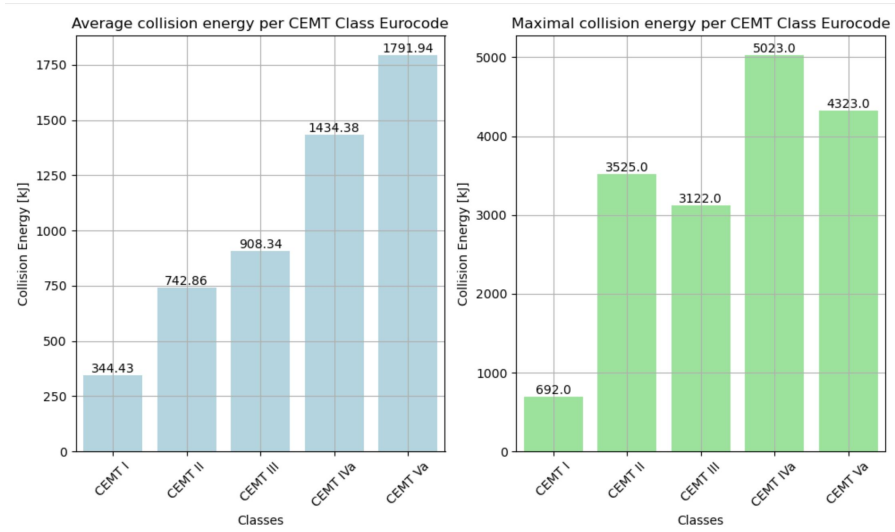


Figure C.6: Average & maximal collision energy based on Eurocode per CEMT class for location E - at the inner gate of the lock

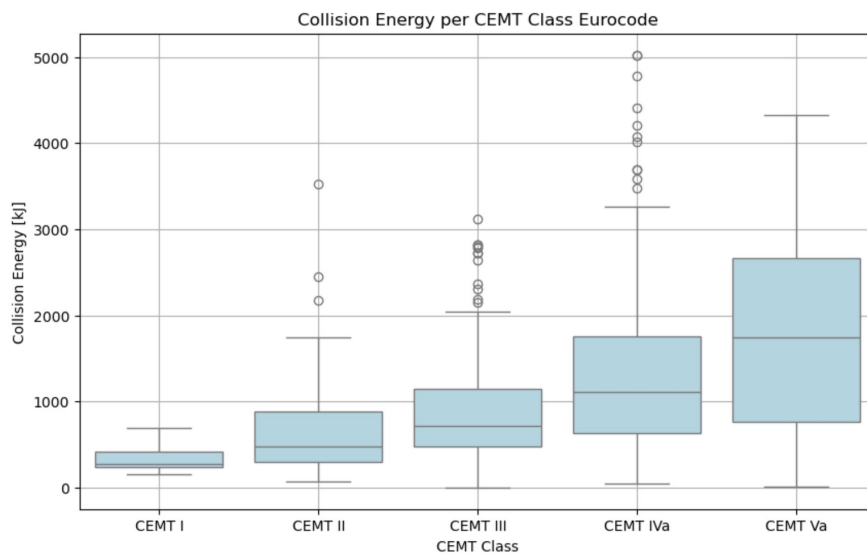


Figure C.7: Boxplot collision energy based on Eurocode per CEMT class for location E - at the inner gate of the lock

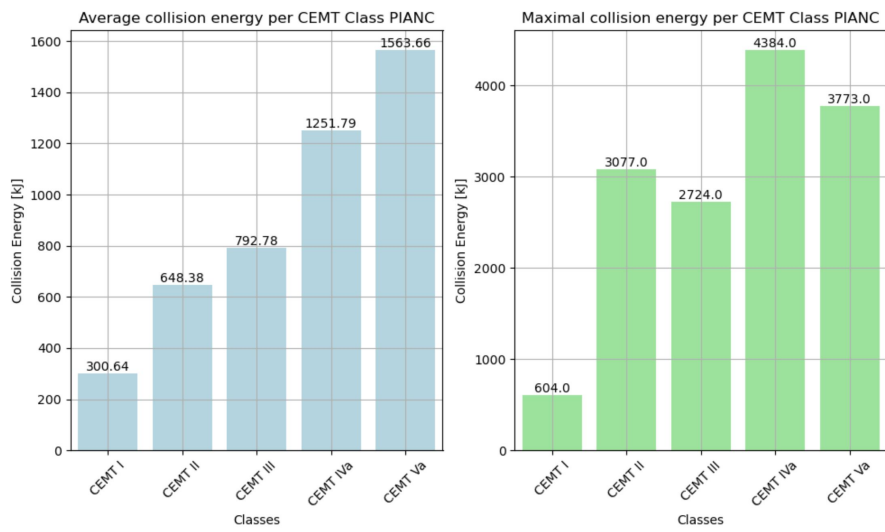


Figure C.8: Average & maximal collision energy based on PIANC per CEMT class for location E - at the inner gate of the lock

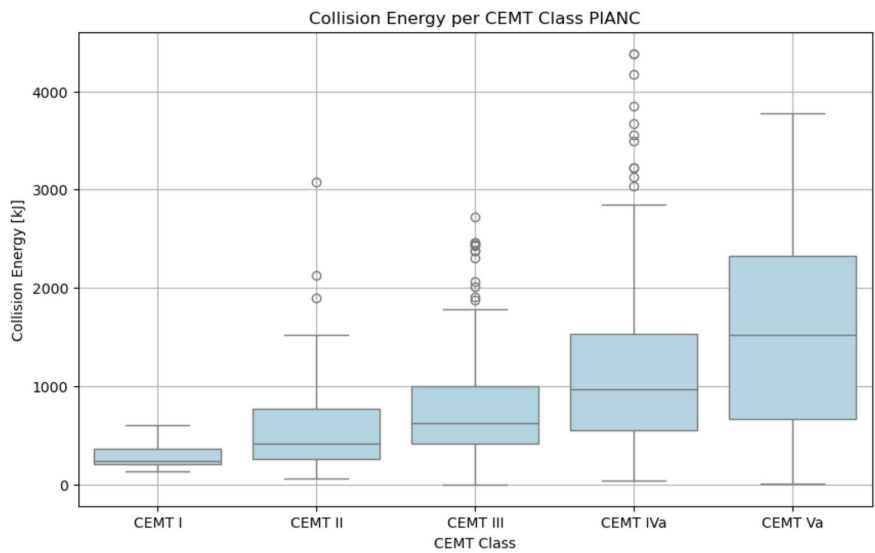


Figure C.9: Boxplot collision energy based on PIANC per CEMT class for location E - at the inner gate of the lock

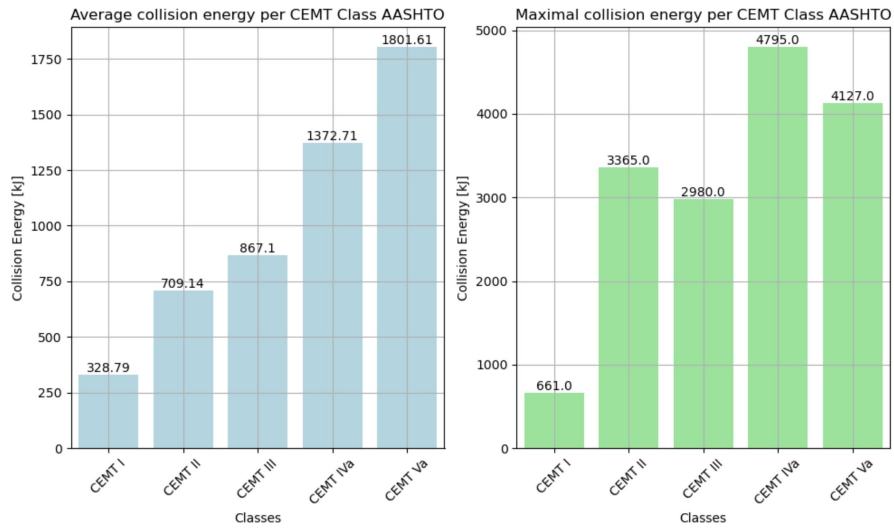


Figure C.10: Average & maximal collision energy based on AASHTO per CEMT class for location E - at the inner gate of the lock

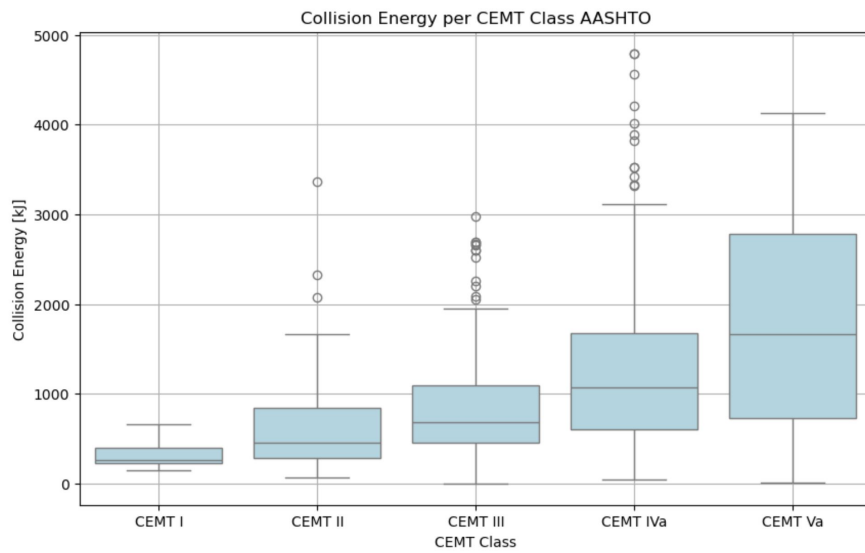


Figure C.11: Boxplot collision energy based on AASHTO per CEMT class for location E - at the inner gate of the lock

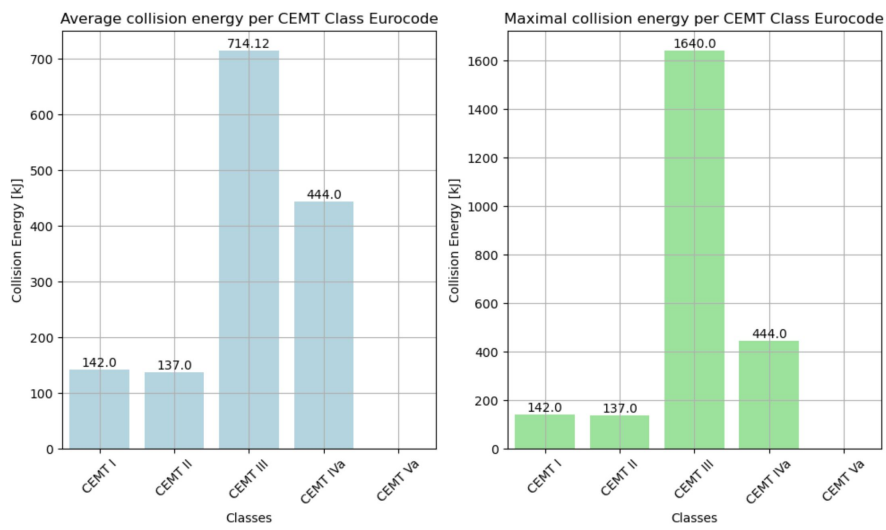


Figure C.12: Average & maximal collision energy based on Eurocode per CEMT class for location E during closing - at the inner gate of the lock

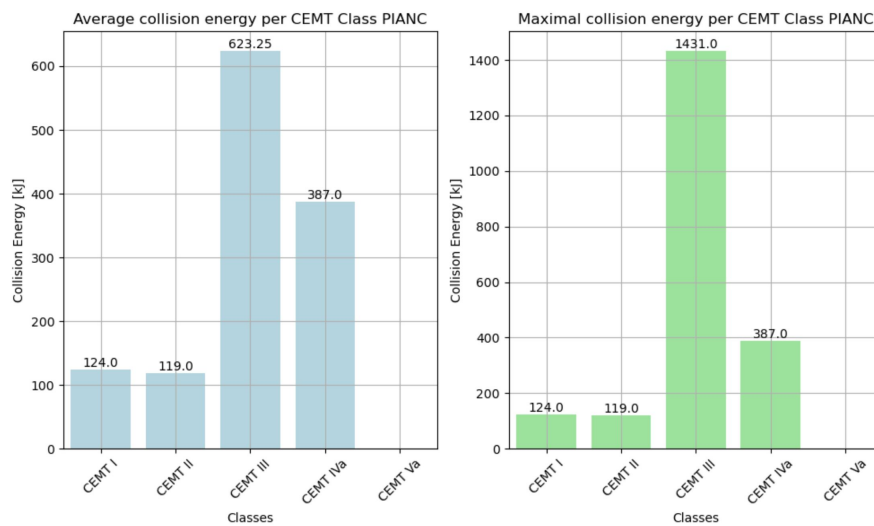


Figure C.13: Average & maximal collision energy based on PIANC per CEMT class for location E during closing - at the inner gate of the lock

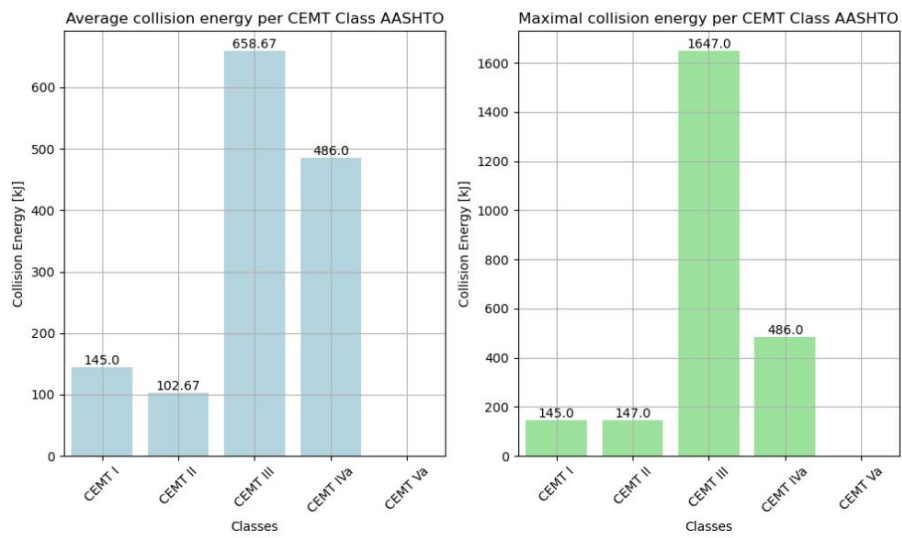


Figure C.14: Average & maximal collision energy based on AASHTO per CEMT class for location E during closing - at the inner gate of the lock

D

Results RFEM sensitivity analysis Macharen lock gate

In this appendix, all the results of the sensitivity analysis on the influence of various components of the lock gate on its capacity are presented. This analysis is conducted in Section 4.3.1 of Chapter 4.

D.1. Load & deformation capacity scenario 1 & 2

Witteveen + Bos
Van Twickelostraat 2, 7400 AE DEVENTER
Tel: +31 5706 9708 0 - Fax: +31 5706 9734 4



Model:
Macharen_Plates_Double_base_FFT

Date 17.2.2024 Page 1/10
Sheet 1

LOADS

1 Loads



Witteveen + Bos
Van Twickelostraat 2, 7400 AE DEVENTER
Tel: +31 5706 9708 0 - Fax: +31 5706 9734 4

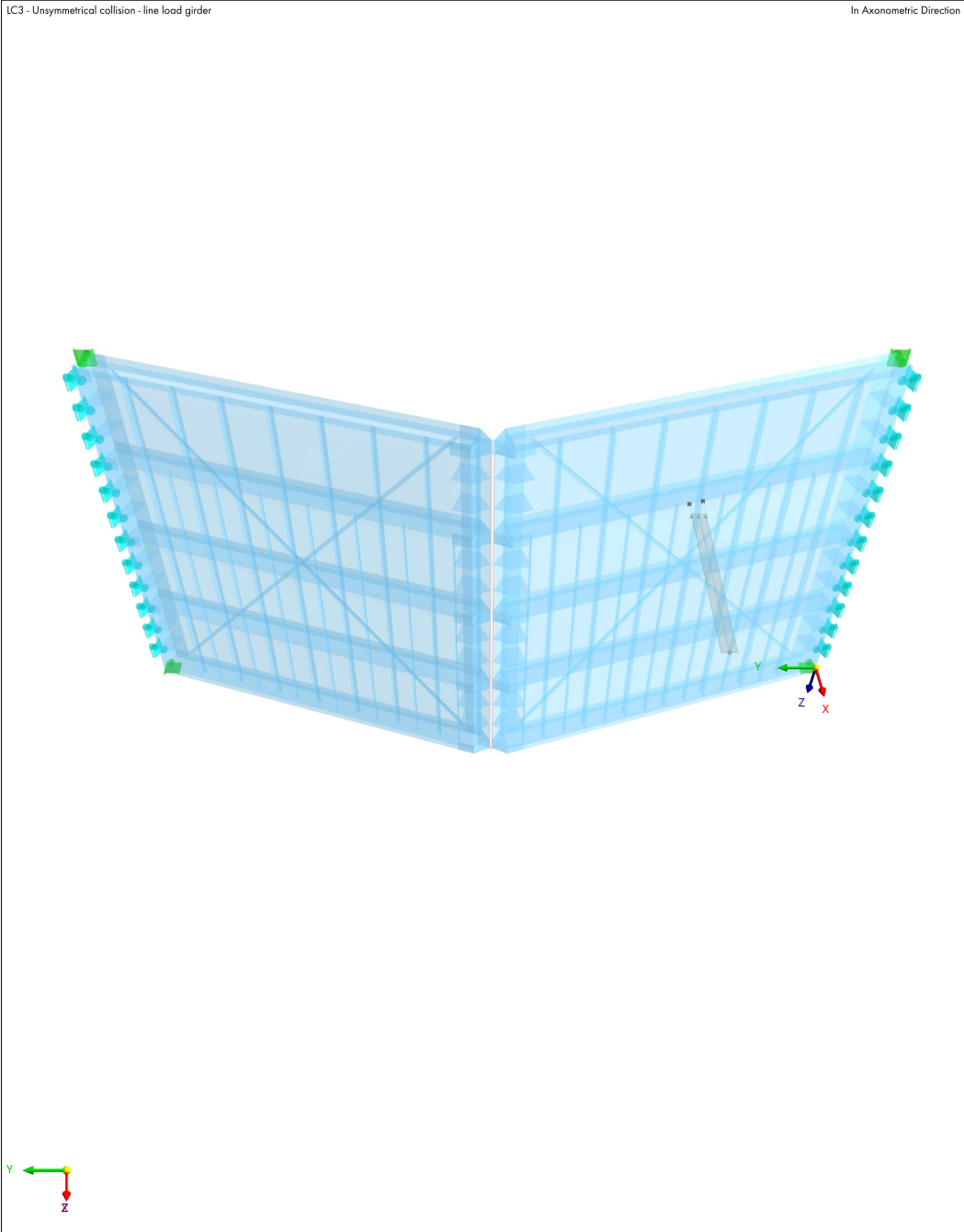


Model:
Macharen_Plates_Double_base_FFT

Date 17.2.2024 Page 2/10
Sheet 1

MODEL

1.1.1 **LC3: LOADING, IN AXONOMETRIC DIRECTION**



Witteveen + Bos
Van Twickelstraat 2, 7400 AE DEVENTER
Tel: +31 5706 9708 0 - Fax: +31 5706 9734 4

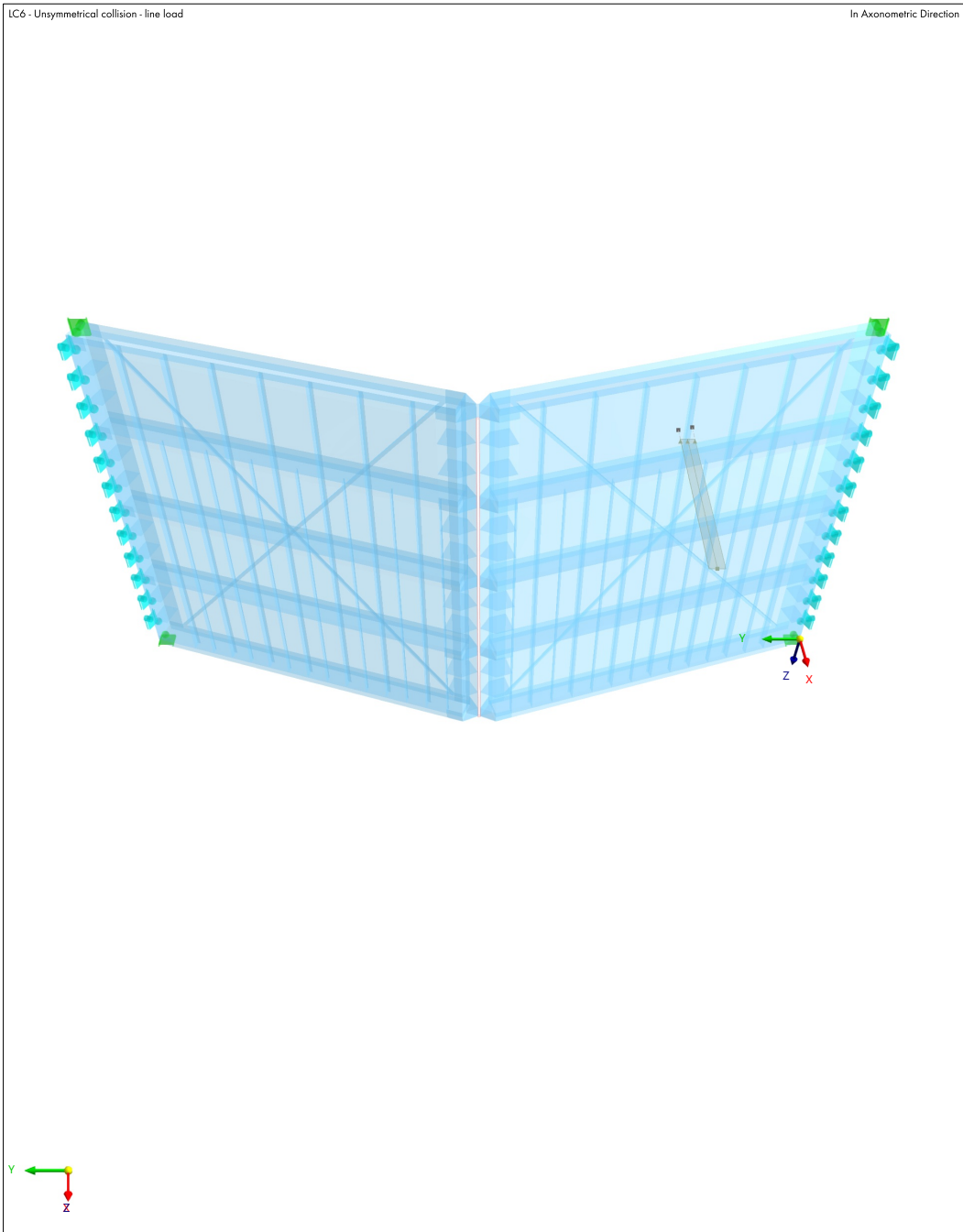


Model:
Macharen_Plates_Double_base_FFT

Date 17.2.2024 Page 3/10
Sheet 1

MODEL

1.2.1 **LC6: LOADING, IN AXONOMETRIC DIRECTION**



Witteveen + Bos
Van Twickelostraat 2, 7400 AE DEVENTER
Tel: +31 5706 9708 0 - Fax: +31 5706 9734 4



Model:
Macharen_Plates_Double_base_FFT

Date 17.2.2024 Page 4/10
Sheet 1

MODEL

2 Static Analysis Results



Witteveen + Bos
 Van Twickelostraat 2, 7400 AE DEVENTER
 Tel: +31 5706 9708 0 - Fax: +31 5706 9734 4



Model:
 Macharen_Plates_Double_base_FFT

Date 17.2.2024 Page 5/10
 Sheet 1

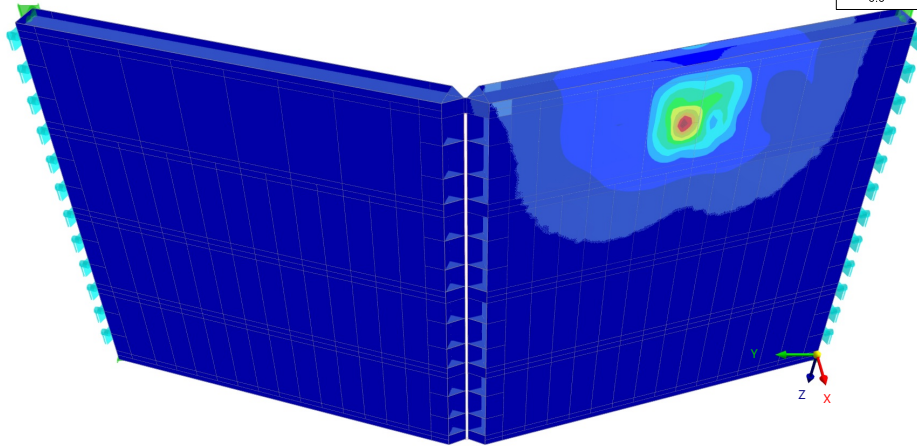
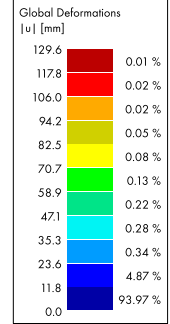
MODEL

2.1 **LC6: GLOBAL DEFORMATIONS |U|, IN AXONOMETRIC DIRECTION**

Static Analysis

LC6 - Unsymmetrical collision - line load
 Static Analysis
 Load Increment No. 50 | Factor: 1.000
 Displacements |u| [mm]

In Axonometric Direction



max |u| : 129.6 | min |u| : 0.0 mm



Witteveen + Bos
 Van Twickelostraat 2, 7400 AE DEVENTER
 Tel: +31 5706 9708 0 - Fax: +31 5706 9734 4



Model:
 Macharen_Plates_Double_base_FFT

Date: 17.2.2024 Page: 6/10
 Sheet: 1

MODEL

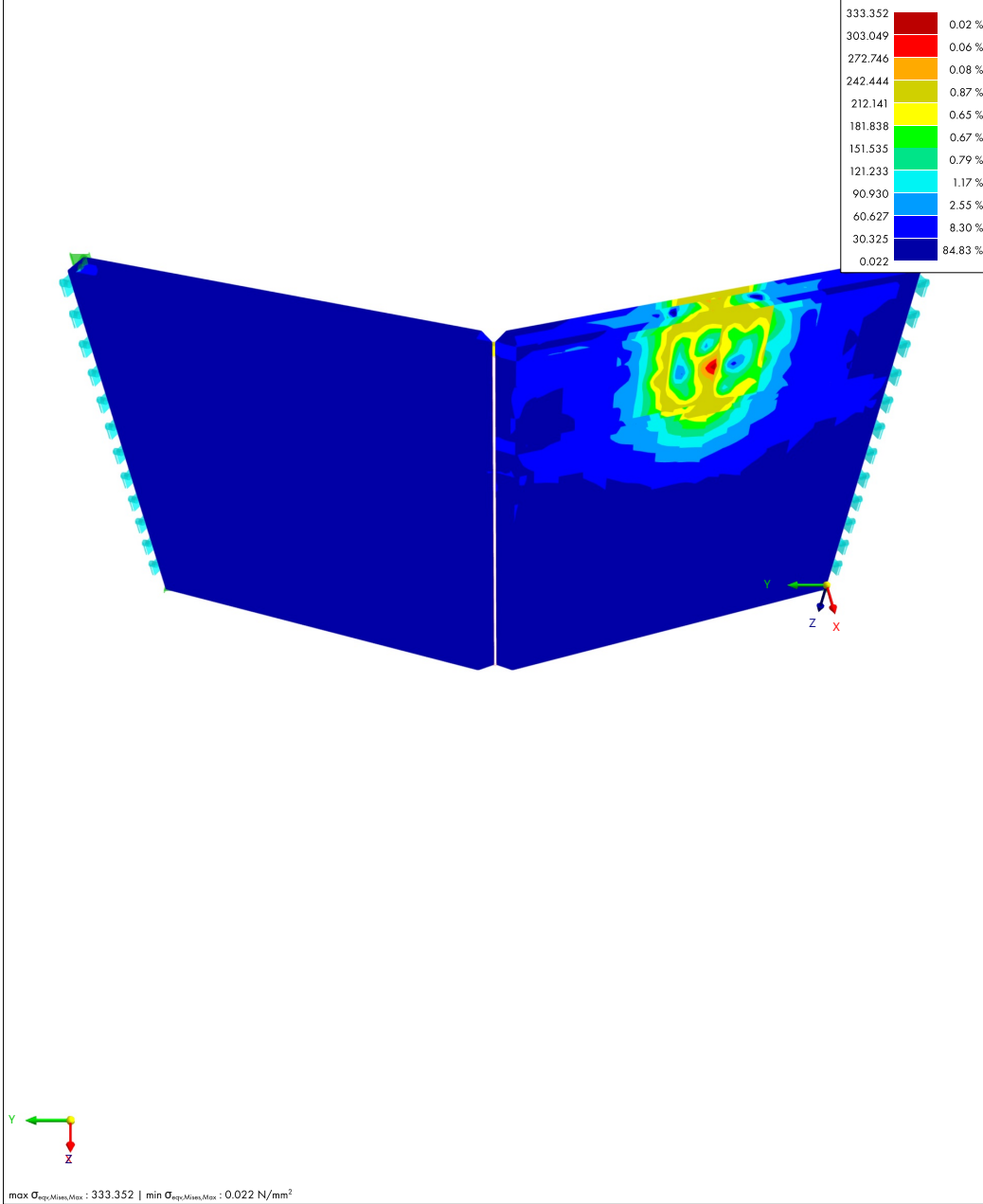
2.2 **LC6: $\sigma_{eqv,Mises}$ $\sigma_{eqv,Mises,Max}$, IN AXONOMETRIC DIRECTION**

Static Analysis

LC6 - Unsymmetrical collision - line load
 Static Analysis
 Load Increment No. 50 | Factor: 1.000
 Equivalent Stresses von Mises $\sigma_{eqv,Mises,Max}$ [N/mm²]

In Axonometric Direction

Surfaces	Stresses	Equivalent Stresses	$\sigma_{eqv,Mises}$
		$\sigma_{eqv,Mises,Max}$	[N/mm ²]
333.352	0.02 %		
303.049	0.06 %		
272.746	0.08 %		
242.444	0.87 %		
212.141	0.65 %		
181.838	0.67 %		
151.535	0.79 %		
121.233	1.17 %		
90.930	2.55 %		
60.627	8.30 %		
30.325	84.83 %		
0.022			



max $\sigma_{eqv,Mises,Max}$: 333.352 | min $\sigma_{eqv,Mises,Max}$: 0.022 N/mm²



Witteveen + Bos
 Van Twickelostraat 2, 7400 AE DEVENTER
 Tel: +31 5706 9708 0 - Fax: +31 5706 9734 4



Model:
 Macharen_Plates_Double_base_FFT

Date: 17.2.2024 Page: 7/10
 Sheet: 1

MODEL

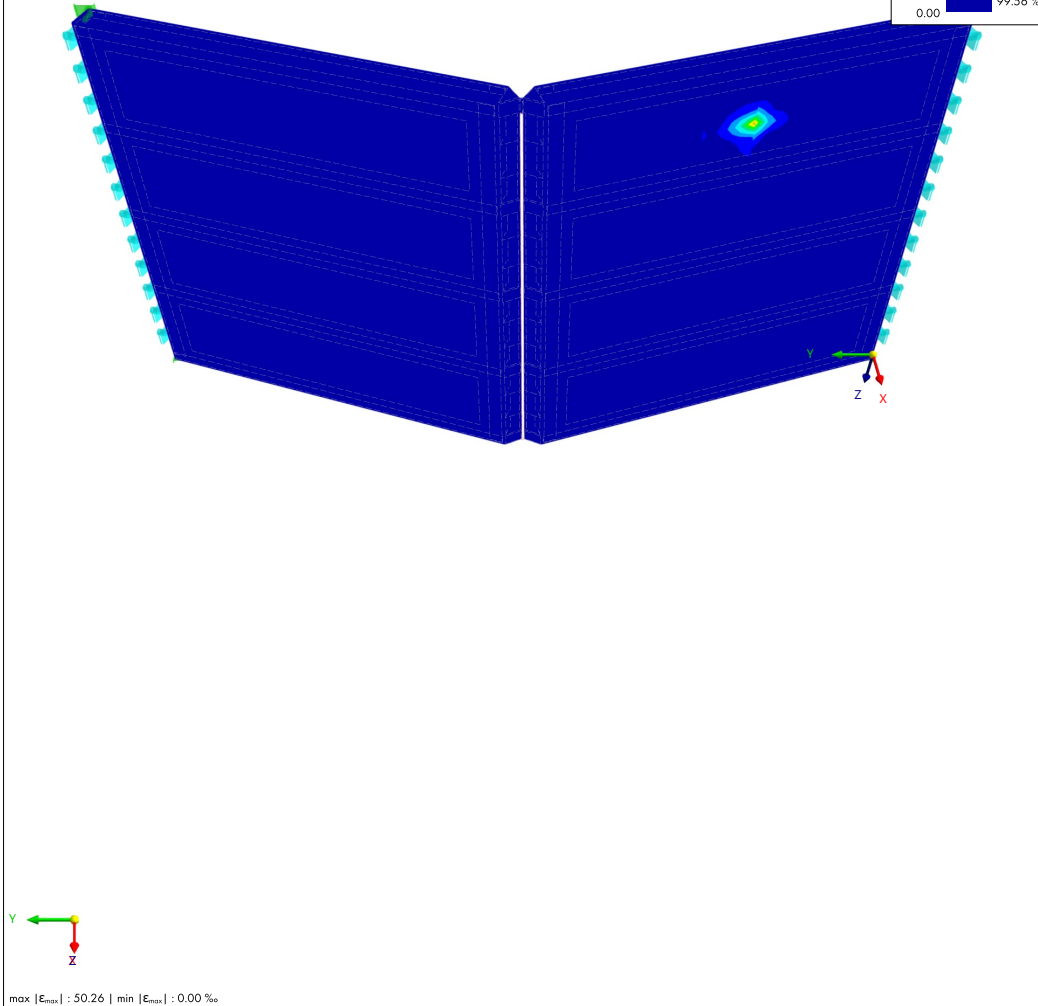
2.3 **LC6: MAXIMUM TOTAL STRAINS $|E_{max}|$, IN AXONOMETRIC DIRECTION**

Static Analysis

LC6 - Unsymmetrical collision - line load
 Static Analysis
 Load Increment No. 50 | Factor: 1.000
 Maximum Strains $|E_{max}|$ [%]

In Axonometric Direction

Surfaces Strains	Maximum Total Strains
$ E_{max} $ [%]	$ E_{max} $ [%]
50.26	0.00 %
45.69	0.00 %
41.12	0.00 %
36.55	0.03 %
31.98	0.02 %
27.41	0.02 %
22.84	0.03 %
18.28	0.05 %
13.71	0.08 %
9.14	0.20 %
4.57	99.56 %
0.00	



Witteveen + Bos
 Van Twickelostraat 2, 7400 AE DEVENTER
 Tel: +31 5706 9708 0 - Fax: +31 5706 9734 4



Model: **Macharen_Plates_Double_base_FFT**

Date: 17.2.2024 Page: 8/10
 Sheet: 1

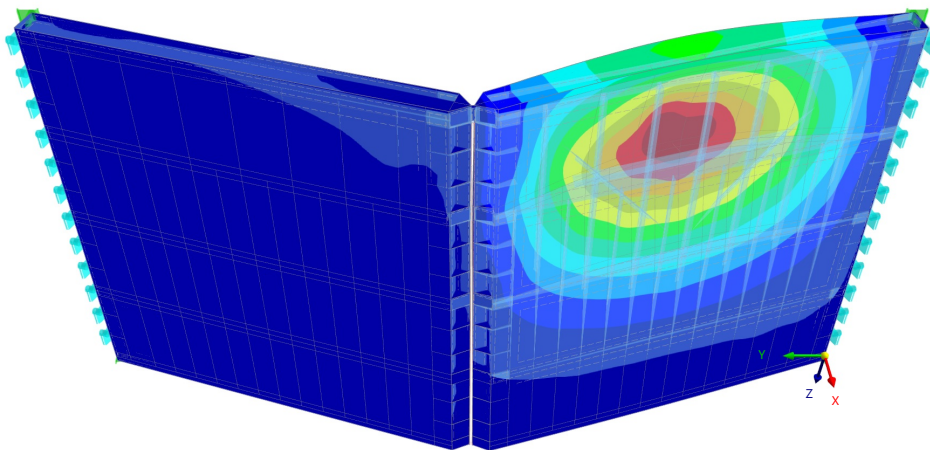
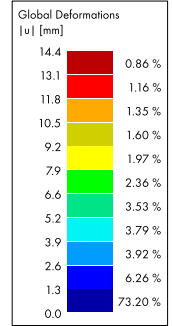
MODEL

2.4 **LC3: GLOBAL DEFORMATIONS |U|, IN AXONOMETRIC DIRECTION**

Static Analysis

LC3 - Unsymmetrical collision - line load girder
 Static Analysis
 Load Increment No. 50 | Factor: 1.000
 Displacements |u| [mm]

In Axonometric Direction



max |u| : 14.4 | min |u| : 0.0 mm



Witteveen + Bos
 Van Twickelostraat 2, 7400 AE DEVENTER
 Tel: +31 5706 9708 0 - Fax: +31 5706 9734 4



Model:
Macharen_Plates_Double_base_FFT

Date: 17.2.2024 Page: 9/10
 Sheet: 1

MODEL

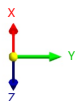
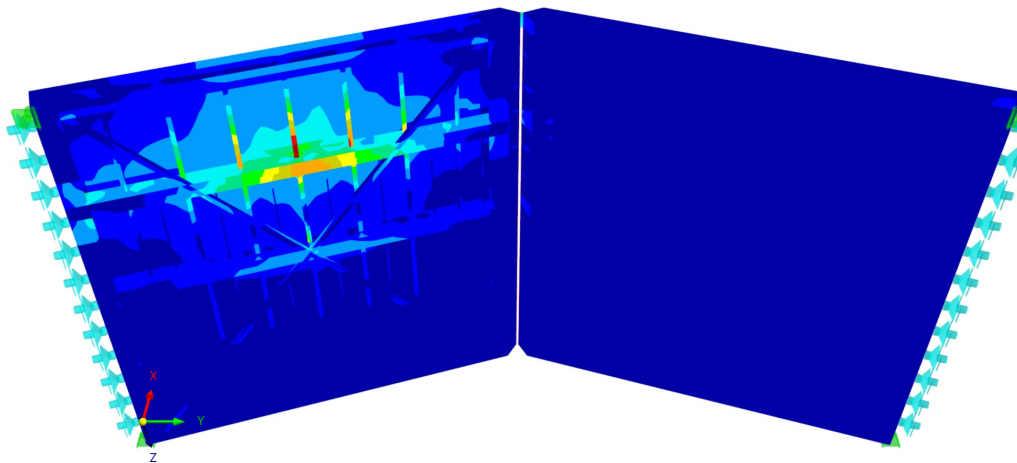
2.5 **LC3: $\sigma_{eqv,Mises}$ $\sigma_{eqv,Mises,Max}$, IN AXONOMETRIC DIRECTION**

Static Analysis

LC3 - Unsymmetrical collision - line load girder
 Static Analysis
 Load Increment No. 50 | Factor: 1.000
 Equivalent Stresses von Mises $\sigma_{eqv,Mises,Max}$ [N/mm²]

In Axonometric Direction

Surfaces	Stresses	Equivalent Stresses	$\sigma_{eqv,Mises}$
		$\sigma_{eqv,Mises,Max}$	[N/mm ²]
235.223		0.01 %	
213.840		0.01 %	
192.458		0.09 %	
171.075		0.09 %	
149.693		0.15 %	
128.310		0.29 %	
106.927		0.56 %	
85.545		1.31 %	
64.162		5.53 %	
42.780		11.99 %	
21.397		79.96 %	
0.015			



max $\sigma_{eqv,Mises,Max}$: 235.223 | min $\sigma_{eqv,Mises,Max}$: -0.015 N/mm²



Witteveen + Bos
 Van Twickelostraat 2, 7400 AE DEVENTER
 Tel: +31 5706 9708 0 - Fax: +31 5706 9734 4



Model:
 Macharen_Plates_Double_base_FFT

Date 17.2.2024 Page 10/10
 Sheet 1

MODEL

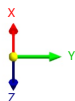
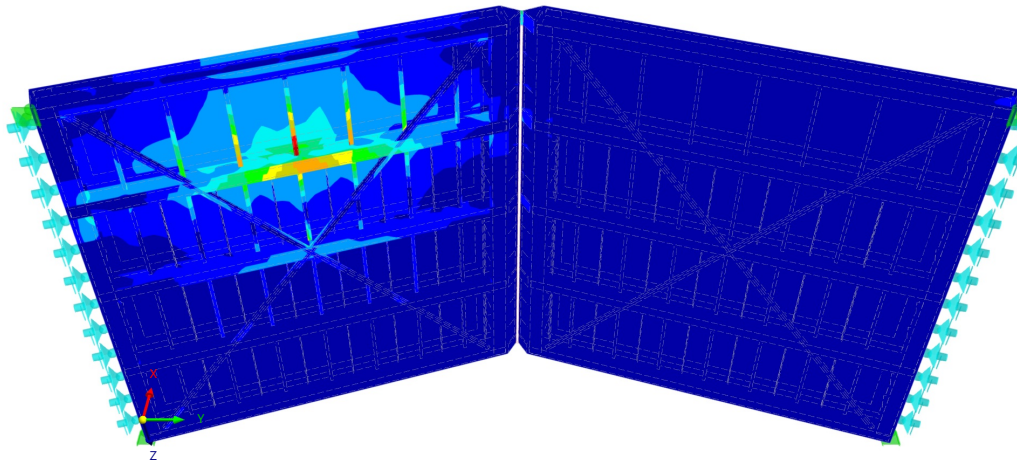
2.6 **LC3: MAXIMUM TOTAL STRAINS $|E_{max}|$, IN AXONOMETRIC DIRECTION**

Static Analysis

LC3 - Unsymmetrical collision - line load girder
 Static Analysis
 Load Increment No. 50 | Factor: 1.000
 Maximum Strains $|E_{max}|$ [%]

In Axonometric Direction

Surfaces Strains Maximum Total Strains $ E_{max} $ [%]	
1.16	0.01 %
1.05	0.01 %
0.95	0.07 %
0.84	0.09 %
0.74	0.12 %
0.63	0.25 %
0.53	0.45 %
0.42	1.11 %
0.32	5.17 %
0.21	11.44 %
0.11	81.27 %
0.00	



max $|E_{max}|$: 1.16 | min $|E_{max}|$: 0.00 ‰



D.2. Load & deformation capacity scenario 3

Witteveen + Bos
Van Twickelostraat 2, 7400 AE DEVENTER
Tel: +31 5706 9708 0 - Fax: +31 5706 9734 4



Model:
Macharen_Plates_Double_base_noskin_FFT

Date 14.2.2024 Page 1/6
Sheet 1

LOADS

1 Loads

RFEM 6.05.0004



Witteveen + Bos
Van Twickelstraat 2, 7400 AE DEVENTER
Tel: +31 5706 9708 0 - Fax: +31 5706 9734 4



Model:
Macharen_Plates_Double_base_noskin_FFT

Date 14.2.2024 Page 2/6
Sheet 1

MODEL

1.1.1 **LC6: LOADING, IN AXONOMETRIC DIRECTION**

LC6 - Unsymmetrical collision - line load

In Axonometric Direction



Witteveen + Bos
Van Twickelostraat 2, 7400 AE DEVENTER
Tel: +31 5706 9708 0 - Fax: +31 5706 9734 4



Model:
Macharen_Plates_Double_base_noskin_FFT

Date 14.2.2024 Page 3/6
Sheet 1

MODEL

2 Incremental Stability Analysis Results

Witteveen + Bos



Witteveen + Bos
 Van Twickelstraat 2, 7400 AE DEVENTER
 Tel: +31 5706 9708 0 - Fax: +31 5706 9734 4



Model:
 Macharen_Plates_Double_base_noskin_FFT

Date 14.2.2024 Page 4/6
 Sheet 1

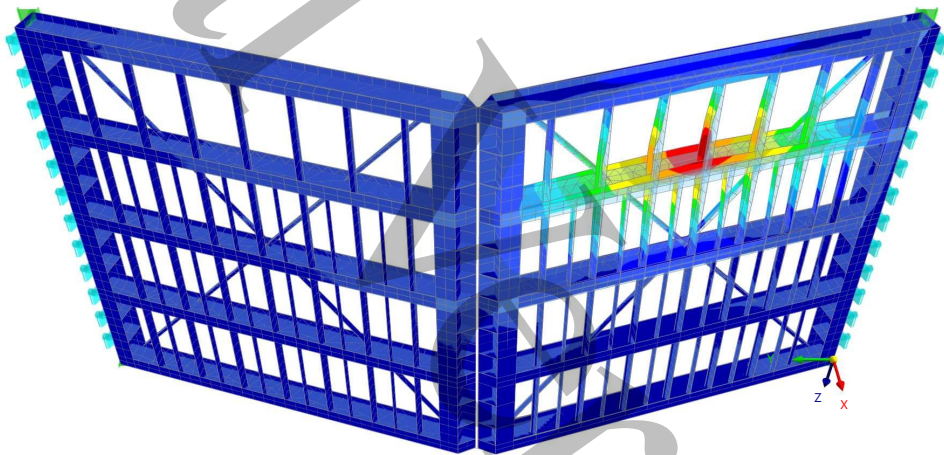
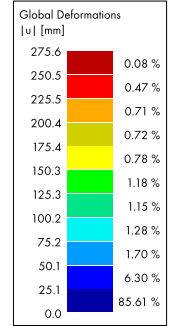
MODEL

2.1 **LC6: GLOBAL DEFORMATIONS |U|, IN AXONOMETRIC DIRECTION**

Incremental Stability Analysis

LC6 - Unsymmetrical collision - line load
 Incremental Stability Analysis
 Load Increment No. 188 | Factor: 5.610
 Displacements |u| [mm]

In Axonometric Direction



max |u| : 275.6 | min |u| : 0.0 mm



Witteveen + Bos
 Van Twickelostraat 2, 7400 AE DEVENTER
 Tel: +31 5706 9708 0 - Fax: +31 5706 9734 4



Model:
 Macharen_Plates_Double_base_noskin_FFT

Date 14.2.2024 Page 5/6
 Sheet 1

MODEL

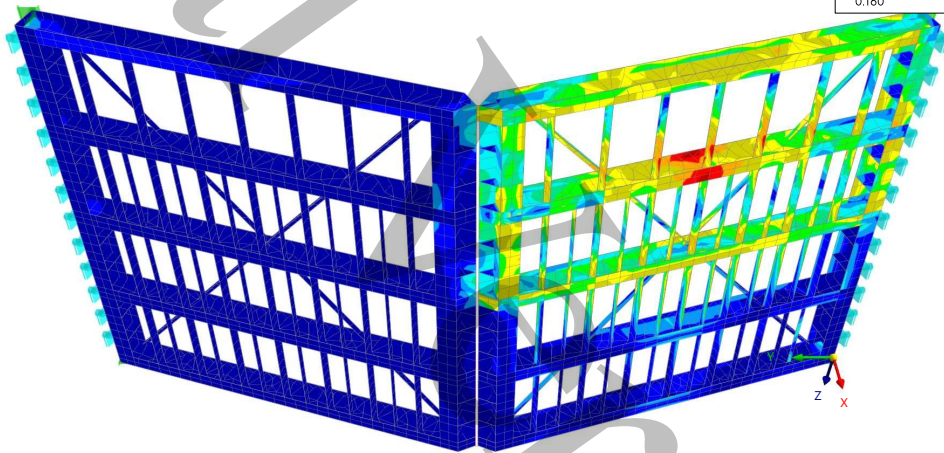
2.2 **LC6: $\sigma_{eqv,Mises}$ $\sigma_{eqv,Mises,Max}$, IN AXONOMETRIC DIRECTION**

Incremental Stability Analysis

LC6 - Unsymmetrical collision - line load
 Incremental Stability Analysis
 Load Increment No. 188 | Factor: 5.610
 Equivalent Stresses von Mises $\sigma_{eqv,Mises,Max}$ [N/mm²]

In Axonometric Direction

Surfaces Stresses Equivalent Stresses	
$\sigma_{eqv,Mises}$	
$\sigma_{eqv,Mises,Max}$ [N/mm ²]	
332.117	0.07 %
301.939	0.23 %
271.762	0.72 %
241.584	4.79 %
211.406	4.47 %
181.228	4.89 %
151.050	5.02 %
120.872	5.41 %
90.694	5.15 %
60.516	9.95 %
30.338	59.30 %
0.160	



max $\sigma_{eqv,Mises,Max}$: 332.117 | min $\sigma_{eqv,Mises,Max}$: 0.160 N/mm²



Witteveen + Bos
 Van Twickelostraat 2, 7400 AE DEVENTER
 Tel: +31 5706 9708 0 - Fax: +31 5706 9734 4



Model:
 Macharen_Plates_Double_base_noskin_FFT

Date 14.2.2024 Page 6/6
 Sheet 1

MODEL

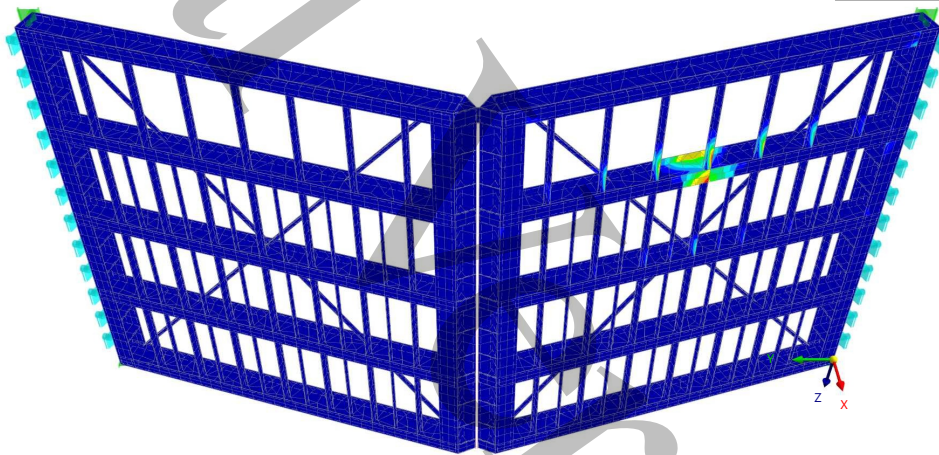
2.3 **LC6: MAXIMUM TOTAL STRAINS $|E_{max}|$, IN AXONOMETRIC DIRECTION**

Incremental Stability Analysis

LC6 - Unsymmetrical collision - line load
 Incremental Stability Analysis
 Load Increment No. 188 | Factor: 5.610
 Maximum Strains $|E_{max}|$ [%]

In Axonometric Direction

Surfaces Strains Maximum Total Strains $ E_{max} $ [%]	
50.17	0.00 %
45.61	0.01 %
41.05	0.02 %
36.49	0.06 %
31.93	0.06 %
27.37	0.09 %
22.81	0.14 %
18.24	0.19 %
13.68	0.29 %
9.12	0.82 %
4.56	98.32 %
0.00	



max $|E_{max}|$: 50.17 | min $|E_{max}|$: 0.00 %



D.3. Load & deformation capacity scenario 4

Witteveen + Bos
Van Twickelostraat 2, 7400 AE DEVENTER
Tel: +31 5706 9708 0 - Fax: +31 5706 9734 4



Model:
Macharen_Plates_Double_noskin_nostrut_nostiff_surfaceload

Date 14.2.2024 Page 1/6
Sheet 1

LOADS

1 Loads



Witteveen + Bos
 Van Twickelostraat 2, 7400 AE DEVENTER
 Tel: +31 5706 9708 0 - Fax: +31 5706 9734 4

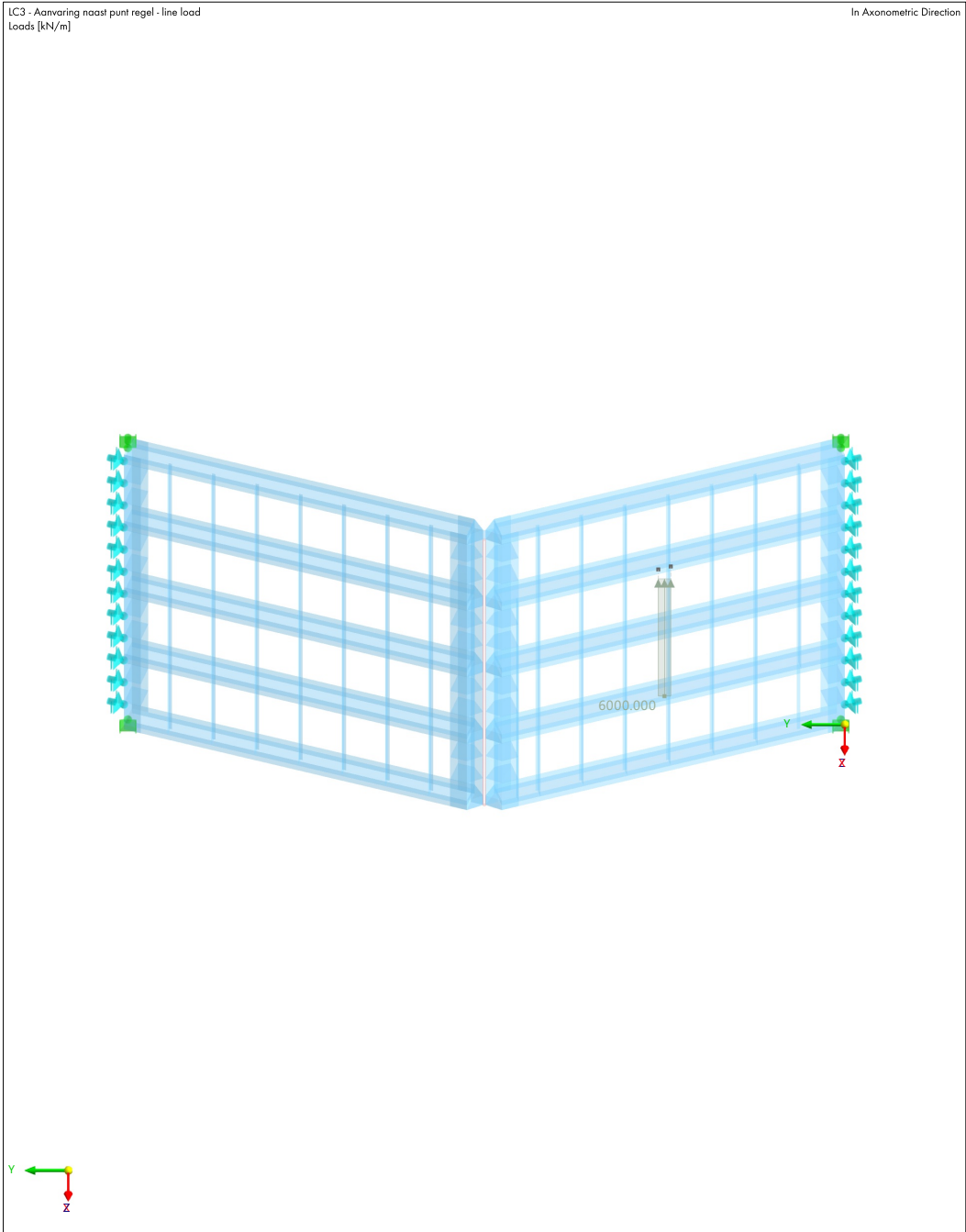


Model:
Macharen_Plates_Double_noskin_nostrut_nostiff_surfaceload

Date 14.2.2024 Page 2/6
 Sheet 1

MODEL

1.1.1 **LC3: LOADING, IN AXONOMETRIC DIRECTION**



Witteveen + Bos
Van Twickelostraat 2, 7400 AE DEVENTER
Tel: +31 5706 9708 0 - Fax: +31 5706 9734 4



Model:
Macharen_Plates_Double_noskin_nostrut_nostiff_surfaceload

Date 14.2.2024 Page 3/6
Sheet 1

MODEL

2 Incremental Stability Analysis Results



Witteveen + Bos
 Van Twickelostraat 2, 7400 AE DEVENTER
 Tel: +31 5706 9708 0 - Fax: +31 5706 9734 4



Model:
Macharen_Plates_Double_noskin_nostrut_nostiff_surfaceload

Date 14.2.2024 Page 4/6
 Sheet 1

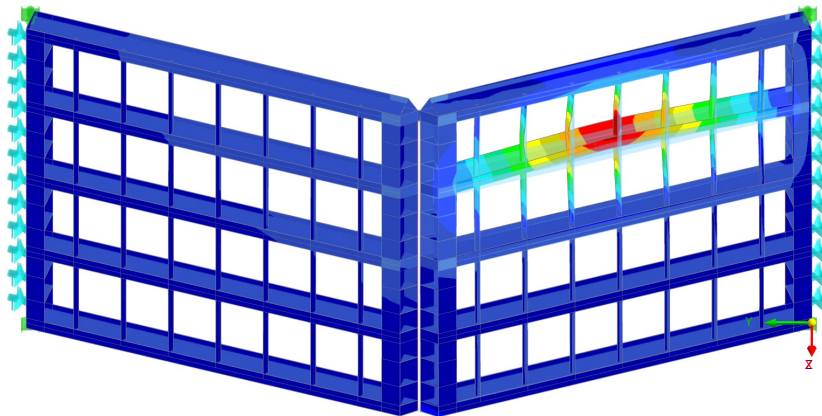
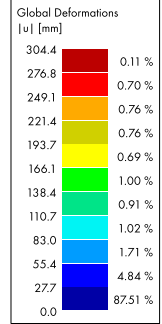
MODEL

2.1 **LC3: GLOBAL DEFORMATIONS |U|, IN AXONOMETRIC DIRECTION**

Incremental Stability Analysis

LC3 - Aanvaring naast punt regel - line load
 Incremental Stability Analysis
 Load Increment No. 200 | Factor: 5.280
 Displacements |u| [mm]

In Axonometric Direction



max |u| : 304.4 | min |u| : 0.0 mm



Witteveen + Bos
 Van Twickelostraat 2, 7400 AE DEVENTER
 Tel: +31 5706 9708 0 - Fax: +31 5706 9734 4



Model:
Macharen_Plates_Double_noskin_nostrut_nostiff_surfaceload

Date 14.2.2024 Page 5/6
 Sheet 1

MODEL

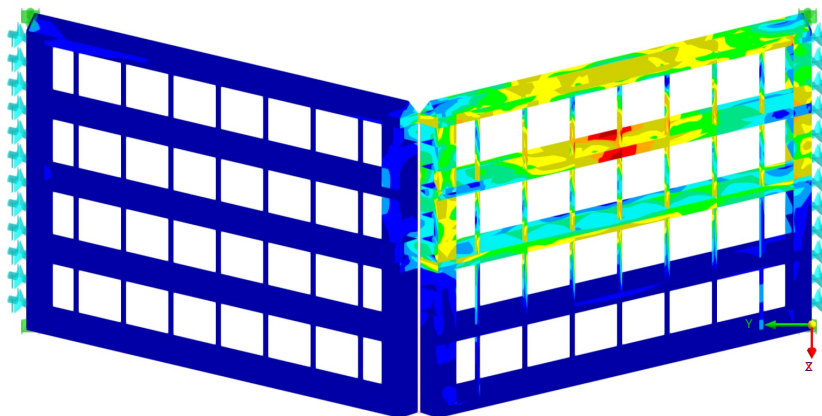
2.2 **LC3: $\sigma_{eqv,Mises}$ $\sigma_{eqv,Mises,Max}$, IN AXONOMETRIC DIRECTION**

Incremental Stability Analysis

LC3 - Aanvaring naast punt regel - line load
 Incremental Stability Analysis
 Load Increment No. 200 | Factor: 5.280
 Equivalent Stresses von Mises $\sigma_{eqv,Mises,Max}$ [N/mm²]

In Axonometric Direction

Surfaces	Stresses	Equivalent Stresses	$\sigma_{eqv,Mises}$
		$\sigma_{eqv,Mises,Max}$	[N/mm ²]
336.784		0.09 %	
306.180		0.25 %	
275.577		0.58 %	
244.973		5.09 %	
214.370		4.58 %	
183.766		4.62 %	
153.162		4.96 %	
122.559		5.43 %	
91.955		4.30 %	
61.352		5.89 %	
30.748		64.22 %	
0.144			



max $\sigma_{eqv,Mises,Max}$: 336.784 | min $\sigma_{eqv,Mises,Max}$: 0.144 N/mm²



Witteveen + Bos
 Van Twickelostraat 2, 7400 AE DEVENTER
 Tel: +31 5706 9708 0 - Fax: +31 5706 9734 4



Model:
 Macharen_Plates_Double_noskin_nostrut_nostiff_surfaceload

Date 14.2.2024 Page 6/6
 Sheet 1

MODEL

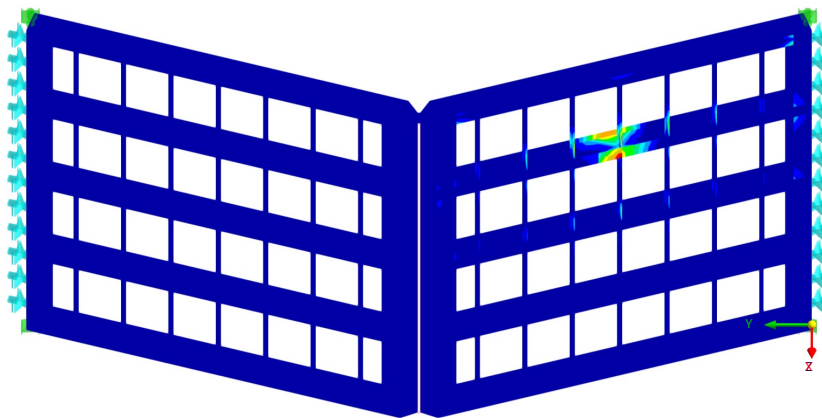
2.3 **LC3: MAXIMUM TOTAL STRAINS $|E_{max}|$, IN AXONOMETRIC DIRECTION**

Incremental Stability Analysis

LC3 - Aanvaring naast punt regel - line load
 Incremental Stability Analysis
 Load Increment No. 200 | Factor: 5.280
 Maximum Strains $|E_{max}|$ [%]

In Axonometric Direction

Surfaces Strains Maximum Total Strains $ E_{max} $ [%]	
49.78	0.00 %
45.26	0.02 %
40.73	0.06 %
36.21	0.05 %
31.68	0.08 %
27.15	0.13 %
22.63	0.14 %
18.10	0.19 %
13.58	0.36 %
9.05	1.33 %
4.53	97.64 %
0.00	



max $|E_{max}|$: 49.78 | min $|E_{max}|$: 0.00 %



E

Results RFEM gate model validation

This appendix includes the results supporting the validation with the analytical model. First, the lock gate is validated for strength using geometrically linear analysis. This analysis assumes a situation of pure bending. When nonlinear analysis is performed with RFEM, deformations of the horizontal girder are considered as well. At a certain point, the girder collapses due to lateral torsional buckling. This moment is validated through a large deformations analysis, where the geometry and stiffness of the profile play a crucial role.

E.1. Simplified gate model RFEM results

Witteveen + Bos
Van Twickelstraat 2, 7400 AE DEVENTER
Tel: +31 5706 9708 0 - Fax: +31 5706 9734 4



Model:
Macharen_Validation

Date 7.3.2024 Page 1/11
Sheet 1

LOADS

1 Loads



Witteveen + Bos
 Van Twickelostraat 2, 7400 AE DEVENTER
 Tel: +31 5706 9708 0 - Fax: +31 5706 9734 4

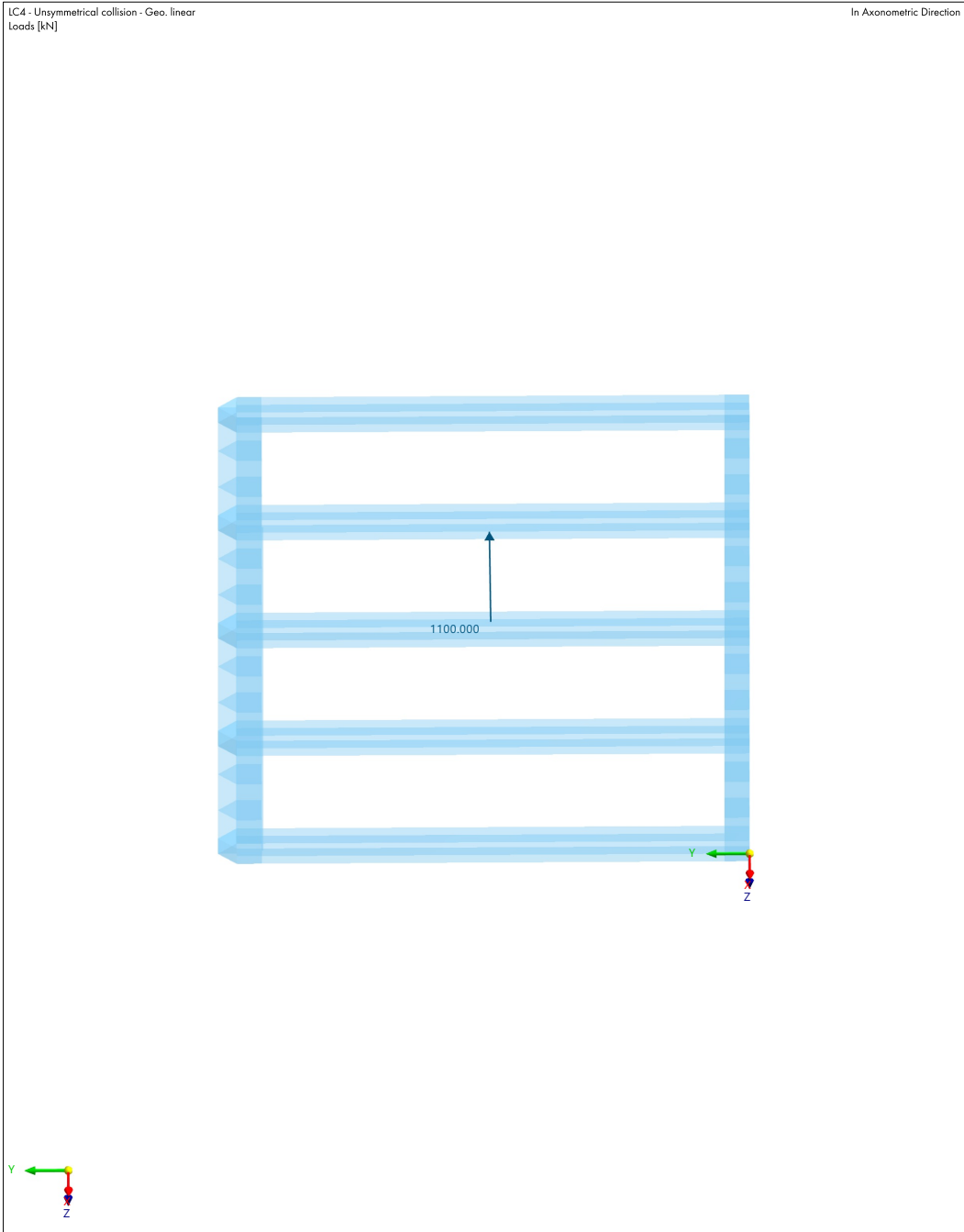


Model:
Macharen_Validation

Date: 7.3.2024 Page: 2/11
 Sheet: 1

MODEL

1.1.1 **LC4: LOADING, IN AXONOMETRIC DIRECTION**



Witteveen + Bos
Van Twickelstraat 2, 7400 AE DEVENTER
Tel: +31 5706 9708 0 - Fax: +31 5706 9734 4



Model:
Macharen_Validation

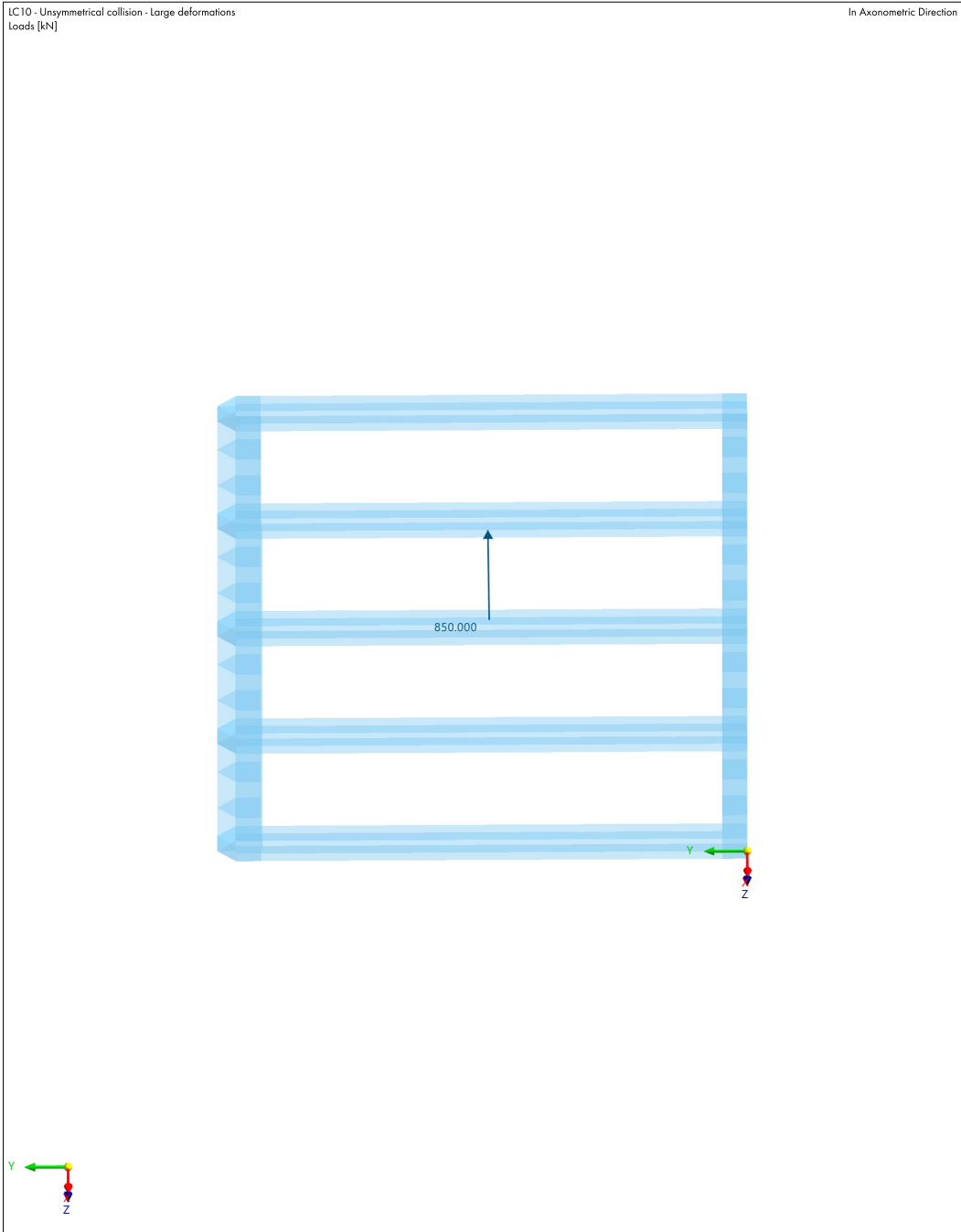
Date 7.3.2024 Page 3/11
Sheet 1

MODEL

1.2.1 **LC10: LOADING, IN AXONOMETRIC DIRECTION**

LC10 - Unsymmetrical collision - Large deformations
Loads [kN]

In Axonometric Direction



Witteveen + Bos
Van Twickelstraat 2, 7400 AE DEVENTER
Tel: +31 5706 9708 0 - Fax: +31 5706 9734 4



Model:
Macharen_Validation

Date 7.3.2024 Page 4/11
Sheet 1

MODEL

2 Static Analysis Results



Witteveen + Bos
 Van Twickelostraat 2, 7400 AE DEVENTER
 Tel: +31 5706 9708 0 - Fax: +31 5706 9734 4



Model:
Macharen_Validation

Date: 7.3.2024 Page: 5/11
 Sheet: 1

MODEL

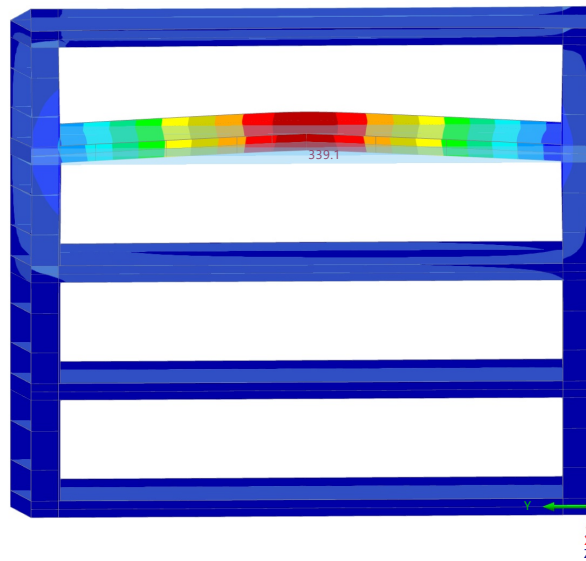
2.1 **LC4: GLOBAL DEFORMATIONS |U|, IN AXONOMETRIC DIRECTION**

Static Analysis

LC4 - Unsymmetrical collision - Geo. linear
 Static Analysis
 Load Increment No. 47 | Factor: 0.940
 Displacements |u| [mm]

In Axonometric Direction

Global Deformations u [mm]	
339.1	1.32 %
308.2	1.23 %
277.4	1.12 %
246.6	1.09 %
215.8	1.08 %
184.9	1.07 %
154.1	1.06 %
123.3	1.06 %
92.5	1.09 %
61.6	3.82 %
30.8	86.06 %
0.0	



Y
 Z
 max |u| : 339.1 | min |u| : 0.0 mm



Witteveen + Bos
 Van Twickelostraat 2, 7400 AE DEVENTER
 Tel: +31 5706 9708 0 - Fax: +31 5706 9734 4



Model:
Macharen_Validation

Date: 7.3.2024 Page: 6/11
 Sheet: 1

MODEL

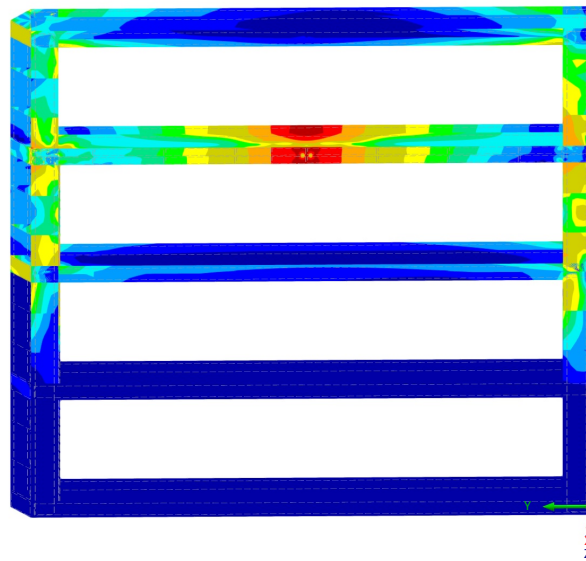
2.2 **LC4: $\sigma_{eqv,Mises}$ $\sigma_{eqv,Mises,Max}$, IN AXONOMETRIC DIRECTION**

Static Analysis

LC4 - Unsymmetrical collision - Geo. linear
 Static Analysis
 Load Increment No. 47 | Factor: 0.940
 Equivalent Stresses von Mises $\sigma_{eqv,Mises,Max}$ [N/mm²]

In Axonometric Direction

Surfaces	Stresses	Equivalent Stresses	$\sigma_{eqv,Mises}$
		$\sigma_{eqv,Mises,Max}$	[N/mm ²]
337.650	0.34 %		
306.966	0.71 %		
276.281	1.49 %		
245.596	5.78 %		
214.911	4.33 %		
184.226	5.91 %		
153.541	6.04 %		
122.856	7.77 %		
92.172	11.73 %		
61.487	12.97 %		
30.802	42.93 %		
0.117			



max $\sigma_{eqv,Mises,Max}$: 337.650 | min $\sigma_{eqv,Mises,Max}$: 0.117 N/mm²



Witteveen + Bos
 Van Twickelostraat 2, 7400 AE DEVENTER
 Tel: +31 5706 9708 0 - Fax: +31 5706 9734 4



Model:
 Macharen_Validation

Date: 7.3.2024 Page: 7/11
 Sheet: 1

MODEL

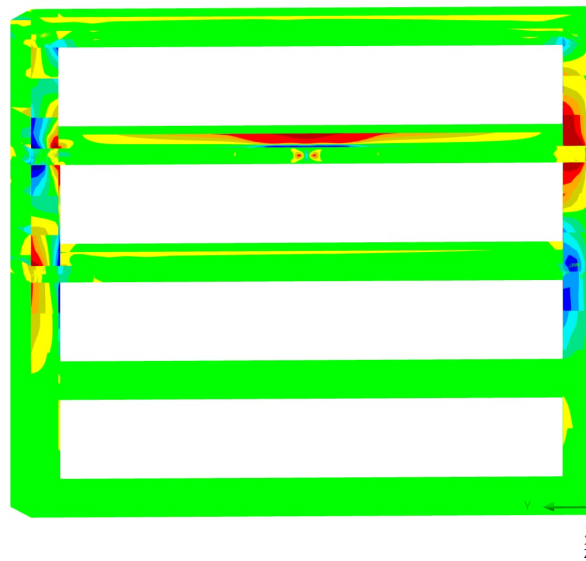
2.3 **LC4: BASIC STRESSES $\sigma_{y,z}$ IN AXONOMETRIC DIRECTION**

Static Analysis

LC4 - Unsymmetrical collision - Geo. linear
 Static Analysis
 Load Increment No. 47 | Factor: 0.940
 Axial Stresses $\sigma_{y,z}$ [N/mm²]

In Axonometric Direction

Surfaces	Stresses	Basic Stresses
318.820		0.41 %
258.627		1.33 %
198.434		1.37 %
138.240		2.34 %
78.047		8.87 %
17.854		76.43 %
-42.339		4.80 %
-102.533		1.97 %
-162.726		1.29 %
-222.919		1.06 %
-283.112		
-343.306		0.13 %



max $\sigma_{y,z}$: 318.820 | min $\sigma_{y,z}$: -343.306 N/mm²



Witteveen + Bos
Van Twickelstraat 2, 7400 AE DEVENTER
Tel: +31 5706 9708 0 - Fax: +31 5706 9734 4



Model:
Macharen_Validation

Date 7.3.2024 Page 8/11
Sheet 1

MODEL

3 Incremental Stability Analysis Results



Witteveen + Bos
 Van Twickelostraat 2, 7400 AE DEVENTER
 Tel: +31 5706 9708 0 - Fax: +31 5706 9734 4



Model:
Macharen_Validation

Date: 7.3.2024 Page: 9/11
 Sheet: 1

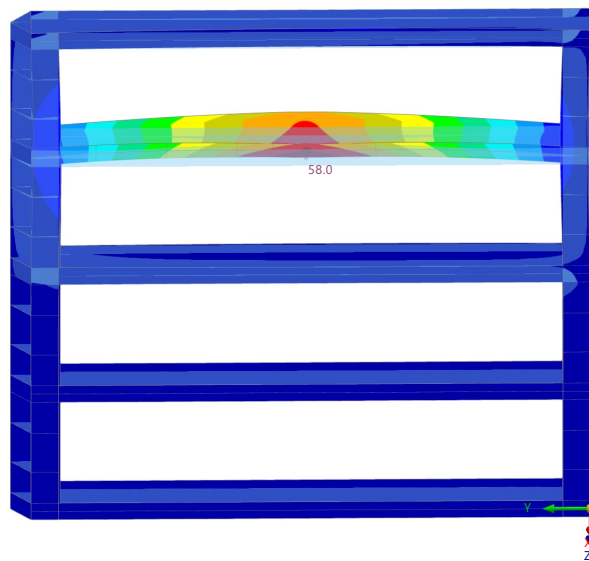
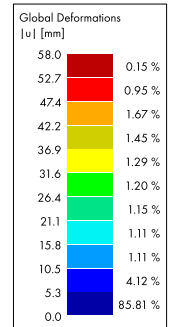
MODEL

3.1 **LC10: GLOBAL DEFORMATIONS |U|, IN AXONOMETRIC DIRECTION**

Incremental Stability Analysis

LC10 - Unsymmetrical collision - Large deformations
 Incremental Stability Analysis
 Load Increment No. 15 | Factor: 0.755
 Displacements |u| [mm]

In Axonometric Direction



max |u| : 58.0 | min |u| : 0.0 mm



Witteveen + Bos
 Van Twickelostraat 2, 7400 AE DEVENTER
 Tel: +31 5706 9708 0 - Fax: +31 5706 9734 4



Model:
 Macharen_Validation

Date: 7.3.2024 Page: 10/11
 Sheet: 1

MODEL

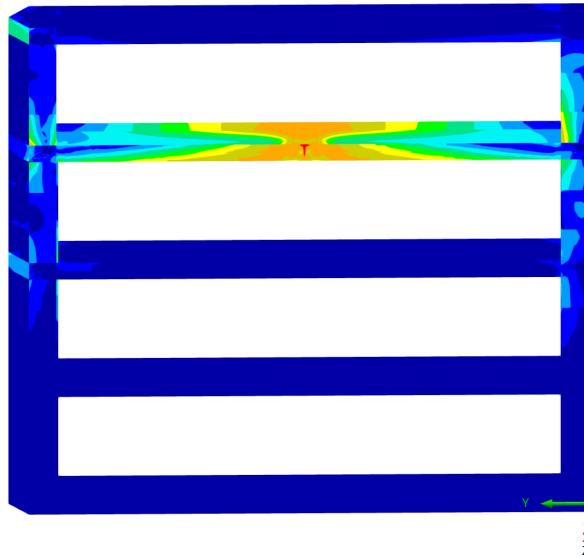
3.2 **LC10: $\sigma_{eqv,Mises}$ $\sigma_{eqv,Mises,Max}$ IN AXONOMETRIC DIRECTION**

Incremental Stability Analysis

LC10 - Unsymmetrical collision - Large deformations
 Incremental Stability Analysis
 Load Increment No. 15 | Factor: 0.755
 Equivalent Stresses von Mises $\sigma_{eqv,Mises,Max}$ [N/mm²]

In Axonometric Direction

Surfaces	Stresses	Equivalent Stresses	$\sigma_{eqv,Mises}$
		$\sigma_{eqv,Mises,Max}$	[N/mm ²]
319.494	0.00 %		
290.451	0.03 %		
261.408	1.28 %		
232.365	1.13 %		
203.321	1.08 %		
174.278	1.39 %		
145.235	2.49 %		
116.192	3.66 %		
87.149	5.50 %		
58.106	12.66 %		
29.062	70.78 %		
0.019			



max $\sigma_{eqv,Mises,Max}$: 319.494 | min $\sigma_{eqv,Mises,Max}$: 0.019 N/mm²



Witteveen + Bos
 Van Twickelostraat 2, 7400 AE DEVENTER
 Tel: +31 5706 9708 0 - Fax: +31 5706 9734 4



Model:
 Macharen_Validation

Date 7.3.2024 Page 11/11
 Sheet 1

MODEL

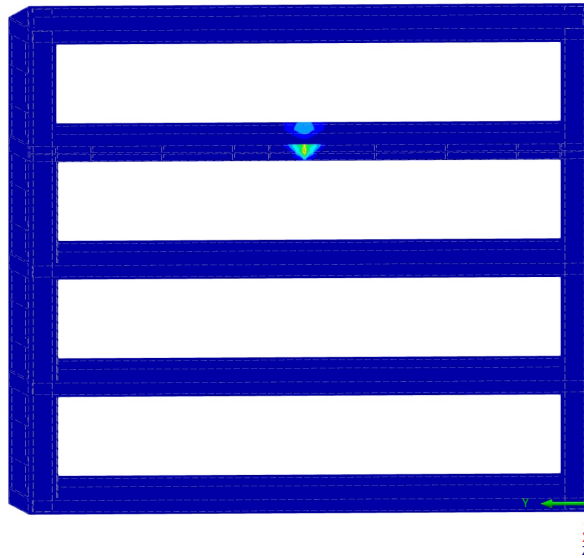
3.3 **LC10: MAXIMUM TOTAL STRAINS $|\epsilon_{max}|$, IN AXONOMETRIC DIRECTION**

Incremental Stability Analysis

LC10 - Unsymmetrical collision - Large deformations
 Incremental Stability Analysis
 Load Increment No. 15 | Factor: 0.755
 Maximum Strains $|\epsilon_{max}|$ [%]

In Axonometric Direction

Surfaces Strains Maximum Total Strains $ \epsilon_{max} $ [%]		
31.15		0.00 %
28.32		0.00 %
25.49		0.00 %
22.66		0.01 %
19.82		0.01 %
16.99		0.02 %
14.16		0.03 %
11.33		0.04 %
8.50		0.17 %
5.66		0.28 %
2.83		99.45 %
0.00		



max $|\epsilon_{max}|$: 31.15 | min $|\epsilon_{max}|$: -0.00 %



F

Buckling capacity horizontal girders

The buckling capacity of the horizontal DIN550 profiles is calculated in this appendix to subsequently check whether the applied load of a symmetrical collision from Section 6.2.2 does not exceed this capacity. This is done based on formulas from Eurocode 3: Design of steel structures - Part 1-1: General rules and rules for buildings (Eurocode, 2016a).

F.1. Determination buckling stability

The buckling stability of a compression-loaded bar is determined based on the design value of the compressive force N_{Ed} and the design value of the buckling resistance of the compression-loaded bar $N_{b,Rd}$. Here, N_{Ed} is derived from RFEM and is equal to 4,492 kN, which must not exceed $N_{b,Rd}$. If this force is greater than $N_{b,Rd}$, the loaded bar fails due to buckling. This leads to the following equation:

$$\frac{N_{Ed}}{N_{b,Rd}} \leq 1.0 \quad (E1)$$

With,

$$N_{b,Rd} = \frac{\chi A f_y}{\gamma_{M1}} \quad (E2)$$

In which,

- χ = buckling factor [-]
- A = cross-sectional area for section [mm²]
- f_y = yield stress; 355 [N/mm²]
- γ_{M1} = stability check; 1.0 for buildings [-]

To determine the buckling resistance $N_{b,Rd}$, the slenderness ratio $\bar{\lambda}$ and the buckling factor χ first need to be determined. These parameters are interrelated because χ depends on $\bar{\lambda}$.

Buckling factor

The buckling factor χ is a factor derived from an empirical formula:

$$\chi = \frac{1}{\phi + \sqrt{\phi^2 - \bar{\lambda}^2}} \quad (E3)$$

With,

$$\phi = 0.5 [1 + \alpha (\bar{\lambda} - 0.2) + \bar{\lambda}^2] \quad (E4)$$

$$\bar{\lambda} = \sqrt{\frac{A f_y}{N_{cr}}} = \frac{L_{cr}}{i} \frac{1}{\lambda_1} \quad \text{and} \quad \lambda_1 = \pi \sqrt{\frac{E}{f_y}} \quad (E5)$$

The parameters to determine λ_1 are known. The modulus of elasticity of the steel is $210,000 \text{ N/mm}^2$ and the yield strength for S355 is equal to 355 N/mm^2 . Substituting these values yields a value of 76,4 for λ_1 . The slenderness ratio $\bar{\lambda}$ depends on L_{cr} , which is the buckling length in the considered buckling plane. This length is characterised by the distance between two vertical INP profiles for buckling about the y-axis and for the current design of the lock gate this is equal to 1,000 mm. For buckling around the z-axis this distance is equal to the total length of the horizontal girder, namely 8,200 mm. The parameter i represents the radius of inertia about the considered axis and is defined as $\sqrt{I/A}$. The moments of inertia about the z- and y-axis are equal to $1.35 \times 10^8 \text{ N/mm}^4$ and $1.38 \times 10^9 \text{ N/mm}^4$ respectively. The cross-sectional area for this section is equal to $25,840 \text{ mm}^2$, refer to Section 5.1.2 for the calculation of these values. When Formula F.5 is substituted, it yields a value of $\bar{\lambda}_z = 0.47$ and $\bar{\lambda}_y = 0.18$ for the slenderness ratios.

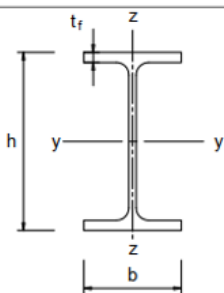
Doorsnede	Begrenzungen	Knik om de as	Knikkromme		
			S 235 S 275 S 355 S 420	S 460	
	$h/b > 1,2$	$t_f \leq 40 \text{ mm}$	y-y	a	a_0
			z-z	b	a_0
	$h/b \leq 1,2$	$40 \text{ mm} < t_f \leq 100 \text{ mm}$	y-y	b	a
			z-z	c	a
		$t_f \leq 100 \text{ mm}$	y-y	b	a
			z-z	c	a
$t_f > 100 \text{ mm}$	y-y	d	c		
	z-z	d	c		

Table F.1: Choice table for the buckling curves for a cross-section Eurocode (2016a)

Depending on the shape of the cross-section, a specific value for the imperfection factor α must be used. Eurocode (2016a) provides five different options for the shape of the so-called instability curves or buckling curves $a_0, a, b, c,$ and d . The choice of the buckling curve is determined by Table F.1 and the value to be used for the imperfection factor α is determined by Table F.2. For the situation to be calculated, these values are therefore equal to $\alpha_z = 0.34$ and $\alpha_y = 0.21$.

Knikkromme	a_0	a	b	c	d
Imperfectiefactor α	0,13	0,21	0,34	0,49	0,76

Table F.2: Imperfection factors for the buckling curves Eurocode (2016a)

The imperfection factors are now known, so the value ϕ for determining the reduction factor χ , is calculated. This is a matter of substituting Formula F.4, resulting in a value of $\phi_z = 0.65$ and $\phi_y = 0.51$. These values are used in Equation F.3, after which the buckling factors are determined. The buckling factor is determined either this way or by using Figure F.1. In both situations, values of $\chi_z = 0.90$ and $\chi_y = 1.00$ are obtained.

Now that all parameters are known, Equation F.2 to determine the buckling resistance $N_{b,Rd}$ is filled in. Additionally, the unity checks show that the buckling resistance is not exceeded by the compressive force considering both axis, meaning that the loaded bar will not buckle.

$$N_{b,Rd,z} = \frac{0.90 \times 25,840 \times 355}{1.0} = 8.25 \times 10^6 \text{ N} = 8,250 \text{ kN}$$

$$N_{b,Rd,y} = \frac{1.00 \times 25,840 \times 355}{1.0} = 9.21 \times 10^6 \text{ N} = 9,211 \text{ kN}$$

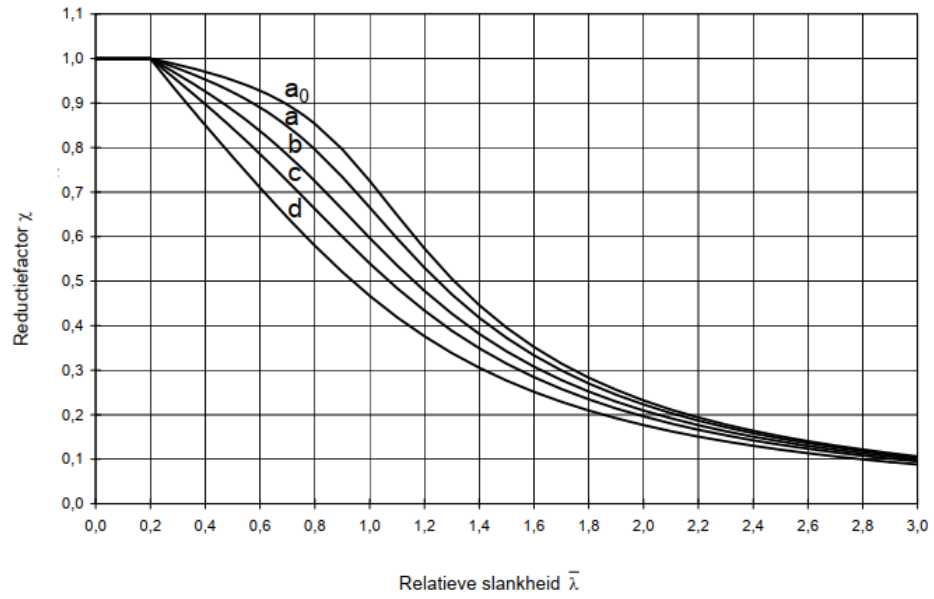


Figure F.1: Slenderness factor $\bar{\lambda}$ against imperfection factor χ for buckling curves a_0 , a , b , c & d Eurocode (2016a)

$$\frac{4,492}{8,250} = 0.54 \leq 1.00$$

$$\frac{4,492}{9,211} = 0.49 \leq 1.00$$

G

Results RFEM for determining energy absorption capacity

In this appendix, the output from RFEM is provided for determining the energy absorption capacity in the case of both an unsymmetrical and a symmetrical collisions. This output can be used to support the understanding of the force distribution and deformation in the lock gate.

G.1. Unsymmetrical collision phase 1

Witteveen + Bos
Van Twickelostraat 2, 7400 AE DEVENTER
Tel: +31 5706 9708 0 - Fax: +31 5706 9734 4



Model:
Macharen_Scenario3_Class2

Date 7.5.2024 Page 1/5
Sheet 1

LOADS

1 Loads



Witteveen + Bos
 Van Twickelostraat 2, 7400 AE DEVENTER
 Tel: +31 5706 9708 0 - Fax: +31 5706 9734 4



Model:
 Macharen_Scenario3_Class2

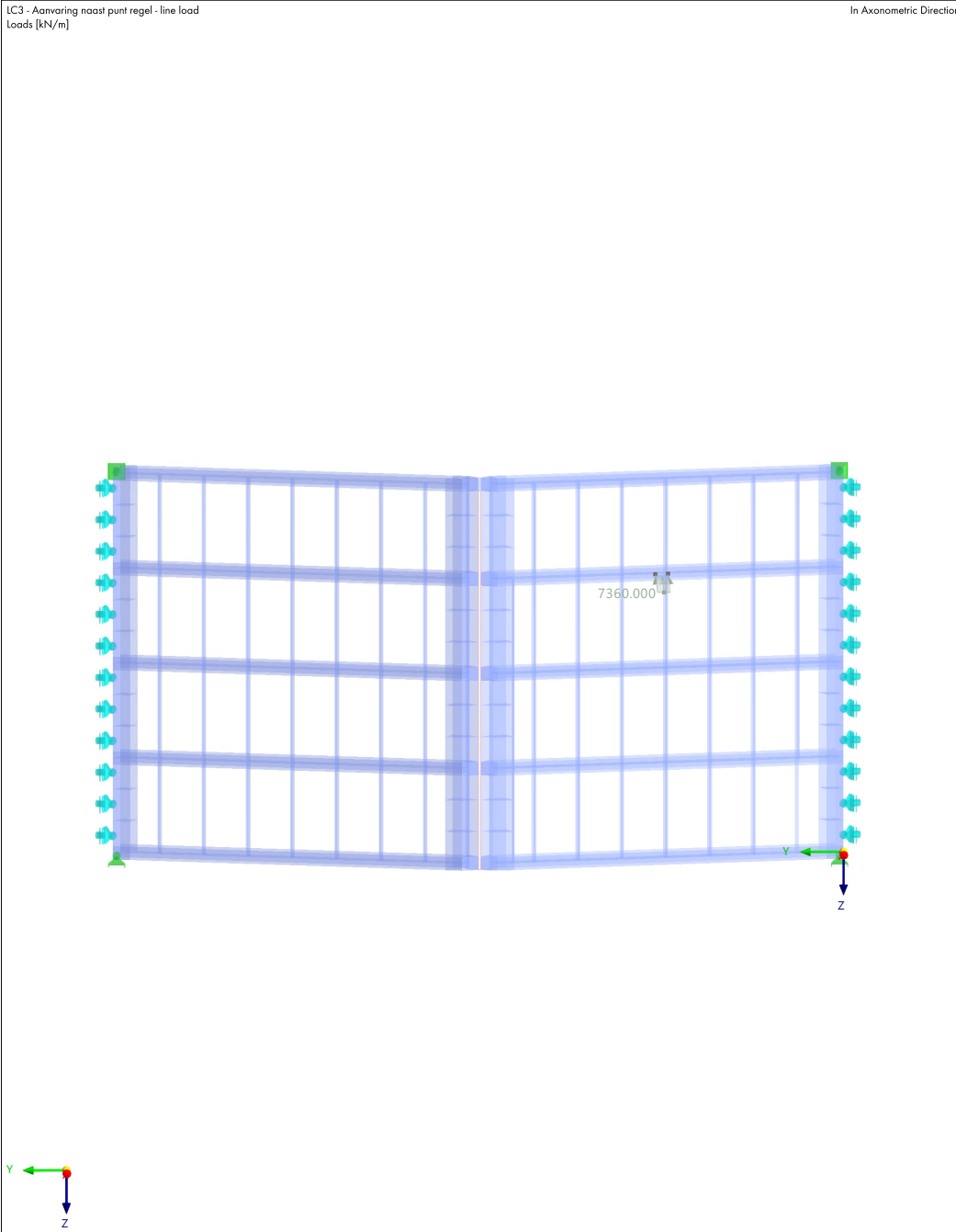
Date 7.5.2024 Page 2/5
 Sheet 1

MODEL

1.1.1 **LC3: LOADING, IN AXONOMETRIC DIRECTION**

LC3 - Aanvaring naast punt regel - line load
 Loads [kN/m]

In Axonometric Direction



Witteveen + Bos
Van Twickelostraat 2, 7400 AE DEVENTER
Tel: +31 5706 9708 0 - Fax: +31 5706 9734 4



Model:
Macharen_Scenario3_Class2

Date 7.5.2024 Page 3/5
Sheet 1

MODEL

2 Static Analysis Results



Witteveen + Bos
 Van Twickelostraat 2, 7400 AE DEVENTER
 Tel: +31 5706 9708 0 - Fax: +31 5706 9734 4



Model:
 Macharen_Scenario3_Class2

Date: 7.5.2024 Page: 4/5
 Sheet: 1

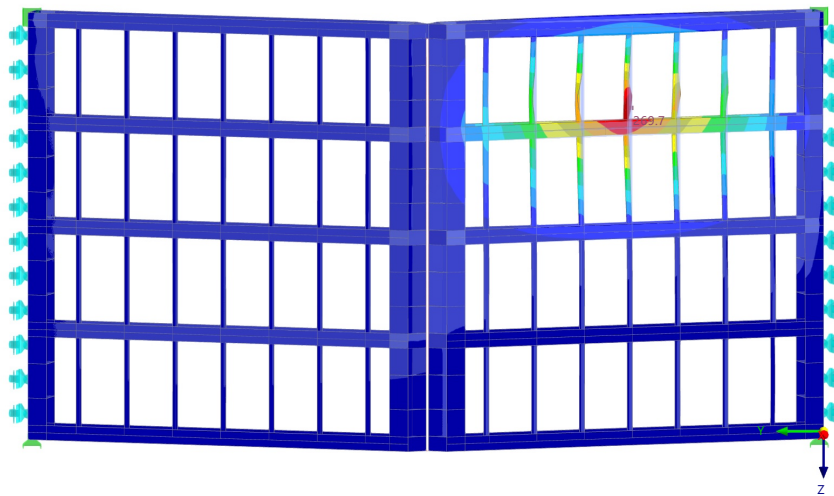
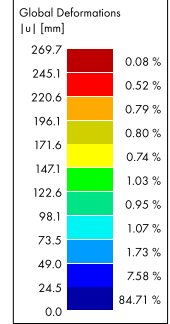
MODEL

2.1 **LC3: GLOBAL DEFORMATIONS |U|, IN AXONOMETRIC DIRECTION**

Static Analysis

LC3 - Aanvaring naast punt regel - line load
 Static Analysis
 Load Increment No. 50 | Factor: 1.000
 Displacements |u| [mm]

In Axonometric Direction



max |u| : 269.7 | min |u| : 0.0 mm



Witteveen + Bos
 Van Twickelostraat 2, 7400 AE DEVENTER
 Tel: +31 5706 9708 0 - Fax: +31 5706 9734 4



Model:
 Macharen_Scenario3_Class2

Date 7.5.2024 Page 5/5
 Sheet 1

MODEL

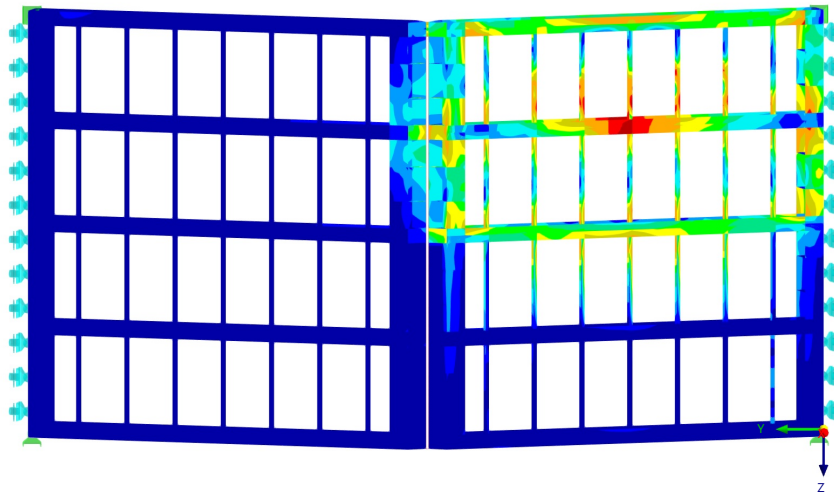
2.2 **LC3: $\sigma_{eqv,Mises}$ $\sigma_{eqv,Mises,Max}$, IN AXONOMETRIC DIRECTION**

Static Analysis

LC3 - Aanvaring naast punt regel - line load
 Static Analysis
 Load Increment No. 50 | Factor: 1.000
 Equivalent Stresses von Mises $\sigma_{eqv,Mises,Max}$ [N/mm²]

In Axonometric Direction

Surfaces Stresses	Equivalent Stresses $\sigma_{eqv,Mises}$
$\sigma_{eqv,Mises,Max}$ [N/mm ²]	$\sigma_{eqv,Mises}$
456.450	0.12 %
414.976	0.35 %
373.502	1.70 %
332.028	2.11 %
290.554	2.95 %
249.080	4.56 %
207.605	5.57 %
166.131	6.75 %
124.657	6.47 %
83.183	7.63 %
41.709	61.80 %
0.235	



max $\sigma_{eqv,Mises,Max}$: 456.450 | min $\sigma_{eqv,Mises,Max}$: 0.235 N/mm²



G.2. Unsymmetrical collision phase 2a

Witteveen + Bos
Van Twickelostraat 2, 7400 AE DEVENTER
Tel: +31 5706 9708 0 - Fax: +31 5706 9734 4



Model:
Macharen_Scenario3_Class2_phase2

Date 18.2.2024 Page 1/4
Sheet 1

LOADS

1 Loads



Witteveen + Bos
 Van Twickelostraat 2, 7400 AE DEVENTER
 Tel: +31 5706 9708 0 - Fax: +31 5706 9734 4

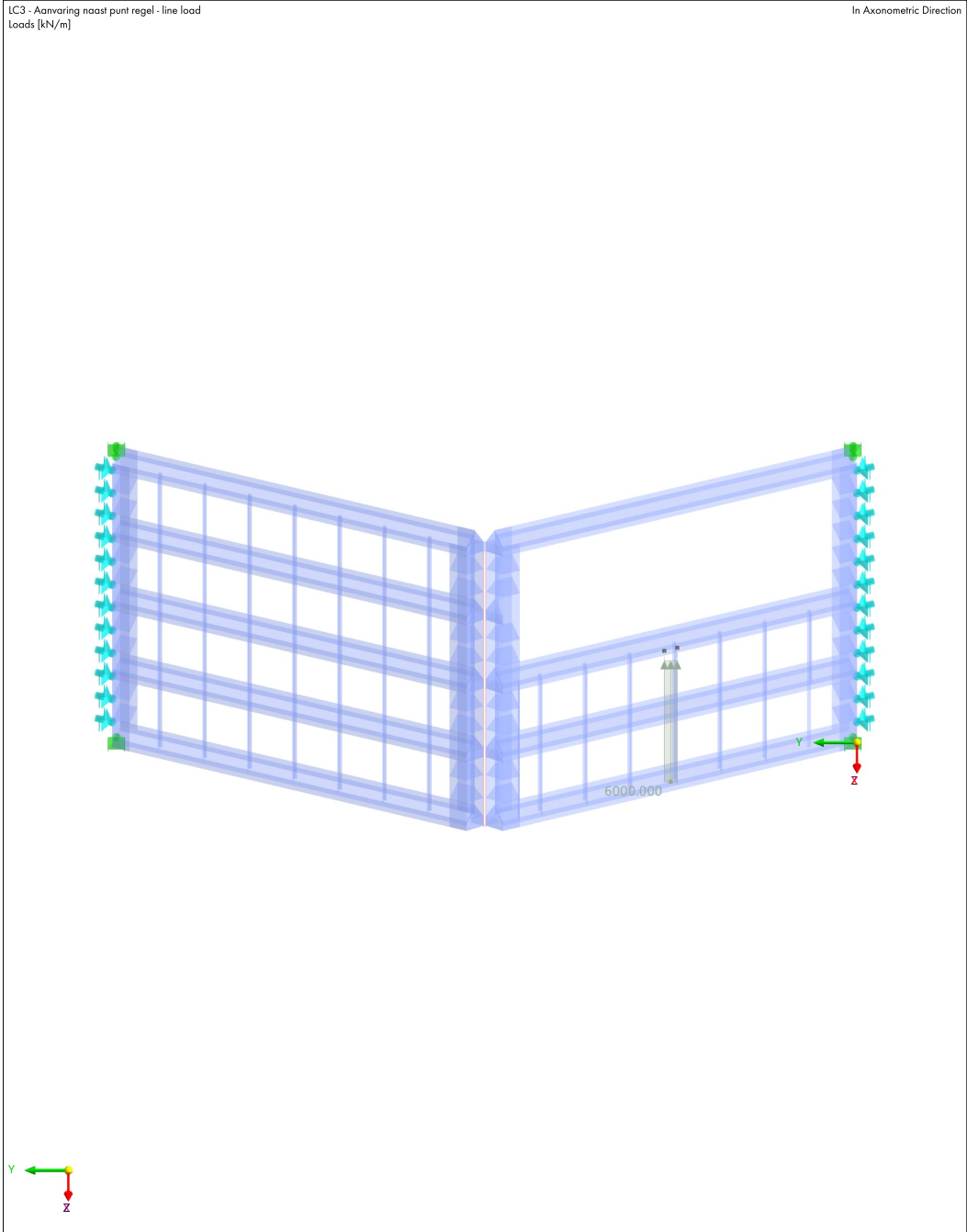


Model:
 Macharen_Scenario3_Class2_phase2

Date 18.2.2024 Page 2/4
 Sheet 1

MODEL

1.1.1 **LC3: LOADING, IN AXONOMETRIC DIRECTION**



Witteveen + Bos
Van Twickelostraat 2, 7400 AE DEVENTER
Tel: +31 5706 9708 0 - Fax: +31 5706 9734 4



Model:
Macharen_Scenario3_Class2_phase2

Date 18.2.2024 Page 3/4
Sheet 1

MODEL

2 Static Analysis Results



Witteveen + Bos
 Van Twickelostraat 2, 7400 AE DEVENTER
 Tel: +31 5706 9708 0 - Fax: +31 5706 9734 4



Model:
 Macharen_Scenario3_Class2_phase2

Date 18.2.2024 Page 4/4
 Sheet 1

MODEL

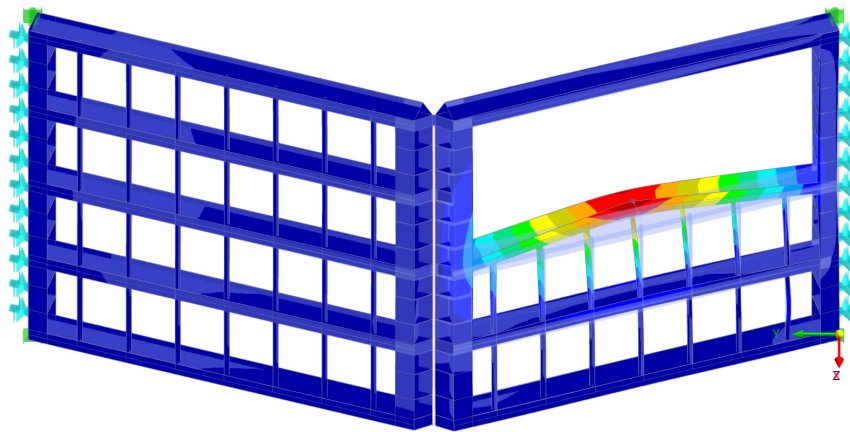
2.1 **LC3: GLOBAL DEFORMATIONS |U|, IN AXONOMETRIC DIRECTION**

Static Analysis

LC3 - Aanvaring naast punt regel - line load
 Static Analysis
 Load Increment No. 122 | Factor: 0.976
 Displacements |u| [mm]

In Axonometric Direction

Global Deformations u [mm]	Percentage
285.5	0.08 %
259.6	0.78 %
233.6	0.64 %
207.7	0.67 %
181.7	0.67 %
155.7	0.74 %
129.8	0.77 %
103.8	0.85 %
77.9	1.34 %
51.9	5.22 %
26.0	88.23 %
0.0	



max |u| : 285.5 | min |u| : 0.0 mm



G.3. Unsymmetrical collision phase 3a

Witteveen + Bos
Van Twickelostraat 2, 7400 AE DEVENTER
Tel: +31 5706 9708 0 - Fax: +31 5706 9734 4



Model:
Macharen_Scenario3_Class2_phase3

Date 18.2.2024 Page 1/4
Sheet 1

LOADS

1 Loads



Witteveen + Bos
Van Twickelostraat 2, 7400 AE DEVENTER
Tel: +31 5706 9708 0 - Fax: +31 5706 9734 4

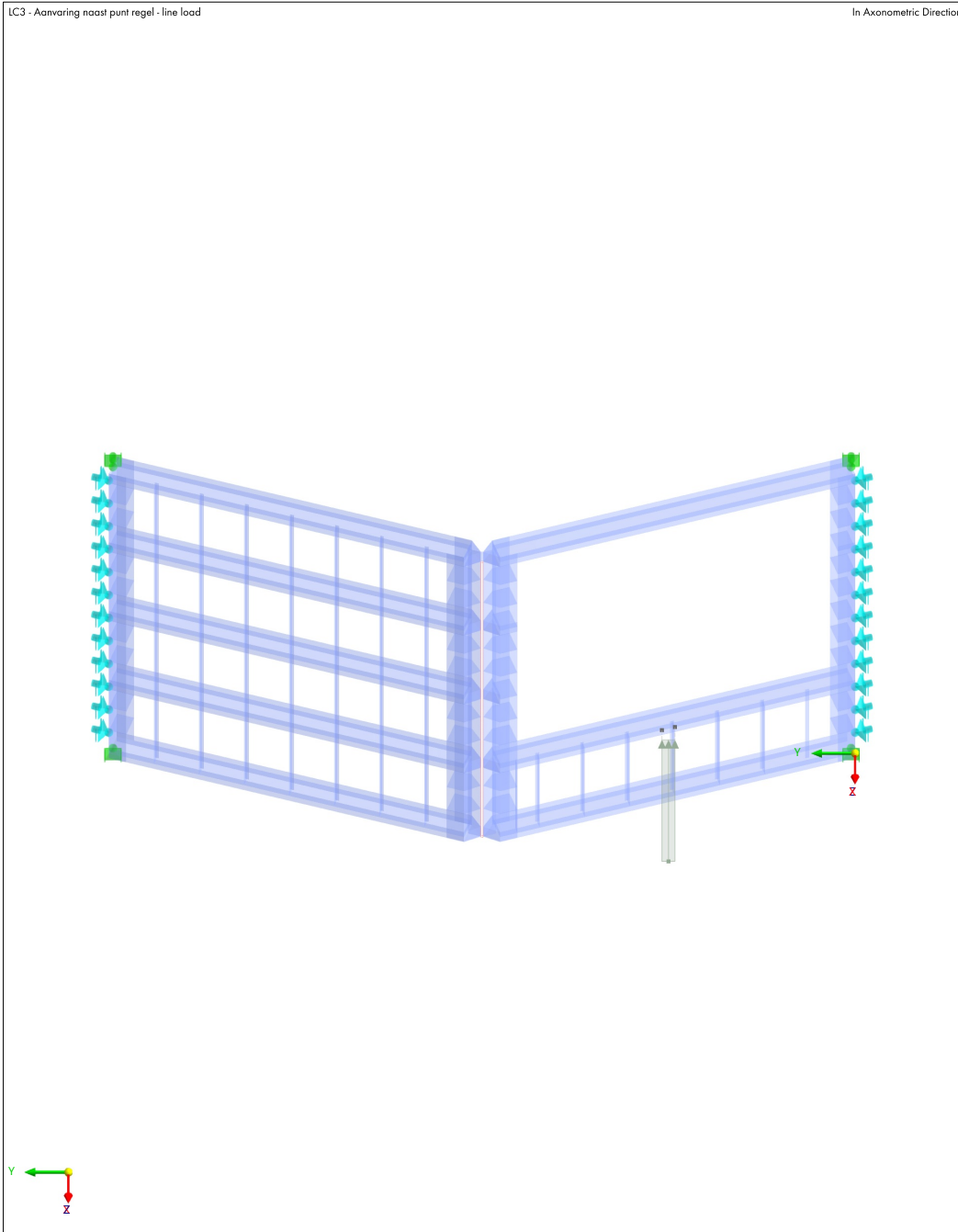


Model:
Macharen_Scenario3_Class2_phase3

Date 18.2.2024 Page 2/4
Sheet 1

MODEL

1.1.1 **LC3: LOADING, IN AXONOMETRIC DIRECTION**



Witteveen + Bos
Van Twickelostraat 2, 7400 AE DEVENTER
Tel: +31 5706 9708 0 - Fax: +31 5706 9734 4



Model:
Macharen_Scenario3_Class2_phase3

Date 18.2.2024 Page 3/4
Sheet 1

MODEL

2 Static Analysis Results



Witteveen + Bos
 Van Twickelostraat 2, 7400 AE DEVENTER
 Tel: +31 5706 9708 0 - Fax: +31 5706 9734 4



Model:
 Macharen_Scenario3_Class2_phase3

Date: 18.2.2024 Page: 4/4
 Sheet: 1

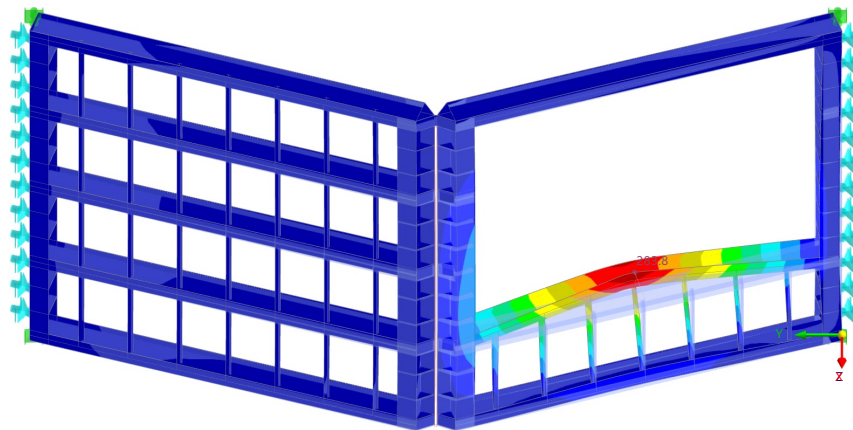
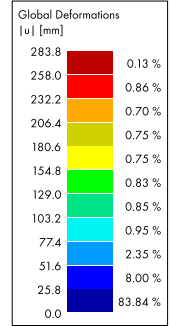
MODEL

2.1 **LC3: GLOBAL DEFORMATIONS |U|, IN AXONOMETRIC DIRECTION**

Static Analysis

LC3 - Aanvaring naast punt regel - line load
 Static Analysis
 Load Increment No. 123 | Factor: 0.984
 Displacements |u| [mm]

In Axonometric Direction



max |u| : 283.8 | min |u| : 0.0 mm



G.4. Unsymmetrical collision phase 2b & 3b

Witteveen + Bos
Van Twickelostraat 2, 7400 AE DEVENTER
Tel: +31 5706 9708 0 - Fax: +31 5706 9734 4



Model:
Macharen_Scenario3_Class2

Date 8.3.2024 Page 1/6
Sheet 1

LOADS

2 Loads



Witteveen + Bos
 Van Twickelostraat 2, 7400 AE DEVENTER
 Tel: +31 5706 9708 0 - Fax: +31 5706 9734 4



Model:
 Macharen_Scenario3_Class2

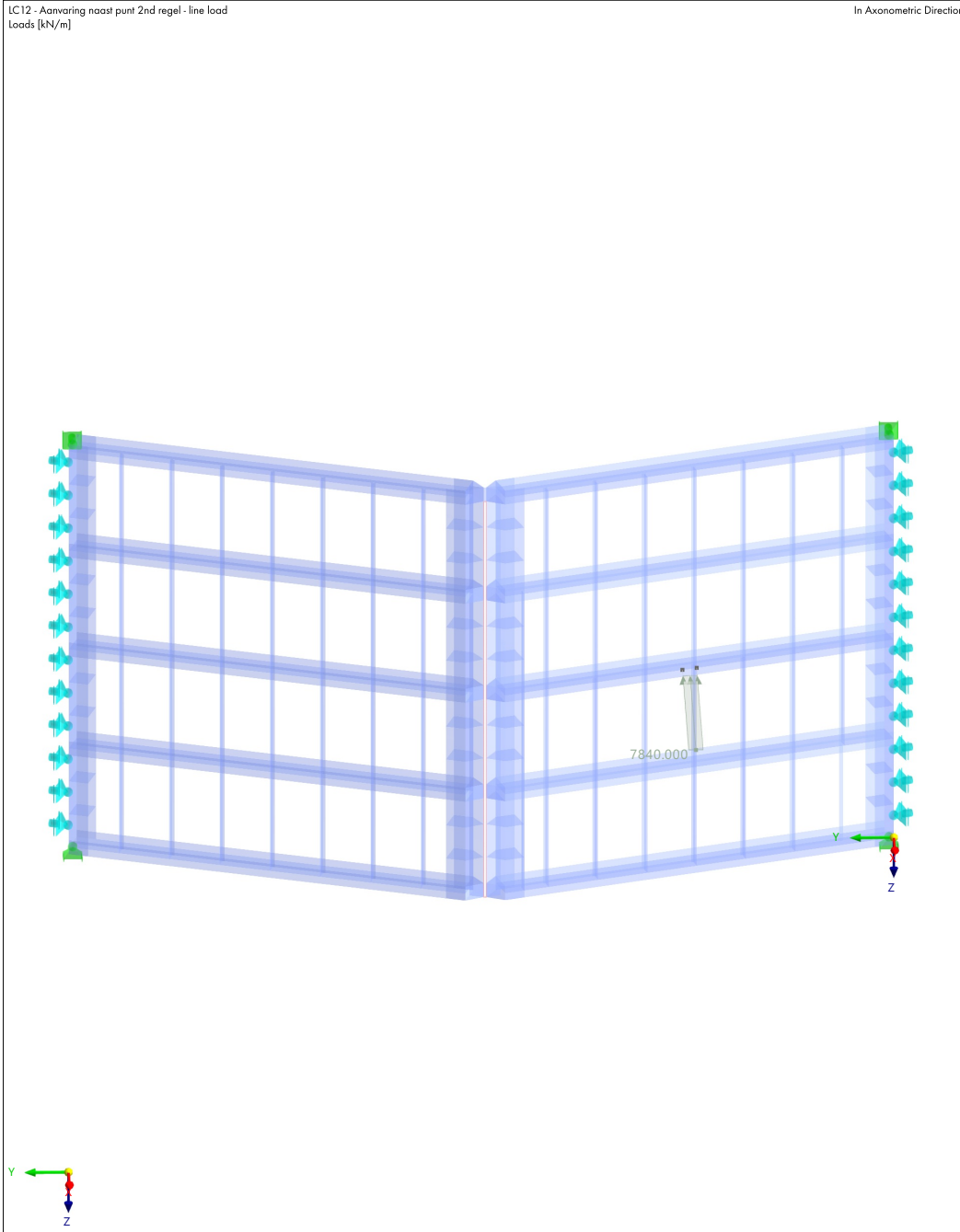
Date 8.3.2024 Page 2/6
 Sheet 1

MODEL

2.1.1 **LC12: LOADING, IN AXONOMETRIC DIRECTION**

LC12 - Aanvaring naast punt 2nd regel - line load
 Loads [kN/m]

In Axonometric Direction



Witteveen + Bos
Van Twickelostraat 2, 7400 AE DEVENTER
Tel: +31 5706 9708 0 - Fax: +31 5706 9734 4



Model:
Macharen_Scenario3_Class2

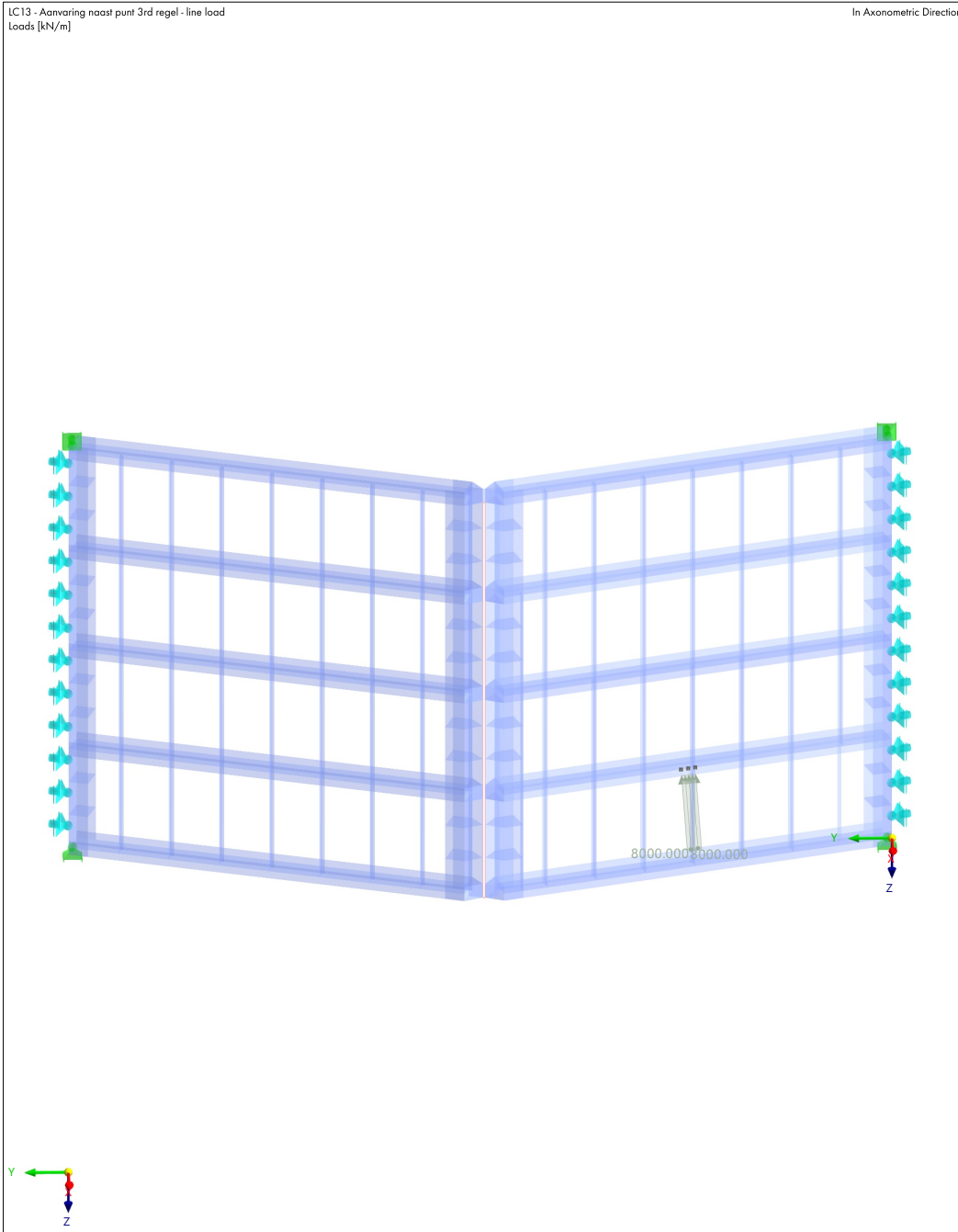
Date 8.3.2024 Page 3/6
Sheet 1

MODEL

2.2.1 LC13: LOADING, IN AXONOMETRIC DIRECTION

LC13 - Aanvaring naast punt 3rd regel - line load
Loads [kN/m]

In Axonometric Direction



Witteveen + Bos
Van Twickelstraat 2, 7400 AE DEVENTER
Tel: +31 5706 9708 0 - Fax: +31 5706 9734 4



Model:
Macharen_Scenario3_Class2

Date 8.3.2024 Page 4/6
Sheet 1

MODEL

3 Static Analysis Results



Witteveen + Bos
 Van Twickelostraat 2, 7400 AE DEVENTER
 Tel: +31 5706 9708 0 - Fax: +31 5706 9734 4



Model:
 Macharen_Scenario3_Class2

Date 8.3.2024 Page 5/6
 Sheet 1

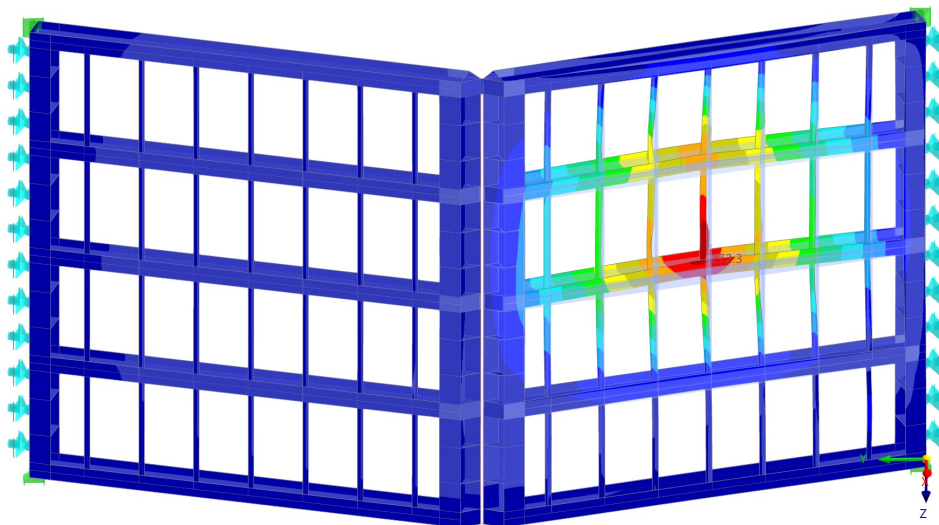
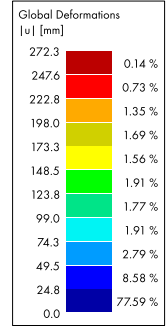
MODEL

3.1 **LC12: GLOBAL DEFORMATIONS |U|, IN AXONOMETRIC DIRECTION**

Static Analysis

LC12 - Aanvaring naast punt 2nd regel - line load
 Static Analysis
 Load Increment No. 50 | Factor: 1.000
 Displacements |u| [mm]

In Axonometric Direction



max |u| : 272.3 | min |u| : 0.0 mm



Witteveen + Bos
 Van Twickelstraat 2, 7400 AE DEVENTER
 Tel: +31 5706 9708 0 - Fax: +31 5706 9734 4



Model:
 Macharen_Scenario3_Class2

Date 8.3.2024 Page 6/6
 Sheet 1

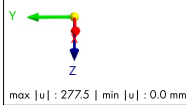
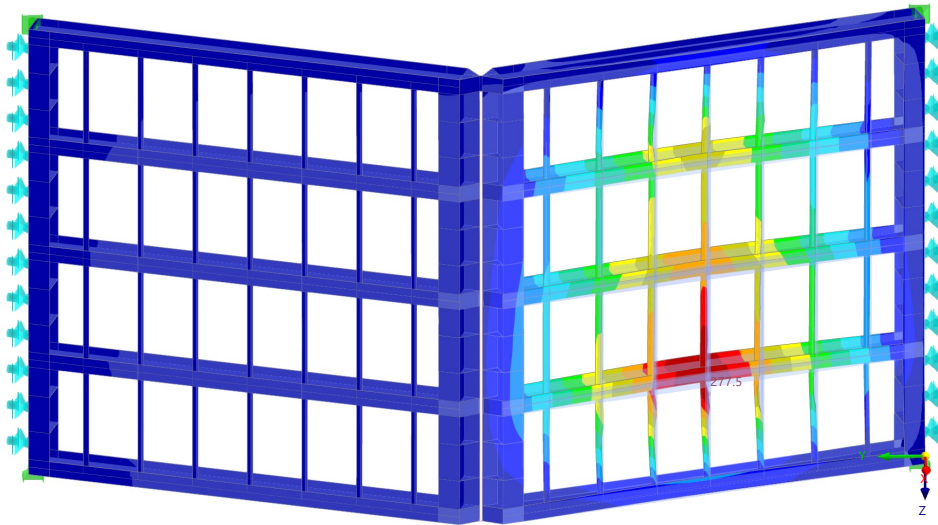
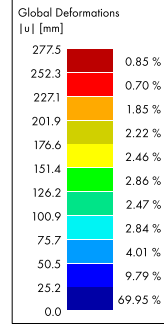
MODEL

3.2 **LC13: GLOBAL DEFORMATIONS |U|, IN AXONOMETRIC DIRECTION**

Static Analysis

LC13 - Aanvaring naast punt 3rd regel - line load
 Static Analysis
 Load Increment No. 95 | Factor: 0.950
 Displacements |u| [mm]

In Axonometric Direction



G.5. Symmetrical collision

Witteveen + Bos
Van Twickelostraat 2, 7400 AE DEVENTER
Tel: +31 5706 9708 0 - Fax: +31 5706 9734 4



Model:
Macharen_Scenario3_Class2

Date 22.2.2024 Page 1/16
Sheet 1

LOADS

1 Loads



Witteveen + Bos
 Van Twickelostraat 2, 7400 AE DEVENTER
 Tel: +31 5706 9708 0 - Fax: +31 5706 9734 4



Model:
 Macharen_Scenario3_Class2

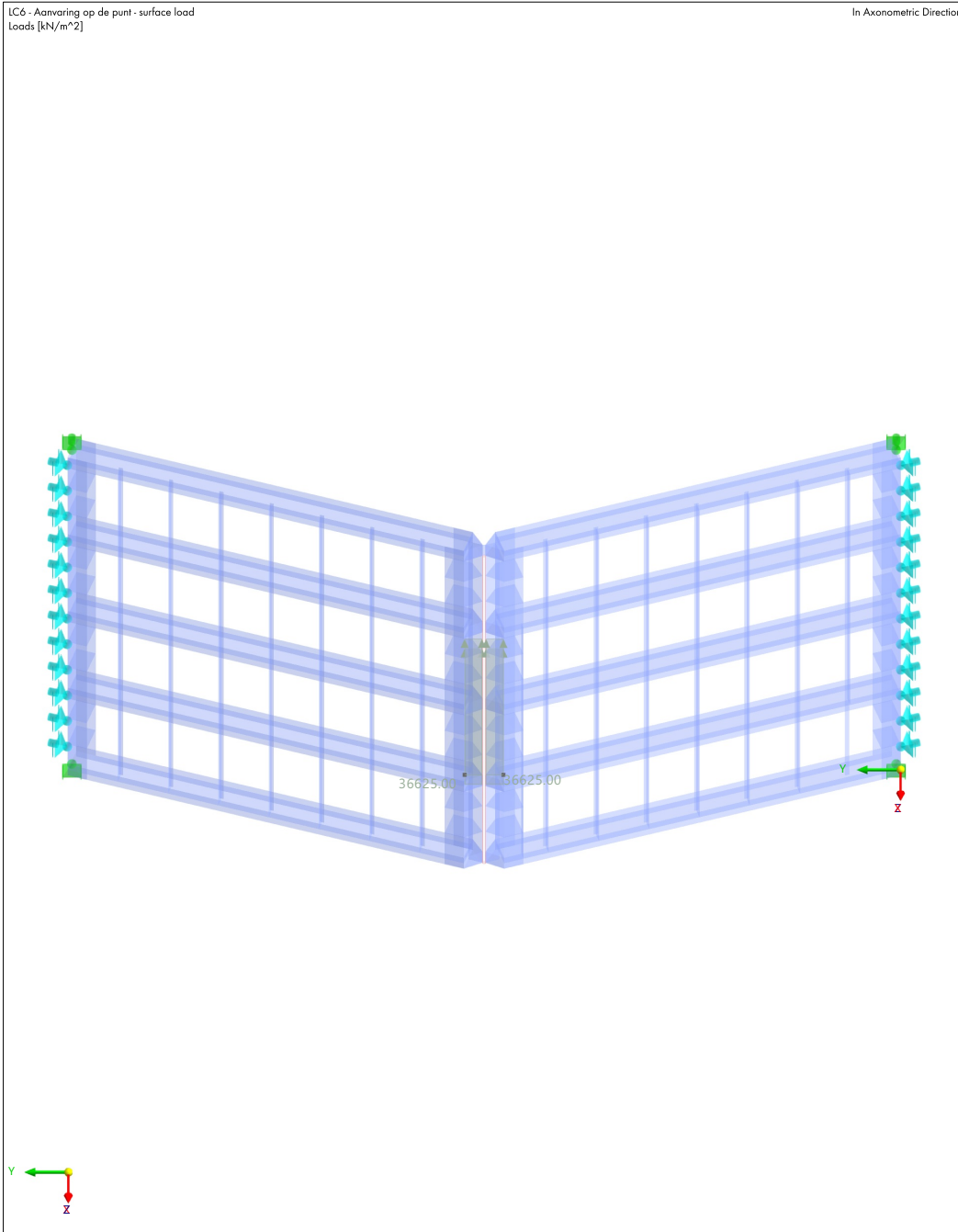
Date 22.2.2024 Page 2/16
 Sheet 1

MODEL

1.1.1 **LC6: LOADING, IN AXONOMETRIC DIRECTION**

LC6 - Aanvaring op de punt - surface load
 Loads [kN/m²]

In Axonometric Direction



Witteveen + Bos
 Van Twickelostraat 2, 7400 AE DEVENTER
 Tel: +31 5706 9708 0 - Fax: +31 5706 9734 4



Model:
 Macharen_Scenario3_Class2

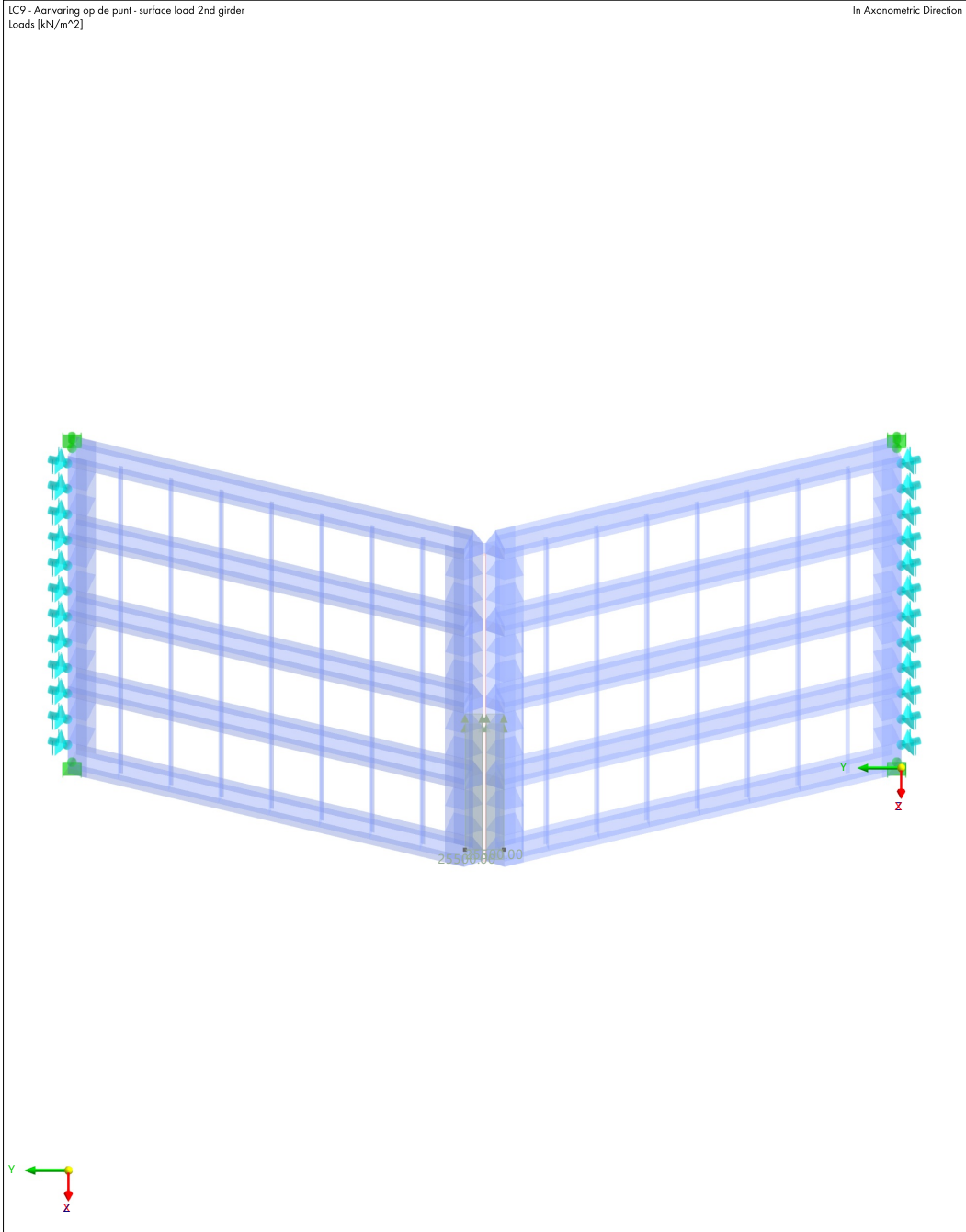
Date 22.2.2024 Page 3/16
 Sheet 1

MODEL

1.2.1 LC9: LOADING, IN AXONOMETRIC DIRECTION

LC9 - Aanvaring op de punt - surface load 2nd girder
 Loads [kN/m²]

In Axonometric Direction



Witteveen + Bos
Van Twickelostraat 2, 7400 AE DEVENTER
Tel: +31 5706 9708 0 - Fax: +31 5706 9734 4



Model:
Macharen_Scenario3_Class2

Date 22.2.2024 Page 4/16
Sheet 1

MODEL

2 Static Analysis Results



Witteveen + Bos
 Van Twickelostraat 2, 7400 AE DEVENTER
 Tel: +31 5706 9708 0 - Fax: +31 5706 9734 4



Model:
 Macharen_Scenario3_Class2

Date 22.2.2024 Page 5/16
 Sheet 1

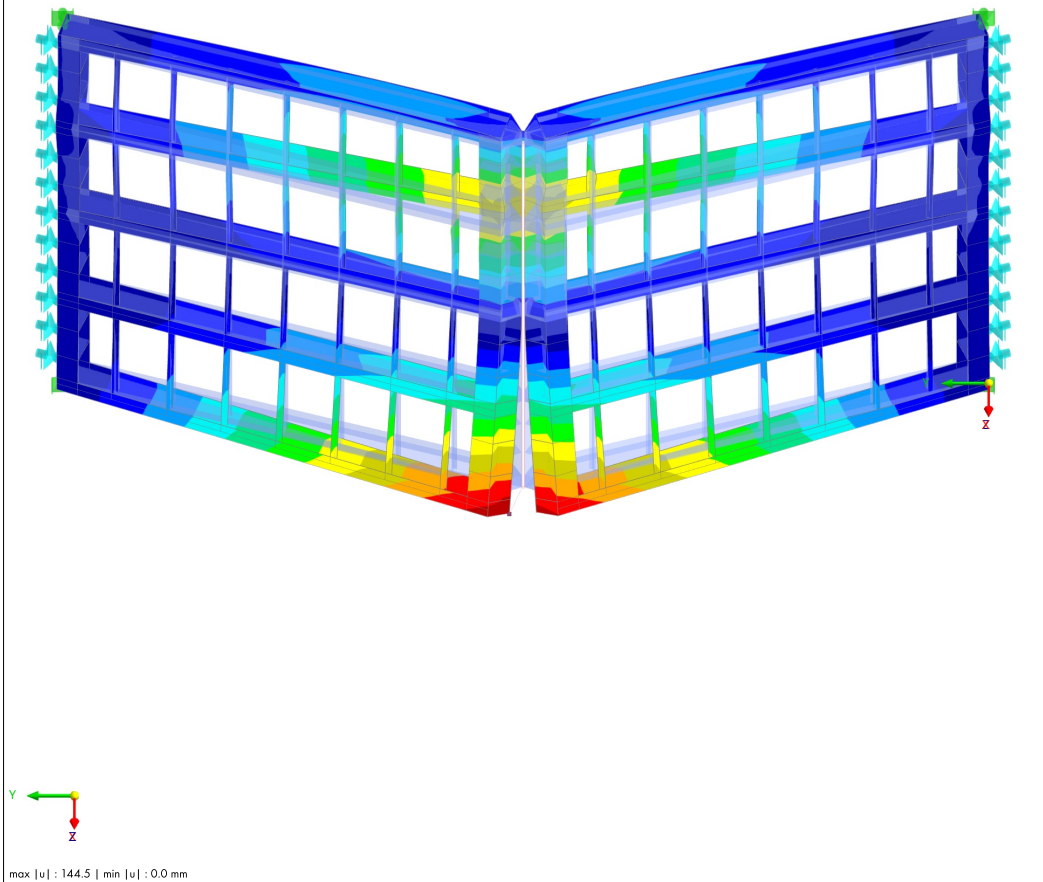
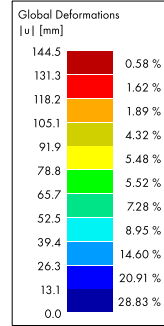
MODEL

2.1 **LC6: GLOBAL DEFORMATIONS |U|, IN AXONOMETRIC DIRECTION**

Static Analysis

LC6 - Aanvaring op de punt - surface load
 Static Analysis
 Load Increment No. 49 | Factor: 0.980
 Displacements |u| [mm]

In Axonometric Direction



Witteveen + Bos
 Van Twickelostraat 2, 7400 AE DEVENTER
 Tel: +31 5706 9708 0 - Fax: +31 5706 9734 4



Model:
 Macharen_Scenario3_Class2

Date 22.2.2024 Page 6/16
 Sheet 1

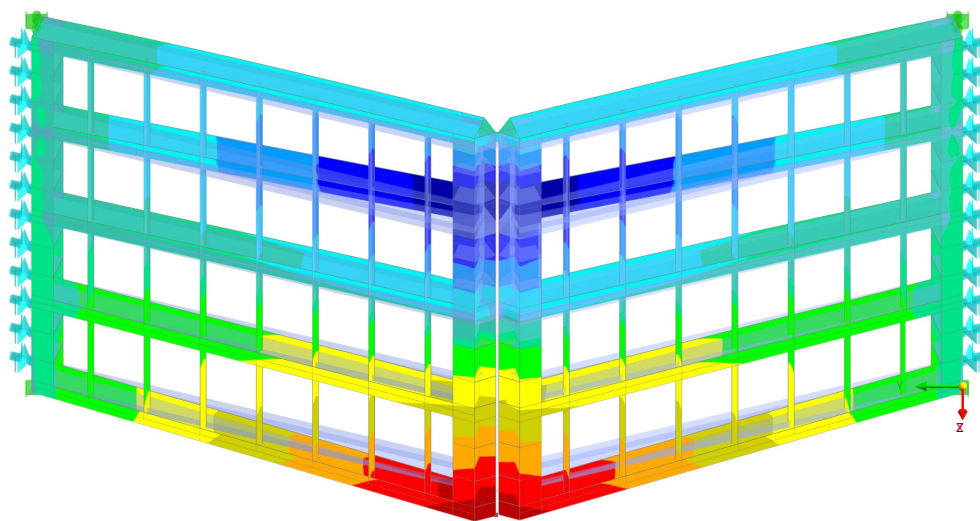
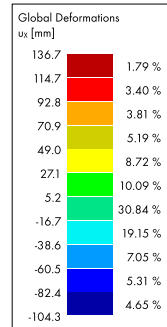
MODEL

2.2 **LC6: GLOBAL DEFORMATIONS u_x , IN AXONOMETRIC DIRECTION**

Static Analysis

LC6 - Aanvaring op de punt - surface load
 Static Analysis
 Load Increment No. 49 | Factor: 0.980
 Displacements u_x [mm]

In Axonometric Direction



max u_x : 136.7 | min u_x : -104.3 mm



Witteveen + Bos
 Van Twickelostraat 2, 7400 AE DEVENTER
 Tel: +31 5706 9708 0 - Fax: +31 5706 9734 4



Model:
 Macharen_Scenario3_Class2

Date 22.2.2024 Page 7/16
 Sheet 1

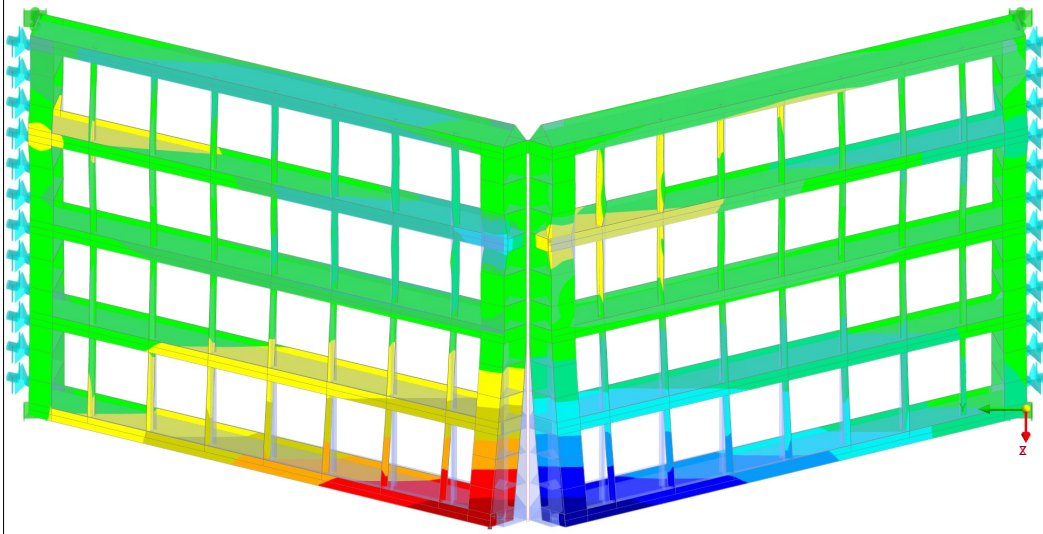
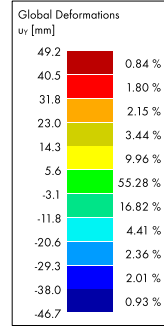
MODEL

2.3 LC6: GLOBAL DEFORMATIONS u_y , LINE SUPPORTS p_z , IN AXONOMETRIC DIRECTION

Static Analysis

LC6 - Aanvaring op de punt - surface load
 Static Analysis
 Load Increment No. 49 | Factor: 0.980
 Displacements u_y [mm]
 Lines | Local Reaction Forces p_z [kN/m]

In Axonometric Direction



max u_y : 49.2 | min u_y : -46.7 mm
 Lines | max p_z : 0.000 | min p_z : -14927.800 kN/m



Witteveen + Bos
 Van Twickelstraat 2, 7400 AE DEVENTER
 Tel: +31 5706 9708 0 - Fax: +31 5706 9734 4



Model:
 Macharen_Scenario3_Class2

Date 22.2.2024 Page 8/16
 Sheet 1

MODEL

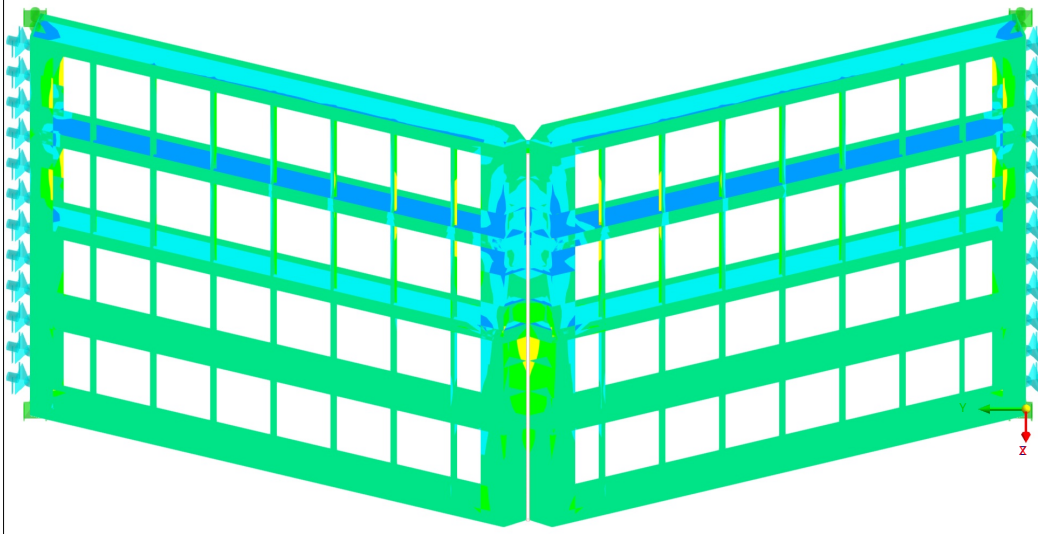
2.4 LC6: BASIC INTERNAL FORCES N_y , LINE SUPPORTS P_z , IN AXONOMETRIC DIRECTION

Static Analysis

LC6 - Aanvaring op de punt - surface load
 Static Analysis
 Load Increment No. 49 | Factor: 0.980
 Surfaces | Axial Forces n_y [kN/m]
 Lines | Local Reaction Forces p_z [kN/m]

In Axonometric Direction

Surfaces Internal Forces Basic Internal Forces n_y [kN/m]		
10794.300	0.00 %	
9121.790	0.01 %	
7449.300	0.01 %	
5776.800	0.29 %	
4104.310	1.59 %	
2431.810	5.37 %	
759.316	71.04 %	
-913.180	14.68 %	
-2585.680	6.78 %	
-4258.170		
-7603.160	0.22 %	



Surfaces | max n_y : 10794.300 | min n_y : -7603.160 kN/m
 Lines | max p_z : 0.000 | min p_z : -14927.800 kN/m



Witteveen + Bos
 Van Twickelostraat 2, 7400 AE DEVENTER
 Tel: +31 5706 9708 0 - Fax: +31 5706 9734 4



Model:
 Macharen_Scenario3_Class2

Date 22.2.2024 Page 9/16
 Sheet 1

MODEL

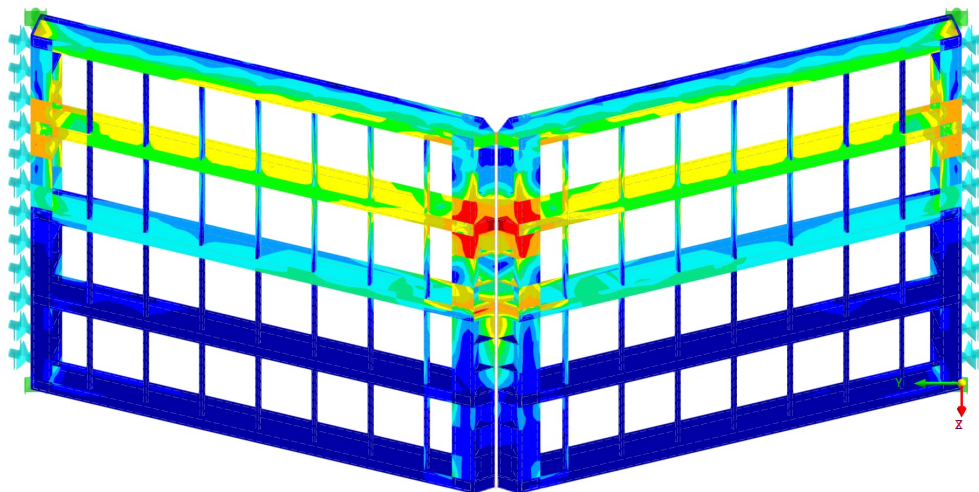
2.5 **LC6: $\sigma_{eqv,Mises}$ $\sigma_{eqv,Mises,Max}$, IN AXONOMETRIC DIRECTION**

Static Analysis

LC6 - Aanvaring op de punt - surface load
 Static Analysis
 Load Increment No. 49 | Factor: 0.980
 Equivalent Stresses von Mises $\sigma_{eqv,Mises,Max}$ [N/mm²]

In Axonometric Direction

Surfaces Stresses	Equivalent Stresses $\sigma_{eqv,Mises}$
$\sigma_{eqv,Mises,Max}$ [N/mm ²]	
456.450	0.07 %
415.010	1.43 %
373.570	3.61 %
332.130	2.95 %
290.690	8.28 %
249.250	7.70 %
207.810	5.80 %
166.370	11.63 %
124.930	9.30 %
83.490	14.48 %
42.050	34.75 %
0.611	



max $\sigma_{eqv,Mises,Max}$: 456.450 | min $\sigma_{eqv,Mises,Max}$: 0.611 N/mm²



Witteveen + Bos
 Van Twickelostraat 2, 7400 AE DEVENTER
 Tel: +31 5706 9708 0 - Fax: +31 5706 9734 4



Model:
 Macharen_Scenario3_Class2

Date 22.2.2024 Page 10/16
 Sheet 1

MODEL

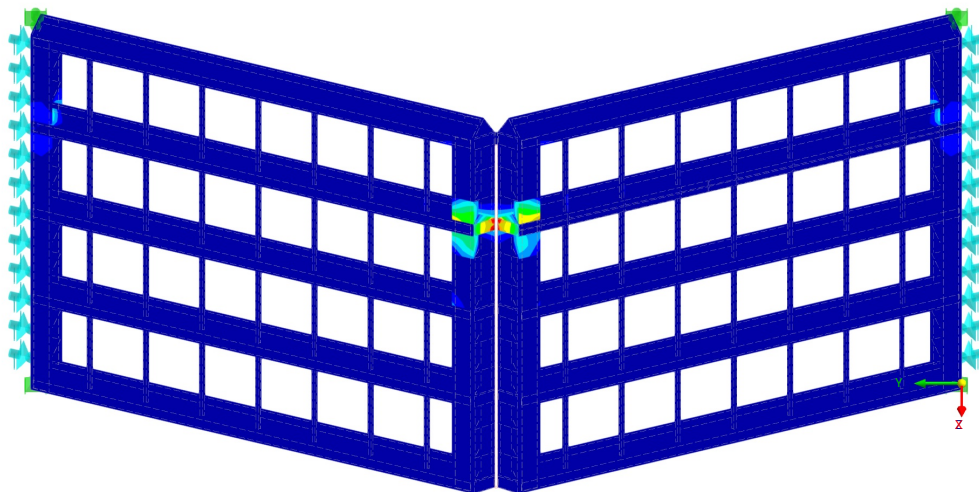
2.6 **LC6: MAXIMUM TOTAL STRAINS $|E_{max}|$, IN AXONOMETRIC DIRECTION**

Static Analysis

LC6 - Aanvaring op de punt - surface load
 Static Analysis
 Load Increment No. 49 | Factor: 0.980
 Maximum Strains $|E_{max}|$ [%]

In Axonometric Direction

Surfaces Strains	Maximum Total Strains
$ E_{max} $ [%]	$ E_{max} $ [%]
44.99	0.00 %
40.90	0.01 %
36.81	0.02 %
32.72	0.07 %
28.63	0.26 %
24.54	0.35 %
20.45	0.42 %
16.36	0.58 %
12.27	0.60 %
8.18	1.66 %
4.09	96.02 %
0.00	



max $|E_{max}|$: 44.99 | min $|E_{max}|$: 0.00 %



Witteveen + Bos
 Van Twickelostraat 2, 7400 AE DEVENTER
 Tel: +31 5706 9708 0 - Fax: +31 5706 9734 4



Model:
 Macharen_Scenario3_Class2

Date 22.2.2024 Page 11/16
 Sheet 1

MODEL

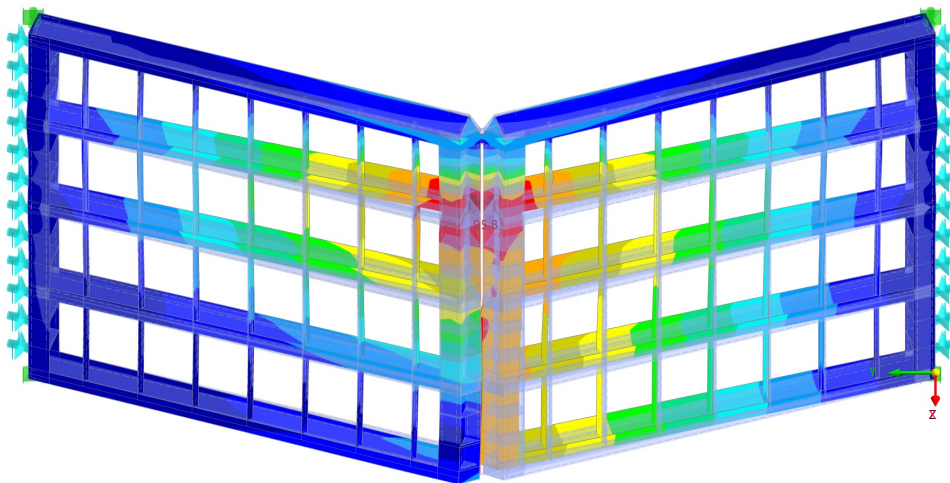
2.7 **LC9: GLOBAL DEFORMATIONS |U|, IN AXONOMETRIC DIRECTION**

Static Analysis

LC9 - Aanvaring op de punt - surface load 2nd girder
 Static Analysis
 Load Increment No. 50 | Factor: 1.000
 Displacements |u| [mm]

In Axonometric Direction

Global Deformations u [mm]	
95.8	1.23 %
87.1	3.22 %
78.4	10.39 %
69.7	5.76 %
61.0	5.75 %
52.3	5.70 %
43.5	5.84 %
34.8	6.81 %
26.1	10.61 %
17.4	17.20 %
8.7	27.48 %
0.0	



max |u| : 95.8 | min |u| : 0.0 mm



Witteveen + Bos
 Van Twickelostraat 2, 7400 AE DEVENTER
 Tel: +31 5706 9708 0 - Fax: +31 5706 9734 4



Model:
 Macharen_Scenario3_Class2

Date 22.2.2024 Page 12/16
 Sheet 1

MODEL

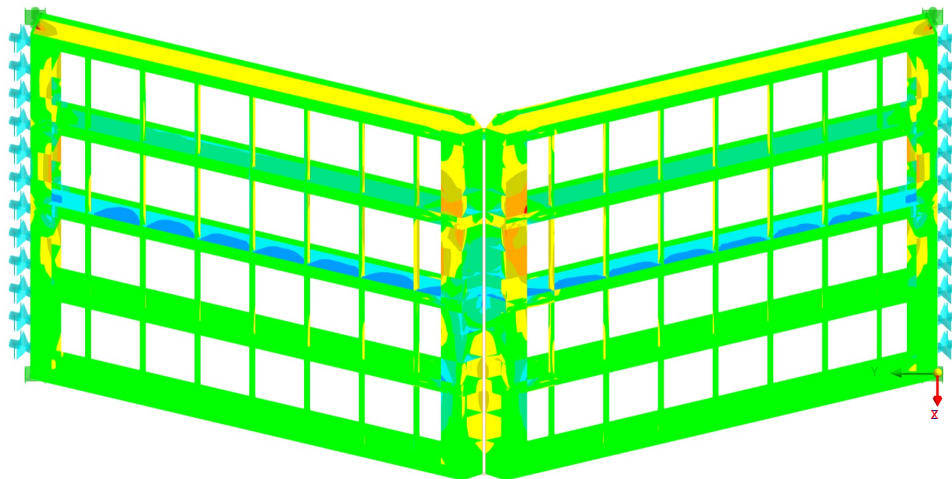
2.8 **LC9: BASIC INTERNAL FORCES N_y , IN AXONOMETRIC DIRECTION**

Static Analysis

LC9 - Aanvaring op de punt - surface load 2nd girder
 Static Analysis
 Load Increment No. 50 | Factor: 1.000
 Axial Forces n_y [kN/m]

In Axonometric Direction

Surfaces Internal Forces Basic Internal Forces n_y [kN/m]		
6693.230		0.00 %
5450.010		0.02 %
4206.800		0.59 %
2963.580		2.28 %
1720.370		12.83 %
477.152		66.57 %
-766.064		10.77 %
-2009.280		3.77 %
-3252.490		3.03 %
-4495.710		
-6982.140		0.14 %



max n_y : 6693.230 | min n_y : -6982.140 kN/m



Witteveen + Bos
 Van Twickelostraat 2, 7400 AE DEVENTER
 Tel: +31 5706 9708 0 - Fax: +31 5706 9734 4



Model:
 Macharen_Scenario3_Class2

Date 22.2.2024 Page 13/16
 Sheet 1

MODEL

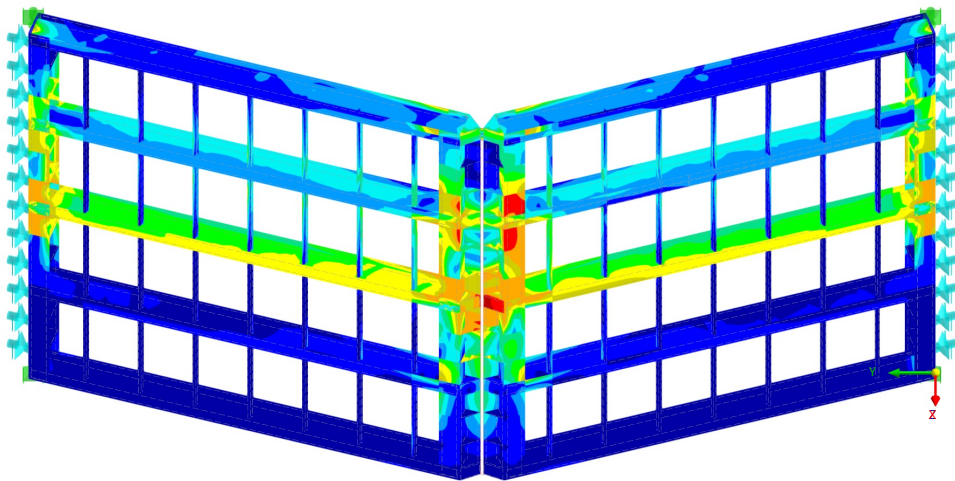
2.9 **LC9: $\sigma_{eqv,Mises}$ $\sigma_{eqv,Mises,Max}$, IN AXONOMETRIC DIRECTION**

Static Analysis

LC9 - Aanvaring op de punt - surface load 2nd girder
 Static Analysis
 Load Increment No. 50 | Factor: 1.000
 Equivalent Stresses von Mises $\sigma_{eqv,Mises,Max}$ [N/mm²]

In Axonometric Direction

Surfaces Stresses	Equivalent Stresses $\sigma_{eqv,Mises}$
$\sigma_{eqv,Mises,Max}$ [N/mm ²]	
456.450	0.09 %
-415.040	0.76 %
373.630	2.90 %
332.220	3.06 %
290.810	6.81 %
249.400	7.26 %
207.990	6.27 %
166.580	9.24 %
125.170	13.25 %
83.760	20.36 %
42.350	30.01 %
0.940	



max $\sigma_{eqv,Mises,Max}$: 456.450 | min $\sigma_{eqv,Mises,Max}$: 0.940 N/mm²



Witteveen + Bos
 Van Twickelostraat 2, 7400 AE DEVENTER
 Tel: +31 5706 9708 0 - Fax: +31 5706 9734 4



Model:
 Macharen_Scenario3_Class2

Date 22.2.2024 Page 14/16
 Sheet 1

MODEL

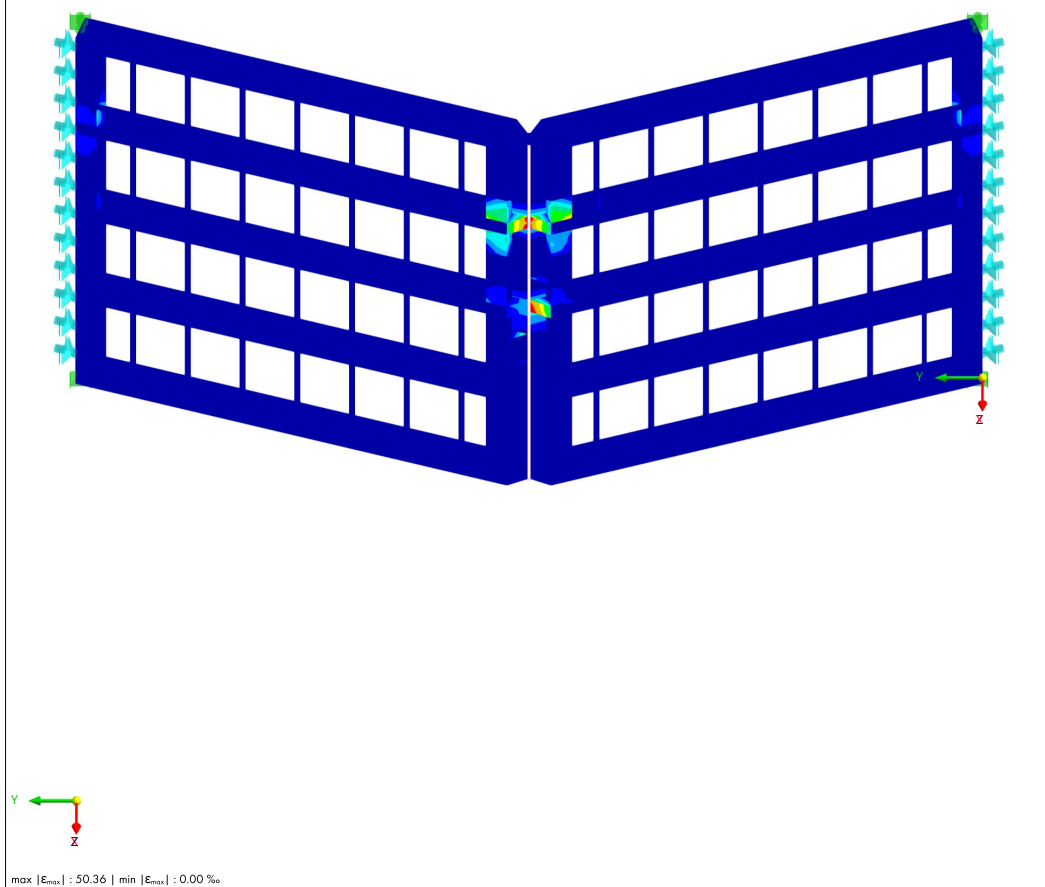
2.10 **LC9: MAXIMUM TOTAL STRAINS $|E_{max}|$, IN AXONOMETRIC DIRECTION**

Static Analysis

LC9 - Aanvaring op de punt - surface load 2nd girder
 Static Analysis
 Load Increment No. 50 | Factor: 1.000
 Maximum Strains $|E_{max}|$ [%]

In Axonometric Direction

Surfaces	Strains
Maximum Total Strains	
$ E_{max} $ [%]	
50.36	0.00 %
45.78	0.02 %
41.20	0.03 %
36.63	0.05 %
32.05	0.12 %
27.47	0.33 %
22.89	0.44 %
18.32	0.72 %
13.74	0.98 %
9.16	2.00 %
4.58	95.31 %
0.00	



Witteveen + Bos
 Van Twickelostraat 2, 7400 AE DEVENTER
 Tel: +31 5706 9708 0 - Fax: +31 5706 9734 4



Model:
 Macharen_Scenario3_Class2

Date 22.2.2024 Page 15/16
 Sheet 1

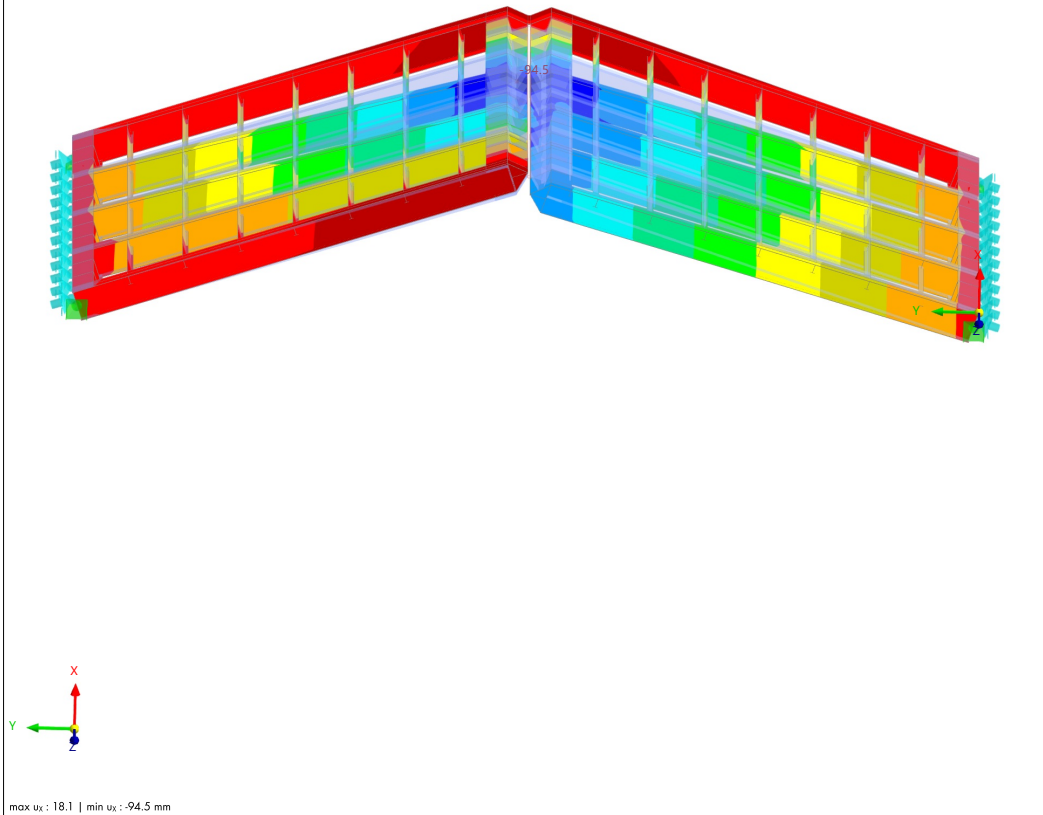
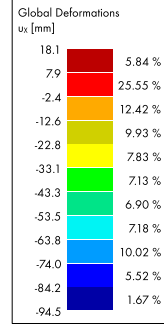
MODEL

2.11 **LC9: GLOBAL DEFORMATIONS u_x , IN AXONOMETRIC DIRECTION**

Static Analysis

LC9 - Aanvaring op de punt - surface load 2nd girder
 Static Analysis
 Load Increment No. 50 | Factor: 1.000
 Displacements u_x [mm]

In Axonometric Direction



Witteveen + Bos
 Van Twickelstraat 2, 7400 AE DEVENTER
 Tel: +31 5706 9708 0 - Fax: +31 5706 9734 4



Model:
 Macharen_Scenario3_Class2

Date 22.2.2024 Page 16/16
 Sheet 1

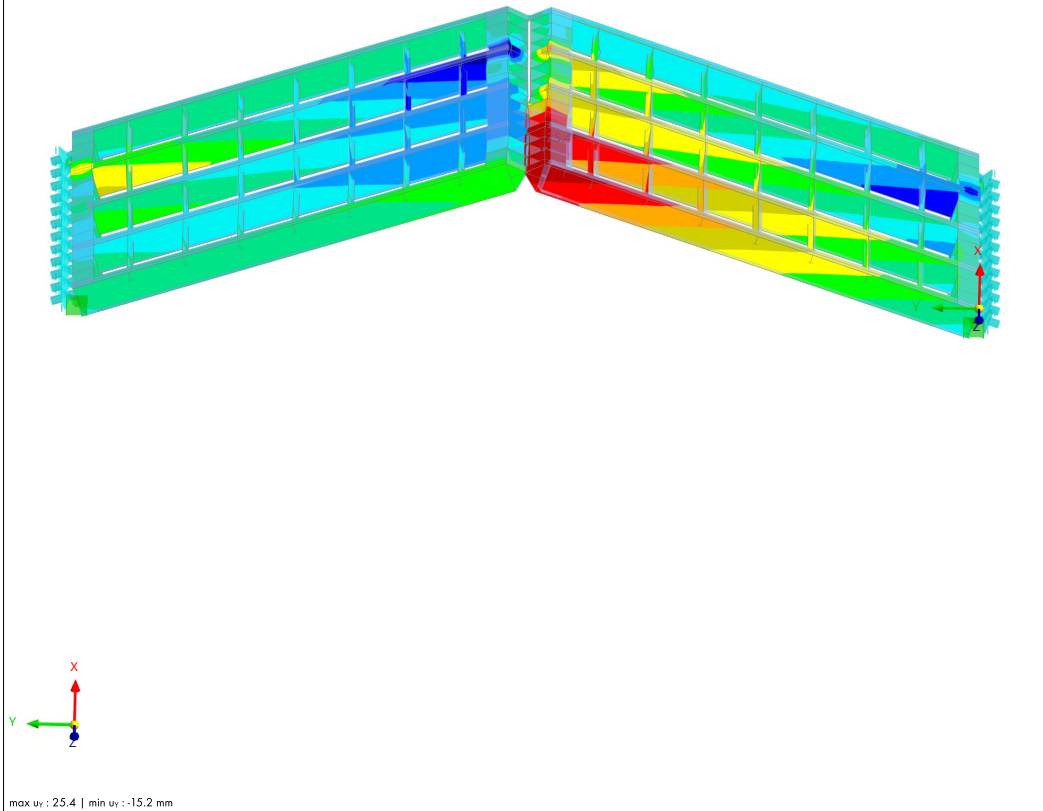
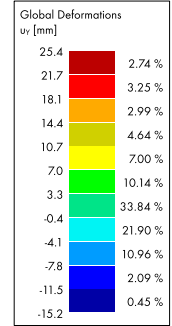
MODEL

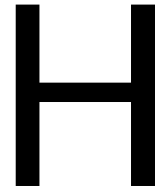
2.12 **LC9: GLOBAL DEFORMATIONS U_Y , IN AXONOMETRIC DIRECTION**

Static Analysis

LC9 - Aanvaring op de punt - surface load 2nd girder
 Static Analysis
 Load Increment No. 50 | Factor: 1.000
 Displacements u_y [mm]

In Axonometric Direction





Index vs. Energy plots per CEMT class

In this appendix, all remaining plots of the potential collision energies and calculated capacities per lock gate design are documented found. These plots are generated per CEMT class to clearly indicate which portion of vessels per class can be stopped in the event of a collision and which cannot. This is done for the three designs formulated in Section 7.2 of Chapter 6.

H.1. Original lock gate design in S235 steel

In this section, all plots are presented to determine the percentage of vessels that can be stopped based on the specified energy absorption capacity. This is done for the original lock gate design in S235 steel and, per CEMT class. These results are obtained by expanding the AIS dataset, which is also used in Chapter 3. Using the programmed dataset, the percentages are calculated for which the vessels do not exceed the specified (capacity) limits.

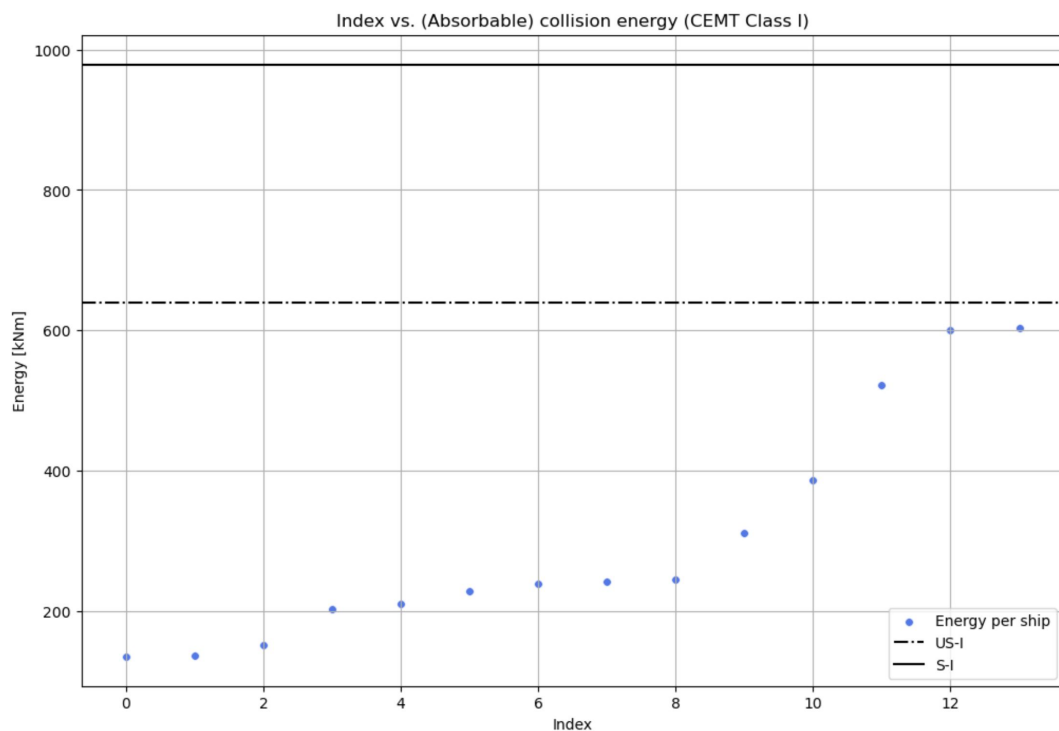


Figure H.1: Index [-] vs. Energy [kJNm] for the original lock gate design in S235 steel and CEMT class I: the percentage of data points below the energy absorption capacity in the case of an unsymmetrical and a symmetrical collision is 100% and 100%, respectively.

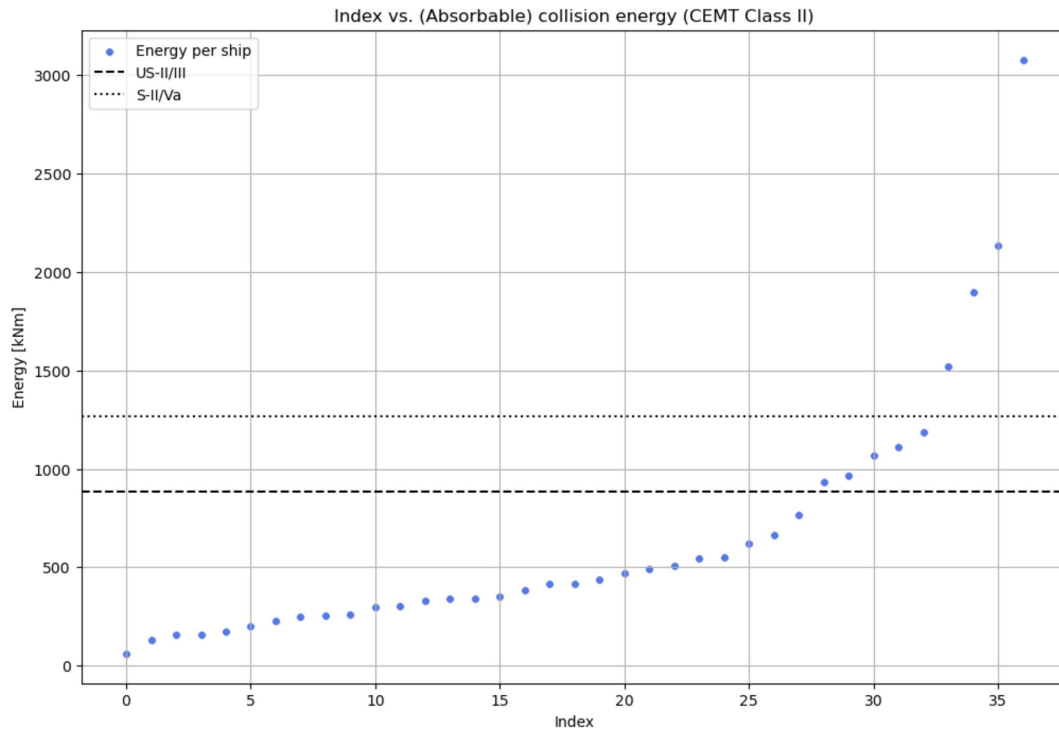


Figure H.2: Index [-] vs. Energy [kNm] for the original lock gate design in S235 steel and CEMT class II: the percentage of data points below the energy absorption capacity in the case of an unsymmetrical and a symmetrical collision is 76% and 89%, respectively.

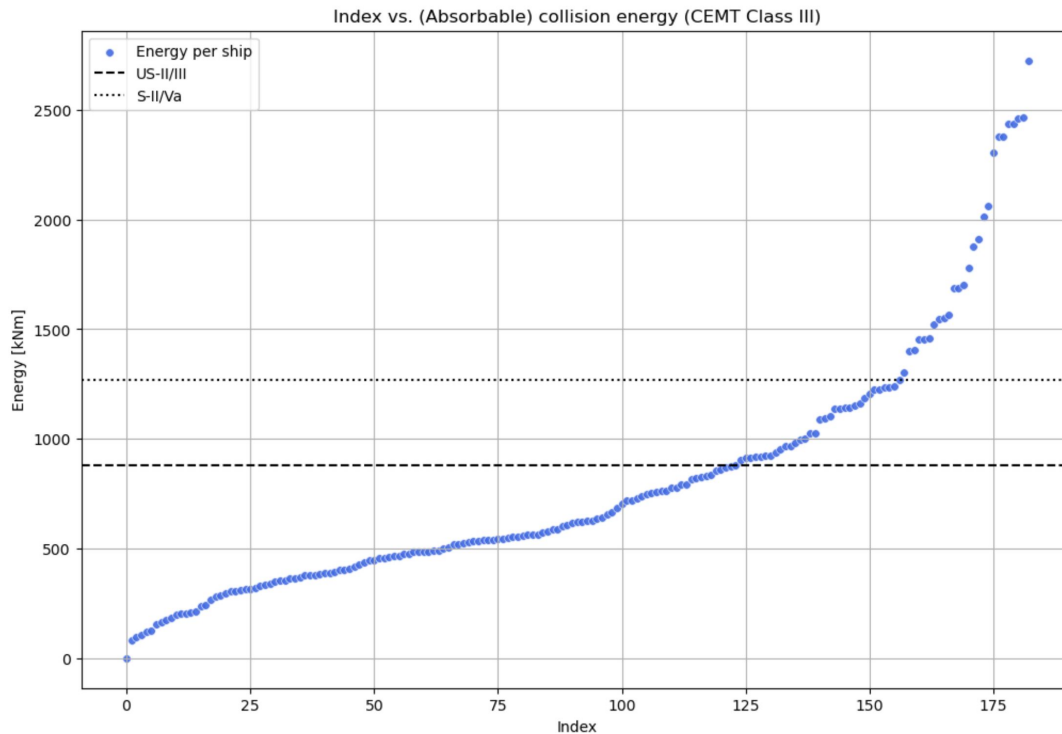


Figure H.3: Index [-] vs. Energy [kNm] for the original lock gate design in S235 steel and CEMT class III: the percentage of data points below the energy absorption capacity in the case of an unsymmetrical and a symmetrical collision is 68% and 85%, respectively.

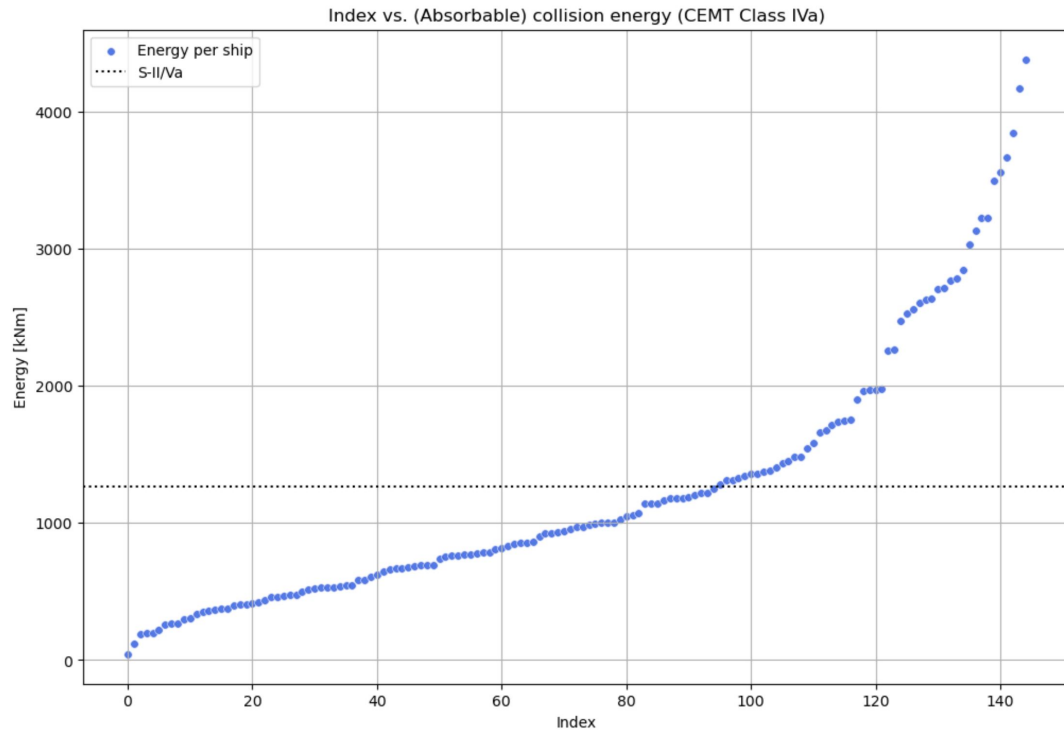


Figure H.4: Index [-] vs. Energy [kNm] for the original lock gate design in S235 steel and CEMT class IVa: the percentage of data points below the energy absorption capacity in the case of a symmetrical collision is 66%.

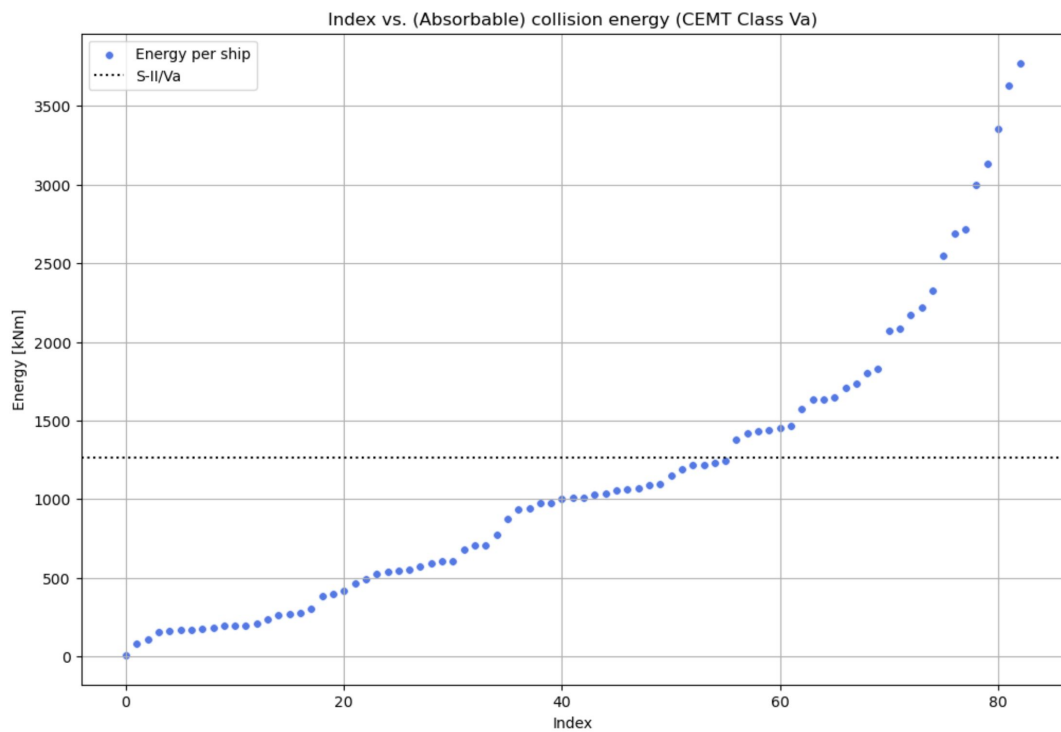


Figure H.5: Index [-] vs. Energy [kNm] for the original lock gate design in S235 steel and CEMT class Va: the percentage of data points below the energy absorption capacity in the case of a symmetrical collision is 67%.

H.2. Original lock gate design in S355 steel

In this section, all plots are presented to determine the percentage of vessels that can be stopped based on the specified energy absorption capacity. This is done for the original lock gate design in S355 steel, excluding CEMT class I. Since this design generally generates a higher capacity, and all calculated collision energies of vessels belonging to CEMT class I can be absorbed by the original design with S235 steel. Using the programmed AIS dataset, the percentages are calculated for which the vessels do not exceed the specified capacity limits.

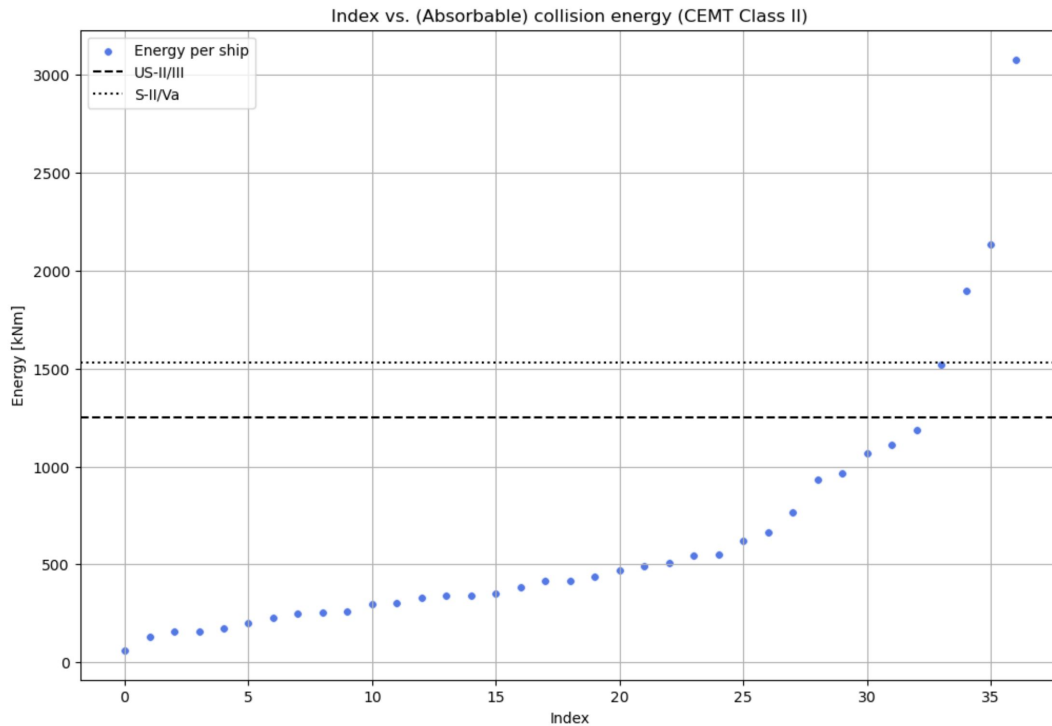


Figure H.6: Index [-] vs. Energy [kNm] for the original lock gate design in S355 steel and CEMT class II: the percentage of data points below the energy absorption capacity in the case of an unsymmetrical and a symmetrical collision is 89% and 92%, respectively.

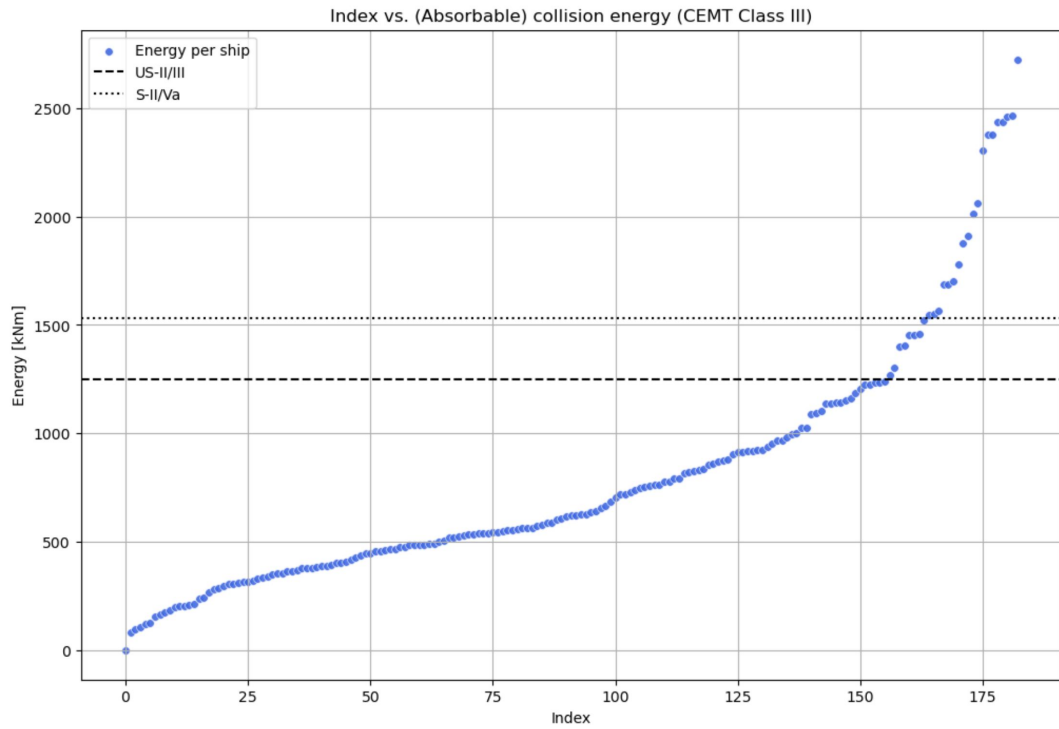


Figure H.7: Index [-] vs. Energy [kNm] for the original lock gate design in S355 steel and CEMT class III: the percentage of data points below the energy absorption capacity in the case of an unsymmetrical and a symmetrical collision is 85% and 90%, respectively.

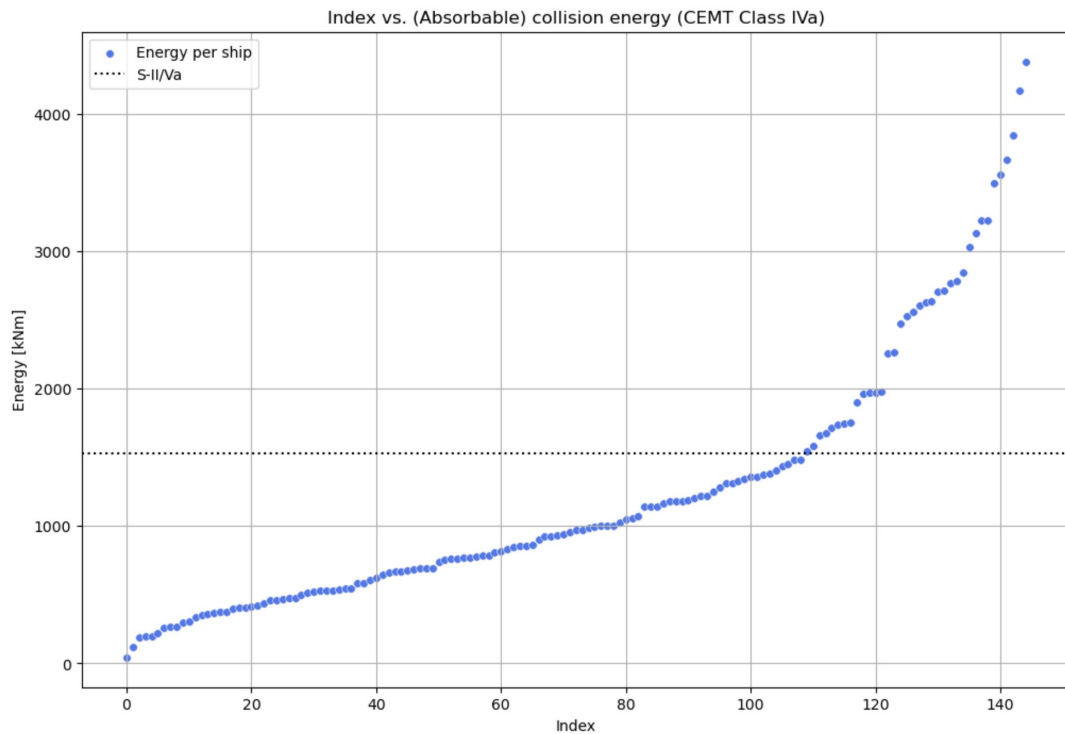


Figure H.8: Index [-] vs. Energy [kNm] for the original lock gate design in S355 steel and CEMT class IVa: the percentage of data points below the energy absorption capacity in the case of a symmetrical collision is 75%.

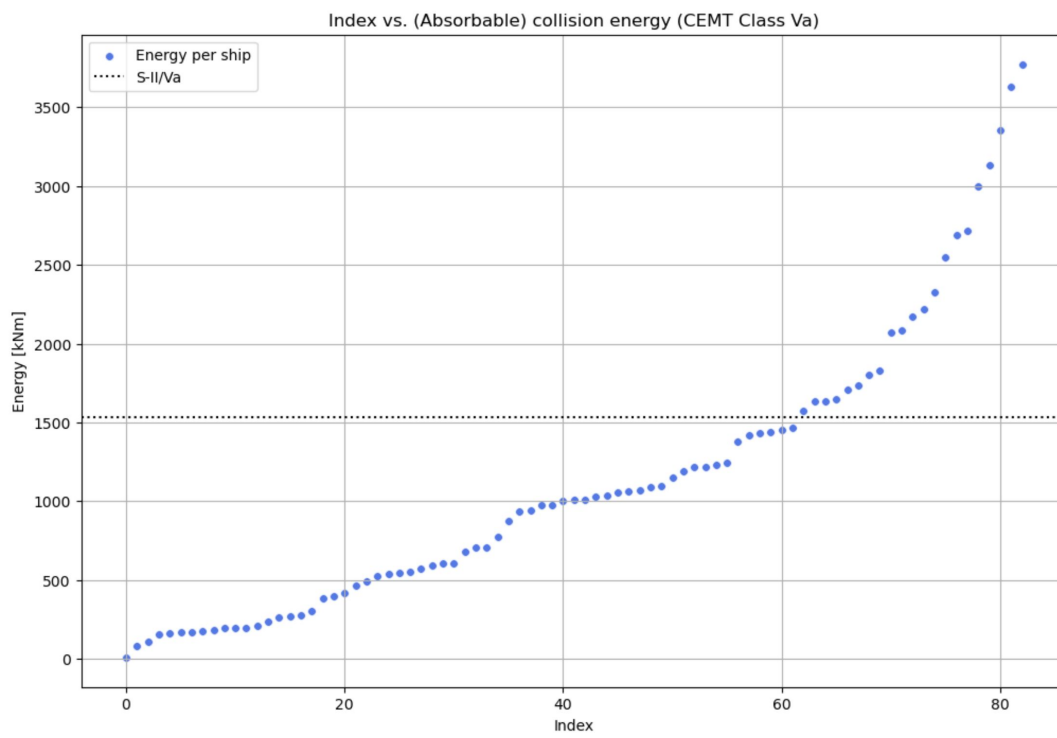


Figure H.9: Index [-] vs. Energy [kNm] for the original lock gate design in S355 steel and CEMT class Va: the percentage of data points below the energy absorption capacity in the case of a symmetrical collision is 75%.

H.3. New lock gate design in S355 steel

In this section, all plots are presented to determine the percentage of vessels that can be stopped based on the specified energy absorption capacity. This is done for the new lock gate design in S355 steel, excluding CEMT class I. Since the new design generates an higher capacity, and all calculated collision energies of vessels belonging to CEMT class I can be absorbed by the original design of the lock gate. Using the programmed AIS dataset, the percentages are calculated for which the vessels do not exceed the specified capacity limits.

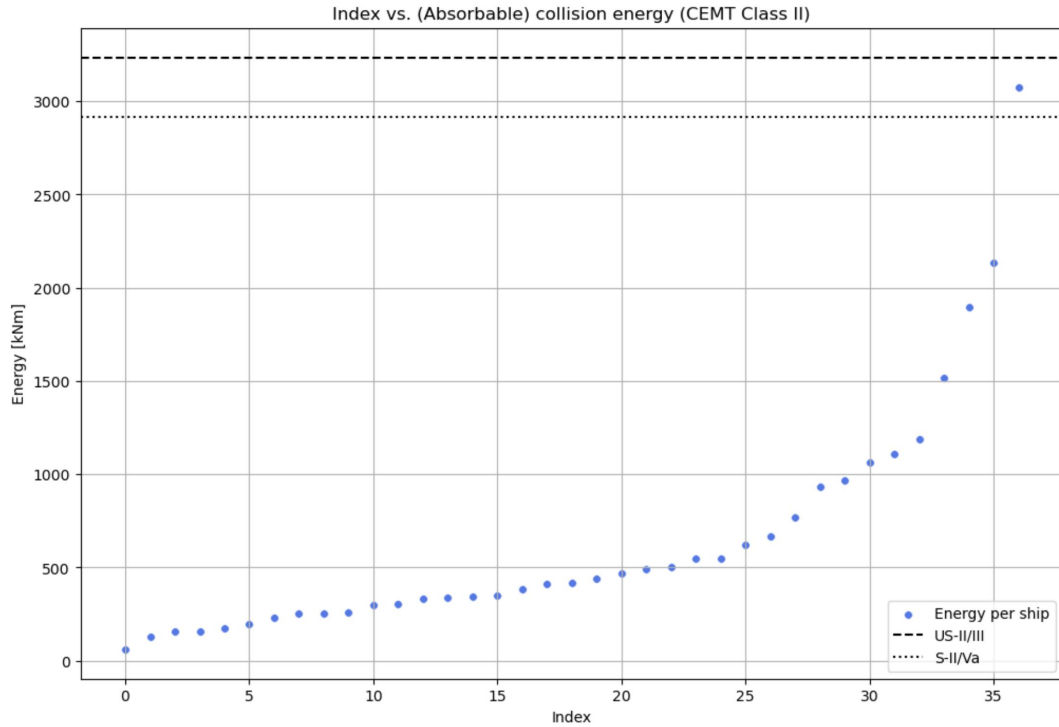


Figure H.10: Index [-] vs. Energy [kJNm] for the new lock gate design in S355 steel and CEMT class II: the percentage of data points below the energy absorption capacity in the case of an unsymmetrical and a symmetrical collision is 100% and 97%, respectively.

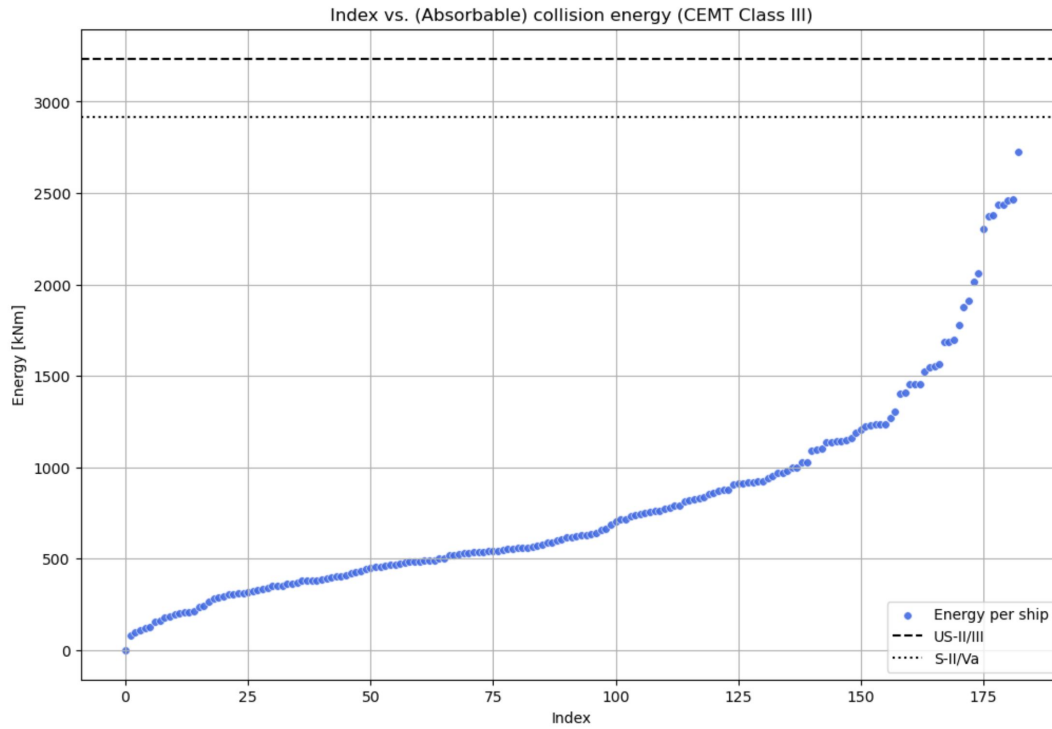


Figure H.11: Index [-] vs. Energy [kNm] for the new lock gate design in S355 steel and CEMT class III: the percentage of data points below the energy absorption capacity in the case of an unsymmetrical and a symmetrical collision is 100% and 100%, respectively.

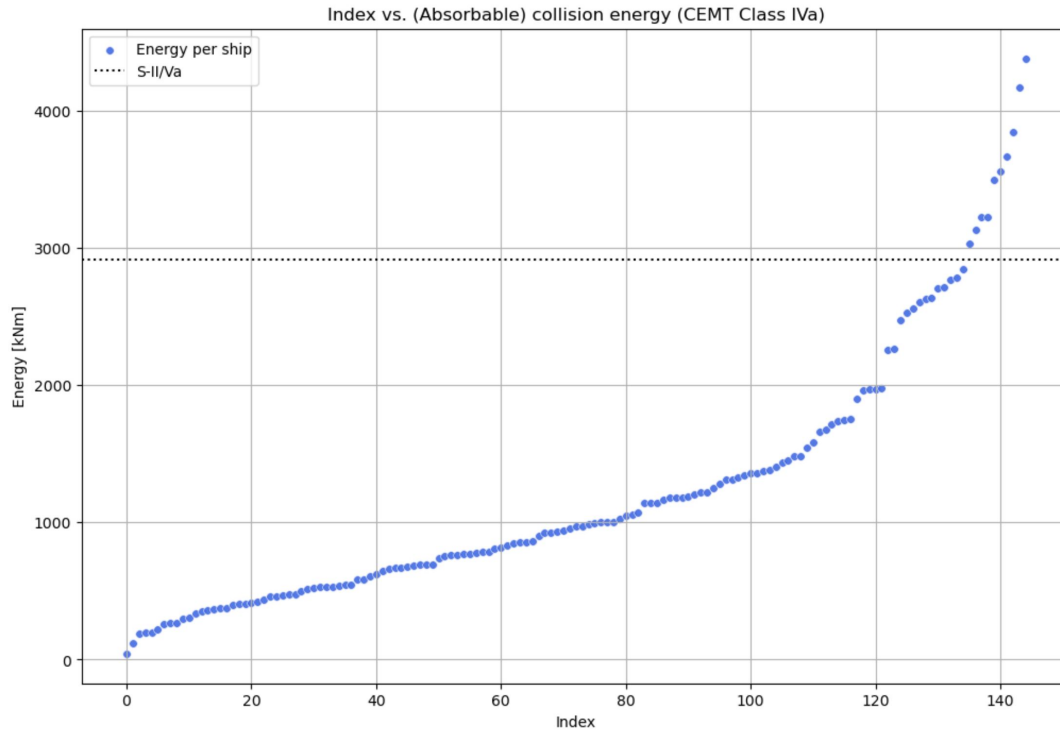


Figure H.12: Index [-] vs. Energy [kNm] for the new lock gate design in S355 steel and CEMT class IVa: the percentage of data points below the energy absorption capacity in the case of a symmetrical collision is 93%.

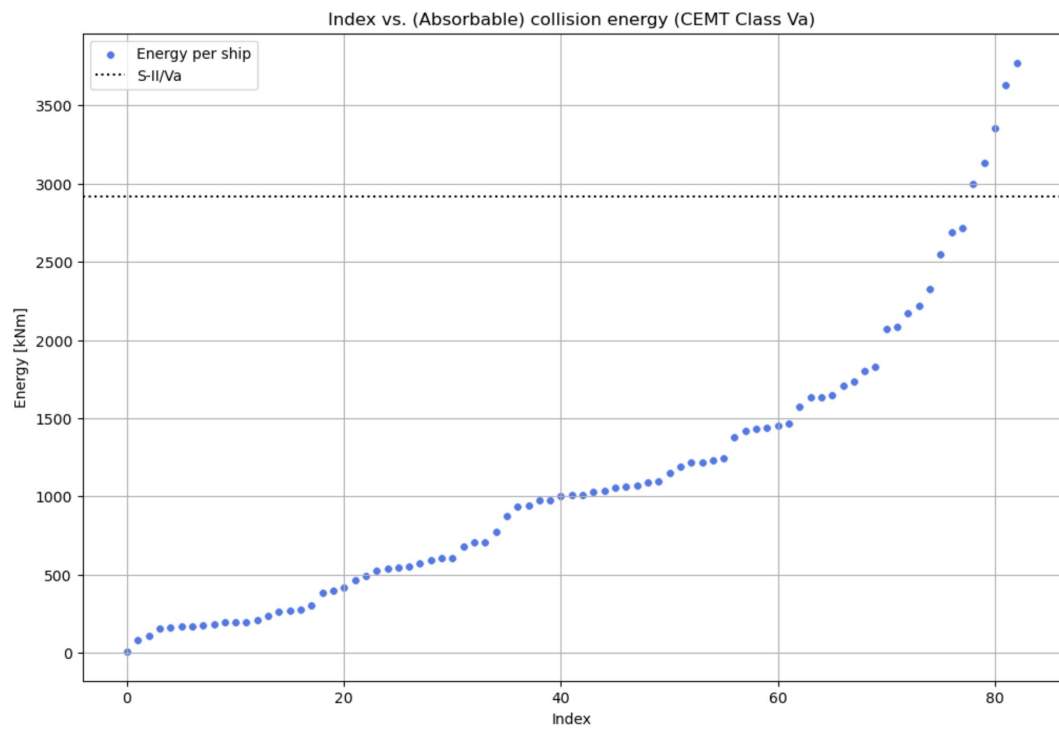


Figure H.13: Index [-] vs. Energy [kNm] for the new lock gate design in S355 steel and CEMT class Va: the percentage of data points below the energy absorption capacity in the case of a symmetrical collision is 94%.